On-Chip Multiplexers for Transferable Nanomaterials: Design, Fabrication and Applications

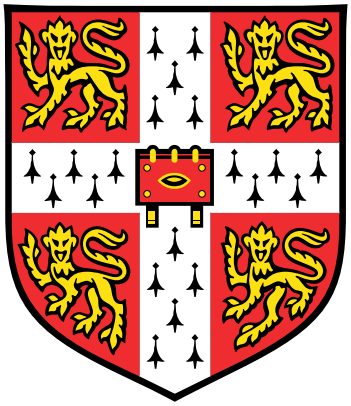

Jack Oliver Batey

Department of Physics
University of Cambridge

This dissertation is submitted for the degree of
Doctor of Philosophy

Darwin College

May 2020

I would like to dedicate this thesis to my parents Jane and Barry, who inspire me to achieve the most I can in life. Without their love and support, this work would not have been possible.

Declaration

I hereby declare that except where specific reference is made to the work of others, the contents of this dissertation are original and have not been submitted in whole or in part for consideration for any other degree or qualification in this, or any other university. This dissertation is my own work and contains nothing which is the outcome of work done in collaboration with others, except as specified in the text and Acknowledgements. This dissertation contains fewer than 65,000 words including appendices, bibliography, footnotes, tables and equations and has fewer than 150 figures.

Jack Oliver Batey
May 2020

Acknowledgements

Firstly, I would like to thank my supervisor, Charles Smith. Charles has been a fantastic mentor over the years, who has always been there to encourage me when yet another device did not work, and whose kindness, sense of humour and seemingly boundless knowledge made for great chats and discussions, which I will always remember. Next, Luke Smith. It is difficult to describe how much I owe to Luke, since he has been there to help me every day, whether that be with fabricating devices, teaching me everything I know about circuits and cryogenic measurements, or taking the time to discuss results. Above all of that however, Luke's kindness and unwavering willingness to help makes him a truly great friend. It has been a pleasure to work so closely with Charles and Luke over the years, for which I feel truly lucky.

Other members of SP who I'd like to thank include Melanie Tribble, not only for keeping the clean rooms, in which I spent so much of my time, running smoothly, but also for her continued extra effort organising social events, without which SP and the Cavendish as a whole would have been a much less enjoyable place to work. I'd like to thank Shak, Ben and Kaveh, who are always smiling, willing to chat and willing to help. Finally, I'd like to mention Ankita, who was always around for another cup of tea when PhD life was a bit much, and who has become a really great friend.

Needless to say, I must thank those with who I shared the CGC experience, in particular Mus, Cyan, Alex, Arelo and Jeff, who have all become close friends and with who I share some of my best memories of my time in Cambridge. Together, we went through a truly unique PhD experience which I am sure none of us will ever forget. Coffee breaks at the Maxwell Centre, always attended by Mus, was a particular highlight of day-to-day life as a PhD student.

Finally, I'd like to acknowledge and thank all of the people from Darwin College, particularly the faces from Darwin Bar, who made Darwin such a unique and enjoyable place to spend 4 years of my life. Special mention goes to two Darwin members, Millie and Andy, my housemates for two years and who are among my closest friends. Together we shared some almighty sessions and unforgettable memories.

Abstract

The development of scalable, on-chip multiplexing technology, capable of electrically characterising an array of nanomaterial field-effect transistors at cryogenic temperatures, is described. The channel in each transistor in the array is a nanomaterial which is transferred onto the multiplexer device, and each transistor in the array can be measured individually. The underlying multiplexer device is fabricated from a GaAs / $Al_xGa_{1-x}As$ heterostructure; nanomaterials successfully incorporated into the multiplexer circuit are monolayer graphene and InAs nanowires. Two device designs are presented: the first can characterise up to 16 field-effect transistors; the second, up to 128. A 16-output multiplexer, with 11 functioning graphene field-effect transistors is the primary focus of this thesis. This device is characterised by multiple magneto-transport experiments, which demonstrate that the multiplexing technique can be used to collect reproducible data that is consistent with existing results, at a rate higher than what would otherwise be possible. In the absence of a magnetic field, transistors are characterised by calculating commonly used metrics, such as the carrier mobility and the intrinsic carrier density, which are found to be consistent over multiple device cool-downs. In weak magnetic fields, the scattering processes are investigated by analysing weak localisation signals and reproducible conductance fluctuations. In strong magnetic fields, Landau quantisation is observed in some of the graphene channels. The level spacing is used to calculate the Fermi velocity of carriers and the cyclotron mass of carriers in each Landau level, which provides conclusive evidence that the intrinsic properties of graphene are not significantly altered by the multiplexing technique. From the magneto-transport experiments, it is evident that many-body electron interactions are relevant to the observed transport phenomena. At low temperature and strong magnetic field, a transition into an insulating state is observed in one of the channels, which also is likely to be caused by many-body effects. Finally, initial results from ongoing work are presented, which includes extending the device design so that it can operate at both room temperature and cryogenic temperature, and the measurement of InAs nanowire field-effect transistors.

Table of contents

List of figures **xv**

List of tables **xix**

1 Introduction **1**
1.1 Motivation for multiplexing 1
1.2 Background and review of relevant topics 3
1.2.1 Conductivity of graphene 3
1.2.2 Weak localisation 10
1.2.3 Universal conductance fluctuations 16
1.2.4 Quantum Hall effect 19
1.2.5 Ground states of the zero-energy Landau level 22
1.3 Conclusions 24

2 Device Design, Fabrication and Characterisation **27**
2.1 Multiplexer designs 27
2.1.1 Tiered structure: 16 outputs 27
2.1.2 Double-tiered structure: 128 outputs 32
2.2 Fabrication methods 33
2.2.1 Mesa pattern 34
2.2.2 Ohmic contacts 34
2.2.3 Back gate metallisation 35
2.2.4 Deposition of Al_2O_3 35
2.2.5 Addressing gates 36
2.3 Electrical characterisation 36
2.3.1 Channel addressing 36
2.3.2 Strong magnetic fields 37
2.3.3 Weak magnetic fields 38

2.4 Graphene transfer . . . 40
2.4.1 Surface pre-treatment . . . 41
2.5 Characterisation of device CVD-MUX-A . . . 43
2.5.1 SEM imaging of channels . . . 43
2.5.2 Estimating the channel aspect ratio . . . 43
2.5.3 Raman spectroscopy of graphene . . . 45
2.6 Conclusions . . . 54

3 Electrical Transport Measurements of Multiplexed Graphene Field-Effect Transistors at Zero Magnetic Field 57
3.1 Introduction . . . 57
3.2 Results and Analysis . . . 57
3.2.1 Reproducibility of device parameters . . . 64
3.2.2 Comparison of extracted parameters to literature . . . 64
3.2.3 Scattering time and the mean free path . . . 68
3.2.4 The minimum conductivity . . . 69
3.2.5 Correlations between device parameters . . . 69
3.2.6 Correlations between device parameters and Raman peak properties 73
3.3 Conclusions . . . 73

4 Low-Field Magneto-Transport Measurements of Multiplexed Graphene Field-Effect Transistors 75
4.1 Methods . . . 76
4.1.1 Choosing experimental parameters . . . 76
4.1.2 The averaging procedure . . . 79
4.1.3 Approximating the series resistance . . . 79
4.2 Gate-voltage dependence of quantum interference . . . 80
4.2.1 Weak localisation . . . 80
4.2.2 Conductance fluctuations . . . 87
4.3 Magneto-transport in all channels . . . 90
4.3.1 Weak localisation . . . 90
4.3.2 Conductance fluctuations . . . 95
4.4 Temperature dependence of magneto-transport . . . 97
4.4.1 Weak localisation . . . 97
4.4.2 Conductance fluctuations . . . 98
4.5 Conclusions . . . 100

5 High-Field Magneto-Transport Measurements of Multiplexed Graphene Field-Effect Transistors 105
5.1 Introduction . . . 105
5.2 Results and analysis of high-field magneto-transport measurements . . . 106
5.2.1 The quantum Hall effect in channels 2, 3, 4 and 7 . . . 106
5.2.2 Insulating transition of channel 2 . . . 116
5.3 Conclusions . . . 128

6 Ongoing Work and Conclusions 131
6.1 Introduction . . . 131
6.2 Mechanically exfoliated graphene . . . 131
6.3 Multiplexing at room temperature . . . 132
6.4 Indium arsenide nanowires . . . 135
6.5 Thesis conclusions . . . 140

References 145

Appendix A Spatial heat maps and histograms of Raman spectroscopy peak properties 163

Appendix B Statistical tests, explained 175

List of figures

1.1 Schematic diagram of a spatial multiplexing device. 2
1.2 Diagram of graphene unit cell and the corresponding Brillouin zone. 4
1.3 Results of conductivity measured as a function of gate voltage in graphene field-effect transistors, taken from existing literature. 6
1.4 The quantum Hall effect and Landau level splitting measured in graphene Hall bars, taken from Ref. [124]. 22

2.1 AutoCAD drawings of the mesa layer of the device photolithography mask. 29
2.2 AutoCAD drawings of the remaining layers of the device photolithography mask. 30
2.3 A section of AutoCAD drawing and the corresponding SEM image, showing source and drain contacts overlapping the back gate structure. 32
2.4 AutoCAD drawing of mesa and addressing gate layers of a 128-output multiplexer photolithography mask, along with photograph of a real device. 33
2.5 Circuit diagram of experimental set-up used to measure the electronic properties of the multiplexer. 36
2.6 Channel addressing curves of a shorted multiplexer device. 38
2.7 Conductance measured as a function of magnetic field up to 10 T, of a shorted multiplexer device. 39
2.8 Weak localisation effect measured in a shorted multiplexer device. 40
2.9 Images of how different surface pre-treatments affect the quality of a graphene transfer process onto a multiplexer. 42
2.10 Scanning electron microscope images of all channels of CVD-MUX-A. . . 44
2.11 Magnification of the source contact region of channel 2 of CVD-MUX-A. . 44
2.12 Example of how the aspect ratio is calculated for non-rectangular graphene channels. 46
2.13 Heat maps showing spatial distribution of peak intensities of Raman spectra taken of all channels of CVD-MUX-A. 48

2.14 Histogram of peak intensities of Raman spectra taken of all channels of CVD-MUX-A. 49
2.15 Heat maps showing spatial distribution of linewidths of Raman spectra taken of all channels of CVD-MUX. 51
2.16 Histogram of peak linewidths of Raman spectra taken of all channels of CVD-MUX-A 52
2.17 Heat maps representing the spatial distribution of the residual carrier density of all channels of CVD-MUX-A. 53
2.18 Histogram of residual carrier density n as obtained from Raman spectra of all channels of CVD-MUX-A. 54

3.1 Resistance measured as a function of gate voltage for all conducting channels of CVD-MUX-A during two separate cool-downs. 58
3.2 Diagram illustrating how doping of the graphene channel leads to conductance asymmetry. 61
3.3 Resistance measured as a function of gate voltage for channels 5, 10 and 14, showing a double peak structure. 62
3.4 Box plot comparing the distribution of devices parameters obtained by modelling the resistance as a function of gate voltage. 65
3.5 The scattering rate and the mean free path plotted as a function of the induced carrier density for each conducting channel of the device. 68
3.6 Histogram of the measured minimum conductivity in each channel. 69
3.7 The extracted device parameters for every channel plotted against each other, in order to identify correlations. 71
3.8 Linear regression plots showing correlation between certain device parameters. 72

4.1 Repeat traces of weak localisation curves for four different excitation voltages. 77
4.2 Conductance measured as a function of magnetic field in channel 3, using four different magnetic field sweep rates. 78
4.3 Conductance measured as a function of magnetic field data in channel 1, at 50 different gate voltages. 80
4.4 Fit of resistance as a function of gate voltage for electron and hole transport regions of channel 1. 82
4.5 Box plots of the dephasing rate, intervalley scattering rate and intravalley scattering rates, measured at different gate voltages in channel 1. 83
4.6 The corresponding scattering rates calculates as a function of gate voltage in channel 1. 86

4.7 The variation of the diffusion constant and it's derivative with respect to the back gate voltage. 87
4.8 Measurement and analyses of conductance fluctuations as a function of magnetic field in channel 1. 89
4.9 Measured weak localisation effect in every channel of CVD-MUX-A. . . . 91
4.10 Dephasing length plotted as a function of channel number and estimated probability densities for the dephasing length. 92
4.11 Box plot comparing the distribution of dephasing lengths for different carrier types and measurement methods. 92
4.12 Conductance fluctuations measured as a function of magnetic field for every channel of CVD-MUX-A. 96
4.13 Temperature dependence of dephasing length, intervalley scattering length and intravalley scattering length in channels 1, 2 and 3. 99
4.14 Temperature dependence of the dephasing rate in channels 1, 2 and 3. . . . 100
4.15 Conductance fluctuations measured as a function of magnetic field and temperature for different carrier types in channels 1, 2 and 3. 101
4.16 Analyses of the temperature dependence of conductance fluctuations in channels 1, 2 and 3. 102

5.1 Measurement and analyses of the quantum Hall effect in channel 2. 107
5.2 Measurement and analyses of the quantum Hall effect in channel 3. 108
5.3 Measurement and analyses of the quantum Hall effect in channel 4. 109
5.4 Measurement and analyses of the quantum Hall effect in channel 7. 110
5.5 Box plots of the cyclotron mass in each non-zero Landau level for channels 2, 3, 4 and 7. 114
5.6 The cyclotron frequency and magnetic length plotted as a function of magnetic field. 116
5.7 Resistance measured in channel 2 as a function of magnetic field up to 10 T at fifty different gate voltage values. 117
5.8 A scanning electron microscope image of channel 2 and a magnification of the graphene-metal contact region. 118
5.9 Three-dimensional surface plots of the resistance of channel 2 as a function of source-drain bias voltage and gate voltage, at different temperatures. . . 119
5.10 Various plots of conductance and resistance of channel 2 plotted as a function of magnetic field up to 10 T at different temperatures. 121
5.11 Repeat measurements of conductance at 10 T and low filling factors of channel 2. 123

5.12 Arrhenius plot of conductance and plots of resistance of channel 2 as a function of gate voltage at 10 T and zero source-drain bias. 125
5.13 A Lorentzian fit and a Gaussian fit to the resistance as a function of gate voltage of channel 2. 127

6.1 Images of the mechanically exfoliated graphene flakes on a multiplexer device. 132
6.2 Resistance measured as a function of gate voltage of multiplexed, exfoliated graphene flakes. 133
6.3 Schematic diagrams illustrating the cross section of a heterostructure designed to operate at room temperature. 134
6.4 Addressing gate curves of a shorted multiplexer operating at both 4.2 K and room temperature. 135
6.5 Images of the transfer and contacting process of InAs nanowires on a multiplexer device. 137
6.6 Transfer characteristics of multiplexed InAs nanowires. 138
6.7 Examples of how the drain current is used to calculate the transconductance and subthreshold swing of InAs nanowire field-effect transistors. 139

A.1 Channel 1: Raman spectroscopy peak intensity data. 164
A.2 Channel 2: Raman spectroscopy peak intensity data. 165
A.3 Channel 3: Raman spectroscopy peak intensity data. 166
A.4 Channel 4: Raman spectroscopy peak intensity data. 167
A.5 Channel 5: Raman spectroscopy peak intensity data. 168
A.6 Channel 7: Raman spectroscopy peak intensity data. 169
A.7 Channel 9: Raman spectroscopy peak intensity data. 170
A.8 Channel 10: Raman spectroscopy peak intensity data. 171
A.9 Channel 11: Raman spectroscopy peak intensity data. 172
A.10 Channel 14: Raman spectroscopy peak intensity data. 173
A.11 Channel 16: Raman spectroscopy peak intensity data. 174

List of tables

2.1 Addressing gate combinations required to select each of the 16 multiplexer outputs. 37
2.2 Estimated aspect ratios of irregular shape graphene channels of device CVD-MUX-A. 45
2.3 Statistics describing intensity of Raman spectra taken of the channels of device CVD-MUX-A. 49
2.4 Statistics describing linewidth of Raman spectra taken of the channels of device CVD-MUX-A. 50
2.5 Statistics describing carrier density determined from the *G*-peak position of Raman spectra taken of the channels of device CVD-MUX-A. 52

3.1 Parameters obtained by fitting resistance of each channel of CVD-MUX-A as a function of back gate voltage at 4.2 K. 62
3.2 Parameters obtained by fitting resistance of each channel of CVD-MUX-A as a function of back gate voltage at 0.28 K. 63
3.3 Parameters obtained by performing separate fits to the two peaks observed in the resistance of channels 5, 10 and 14 of CVD-MUX-A, as a function of back gate voltage at 4.2 K. 63
3.4 Parameters obtained by performing separate fits to the two peaks observed in the resistance of channels 5, 10 and 14 of CVD-MUX-A, as a function of back gate voltage at 4.2 K. 63
3.5 Summary of mobilities of CVD-grown graphene field-effect transistors, reported elsewhere. 66
3.6 Statistics of regression analysis between carrier mobilities, contact resistance and intrinsic carrier density for all channels of CVD-MUX-A. 70

4.1 Statistics describing linear regression analysis of scattering lengths with gate voltage for channel 1 of CVD-MUX-A. 81

4.2 Statistics describing linear regression analysis of scattering rates with gate voltage for channel 1 of CVD-MUX-A. 86
4.3 Statistics describing distribution of dephasing lengths for different carrier types and measurement methods. 93
4.4 Results of analysis-of-variance tests quantifying the affect of carrier type and measurement method on dephasing length. 93
4.5 Difference between mean values of the dephasing length when an averaging method is used to collect data and when it is not. 94
4.6 Results of t-tests comparing the dephasing rate when estimated from fitting a weak localisation signal to when it is estimated from an autocorrelation function. 97
4.7 Results of a linear regression analysis of the temperature dependence of the dephasing rate. 98

5.1 Mean values of cyclotron mass of carriers in non-zero Landau levels for channels 2, 3, 4 and 7 of CVD-MUX-A. 113
5.2 Values of resistance and conductance of reproducible plateaux occurring at low filling factors. 123

6.1 Parameters describing the performance of multiplexed InAs nanowire field-effect transistors. 140

Chapter 1

Introduction

1.1 Motivation for multiplexing

The concept of transmitting multiple data streams using a shared medium is not new, and forms the basis of many familiar technologies such as television and radio. The process of transmitting multiple data streams a over shared medium is known as multiplexing, and the devices which achieve this are known as multiplexers. The motivation follows from improving the efficiency of the transmission medium which can be scarce, for example by increasing the bandwidth of an optical cable [1, 2]. Recently, interest has grown in on-chip multiplexing systems. The majority of reported devices focus on multiplexing photonic signals, due to the widespread use of optical communications networks and the development of photonic quantum communication technology [3–8]. Aside from photonic technology, there is interest in utilising low-dimensional semiconductor devices in quantum electronic applications. As examples, it has been shown that current flowing through quantum point contacts defined on a 2-dimensional electron gas (2DEG), residing in a GaAs / $Al_xGa_{1-x}As$ heterostructure, can be spin-polarised using the electric-field alone [9–12], while there is a strong interest in using solid-state quantum dots to host spin and charge qubit states [13–15]. The quantum states hosted by such devices are often fragile and sensitive to fluctuations in the environment, which may arise from charge density inhomogeneities induced by disorder, arising from the materials growth process or device fabrication process, for example. Furthermore, many of the quantum properties of these device arise due to spatial confinement of electronic states. This implies that a high degree of control over the growth and fabrication process at the nanometre scale is required in order to manufacture solid-state quantum electronic devices with consistent performance. The topic of manufacturing devices at the nanometre scale is discussed by Kelly in Refs. [16, 17]. It is argued that current top-town fabrication methods cannot consistently reproduce features on the scale of 7 nm, due to the inherent

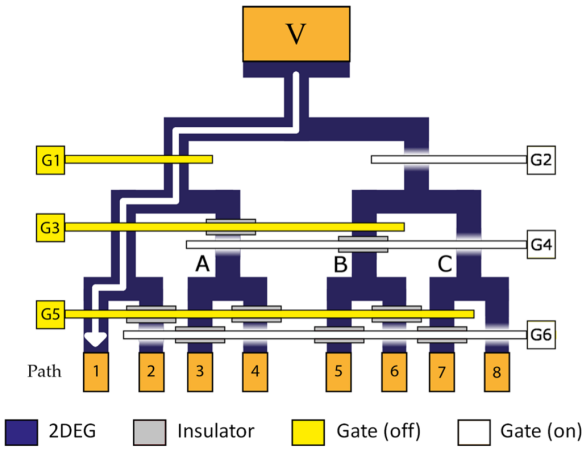

Fig. 1.1 Schematic diagrams showing the principle of operation of the multiplexer technology developed in Ref. [18]. Details of the device operation are provided in the main text.

statistical variation which arises when trying to define features which are composed of a small number of atoms. Although not all solid-state quantum technologies will require precise spatial control down to the 7 nm scale, these arguments highlight the need for statistical analysis of device performance, so that the variance of key metrics can be understood. It is therefore important that an efficient method is developed to measure large numbers of quantum electronic devices, so that enough data can be obtained to perform the necessary statistical analysis.

To this end, Al-Taie *et al.* developed an on-chip multiplexer, capable of measuring the conductance up to 256 split-gate transistors at cryogenic temperature, during a single cool-down [18]. Using the multiplexing technique it was found that 94% of all fabricated transistors conducted, and that 84% of transistors showed quantised conduction after illumination. A previous study measured the conductance of 540 split-gate transistors, however each chip contained only 6 devices and 90 cool-downs were required to measure all of the devices [19]; a similar number is achievable using the multiplexing technique described in Ref. [18] after only 2 cool-downs. Smith *et al.* were able to use the same multiplexing technique to perform a statistical study of the 0.7 anomaly [20–22], a reproducible feature arising in the quantised conductance of a 1D wire at $G = 0.7(2e^2/h)$ [23, 24]. From the studies of Refs. [20–22] the authors found that the anomaly does not occur exactly at $G = 0.7(2e^2/h)$ and varies between devices, and were able to relate the variation to the curvature of the potential barrier induced by the gates, and the disorder potential in the channel. These results were only possible by studying an ensemble of devices. A similar multiplexer device was used to to spatially map the variation of intrinsic charge density of a 1.5 mm$\times$1.95 mm area of GaAs / $Al_xGa_{1-x}As$ heterostructure [20].

The multiplexer technology developed in Ref. [18] is a form of spatial multiplexing, where signals are routed to different locations in space. A schematic diagram taken from Ref. [18] which shows the operating principle of the device is shown in Fig. 1.1. An excitation voltage is applied to an ohmic contact labelled V which is connected to the 2DEG. Negative voltages on selected addressing gates, labelled $G1-6$, are used to deplete carriers from the 2DEG and stop conduction in selected spatial regions, while allowing other regions to remain conductive. The details of how spatial selectivity is achieved are provided in Chapter 2. By turning off selected branches of the 2DEG the excitation signal can be directed to a single chosen output, labelled 1-8. The multiplexing technology developed in Ref. [18] forms the basis of the work presented in this thesis, and is extended so that nanomaterials can be electrically characterised at cryogenic temperature. So far graphene and InAs nanowires have been successfully incorporated into a GaAs / $Al_xGa_{1-x}As$ on-chip multiplexer circuit however, many more materials may be characterised using this technology, in principle. Since nanomaterials such as graphene and InAs nanowires inherently provide spatial confinement in at least one dimension, they are attractive candidates for quantum technology applications, for example as new qubit architectures and nanoscale transistors [25–27]. However, as with previous examples, performance metrics between devices will vary and it is important to develop an efficient method of measuring large numbers of devices made from these nanomaterials. This is the primary motivation for developing an on-chip multiplexing device which is capable of characterising emerging nanomaterials.

In conclusion to this section, the motivations for multiplexing and the technology upon which the present work is based have been described. The next section provides a review of the relevant physics required to interpret and understand the results of magneto-transport experiments presented in later chapters. In the summary of this chapter, the structure of the remainder of the thesis is outlined.

1.2 Background and review of relevant topics

1.2.1 Conductivity of graphene

This section provides an overview of the physics responsible for the observed conductivity behaviour of monolayer graphene, in the absence of an applied magnetic field.

In contrast to conventional semiconductors, which have a parabolic dispersion relation near the minimum (maximum) of the conduction (valence) bands, and a finite, non-zero energy gap separating them, pristine, un-doped graphene has a linear dispersion relation at low energy, with precisely zero band gap and zero carrier density. This result was first

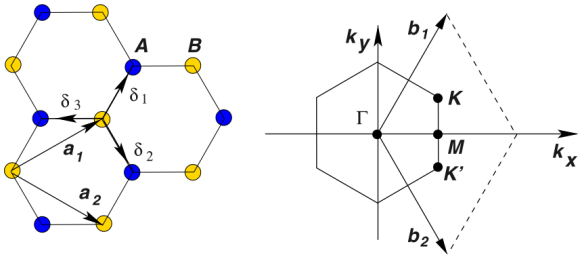

Fig. 1.2 A diagram of the real-space graphene lattice shown on the left, where blue and yellow circles denote carbon atoms on two different sub-lattices, $\mathbf{a}_1$ and $\mathbf{a}_2$ are the lattice unit vectors and δ_i ($i = 1,2,3$) are the nearest-neighbour vectors. The corresponding Brillouin zone is shown on the right, along with the reciprocal lattice unit vectors $\mathbf{b}_1$ and $\mathbf{b}_2$. The corners of the Brillouin zone marked $\mathbf{K}$ and $\mathbf{K}'$ are the points at which the conduction and valance bands cross, and $\mathbf{M}$ is the midpoint between them. Figure taken from Ref. [28].

shown in 1947 by Wallace in Ref. [29], who used a nearest-neighbour tight-binding model to calculate the band structure of graphite. This is a consequence of the hexagonal, honeycomb crystal structure of graphene, which can be thought of as a combination of two triangular sublattices, constructed using C atoms, as shown in the left diagram of Fig. 1.2 which has been taken from Ref. [28]. The lattice is described by the pair of unit vectors:

$$\mathbf{a}_1 = \frac{a}{2}(3,\sqrt{3}), \qquad \mathbf{a}_2 = \frac{a}{2}(3,-\sqrt{3}), \tag{1.1}$$

where $a \approx 1.42\,\text{Å}$. The corresponding reciprocal lattice vectors are:

$$\mathbf{b}_1 = \frac{2\pi}{3a}(1,\sqrt{3}), \qquad \mathbf{b}_2 = \frac{2\pi}{3a}(1,-\sqrt{3}). \tag{1.2}$$

The conduction and valence bands cross at the edges of the Brillouin zone at two non-equivalent points labelled $\mathbf{K}$ and $\mathbf{K}'$ in Fig. 1.2 and are often referred to as two non-equivalent valleys in momentum space. Their coordinates are:

$$\mathbf{K} = \left(\frac{2\pi}{3a}, \frac{2\pi}{3\sqrt{3}a}\right), \qquad \mathbf{K}' = \left(\frac{2\pi}{3a}, \frac{2\pi}{3\sqrt{3}a}\right). \tag{1.3}$$

Since it is possible to define the point of zero energy at the position where conduction and valence bands cross the low energy dynamics of carriers and graphene is described by only considering carriers with momentum $\mathbf{k}$ close to these values. In 1984, reported in Ref. [30], Semenoff expanded the tight-binding model of graphene about the points $\mathbf{K}$ and $\mathbf{K}'$ and then took the continuum limit to derive a continuous, field-theoretic description of low-energy charge carriers in graphene. When considering the dynamics around a single valley, the

result presented in Ref. [30] shows that carrier motion is governed by a 2-dimensional Weyl equation with the following Hamiltonian:

$$H = \hbar v_F \boldsymbol{\sigma} \cdot \mathbf{k}, \tag{1.4}$$

where $v_F \approx 1 \times 10^6$ ms^{-1} is the Fermi velocity of a charge carrier in graphene, $\boldsymbol{\sigma} = (\sigma_x, \sigma_y)$ is a vector of two-dimensional Pauli matrices, and $\mathbf{k} = (k_x, k_y)$ is a two-dimensional momentum vector. The eigenvalues of the Hamiltonian Eqn. 1.4 are given by:

$$E(\mathbf{k}) = \pm \hbar v_F |\mathbf{k}|, \tag{1.5}$$

where $+$ refers to electron states and $-$ refers to hole states. Since $\mathbf{k}$ is a continuous variable and since the energy of electrons $E_e(\mathbf{k})$ (positive solution of Eqn. 1.5) and holes, $E_h(\mathbf{k})$ (negative solution of Eqn. 1.5) are symmetric about zero, that is $|E_e| = |E_h|$, it can be seen that as $\mathbf{q} \to 0$, both $E_e, E_h \to 0$ and there is no gap in the spectrum. Instead of a band gap, the carrier type switches from electrons to holes as $\mathbf{q}$ changes from positive to negative. This result showed that the low-energy dynamics of carriers in graphene agree with the result derived earlier by Wallace.

The Hamiltonian Eqn. 1.4 can be used as a starting point to calculate the conductivity of a graphene sample as a function of the carrier density, which is necessary to understand the behaviour of graphene field-effect transistors (GFETs). Initial progress was made by the authors of Refs. [31, 32], who neglected all forms of impurity scattering and electron-electron interactions in their calculations. The authors employ different methods to calculate the conductivity: Ref. [31] uses the Kubo formalism (linear response theory) to calculate a conductivity tensor, while Ref. [32] uses the Landauer formula which connects non-interacting incoming and outgoing states by a scattering matrix.

Both report a non-zero conductivity of $\sigma = 4e^2/\pi h$ at the point of zero carrier density n, known as the Dirac point, where the conduction and valence bands cross. At non-zero carrier density, they predict that the conductivity is constant function of n. However, experimental results from graphene field effect transistors showed that this is not true: Ref [33] found the minimum conductivity, across 15 samples, to be approximately $\sigma_{min} \approx 4e^2/h$, but not universally, and independent of the carrier mobility, with the conductivity increasing linearly as a function of carrier density; Ref [34] found the minimum values of conductivity to vary between 2-20 e^2/h but found that the conductance was linearly dependent on carrier density for high mobility samples, and sub-linearly dependent on carrier density for low mobility samples.

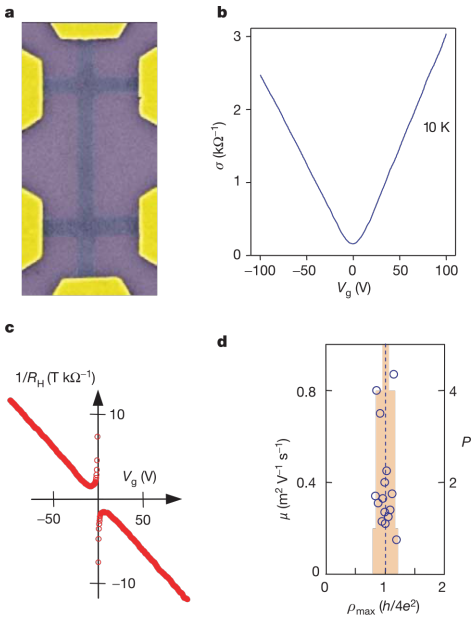

(a) The electric field effect in a back-gated graphene Hall bar. Sub-figure (b) shows the linear dependence of σ on n and sub-figure with the gradients of the curve approximately equal either side of the minimum (d) shows the mobility independent variation of the maximum resistance about the value $4\,e^2/h$.

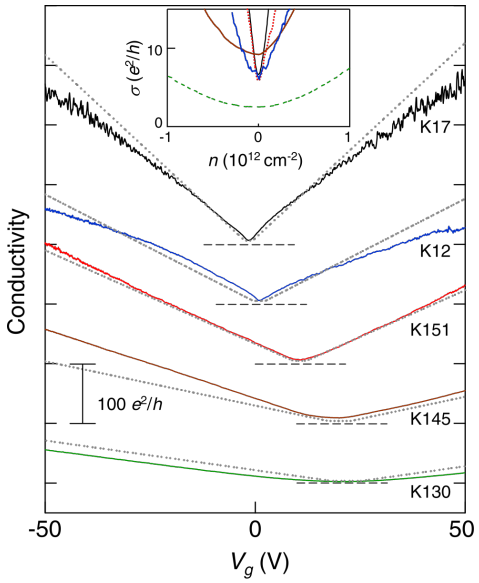

(b) Plots of σ against V_g for devices with varying levels of disorder. The traces labelled K17 and K12 show sub-linear behaviour while the other traces show behaviour closer to linear, however with different gradients for electrons and holes. The traces are offset vertically by $100\,e^2/h$.

Fig. 1.3 Figures taken from Refs. [33, 34], showing the observed dependence of conductivity on gate voltage.

The variation of the shape of the observed $\sigma(V_g)$ curves is caused by interplay between different types of impurities (neutral, charged, short-range and long-range) but it has been shown in Refs. [35–38] that scattering from charged impurities in the substrate is the dominant mechanism which dictates the V_g dependence of σ. A simple argument provided in the above references based upon Fermi's golden rule demonstrates that Coulomb impurity scattering dominates near the Dirac point. Fermi's golden rule states that the scattering rate $1/\tau$ from some initial state $|i\rangle$ to final state $|f\rangle$ is proportional to the probability of the transition occurring, represented by the transition matrix element:

$$\frac{1}{\tau} \approx \frac{2\pi}{\hbar} |\langle f|V|i\rangle|^2 \delta(E_f - E_i), \tag{1.6}$$

where $|\langle f|V|i\rangle| = \int \psi_f^* V \psi_i d^2\mathbf{r}$ is the 2-dimensional overlap integral of the final wavefunction with the initial wavefunction, and E_F and E_i are the energies of the final and initial states, respectively. Short-range, neutral scattering impurities such as lattice defects, are modelled using delta functions $V = u\delta(\mathbf{r})$. The problem can be illustrated by considering the scattering rate of a plane wave with momentum $\mathbf{k}$ into a *continuum* of states of momentum $\mathbf{k}'$. Note a proper treatment would consider the scattering of Bloch states, however for the purposes of illustrating how the scattering rate depends on carrier density n, plane waves will suffice. The overlap integral in 2-dimensions is given by:

$$|\langle \mathbf{k}'|V|\mathbf{k}\rangle| = \int \left(\frac{e^{-i\mathbf{k}'\cdot\mathbf{r}}}{\sqrt{A}}\right) u\delta(\mathbf{r}) \left(\frac{e^{i\mathbf{k}\cdot\mathbf{r}}}{\sqrt{A}}\right) d^2\mathbf{r} = \frac{u}{A}, \tag{1.7}$$

where A is the 2-dimensional volume element and the final equality is obtained by using the definition of the Fourier transform of the Dirac delta function is equal to 1 and the fact that the integral over space of $\delta(\mathbf{r})$ is equal to 1. Substituting the result from Eqn. 1.7 into Eqn. 1.6, summing over all possible final momenta $\mathbf{k}'$, and finally taking the continuum limit by making the substitution $(1/A)\sum_{\mathbf{k}} \to 1/(2\pi)^2 \int d^2\mathbf{k}'$ the scattering rate becomes:

$$\begin{aligned}
\frac{1}{\tau} &= \frac{2\pi}{\hbar}\frac{u^2}{A^2}\sum_{\mathbf{k}'} \delta(E_{\mathbf{k}} - E_{\mathbf{k}'}) \\
&= \frac{2\pi}{\hbar}\frac{u^2}{A^2}\frac{A}{(2\pi)^2}\int \delta(E_{\mathbf{k}} - E_{\mathbf{k}'}) d^2\mathbf{k}' \\
&= \frac{2\pi u^2}{A\hbar} D(E),
\end{aligned} \tag{1.8}$$

where the second line is obtained by taking the continuum limit and the final line is obtained using the definition of the density of states $D(E) = 1/(2\pi)^2 \int \delta(E_{\mathbf{k}} - E_{\mathbf{k}'}) d^2\mathbf{k}'$. This is the

scattering rate of plane wave in an initial state $|\mathbf{k}\rangle$ to a continuum of final states $|\mathbf{k}'\rangle$ due to a *single* short-range scattering centre. Notice that the result depends on the macroscopic area A. When considering multiple short-range scattering centres, as is the case in any realistic system, the scattering rate must be multiplied by the number of scattering centres $N_{imp} = n_{imp}A$, where n_{imp} is the density of scattering centres. This makes the final scattering rate of a plane wave in an initial state $|\mathbf{k}\rangle$ to a continuum of final states $|\mathbf{k}'\rangle$ due to multiple short-range scattering centres independent of A:

$$\frac{1}{\tau} = \frac{2\pi}{\hbar} u^2 n_{imp} D(E). \tag{1.9}$$

From Eqn. 1.9 it can be seen then that $1/\tau \propto D(E)$. Since in graphene $D(E) \propto E$ and $E \propto k \propto \sqrt{n}$, see Eqn. (15) of Ref. [28], it follows that $D(E) \to 0$ as $n \to 0$. Equation 1.9 therefore implies that $\tau \to \infty$ as $n \to 0$, demonstrating that short-range scattering becomes irrelevant at low carrier densities. The calculation can be repeated for the Coulomb potential where $V \propto 1/r$, however the full calculation is much more difficult due to screening effects. The Fourier transform of the screened Coulomb interaction can be approximated as [38, 39]:

$$V_c(\mathbf{q}) \approx \frac{\hbar v \pi}{2k_F}. \tag{1.10}$$

Since the approximated form of V_c is independent of $\mathbf{r}$, it can be moved out of the overlap integral which then simply evaluates to $1/A$, and the scattering rate is given by:

$$\frac{1}{\tau} \approx \frac{2\pi}{\hbar} \left(\frac{\pi \hbar v}{2k_F} \right)^2 n_{imp} D(E) = \frac{4\pi \hbar^3 A_c^2 n_{imp}}{D(E)}, \tag{1.11}$$

where $D(E) = 2A_c E/\pi v^2$ has been taken from Ref. [28] to calculate the final equality and $A_c = 3\sqrt{3}a^2/2$ is the area of the unit cell in graphene. From Eqn. 1.11 it can be seen that $1/\tau \propto 1/D(E)$ and so the rate $1/\tau \to \infty$ as $D(E) \to 0$, demonstrating that Coulomb scattering dominates at low carrier density.

This result led to numerous groups calculating the conductivity in the presence of charged impurities, in an attempt to explain the observed linear and sub-linear $\sigma(n)$ and to predict a value of the minimum conductivity around the charge neutrality region which agreed with experiment. Ando calculated the static polarisation function and used it within a Boltzmann theory to show that $\sigma(n) \propto n$ in agreement with experiment, however was unable to explain the non-zero residual conductivity [40]. Hwang *et al.* studied the behaviour of $\sigma(n)$ numerically in the presence of charged impurities within a Drude-Boltzmann formalism and found that while they were able to reproduce the linear/sub-linear shape of $\sigma(n)$, the theory is not applicable at low carrier densities and predicts $\lim_{n\to 0} \sigma(n) = 0$ [37]. The

authors of Ref. [38] were able to reproduce both linear and sub-linear $\sigma(n)$ curves from numerical calculations by considering both charged and short-range scattering centres in a Kubo formalism. Furthermore, they were able to reproduce a minimum conductivity of the order $4e^2/h$ in agreement with experiment, however the results depended weakly on the size of the model and no analytical results were provided. The success of this numerical experiment in reproducing experimentally observed shapes of $\sigma(n)$ and the correct minimum conductivity is a strong suggestion that the conductivity near the charge neutrality region is explained solely by the effect of impurities and not by universal physics as considered in Refs. [41–45], which discuss the appearance of a universal conductivity minimum in a variety of systems including: disordered, 2D semiconductor systems; disordered superconductors and disordered graphene.

Considering only charged impurity scattering within a Boltzmann formalism and using the random phase approximation, the authors of Ref. [36] provided analytical expressions of the carrier mobility, the width of the change neutrality region, the magnitude of the minimum conductivity and the shift of the Dirac voltage away from zero. When the carrier density induced by the gate becomes less than the constant residual density n_0 induced in the graphene by the charged impurities in the substrate, which have density n_{imp}, the conductivity stays approximately constant. When $n > n_0$, the conductivity was found to increase linearly with n:

$$\sigma(n) = \begin{cases} (20e^2/h)n_0/n_{imp} & \text{if } n < n_0 \\ (20e^2/h)n/n_{imp} & \text{if } n > n_0. \end{cases} \tag{1.12}$$

Equation 1.12 defines two different transport regimes and the analytical expression for n_0 can be found within Ref. [36]. The analytical expressions derived in Ref. [36] agree with experimental observations, but the theory does not say anything about the transport mechanism in the charge neutrality region. It is believed that in this regime, $n < |n_0|$, the random potential due to charged impurities creates spatially inhomogeneous doping, termed electron-hole puddles, which have been observed experimentally in scanning-probe experiments [46]. The transport must be treated statistically as in Refs. [36, 47, 48] which are all in qualitative agreement with each other. Trushin and Schliemann showed in Ref. [49] that by taking into account coherent electron-hole states, which are represented by off-diagonal elements of the distribution function in a Boltzmann theory, a non-universal residual conductivity naturally arises. The conductivity is found to take the form:

$$\sigma(n) = Ce\left|\frac{n}{n_{imp}}\right| + \sigma_{res}, \tag{1.13}$$

for some constant $C = \mu/n_{imp}$, where μ is the carrier mobility, and residual conductivity σ_{res}. Equation 1.13 says that the conductivity remains non-zero at $n = 0$ and that $\sigma(n)$ increases linearly when $|n| \neq 0$. Charged impurity scattering was studied systematically in Ref. [50], where the authors deposited a controlled density of potassium ions onto the surface of a graphene field-effect transistor in ultra-high vacuum conditions. These experiments found that as potassium ions dope the graphene, $\sigma(n)$ transitions from sub-linear to linear, and that the conductivity reaches a non-universal minimum at the charge neutrality region, the width of which increases as n_{imp} increases, as expected from Refs. [36, 49]. The constant C was calculated to be $C = 5 \times 10^{15}\,\mathrm{V^{-1}s^{-1}}$ in agreement with the prediction made in Refs. [36, 37], although it was shown in Ref. [51] that C takes different values for electrons and holes, that is, they have different mobility values, because the scattering cross section for electrons with charged impurities is different to that of holes with charged impurities. The different mobility values of electrons and holes leads to an asymmetry in $\sigma(n)$ about the minimum conductivity, as in the curve labelled K145 in Fig. 1.3b, taken from Ref. [34].

In summary, the existing investigations explain the observed linear dependence of $\sigma(n)$ as a consequence of charged impurities in the substrate material. The sub-linear dependence at higher densities can be explained by short-range scattering centres becoming relevant to the transport. Near the Dirac point the behaviour is non-universal, and the current saturates at a value which is proportional to the carrier density induced in graphene n_0, due to charged impurities in the substrate. This explains why the minimum conductivity has been shown to vary between experimental samples. In the charge neutrality regions, p-type and n-type regions coexists and it is believed that percolation currents are responsible for the non-zero conductivity.

1.2.2 Weak localisation

Although short-range scattering centres have been shown to to play a negligible role in the transport in the absence of a magnetic field, they do become important when an external magnetic field is applied, in that they have been shown to facilitate the observation of the weak localisation effect in graphene. This will be shown presently. Before discussing weak localisation in graphene, a brief explanation of the weak localisation effect in non-relativistic systems is given.

Weak localisation is the name given to two corrections to the conductance of disordered conductors which becomes observable when the elastic scattering time τ becomes less than the inelastic scattering time τ_ϕ. Note an elastic scattering event is when the initial state and the final state have different momenta $\mathbf{k}$ and $\mathbf{k}'$ but equal energy E; inelastic scattering is defined as the case where the energy of the initial state E and the final state E' are not

equal, $E \neq E'$. In this regime, a particle can undergo multiple elastic scattering events while maintaining a coherent phase relationship with other states. This notion of coherence is understood more clearly in the interpretation of weak localisation provided by Bergmann in 1983 [52]. Suppose that a particle with momentum $\mathbf{k}$ undergoes a sequence of $n+1$ elastic scattering events $\mathbf{k} \to \mathbf{k}_1 \to \mathbf{k}_2 \to \ldots \to \mathbf{k}_n \to -\mathbf{k}$ into a final state with momentum $-\mathbf{k}$, and that this sequence has a quantum mechanical probability amplitude A'. Here, $\mathbf{k}_i$ are the momenta of the $1 \leq i \leq n$ intermediate states. Then there exist a second, time-reversed scattering sequence which with an equivalent amplitude $A'' = A' = A$, which is the sequence: $\mathbf{k} \to -\mathbf{k}_n \to \ldots \to -\mathbf{k}_2 \to -\mathbf{k}_1 \to -\mathbf{k}$, so that momentum is transferred in the reverse order. Both scattering sequences have equal amplitude because the probability of a transition from a state $|\mathbf{k}\rangle$ to a state $|-\mathbf{k}\rangle$ is proportional to the product of the transition probabilities from one intermediate state to the next:

$$\mathbb{P}(|\mathbf{k}\rangle \to |-\mathbf{k}\rangle) \propto \prod_{i}^{n} |\langle i+1|V_i|i\rangle|^2, \tag{1.14}$$

where $|i\rangle = |\mathbf{k}_i\rangle$ and V_i is the potential of the elastic scattering centre which causes the transition $|i\rangle \to |i+1\rangle$. The value of the product 1.14 is equal for both sequences since $|\langle \mathbf{k}_{i+1}|V_i|\mathbf{k}_i\rangle| = |\langle -\mathbf{k}_i|V_i|-\mathbf{k}_{i+1}\rangle|$ due to the symmetry of the sequences about the origin. Furthermore, since all states in the process have the same energy, the time-dependent phase acquired by the system, $\exp(-iE(n+1)\tau/\hbar)$ is equal for both scattering sequences. This means that there is exactly zero phase difference between a state where back scattering is achieved via the first scattering sequence and where back scattering is achieved via the second scattering sequence. It is in this sense that the back scattering is phase coherent. By the path integral formulation of quantum mechanics the probability for a system to transition from one state into another is given by the square of the sum of the amplitudes for all possible paths. The sum of the square of the amplitudes for both sequences is:

$$\mathbb{P}(|\mathbf{k}\rangle \to |-\mathbf{k}\rangle) = |A' + A''|^2 = A'^2 + A''^2 + A'^* A'' + A' A''^* = 4|A|^2. \tag{1.15}$$

The sum of the first two terms in Eqn. 1.15 equal $2A^2$ because the amplitudes for each scattering sequence are equal. The sum of the final two terms are equal to $2A^2$ because the amplitudes have exactly zero phase difference. This is twice the magnitude of incoherent processes, and so the probability of back scattering is enhanced within a quantum mechanical theory. In the context of the conductance of a device, coherent back scattering corresponds to a negative correction to the conductance, that is the conductance is reduced due to the weak localisation effect. In 1979, Abrahams showed that at $T = 0\,\mathrm{K}$ a disordered, 2D conductor always becomes insulating, [53], while it was shown separately by Anderson and Gorkov that

at low, but non-zero temperature there is a correction to the resistance proportional to $\ln(T)$ [54, 55] which explained some experimental investigations into the temperature dependence of resistance of thin metallic wires at the time [56]. A year later, Altshuller *et al.* considered the effect of an applied external magnetic field on the localisation properties of a disordered, 2D electron gas, calculating an analytical expression that of the magneto-conductance effect in terms of the dephasing time [57]. A change in conductance is observed because the magnetic field changes the phase relationship between the two scattering sequences considered above. The induced phase difference destroys the constructive interference, hence reducing the probability of back scattering and causing the conductance to increase. When the spin-orbit interaction is accounted for, the opposite is true and the conductance decreases; this was shown by Hikami *et al.* and is called weak anti-localisation [58]. Importantly, the analytical results determined in Refs. [57, 58] could be used by experimental groups to fit data obtained in magneto-transport measurements of disordered 2D systems and extract the relevant scattering times as fitting parameters. This theory was able to explain the magneto-conductance behaviour of many systems under experimental investigation at the time, including thin metallic films, metal-oxide-semiconductor (MOS) inversion layers and both 1D and 3D conductors: a review of the then-current experimental results can be found in Ref. [59].

Extending a theory of impurity scattering in carbon nanotubes, Suzuura and Ando calculated the weak localisation correction to conductivity of electrons on a disordered, 2D honeycomb lattice, which describes the structure of graphene, taking into account the two momentum minima in the first Brillouin zone and the helicity of particles in such a model [60–62]. They found that for scattering potentials with range larger than the lattice constant, time-reversed back scattering sequences interfere destructively and the change in magneto-conductance is positive, that is, there is a weak anti-localisation effect. This arises due to the helicity of carriers in graphene, which means that the pseudospin (sub-lattice) degree of freedom is always parallel to the momentum vector. As a result, as a particle undergoes a scattering sequence and rotates through π radians in k-space, from $\mathbf{k}$ to $-\mathbf{k}$, the pseudospin degree of freedom also rotates, which contributes an additional phase to the state, which is calculated as a Berry phase [63, 62]. The two scattering sequences which give rise to coherent backscattering in the original weak localisation theory discussed above are related through time-reversal symmetry. This means that while one sequence rotates through π radians, the momentum in the time-reversed sequence rotates by $-\pi$ radians, and the phase difference between the two paths is $\phi = \pi - (-\pi) = 2\pi$ and the two amplitudes interfere constructively. However, it was shown in Ref. [62] that a rotation in k-space of 2π corresponds to an additional Berry phase of π, meaning that that the two amplitudes

interfere destructively for helical particles. In graphene, helicity follows from the fact that the dynamics in a single valley are governed by the 2-dimensional Weyl equation, and that states are described using 2-component spinors; see Ref. [28] for an in-depth review of the electronic properties of graphene. However, it is also shown in Ref. [62] that when scattering potentials with range less than the lattice constant are included in the model, the situation changes and conventional weak localisation can be recovered. This is because short range potentials, such as lattice vacancies can scatter particles between momentum valleys, (see Ref. [44]), and therefore causes the states at **K** and **K**′ to mix. This process breaks time-reversal symmetry and so the phase difference between the two scattering sequences is no longer exactly π, and conventional weak-localisation is partially restored. Ultimately, the magneto-conductance in graphene not only depends on inelastic scattering processes, but also elastic intervalley and intravalley scattering times. In addition to intervalley scattering, the anisotropy of the Fermi surface, also called trigonal warping, breaks time-reversal invariance in graphene, which is included in the Hamiltonian by a term which is quadratic in momentum. McCann *et al.* calculated the change in magneto-conductivity $\delta\sigma(B)$ in graphene, taking into account the Fermi surface anisotropy, finding [64]:

$$\delta\sigma(B) = \sigma(B) - \sigma(0) = \frac{e^2}{\pi h}\left[F\left(\frac{B}{B_\phi}\right) - F\left(\frac{B}{B_\phi + 2B_i}\right) - 2F\left(\frac{B}{B_\phi + B_i + B_*}\right)\right]. \quad (1.16)$$

In equation 1.16, $B_\theta = (\hbar/4De)\cdot\tau_\theta^{-1}$ is the characteristic field corresponding the scattering rate τ_θ^{-1}, where $\theta \in \{\phi, i, *\}$ and D is the diffusion constant. The function $F(z) = \ln(z) + \psi(0.5 + 1/z)$ and ψ is the (real) digamma function. The subscripts are as follows: τ_ϕ^{-1} is the dephasing rate, τ_i^{-1} is the intervalley scattering rate and τ_*^{-1} is the intravalley scattering rate, which includes all possible intravalley scattering processes, including scattering due to trigonal warping and any scattering processes which break time-reversal symmetry in a single valley. Scattering due to curvature and strain, crystal dislocations, and to local potential gradients, can all break time-reversal symmetry in a single valley as discussed in Ref. [65]. Equation 1.16 is central to the analysis of magneto-transport experiments of graphene and allows for the dephasing time, the intervalley scattering time and the intravalley scattering time to be extracted from experimental data. The first term is positive and corresponds to a conductance increase when an external magnetic field is applied (weak localisation), while the second two terms are negative and imply weak localisation; Eqn. 1.16 reflects that the change in magneto-conductance depends on the competition between different scattering rates. The corresponding scattering lengths can be obtained from τ_θ^{-1} by using $L_\theta = \sqrt{D\tau_\theta}$, yielding:

$$L_\theta = \sqrt{\frac{\hbar}{4eB_\theta}}. \tag{1.17}$$

Initial magneto-transport experiments in graphene showed neither weak localisation or weak antilocalisation effects [66], where it is believed that surface ripples destroyed time-reversal symmetry in each individual valley. Since then, both weak localisation and weak anti-localisation have been observed in graphene systems, including mechanically exfoliated samples [67–69], CVD-grown graphene samples [70–74] and epitaxial graphene samples [75–79]. The magnitude of the change in magneto-conductivity $\delta\sigma(B)$ is sample dependent, but common values range between 10 and 70 μS. Since it has been shown that at $B = 0$ T, short-range scattering potentials can become relevant at high carrier density, it may be expected that the intervalley scattering rate τ_i^{-1} would increase with increasing carrier density, though this has not been reported by any group so far. By the same reasoning, it may be expected that at low carrier density, when charged impurities dominate at $B = 0$ T, that local potential gradients would break intravalley time-reversal symmetry and the intravalley scattering length L_* would decrease (and τ_*^{-1} would increase) as the carrier density approaches the charge neutrality region. Again, there has been no reported observation of this, while the authors of Ref. [78] observed an increase of L_* as the carrier density was reduced from 10^{13} cm^{-2} to 10^{11} cm^{-2}. Consequently, it seems from the results reported so far, that the influence of short-range and long-range scattering potentials at $B = 0$ T is not reflected in the scattering rates τ_i^{-1} and τ_*^{-1}, extracted from weak localisation measurements.

There has been some evidence that the dephasing length L_ϕ, increases with increasing carrier density: Ref. [68] reports a factor of 10 increase of L_ϕ between back gate voltages -20 V (Dirac point) and -60 V; Ref. [69] reports an increase of approximately 500 nm across a 60 V range, away from the Dirac point, although the uncertainty bars are large enough that it is not obvious if this is a statistically significant change. The authors of Ref. [78] found L_ϕ to be independent of carrier density across two orders of magnitude in both CVD-grown graphene and epitaxial graphene. The conflicting results suggest that there is no universal dependence of the dephasing rate on carrier density, and instead the relationship is sample dependent.

It is more common to examine the temperature dependence of τ_ϕ^{-1} as opposed to the density dependence, to infer the dephasing mechanism, as done by the authors of Ref.[80]. At low temperature, inelastic electron-phonon scattering is suppressed and electron-electron scattering is often the main dephasing mechanism. Electron-electron scattering is considered to comprise of two components. The first is due to the usual Coulomb potential arising between electrons; it was shown by Abrahams and Fukuyama that in this case the momentum

transfer is of the order k_BT, and $\tau_{e-e}^{-1} \propto T\ln(T)$ when $k_BT < \hbar/\tau$, and $\tau_{e-e}^{-1} \propto T^2\ln(1/T)$ when $k_BT > \hbar/\tau$ [81, 82]. Here τ is defined as the momentum relaxation time, which is the scattering time corresponding to the dominant elastic scattering mechanism present in the system and is given by $\tau = l_{mfp}/v_F$. Electron-electron Coulomb scattering dominates when the amount of electron-electron interactions within the dephasing time is small, that is when $\tau_{e-e} \sim \tau_\phi$. Altschuler however, showed when the energy transfer during electron-electron collisions is small, that is $\Delta E = \hbar\Delta\omega \ll k_BT$, then $\tau_{e-e}^{-1} \gg \tau_\phi^{-1}$ and an electron undergoes multiple collisions before losing coherence. This effect is interpreted as an electron scattering from a fluctuating electric field due to the presence of the other electrons in the system. In this case the dephasing rate in 2D is shown to depend on T as $\tau_\phi^{-1} \propto T$ [83]. Note, this type of electron-electron interaction is sometimes called Nyquist scattering in the literature. These results were used to successfully model the behaviour of $\tau_\phi^{-1}(T)$ in GaAs / $Al_xGa_{1-x}As$ heterostructures [84, 85], and have since been shown to describe $\tau_\phi^{-1}(T)$ in graphene. The authors of Ref. [67] modelled $\tau_\phi^{-1}(T)$ as purely linear, concluding that the dominant dephasing mechanism in their mechanically exfoliated graphene samples is due to a large number of quasi-elastic electron-electron collisions. The authors of Refs. [68, 86] observe deviation from linear behaviour, again in mechanically exfoliated graphene, and use the sum of both the high temperature Coulomb and the Nyquist terms to model the behaviour of $\tau_\phi^{-1}(T)$. Alternatively, the authors of Ref. [76] use only the low temperature Coulomb term to model $\tau_\phi^{-1}(T)$ in epitaxial graphene samples and neglect the high-frequency Nyquist scattering. In all of the above experimental reports, the authors attempt to deduce the dephasing mechanism based upon the model which gives the best fit to experimental data. This suggests that statistical tests should be performed in order to quantify and compare how well each model fits the experimental data when the behaviour of $\tau_\phi^{-1}(T)$ is not immediately obvious.

In summary, conventional weak localisation is a decrease of the conductance of a system due to constructive interference of time-reversal symmetric back scattering processes. Weak anti-localisation is a related effect where time-reversal symmetric back scattering processes interfere destructively due to an additional phase factor occurring from the rotation of the spin of a particle. These effects are purely quantum mechanical and arise when the elastic scattering time is less than the inelastic scattering time. Both effects are predicted to occur in graphene and indeed, have been observed experimentally. An external magnetic field breaks time-reversal symmetry and can be used to introduce a phase difference between time-reversal symmetric back scattering processes and causes a change in the magneto-conductivity. The magneto-conductivity can be fit using analytical models which relate $\delta\sigma(B)$ to both the inelastic and elastic scattering rates, in graphene. By studying the dependence of these

scattering rates on other experimental parameters such as the carrier density and temperature, it is possible to deduce the dominant scattering mechanisms present in the system.

1.2.3 Universal conductance fluctuations

A related quantum mechanical effect which becomes relevant at low temperature is the appearance of non-monotonic, reproducible fluctuations in the conductance G of a system as the Fermi energy E_F or an external magnetic field B is varied. This phenomena was observed in low temperature transport measurements of thin metallic rings, diameters $d < 1\,\mu$m, and wires of diameter $d \approx 40\,$nm and length $L < 1\,\mu$m [87–89]. In such devices, the device length is longer than the mean free path and less than or similar to the dephasing length, that is $l_{mfp} < L \leq L_\phi$, and electrons can undergo multiple scattering events while retaining phase coherence across the entire length of the sample. This regime is sometimes termed the mesoscopic transport regime in the literature. In 1985, Stone performed a numerical simulation within the Landauer-Büttiker formalism of a wire with length scale $l_{mfp} < L < L_\phi$ [90], and succeeded to reproduce the aperiodic structure in G observed in the above transport experiments. In the Landauer-Büttiker formalism, G is proportional to the sum of the transmission coefficients of M_c conducting channels [91, 92]. Stone found that the amplitude of the aperiodic structure δG depended on the number of conducting channels as $\delta G \propto M_c^{-0.3}$ and not $\delta G \propto M_c^{-1}$, as would be expected if the M_c transmission channels were uncorrelated. This was the first indication that the appearance of aperiodic conductance fluctuations were caused by the interference of propagating states. The authors of Refs. [93, 94] studied the statistical properties of G in mesoscopic conductors by calculating the correlation function F, which is related to the variance of the fluctuations amplitudes. The expression for F is:

$$F(\Delta E, \Delta B) = \langle G(E_F, B) G(E_F + \Delta E, B + \Delta B) \rangle - \langle G(E_F, B) \rangle^2 , \tag{1.18}$$

where $\langle \ldots \rangle$ denotes ensemble averaging. Notice that the expression in Eqn. 1.18 states that the ensemble average of G, that is the average across identically prepared macroscopic samples with different microscopic disorder configurations, is equal to the average of G over a range of energies or magnetic field strengths, ΔE_F or ΔB, which is an assumption of the theory. An in-depth discussion of the motivation behind this assumption is provided in Ref. [95]. Note, in the relevant literature, this assumption is often called the ergodic assumption, which is a term borrowed from the thermodynamic notion of ergodicity. This means that calculations of G which average over different disorder configurations can be used to analyse the observed fluctuations of $G(E_F, B)$ for a single experimental sample.

Lee found that so long as the sample dimensions are less than L_ϕ and at $T = 0\,\mathrm{K}$, the variance of the conductance amplitude, δG is always of the order of e^2/h, mathematically stated as:

$$\sigma^2(\delta G) = \left\langle \delta G^2 \right\rangle - \langle \delta G \rangle^2 = O(e^2/h), \tag{1.19}$$

where σ^2 denotes variance, and O is big-O notation. This statement is the definition of universal conductance fluctuations. A more heuristic derivation of the result described by Eqn. 1.19 is provided in Ref. [93], which shows that this result follows from the presence of correlations between transmitted states without the use of Feynman diagram calculations. When the sample dimensions exceed L_ϕ however, Eqn. 1.19 does not hold and $\sigma^2(\delta G) < e^2/h$, because the phase of an electron has become randomised after length L_ϕ and correlations between transmitted states are lost across the length of the sample. Finite temperature effects also reduce the amplitude of the conductance fluctuations as discussed in Ref. [95]. In short, a finite temperature causes carriers at the Fermi surface to become distributed across an energy interval of size $k_B T$ about E_F. As particles diffuse across the sample, they acquire different time-dependent phases since they have different initial energies. This introduces a new length scale into the system, the thermal length $L_T = \sqrt{\hbar D/k_B T}$. If $L_T < L_\phi$, then carriers will lose coherence due to Fermi surface smearing, before an inelastic scattering process.

The assumption that changing E_F or B by a finite amount is equivalent to changing the disorder configuration in the sample, leads to the notion of a correlation energy E_c and a correlation field B_c which is the finite amount by which E_F / B must be changed by, in order for the system to be considered as having a new disorder configuration. Although analytical expressions for these quantities exist, it is common in an experimental context to determine these quantities from the autocorrelation function of the conductance fluctuations. The correlation field is often defined to be the change in field at which the normalised autocorrelation function is equal to $\frac{1}{2}$. The autocorrelation function is given by:

$$F(\Delta B) = \int G(B)\, G(B + \Delta B)\, dB, \tag{1.20}$$

and the critical field is defined by $F(B_c) = F(0)/2$. According to Ref. [95], $B_c \sim \phi_o / L_\phi^2$, where $\phi_0 = h/e$ is the magnetic flux quantum. Rearranging this relationship gives an estimate of the dephasing length:

$$L_\phi \sim \sqrt{\frac{h}{eB_c}}. \tag{1.21}$$

Therefore, the correlation field is interpreted as the field required to induce a flux of magnitude ϕ_0 through the area L_ϕ^2. There exist numerous analytical expressions relating the root-mean-square amplitude of the conductance fluctuations to the dephasing length, which depend on the sample dimensions and the temperature; these results will not be used in the present work and so are not described here, instead see Refs. [95–99] for these results. References [97–99] are theoretical studies of universal conductance fluctuations in graphene; similar to weak localisation, elastic scattering effects the amplitude of $\delta G(B)$. It is shown in Ref. [97] that when both intervalley and intravalley scattering are negligible, the variance of the universal conductance fluctuations is four times that of conventional metals, that is $\sigma^2(\delta G(B)) \approx 4e^2/h$; this is reduced to $\approx 2e^2/h$ when intervalley scattering becomes non-negligible and finally reduced to $\approx e^2/h$, as in conventional metals, when both intervalley and intravalley scattering are non-negligible. These results were confirmed in numerical simulations performed in Ref. [98]. To date, conductance fluctuations have been extensively observed in graphene [71, 72, 75, 100–115] however none have reported the predicted value of $\sigma^2(\delta G(B)) \approx 4e^2/h$. Most experiments investigating mechanically exfoliated samples on Si/SiO_2 substrates report a $RMS(\delta G(B)) \approx e^2/h$ [101, 102, 105, 108, 109], where $RMS(\delta G(B)) = \sqrt{\sigma^2(\delta G(B))}$ is the root-mean-square amplitude of the fluctuations, while other authors report considerably smaller amplitudes [103, 110], similar to CVD-grown samples [71, 72]. This demonstrates that conductance fluctuations of realistic graphene samples show the same fluctuation amplitude as normal metals due to the presence of both intervalley and intravalley elastic scattering.

The assumption that changing the Fermi energy or magnetic field is equivalent to changing the disorder configuration implies that mesoscopic systems are insensitive to the phase-randomisation mechanism. However, experimental results suggest this does not hold in graphene, in contrast to the results of analytical work in Ref. [98], but in agreement with numerical simulation of Ref. [97]. The authors of Ref. [109–111], observe that the amplitude of the fluctuations are larger when E_F is varied than when B is varied, which suggests that graphene is in fact sensitive to the phase-randomisation mechanism. This then implies that the assumption underlying the universality of conductance fluctuations does not hold in graphene, and that conductance fluctuations are in fact sample specific. This may not be surprising since the original theory of conductance fluctuations in graphene [97] depends on the intervalley and intravalley scattering rates and so must be dependent upon the disorder configuration. Later numerical simulations in Ref. [116] calculated amplitude of $\delta G(B)$ within multiple screening approximations, in the presence of long-range charged impurities. It was shown that $\delta G(B)$ has a non-linear dependence on the charged impurity concentration

n_{imp}, only approaching a universal value at $n_{imp} = 15 \times 10^{12}\,\mathrm{cm}^{-2}$, a value much larger than what is present in realistic graphene samples.

In summary, reproducible and aperiodic conductance fluctuations appear due to quantum interference of transmitted states in disordered conductors of length $l_{mfp} < L < min\{L_\phi, L_T\}$. It was shown that in non-relativistic conductors such as conventional disordered metals, the variance of the fluctuations has a universal amplitude of approximately e^2/h at zero temperature, however this is reduced by Fermi surface smearing at finite temperature, and is reduced further once the sample dimensions exceed $min\{L_\phi, L_T\}$. This result is based on an assumption that phase-randomisation in a mesoscopic system is the same regardless of the mechanism, and that changing the Fermi energy, the magnetic field and the disorder configuration are all equal. This leads to the notion of a correlation energy and a correlation field, which are the change in Fermi energy or magnetic field required to consider the system as having a different disorder configuration. The correlation in particular is interpreted to be the field required to induce a flux ϕ_0 through an area L_ϕ^2 and can be used be used to estimate L_ϕ. Conductance fluctuations have been observed extensively in graphene samples, however there is both experimental and numerical evidence that the fluctuations are not universal and that the different phase-randomisation mechanisms are not equal. The analytical theory of universal conductance fluctuations in graphene presented in Ref. [98] concludes that the ergodic assumption does hold in graphene, while also concluding that the variance of the fluctuations depends on the disorder configuration, which is somewhat contradictory. The theory does not account for the difference between the amplitude of fluctuations occurring due to a change in Fermi energy, and the amplitude of fluctuations occurring due to a change in magnetic field. Therefore, from the current literature the universality of conductance fluctuations in graphene is debated.

1.2.4 Quantum Hall effect

The classical Hall effect arises when a conductor is placed in a perpendicular magnetic field. Consider a conductor with it's length orientated along the x-axis, $0 \leq x \leq L$, width along the y-axis $0 \leq y \leq W$ and some thickness t in the z-direction. When a potential difference is applied along x, current flows along the x-axis in a straight line between collisions with impurities and phonons. An external, perpendicular magnetic field applied along the z-axis will cause electrons to take curved paths between collisions due to the Lorentz force. This causes charge to accumulate on one side of the sample, at $y = W$, for example. Eventually the electric field due to the imbalance of charge in along the y-axis opposes the Lorentz force and stops further charge accumulation, and a steady-state potential difference along the y-axis is established. This is known as the classical Hall effect and the emergent transverse

potential difference is called the Hall voltage V_H, which is measurable with voltage probes at $y = 0$ and $y = W$. The conductivity σ of the system is defined by Ohm's law in terms of the current density $\mathbf{J}$ and the electric field $\mathbf{E}$ according to $\mathbf{J} = \sigma\mathbf{E}$. Since the electric field components exist along both the x-axis and y-axis, σ takes the form of a rank-2 tensor, where the components of the conductivity tensor and the resistivity tensor are related by tensor inversion:

$$\sigma_{xx} = \frac{\rho_{xx}}{\rho_{xx}^2 + \rho_{xy}^2}, \quad \sigma_{xy} = \frac{\rho_{xy}}{\rho_{xx}^2 + \rho_{xy}^2}, \tag{1.22}$$

$$\rho_{xx} = \frac{\sigma_{xx}}{\sigma_{xx}^2 + \sigma_{xy}^2}, \quad \rho_{xy} = \frac{\sigma_{xy}}{\sigma_{xx}^2 + \sigma_{xy}^2}. \tag{1.23}$$

In two dimensions, when the magnetic field strength is strong enough, the Lorentz force can force electrons into closed cyclotron orbits, with cyclotron frequency $\omega_c = eB/m^*$, where m^* is the cyclotron mass. The energy states corresponding to these closed orbits can become quantised, which was first observed in the inversion layer of a Si metal-oxide semiconductor field-effect transistor (MOSFET) in Ref. [117]. The strong magnetic field regime is defined as $\omega_c\tau \gg 1$ or equivalently, $B\mu \gg 1$, where μ is the carrier mobility and B is the external magnetic field. The quantum Hall effect is characterised by the appearance of plateaux in σ_{xy} at quantised values, accompanied by a zero in σ_{xx} as a function of magnetic field. The plateaux σ_{xy} occur at values:

$$\sigma_{xy} = \frac{e^2}{h}\nu, \tag{1.24}$$

where ν is a quantity called the filling factor. In the integer quantum Hall effect ν is an integer, whereas in the fraction quantum Hall regime, ν takes certain rational values. The longitudinal conductivity only becomes non-zero at the transitions between σ_{xy} plateaux. For a given carrier density n, the plateaux are centred at field values:

$$B = \frac{hn}{e\nu}, \quad \nu = 1, 2, \ldots. \tag{1.25}$$

The quantum Hall effect arises due to the quantisation of energy into discrete bands, often called Landau levels. For an in-depth review of the theory of Landau quantisation and the experimental observation of quantisation in Si inversion layers and GaAs / $Al_xGa_{1-x}As$ heterostructures, see Ref. [118]. By solving the Schrödinger equation for a single particle in the presence of a vector potential $\mathbf{A}$, it can be shown that the spectrum of energy states is the same as that of the quantum harmonic oscillator [119, 120], that is:

$$E_N = \hbar\omega_c(N+\frac{1}{2}), \tag{1.26}$$

where N is an integer indexing the energy states. From Eqn. 1.26 it is clear that Landau levels have equal spacing with an energy separation $\Delta E \propto B$. The corresponding density of states is a series of degenerate delta functions in the absence of disorder; these are broadened to some finite width Γ in the presence of disorder, as is the case in any realistic experimental device. The centre of each peak in the density of states corresponds to extended states, and the tails of the peaks correspond to extended states, as discussed in Refs. [119, 120].

In graphene, the situation is different to 2D semiconductor systems with non-relativistic dispersion relations. The energy spectrum of Landau levels in graphene can be calculated by solving the Dirac equation in the presence of a vector potential **A**, as in Refs. [44, 121]:

$$E_N = sgn(N)\sqrt{2\hbar e v_F^2|N|B} + E_0, \tag{1.27}$$

where E_0 is the energy of the Dirac point. Equation 1.27 shows that the Landau level spacing scales as $\sqrt{B}$ in contrast to the linear spacing of non-relativistic systems described by Eqn. 1.26. Furthermore, the energy of the $N = 0$ Landau level is independent of B. Since the $N = 0$ Landau level lies at the crossing of the valence and conduction band it is shared by both electrons and holes, and so has half the degeneracy of non-zero Landau levels. It has been shown in Ref. [122] that this reduced degeneracy leads to a different sequence of filling factors in the integer quantum Hall effect, and so the σ_{xy} plateaux occur at:

$$\sigma_{xy} = \pm g_s g_v (N+1/2)\frac{e^2}{h}, \quad N = 0,1,2,\ldots, \tag{1.28}$$

where $g_s = g_v = 2$ are the spin and valley degeneracy factors. Equation 1.28 implies a filling factor sequence $\nu = g_s g_v(N+1/2) = 2,6,10,\ldots$. This behaviour was indeed observed in early magneto-transport experiments with graphene Hall bar devices [33, 123], which confirm the relativistic nature of charge carriers in graphene, in the sense they obey the relativistic Dirac equation with zero effective mass. Later experiments found plateaux emerge at filling factors $\nu = 0, \pm 1, \pm 4$ [124] (see Fig. 1.4, taken from Ref. [124]) which are not predicted by the sequence derived in Ref. [122], which suggests a lifting of the SU(4) symmetry of the $N = 0$ Landau level and a change of ground state. Note that SU(4) symmetry refers to the fact that there a four degenerate states in graphene arising from the two valley degrees of freedom and the two sub-lattice degrees of freedom, which is shown explicitly in Section 1.3 of Ref. [125]. A transformation between valleys is described by the time-reversal operator $T\psi_{K,(A,B)} \mapsto \psi^*_{K,(A,B)} = \psi_{K',(A,B)}$; the spatial inversion operator swaps both the valley index and the sub-lattice index, $I\psi_{K,A} \mapsto \psi_{K',B}$, therefore it follows that the

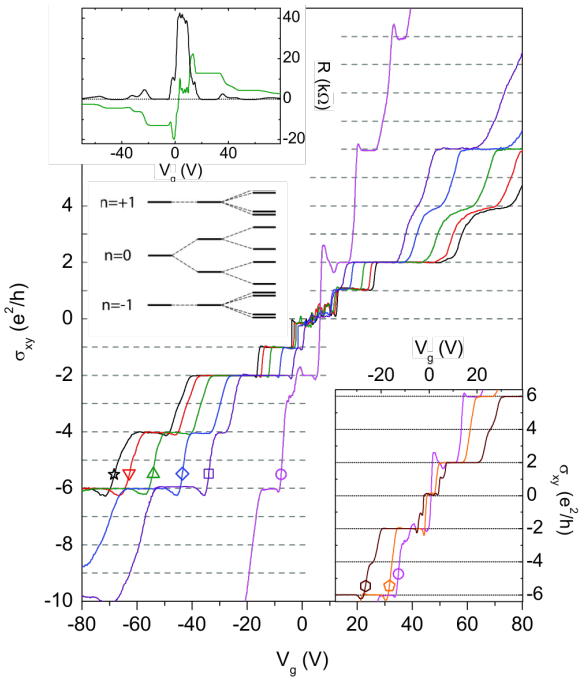

Fig. 1.4 Magneto-conductivity data taken from Ref. [124] which shows the emergence of Hall plateaux at $\nu = 0, \pm 1, \pm 4$. The upper left inset shows $R_{xx}(V_g)$ and $R_{xy}(V_g)$ of the device at $B = 25\,\mathrm{T}$. Lower left inset shows a diagram of the Landau level splitting, and right inset is a more detailed plot of σ_{xy} at $B = 9$, 11.5 and 17.5 T.

transformation $TI\psi_{K,A} \mapsto \psi_{K,B}$. The Hamiltonian describing the dynamics of particles in graphene is invariant under these spinor transformations, meaning that particles in different valleys and particles on different sublattices have the same energy, that is they are degenerate. The transformations T and I are members of the group SU(4), which is why this degeneracy is often referred to as SU(4) symmetry in the literature.

1.2.5 Ground states of the zero-energy Landau level

Various experimental groups have reported seemingly conflicting behaviour of the $N = 0$ Landau level. This is ultimately because the $N = 0$ Landau can undergo a quantum phase transition from a metallic quantum Hall state into a quantum Hall insulator state. The authors of Refs. [124, 126–130] observe values of R_{xx} up to order of $10\,\mathrm{M}\,\Omega$ in the $N = 0$ Landau level, indicating an insulating state. On the other hand, the authors of Refs. [33, 123, 131–133] observe a longitudinal resistance $R_{xx} \approx R_K$ at the $N = 0$ Landau level, where $R_K \approx 25.8\,\mathrm{k}\Omega$ is the von Klitzing constant.

Those that report a large longitudinal resistance also report a well defined plateaux at $\sigma_{xy} = 0$ which indicates a splitting of the $N = 0$ Landau level. Figure 1.4 taken from Ref.

[124] shows $\sigma_{xy}(V_g)$ for various B. At 9 T (denoted by a circle) σ_{xy} changes continuously between $\pm 2e^2/h$, however at 25 T (square) plateaux are beginning to emerge at $\nu = 0, \pm 1, \pm 4$, and are well established at 45 T (star). At 45 T, $R_{xx} \approx 500\,\mathrm{k}\Omega$ which is not expected from the conventional quantum Hall effect, where $R_{xx} \to 0$. This is explained by theoretical arguments made by Das Sarma and Yang as an indication that the system has transitioned into a quantum Hall insulator state [134]. A plateau $\sigma_{xy} = 0$ (implying $\nu = 0$), can only appear once the degeneracy of the zero-energy Landau level is lifted, otherwise the filling factor sequence goes as $\nu = \pm 2, \pm 6, \ldots$ as discussed above. From Eqns. 1.22 and 1.22, when $\sigma_{xy} = 0$,

$$\rho_{xx} = 1/\sigma_{xx}, \quad \rho_{xy} = 0. \tag{1.29}$$

However, from the definition of the Hall effect, $\sigma_{xx} = 0$ when σ_{xy} is constant, that is when there is a plateau for any value of ν including $\nu = 0$, so then from Eqn. 1.29 it is clear that this leads to $\rho_{xx} \to \infty$ and $\rho_{xy} = 0$. This state is very similar to states observed in non-relativistic 2D semiconductor systems know as quantum Hall insulator states [135–137], where $\sigma_{xx} = \sigma_{xy} = 0$, $\rho_{xx} \to \infty$ and the Hall resistivity takes its classical value $\rho_{xy} = B/ne$, where n is the carrier density. It may seem as if ρ_{xy} should also diverge since it is inversely proportional to n, however in graphene the carrier density is not truly zero at the charge neutrality point, unlike when the Fermi level lies within the band gap of a traditional semiconductor. Instead there is a coexistence of electrons and holes and the system is a compensated semimetal, with a net charge density of zero. In this case the value of ρ_{xy} should fluctuate close to zero for the Hall insulator state in graphene. This is indeed observed in the experiments described in Refs. [127, 124], and is shown in by the green curve in the upper left insert of Fig. 1.4 and shown in Fig. 1a of Ref. [127]. Therefore, Ref. [134] explains the behaviour observed in Refs. [127, 124] up to the point of explaining that SU(4) symmetry breaking leads to a gap opening in the zero-energy Landau level which ultimately leads to diverging ρ_{xx}, but it does not say anything about the microscopic mechanism that breaks the SU(4) symmetry. Furthermore the theory described in Ref. [134] only describes the bulk resistivity, that is $\rho_{xx} \to \infty$ in the bulk, and assumes no contribution from edge states.

The microscopic mechanism responsible for a gap opening in the zero Landau level is currently debated. The authors of Ref. [39] show that in the presence of Coulomb interactions and the Zeeman interaction the SU(4) symmetry of the $N = 0$ Landau level is spontaneously broken, and a gap can appear. Reference [39] however, does not say exactly how electrons arrange microscopically to break the symmetry. A phase diagram of the $\nu = 0$ state is theoretically constructed in Ref. [138], possible phases include: charge density wave states, where spin-up and spin-down electrons form pairs on a single sub-lattice; a Kelkulé bond pattern, where double bonds form between alternating pairs of carbon atoms;

a spin-polarised ferromagnetic phase, where the electron spins on both sublattices point in the same direction; and an anti-ferromagnetic phase, where spins on different sublattices point in opposite directions. These states are discussed further in Refs. [139–142], which are in agreement with Ref. [138]. As pointed out in Ref. [138], the phase of the ground state ultimately depends on the anisotropy of energy in the valley-sublattice space which, is difficult to control in electrical transport measurements, however it may be possible to induce phase transitions in tilted magnetic fields. This makes it difficult to probe the microscopic configuration of electrons and determine which phase the system is in. Another mechanism called magnetic catalysis has also been proposed as a candidate for opening a gap in the $N = 0$ Landau level [143, 144]. In this scenario, a magnetic field enhances the attractive interaction between electrons and holes and forms bound states; the bound states have integer spin and can condense into a collective state and subsequently open a gap in the single-particle spectrum. Again, the suggested experimental probes of this effect are limited and will be discussed later, in the context of the results presented in Chapter 5.

In summary, the quantum Hall effect in graphene differs from that in conventional 2D semiconductors due to the relativistic nature of states near the Dirac point. The Landau level separation scales as $\sqrt{B}$ and there is a robust Landau level at the Dirac point which has energy independent of B. This level is shared by electron and hole states and so has half the degeneracy of non-zero Landau levels, which produces the filling factor sequence $\nu = \pm 2, \pm 6, \pm 10, \ldots$ in contrast to non-relativistic systems. Experiments have revealed that the zero Landau level can split, causing new plateaux to appear at $\nu = 0, \pm 1, \pm 4$, however the microscopic mechanism behind this is debated.

This section concludes the background and review of topics relevant to the interpretation and analysis of data presented in later experimental chapters.

1.3 Conclusions

This chapter explains the motivation for developing an on-chip multiplexer which is capable of electrically characterising nanomaterials at cryogenic temperature and provides a review of topics relevant to the interpretation of data presented in the following chapters.

In Chapter 2, a detailed description of the new multiplexer design and fabrication methods is provided, including a description of how graphene grown by chemical vapour deposition (CVD), is included in the multiplexer technology.

As will be discussed in Chapter 2, two multiplexer designs were developed; one with 16-outputs used as a prototype and one with 128-outputs. This chapter also covers the transfer and characterisation of CVD-grown graphene onto a 16-output multiplexer device,

named CVD-MUX-A. This device is the topic of study in chapters 3, 4 and 5. In chapter 3 the device is electrically characterised at $T = 4.2\,\mathrm{K}$ and $T = 0.28\,\mathrm{K}$ in the absence of a magnetic field; Chapter 4 examines weak localisation and conductance fluctuation effects in multiplexed GFETs, and Chapter 5 examines the transport properties of multiplexed GFETs in magnetic fields up to 10 T. A common theme will be to compare the experimental transport results to existing literature, in order to understand where multiplexed devices are similar to non-multiplexed devices, and where they are different. It will be shown that most results of the magneto-transport experiments performed here are largely similar to those performed elsewhere with non-multiplexed devices, which shows that the multiplexing approach can be employed without significantly changing the properties of the nanomaterial under test. Chapter 6 presents results from on-going experiments, and results from devices which have not been fully characterised in magneto-transport experiments as with CVD-MUX-A. These include multiplexing mechanically exfoliated graphene, progress towards multiplexing at room temperature, and multiplexing InAs nanowires. Chapter 6 then ends with the thesis conclusions.

Chapter 2

Device Design, Fabrication and Characterisation

This chapter discusses the design, fabrication characterisation of multiplexer devices, as well as the transfer of CVD-grown graphene onto multiplexer devices. The chapter begins by presenting the design of the multiplexers developed in this work: a device with 16 outputs, used for proof-of-principle experiments, and a larger multiplexer device with 128 outputs, which can be used for high-throughput electrical characterisation of nanomaterials. The details of the fabrication methods are then given and are followed by electrical transport measurements of a blank multiplexer device, that is with no nanomaterials, and multiplexer outputs connect directly to a common drain contact. The final part of this chapter discusses the transfer and characterisation of graphene onto a multiplexer device. In particular, all of the channels of device CVD-MUX-A are characterised by scanning electron microscopy (SEM) and Raman spectroscopy, since this device is further characterised in the following three chapters in low temperature, magneto-transport experiments. Since the transfer of nanowires onto the multiplexer is performed by collaborators, this is not included here. Nanowires are discussed in Chapter 6, where references of the transfer process are provided.

2.1 Multiplexer designs

2.1.1 Tiered structure: 16 outputs

The multiplexing devices operate by the same principle as those reported in Refs. [18, 20], in that the conductance of a semiconducting mesa structure can be turned on and off in different spatial regions using metallic surface gates, so current from a single input can be routed to one of multiple output nodes. Specifically, the 2DEG inside a GaAs / $Al_xGa_{1-x}As$ heterostructure

is used as the conducting mesa layer, the same as in Ref. [18]. The heterostructure wafer used in this work has wafer numbers V832, grown by Harvey Beere of the Semiconductor Physics group at the University of Cambridge. It has the following structure from the bottom up: bulk GaAs; 40 nm of undoped $Al_{0.3}Ga_{0.7}As$; 40 nm of Si doped $Al_{0.3}Ga_{0.7}As$ and finally 10 nm of GaAs, as a capping layer. The 2DEG resides at the interface of the undoped $Al_{0.3}Ga_{0.7}As$ and the bulk GaAs due to the resultant band structure across the heterostructure [145]. The carrier mobility in the 2DEG is approximately $8 \times 10^5\,\mathrm{cm^2V^{-1}s^{-1}}$ and the carrier concentration is approximately $1.5 \times 10^{11}\,\mathrm{cm^{-2}}$, determined from measurements of separate Hall bar devices, not reported here. Fabrication and measurement of these Hall bar devices was performed by Melanie Tribble of the Semiconductor Physics group at the University of Cambridge.

The present devices described here however are different to those in Ref. [18], in that they are designed to test the electrical properties of nanomaterials which are transferred onto the surface of the multiplexer device at the end of the fabrication process. The source and drain electrode of the device are not connected by a continuous, semiconducting 2DEG and a nanomaterial is used to bridge the gap between the 16 outputs of the multiplexer and a common drain contact, completing the circuit. The 2DEG inside of the GaAs / $Al_xGa_{1-x}As$ heterostructure is only used as a way to direct current from the source electrode to a chosen output which is connected to a nanomaterial, at cryogenic temperature. The design of the multiplexer is largely independent of the type of nanomaterial that is transferred onto it, in that the signal is directed from a source input to one of multiple outputs in the same way for any transferred nanomaterial. The only aspect of the device design which needs to be changed when testing different nanomaterials is how electrical contact is made to the nanomaterial after it has been transferred onto the surface of the multiplexer device. This will be discussed in more detail later. In the following discussion of the AutoCAD designs of the device shown in Figs. 2.1 and 2.2, the length of a feature refers to its size in the vertical direction of the AutoCAD diagram; the length of the mesa structure is 1045 μm, for example (see Fig. 2.1b). Thickness is used to refer to the out-of-plane dimension. Finally, the width refers to the horizontal direction in the AutoCAD diagrams.

The tiered structure with 16 outputs is the most simple design and the one with which the most work has been done, since it's purpose is as a proof-of-principle device, before scaling up to larger multiplexing arrays. The device design is described as tiered because the design can be viewed as a series of tiers, indicated by the black, dashed lines in Fig. 2.1b. At each dashed line the channel splits into two, doubling the number of available channels. The blue and green arrows in Fig. 2.1b show two different current paths from source to drain, which take different directions at the first tier of the mesa structure, and subsequently arrive at different output nodes. As the current passes through each tier of the mesa structure it

must choose one of two paths, which can be controlled by gates deposited onto the surface of the device. Since the channel splits into two more channels at each tier, the n'th tier has 2^n outputs; in this case there are four tiers and therefore $2^4 = 16$ outputs. The mesa structure of a single multiplexer device occupies approximately $1550 \times 1045\,\mu\text{m}^2$ as shown in Fig. 2.1b and the photolithography mask is designed such that 12 multiplexer devices, plus 4 test structures (fourth column), can be fabricated on a single 1 cm$\times$1 cm chip as shown in Fig. 2.1a. The outputs are each 50 μm wide and have a separation of 50 μm.

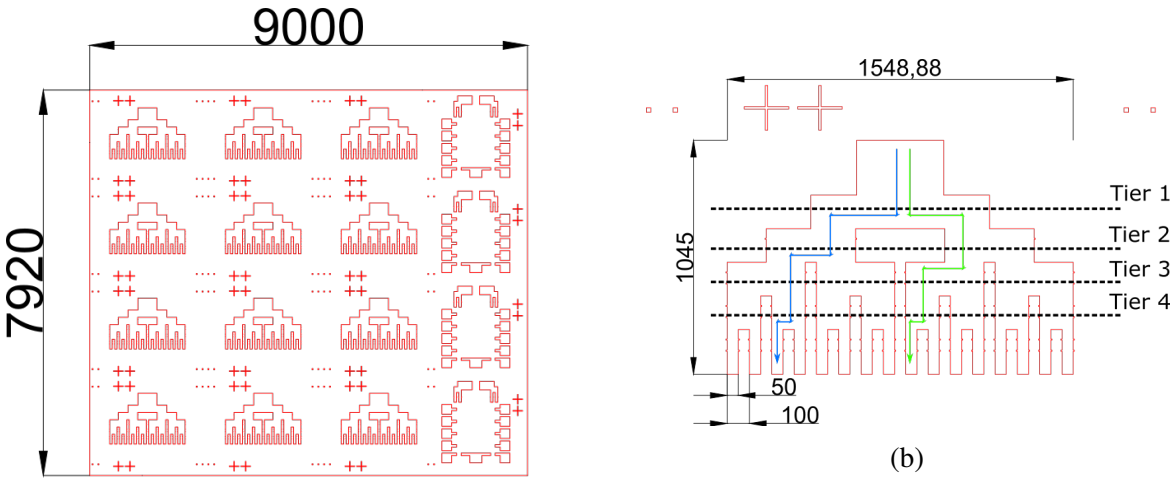

(a) (b)

Fig. 2.1 AutoCAD diagrams of the mesa structure of the 16-output multiplexer, with diagram dimensions measured in μm units. The figure in (a) shows the mesa layer design of the photolithography mask. The mesa structures are organised in a 4×3 grid, the fourth column is for test structures which are not used in the multiplexer device, but to check processing steps. The entire set of 12 multiplexer devices and 4 test structures fit onto a 1×1 cm chip; (b) shows the mesa structure of a a single multiplexer device

Figure 2.2 shows the remaining fabrication steps with the relevant dimensions marked. The second step is to make ohmic contact to the 2DEG in the regions marked in blue in Fig. 2.2a. The source ohmic is 245 μm$\times$420 μm, while ohmic contacts with area 60 μm$\times$75 μm are positioned at the end of each output. The ohmic pattern surrounding the mesa structure does not make contact with the 2DEG, instead these areas will be used for wire-bonding, when the devices are packaged at the end of the fabrication process.

A single back gate is used to modulate the carrier density of the transferred nanomaterial in every channel and is fabricated from a metallic electrode, covered by an insulating, gate dielectric layer. In this sense the gate is only a back gate relative to the nanomaterial channel, it is not a metallic layer on the back of the wafer. After the ohmic contacts have been fabricated, the metal for the back gate is deposited. The design of the back gate metal is

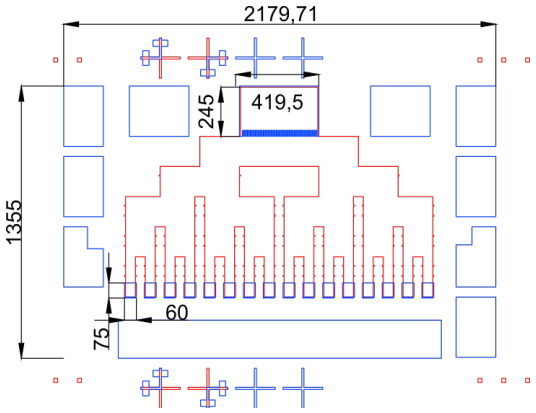

(a) The ohmic contact layer drawn in blue.

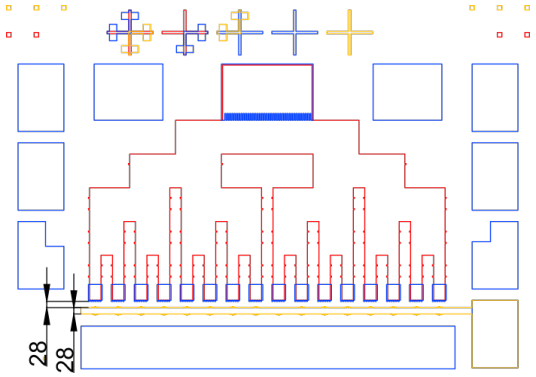

(b) The back gate layer drawn in yellow.

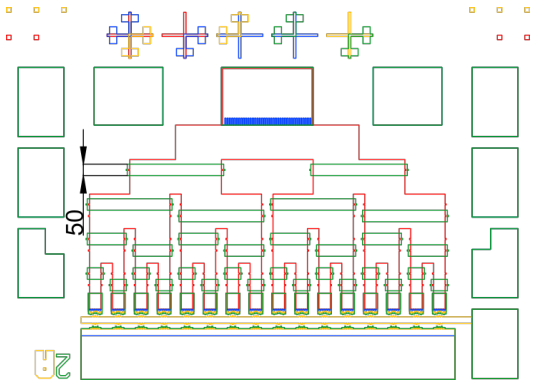

(c) The oxide etch layer drawn in green.

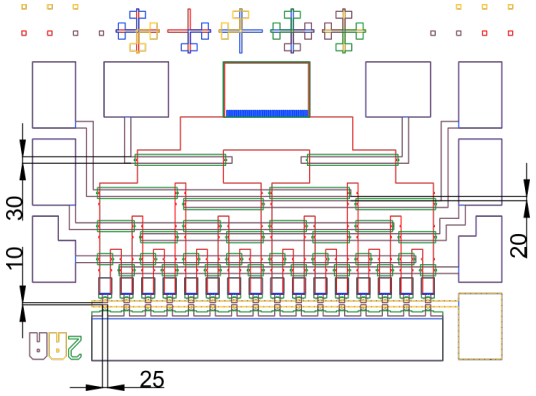

(d) The addressing gate layer drawn in purple.

Fig. 2.2 AutoCAD diagrams of the remaining fabrication layers for a single, 16-output multiplexer device, showing the relevant feature sizes in units of μm. The patterns have been taken from the AutoCad file used to design the photolithography mask. Each subsequent layer is stacked on top of the previous.

shown in Fig. 2.2b. It has width 28 μm and is deposited 28 μm below the output ohmic contacts. The metal thickness used is 50 nm.

In order to specify single outputs, the multiplexer must be able to switch off the 2DEG in selected, spatial regions, in the same way as the device described in Ref. [18]. In the present devices polyimide is not used as in previous designs, and instead an Al_2O_3 layer, thickness 95 nm, is deposited everywhere across the sample surface. Openings are then etched into the insulator inside the regions indicated by green boxes shown in Fig. 2.2c. The openings above the mesa structure have length (vertical direction of diagram 2.2d) 50 μm, and for each tier of the mesa structure there are two rows of openings. For example at Tier 4, there are two rows of 8 openings in the Al_2O_3, which are patterned over every second channel in the tier. The two rows of openings are offset from each other, so that between them, every channel in a given tier has an opening above it. When an addressing gate runs over the Al_2O_3 layer, it cannot pinch-off the 2DEG below when a -0.3 V voltage is applied; when it runs over an opening in the Al_2O_3, it can pinch-off the 2DEG below when a -0.3 V voltage is applied. Therefore, an addressing gate covering the first row of openings will pinch off the 2DEG in 8 channels of the 16 channels in Tier 4, and leave the other 8 open. A second addressing gate over the second row of 8 openings can be used to pinch-off the remaining 8 channels. Openings are also etched over all the ohmic contacts and bond pad regions so that they are not made electrically insulating. This Al_2O_3 layer also provides the back gate dielectric material to the device, and is thick enough to withstand $\pm$20 V applied to the back gate electrode at $T = 4.2$ K without breaking down.

The addressing gates are have length 30 μm and pairs of addressing gates are separated by a 20 μm gap. The ohmic contact pattern is repeated in this layer so that all the ohmic contacts are capped with Ti/Au, which makes wire bonding easier. This pattern also extends each of the 16 multiplexer outputs onto the top surface of the back gate. The common drain electrode also extends onto the back gate. This is most clearly explained using the images in Fig. 2.3. A zoomed image of the back gate layer is shown in Fig. 2.3a and an SEM image of a real device fabricated using this pattern is shown in Fig. 2.3b. The metal which overlaps the back gate is shown in the purple layer in Fig. 2.3a (back gate drawn in yellow) and labelled Source and Drain in Fig. 2.3b. The light grey region between the source and drain contacts is graphene, which has been transferred on top of the pre-patterned contacts and patterned into a square channel.

These features are 25 μm wide and are separated by a 10 μm gap. They are used as bottom contacts to CVD-grown graphene as in the SEM image shown in Fig. 2.3b. The graphene transfer process is discussed further in Section 2.4. When CVD-grown graphene is not the material under test, for example when the multiplexer is used with mechanically

exfoliated graphene or InAs nanowires, a different pattern is used, where the 16 multiplexer outputs and common drain contact are not made to overlap the back gate. In these cases electrical contacts to the nanomaterials are fabricated after transfer using electron beam lithography with custom design patterns.

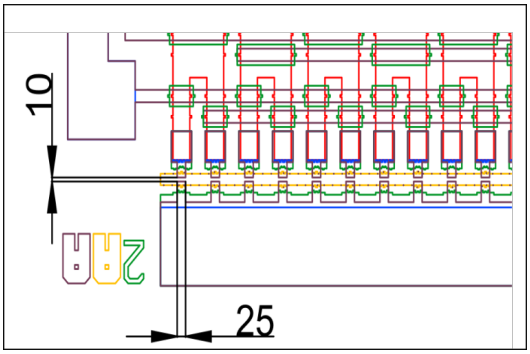

(a) A zoomed image of Fig. 2.2d, showing the addressing layer overlap the back gate.

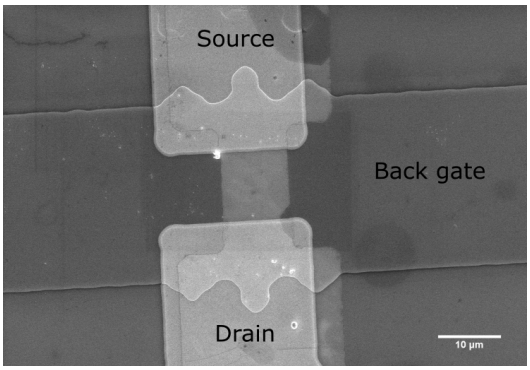

(b) SEM image of the output metal and drain metal overlapping the back gate.

Fig. 2.3 A section of the mask design and SEM image showing how each of the 16 outputs and the common drain are made to overlap the back gate. These features are used as back-contacts for CVD-grown graphene.

2.1.2 Double-tiered structure: 128 outputs

The double-tiered multiplexer can be thought of as two, single-tiered multiplexer devices each with 6 tiers and 64 outputs, joined together at the source electrode with two, separate common drain contacts, as labelled in the microscope image shown in Fig 2.4b. Figure. 2.4a is a schematic diagram of only the mesa layer and the addressing gate layer of the device. The ohmic patterns, back gate pattern and Al_2O_3 etch pattern are designed in a similar way to that of the 16-output multiplexer device. These features have different dimensions which reflects the different shape of the mesa structure. The outputs of the multiplexer have width 40 μm and are separated by 20 μm; consequently, the ohmic contacts at the outputs have width 40 μm and length 35 μm. There are two back gates, one on each side of the multiplexer which are each used to modulate the carrier density of nanomaterials in 64 of the channels. The openings in the Al_2O_3 layer follow a similar pattern to those in the 16-output design: within each tier there are two rows of openings across every second channel in that tier and the two rows are offset from each other, so that between them there is an opening over every channel in the tier.

The contact at the centre of the device is the source electrode, which is labelled in the image shown in Fig. 2.4b. In this design the current can flow to one of two common drain

electrodes. Which drain contact the current flows to is controlled by creating a potential difference between the two drains, which can most easily be achieved by floating one of the drain contacts. Addressing gates are designed to act on both sides of the multiplexer simultaneously, which reduces the number of contacts that are required to address both sides of the multiplexer. This can be seen most clearly for gates labelled A1 and A2 in Fig. 2.4b, which wrap around both sides of the source contact.

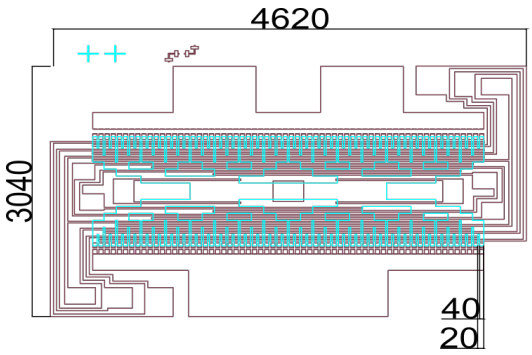

(a) Schematic diagrams of the mesa and addressing gate layers of the 128-output multiplexer device.

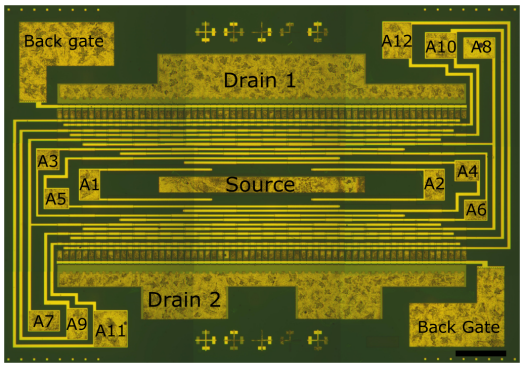

(b) Microscope image of a 128-output multiplexer device.

Fig. 2.4 An AutoCAD diagram of the addressing gate layer and mesa layer of the double-tiered structure is shown in (a) along with the relevant dimensions; (b) shows a microscope image of a completed 128-output multiplexer device.

2.2 Fabrication methods

This section describes the details of the fabrication process. The GaAs / $Al_xGa_{1-x}As$ heterostructure processing can be broken down into five stages which are described in the following sub-sections:

1. Mesa etch
2. Ohmic contact to mesa
3. Back gate deposition
4. Deposition and etch of Al_2O_3
5. Addressing gates deposition

2.2.1 Mesa pattern

The mesa structure is fabricated using photolithography and wet-chemical etching. Shipley 1805 photoresist is spin-coated onto the surface of the heterostructure at 5500 rpm for 60 s and soft-baked at 115 °C for 1 minute to remove the resist solvent. The mesa pattern is then transferred by exposing the resist to UV radiation through a photolithography mask. A Karl Suss MJB3 mask aligner with a 350 W mercury vapour lamp is used as the UV source. This mask aligner is used for all subsequent photolithography steps. After UV exposure, the resist is developed for 40 s in MF-319 developer, rinsed in DI water and dried using N_2 gas. A microscope is used to check that the pattern has been transferred successfully before using an RF asher to remove any resist residue. An RF power of 100 W is applied for 120 s. After the RF ashing stage, the thickness of the resist is measured using a Dektak profilometer, which can be compared to a second measurement after the wet-etch. By comparing the thickness of the resist before and after the etch, the etch depth can be calculated. A mixture of H_2SO_4:H_2O_2:H_2O in a ratio of 1:8:1600 is used to etch both GaAs capping layer and the doped/undoped AlGaAs layers. Etching for 150 s is often found to give an etch depth of 100 nm, sufficient to remove the Si-doped layer of the heterostructure and destroy the 2DEG in the exposed regions. Note however that the etch rate does vary between etches and it is best practice to always measure the etch depth.

2.2.2 Ohmic contacts

For this process Shipley 1813 resist is spin-coated onto the device at 5500 rpm for 60 s and baked at 90 °C, producing a film of approximately 1200 nm. Before developing the pattern in MF-319, the device is immersed in chlorobenzene for 120 s, this is to harden the surface of the resist relative to the resist beneath the surface, so that an undercut can be created in the resist profile. The device is then subject to the same RF plasma ashing as for the mesa pattern and then dipped into a 20 % solution of HCl. The HCl solution is used to remove the oxide induced by RF ashing on the surface before metallisation. A 450 mg slug of AuNiGe alloy is used as the contact material for the device and is deposited using a thermal evaporator with a base pressure of approximately 5×10^{-7} mbar. This amount of AuNiGe results in a layer approximately 200 nm thick after deposition. If a well defined undercut was created during the development of the photoresist, then it should be easily removed in acetone at room temperature after a few minutes, leaving the desired pattern. This process is commonly called the lift-off process. The final step is to anneal the device for 80 s at 430 °C, which causes the AuGeNi to diffuse through the surface of the device and make electrical contact with the 2DEG. At this point a probe station can be used to check contact was made to the

2DEG, and obtain an estimate of the contact resistance. A usual source-drain resistance of a multiplexer device is 3 kΩ at liquid nitrogen temperature.

2.2.3 Back gate metallisation

Initially, the back gate was deposited using Shipley 1813 resist and chlorobenzene, however this process was changed and a two-layer resist process which provides a more reliable undercut. It is important to have a well defined resist undercut before depositing the back gate metal, because otherwise the metal may show lilypadding. This is where the metal forms sharp, unintentional features which protrude from the edges of the gate metal and can cause the back gate dielectric to fail during device operation.

First, lift-off resist 5B (LOR5B) is spun onto the device at 5000 rpm for 60 s and baked on a hotplate at 180 °C, next Shipley 1805 is spun on top of the LOR5B at 5000 rpm for 30 s and the device is baked again at 115 °C for 60 s. Before exposing the sample to UV through the back gate pattern, the resist is removed from the edges of the sample. The back gate pattern is exposed for 3.5 s and developed for 40 s in MF-319 developer, producing an undercut of approximately 0.5 um. The size of the undercut is estimated by eye from during inspection under a microscope and is not measured. For all devices 10 nm of Ti and 40 nm of Au are used for the back gate; this thickness is chosen to keep the back gate as thin as possible while still depositing enough metal to wire-bond onto later. The lift-off is performed using SVC-14 resist stripper. It is common to do the lift-off process at 60 °C by leaving the sample in a vial of SVC-14 which is placed inside of a heated water bath, however the process also works at room temperature for thin metal layers.

2.2.4 Deposition of Al_2O_3

Prior to depositing the back gate oxide, the devices are cleaned in acetone and IPA, dried with N_2 gas and then cleaned with UV-ozone for 3 minutes. A Beneq TFS200 Atomic Layer Deposition (ALD) system is used to deposit the Al_2O_3 layer. Precursor materials are liquid trimethylaluminium $Al_2(CH_3)_6$ and H_2O. Gas pulse times of 2.5 s are used during each cycle of the deposition. The deposition temperature used for all devices is 200 °C. A blank Si/SiO_2 samples is included in the deposition chamber, which also gets coated with Al_2O_3. This is used to measuring the thickness of the deposited film, by ellipsometry.

The etch pattern is defined by photolithography and Shipley 1805 resist, the same as for the mesa etch step. The etchant is a buffered HF solution which removes 2 nm of Al_2O_3 per second at room temperature. Note that this is for Al_2O_3 deposited by ALD; Al_2O_3 deposited by e-beam evaporation may etch at a different rate.

2.2.5 Addressing gates

The addressing gate pattern are defined using the same process as for the back gate, that is a 2-layer resist process, however the metallisation process is different. The sample is held at a 20 ° angle on a rotating stage above the metal source in the thermal evaporator system. This helps ensure the addressing gates form a continuous layer across the multiplexer device, and do not become disconnected at the edges of the mesa structure or openings in the Al_2O_3 layer. Lift of is performed in SVC-14.

2.3 Electrical characterisation

It is important to electrically characterise the properties of a multiplexer device with no nanomaterials transferred onto it, as well as the cryostat wiring. This is because the measured conductance signal during magneto-transport experiments will contain contributions from both the nanomaterial and the 2DEG. Measuring a blank device helps understand the contribution from the 2DEG, so that it can be separated. To this end, a blank, 16-output multiplexer device was taken and the outputs were connected to the common drain contact by wire bonding, so that most of the measured resistance of the device is caused by the 2DEG and the ohmic contacts to the 2DEG. The conductance of channels 2-16 were measured in magnetic fields between -0.2 T and 10 T at $T = 0.28$ K. Measurements are performed using a constant voltage circuit setup, illustrated by the diagram in Fig 2.5.

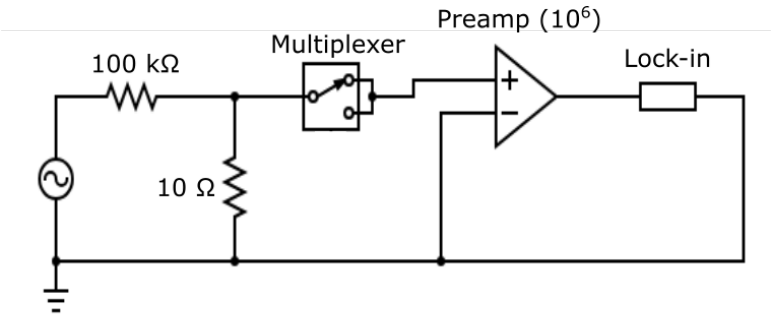

Fig. 2.5 Diagram of the circuit used to measure the conductance of the multiplexer. The AC source voltage typically has 0.1 V magnitude and 77 Hz frequency.

2.3.1 Channel addressing

Before looking at the response of the multiplexer to an external magnetic field, an example is shown here of how a specific output channel is selected. Figure 2.6a shows how current

Channel	Gates
1	A2 A4 A6 A8
2	A2 A4 A6 A7
3	A2 A4 A5 A8
4	A2 A4 A5 A7
5	A2 A3 A6 A8
6	A2 A3 A6 A7
7	A2 A3 A5 A8
8	A2 A3 A5 A7
9	A1 A4 A6 A8
10	A1 A4 A6 A7
11	A1 A4 A5 A8
12	A1 A4 A5 A7
13	A1 A3 A6 A8
14	A1 A3 A6 A7
15	A1 A3 A5 A8
16	A1 A3 A5 A7

Table 2.1 Addressing gate combinations required to select each of the 16 outputs. The gate names correspond to the gates labelled in Fig. 2.6a.

is routed from source to channel 16. As the voltage on A1 is swept from 0 to -0.3 V the 2DEG below is pinched-off, indicated by the black cross in Fig. 2.6a, and current can no longer flow to outputs 1-8. The conductance approximately halves as half of the channels become unavailable for transport. Notice that after approximately -0.25 V on any addressing gate that the conductance becomes constant, which shows that the 2DEG below is fully depleted of carriers, since the conductance cannot be decreased further by increasing the magnitude of the negative applied voltage on the addressing gate. Next, gates A3, A5 and A7 are sequentially taken to -0.3 V. These gates switch off channels 9-12, 13 and 14, and 15, respectively, so that only channel 16 remains open. Table 2.1 shows the combination of gates which are used to address each of the 16 outputs. Since each addressing gate halves the number of conducting channels, for a multiplexer a multiplexer device with n tiers requires n addressing gates to select a single channel.

2.3.2 Strong magnetic fields

Figures 2.7a and 2.7b show conductance G and resistance R of channels 2-16 as a function of magnetic field B. It can be seen that most channels have a resistance of the order of

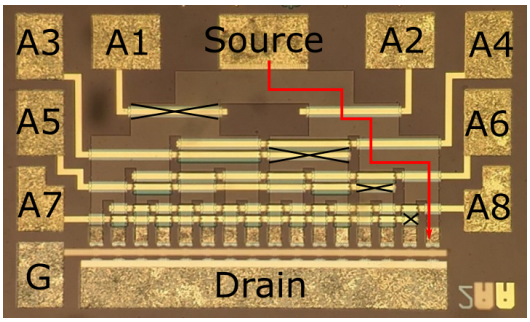

(a) Photograph of a 16-output multiplexer showing the current path from the source to output 16.

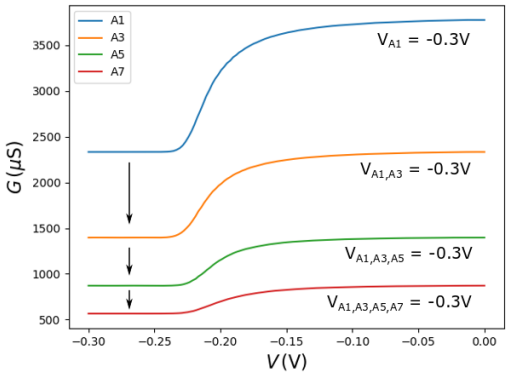

(b) Change of G as addressing gates A1, A3, A5 and A7 are swept from zero to -0.3 V.

Fig. 2.6 An example of channel addressing, where current is directed from the source to output 16 by applying a voltage -0.3 V to addressing gates A1, A3, A5 and A7. The conductance of the device approximately halves as the 2DEG under each addressing gate is pinched-off, since the number of channels is halved.

hundreds of kΩ at 10 T, apart from channel 3 which approaches 7 MΩ. Figures 2.7c and 2.7d show the distribution of the resistance minimum and maximum obtained from these data, denoted R_{min} and R_{max}, respectively. From Fig. 2.7d, 14 of the 15 measured channels have a maximum resistance less then 1 MΩ which suggests that the large resistance of channel 3 is an anomalous result. The mean minimum resistance is $\overline{R}_{min} = 2.9\,\text{k}\Omega$ with standard deviation $\sigma_{R_{min}} = 1.9\,\text{k}\Omega$. The mean maximum resistance is $\overline{R}_{max} = 628\,\text{k}\Omega$ with a standard deviation $\sigma_{R_{max}} = 1824\,\text{k}\Omega$. If the maximum resistance of channel 3 is regarded as anomalous and discounted, the mean and standard deviation of R_{max} become $\overline{R}_{max} = 196\,\text{k}\Omega$ and $\sigma_{R_{max}} = 135\,\text{k}\Omega$. The maximum resistance of channel 3 distorts the distribution of R_{max} values in this data set, increasing the standard deviation by more a factor of 10. From these data it should be expected that in most cases, the resistance of a single channel should be approximately 200 kΩ at 10 T, however there is the possibility that the multiplexer may become considerably more resistive in some channels. The reasons for the behaviour of channel 3 are unclear from these experiments and it can not be ruled out that there was a problem with the lock-in amplifier during measurement of this channel.

2.3.3 Weak magnetic fields

The size of the weak localisation effect in the 2DEG of each channel is investigated in this section. Figure 2.8a shows the change in resistance $\delta R = R(B) - R(0)$ due to a magnetic field $|B| \leq 0.2\,\text{T}$. It can be seen that channels 2 and 3 show larger weak localisation signals

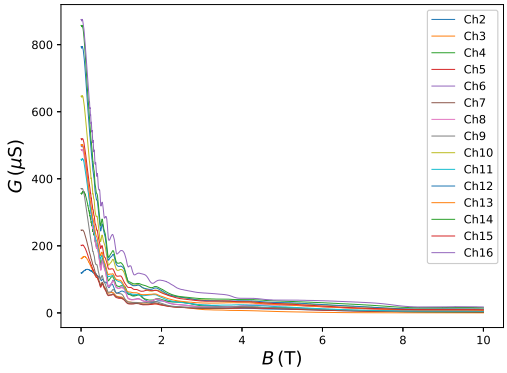

(a) G plotted as a function of B.

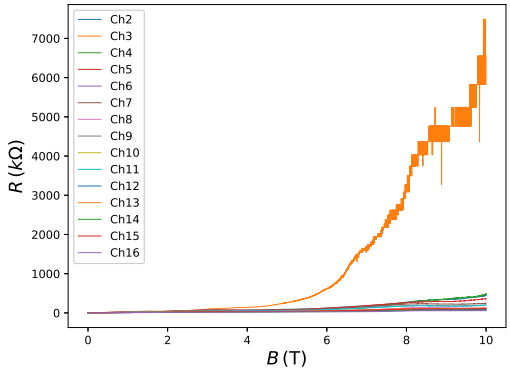

(b) R plotted as a function of B.

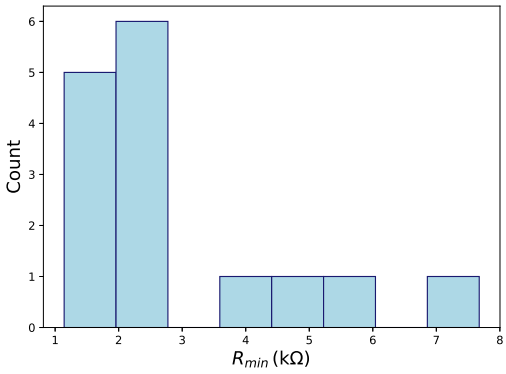

(c) Histogram of the minimum resistance.

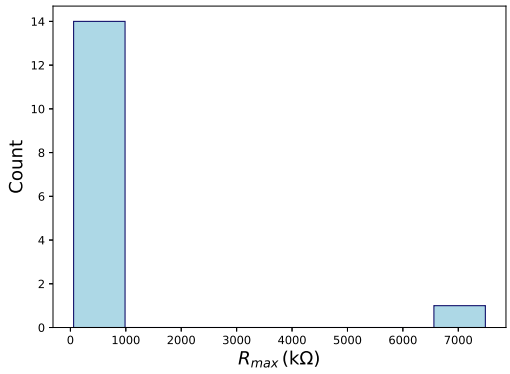

(d) Histogram of the maximum resistance.

Fig. 2.7 Plots of G and R as a function of B for channels 2-16 are shown in (a) and (b), respectively. From the $R(B)$ traces the minimum and maximum resistances are extracted and plotted as histograms in (c) and (d) to show the distribution of R_{min} and R_{max}.

than the remaining 13 conducting channels. The change in magneto-resistance $\Delta(\delta R) = \delta R_{max} - \delta R_{min}$ was calculated for each conducting channel, in order to quantify the magnitude of the weak localisation effect. These values are plotted in a histogram in Fig. 2.8b. Of the 15 channels, the magnitude of the weak localisation effect is larger then 0.1 kΩ for channels 2 and 3 only, which have $\Delta(\delta R) \approx 0.3\,\text{k}\Omega$ and $\Delta(\delta R) \approx 0.9\,\text{k}\Omega$, respectively. The mean value of $\Delta(\delta)R$ is $\Delta(\delta R) = 0.11\,\text{k}\Omega$ with standard deviation $\sigma_{\Delta(\delta R)} = 0.24\,\text{k}\Omega$.

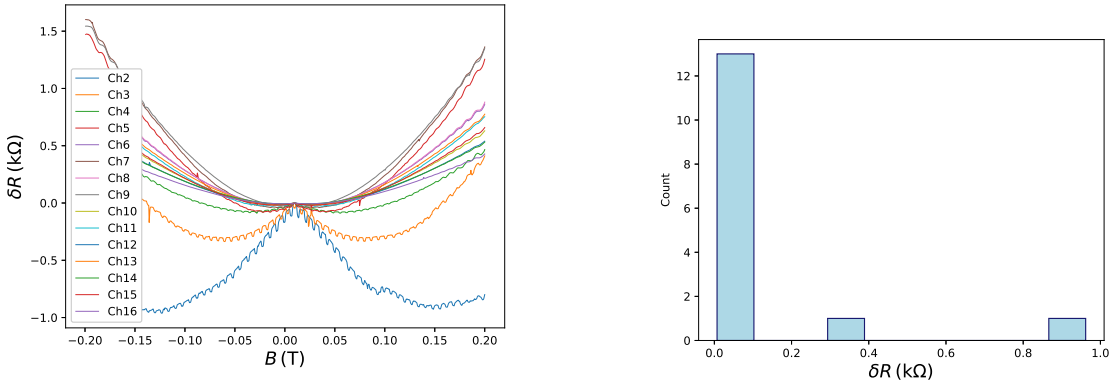

(a) δR plotted as a function of B of channels 2-16.

(b) Histogram of the maximum change in δR of channels 2-16.

Fig. 2.8 Plots of the change in resistance $\delta R = R(B) - R(0)$ of channels 2-16 are shown in (a) and show weak localisation behaviour. The maximum change in magneto-resistance $\Delta(\delta R)$, quantifying the magnitude of the weak localisation effect, is plotted as a histogram in (b). Data collected at $T = 0.28\,\text{K}$.

2.4 Graphene transfer

The monolayer graphene used in this work is grown by chemical vapour deposition (CVD) on Cu by Oliver Burton of the Hoffman group in the Department of Engineering at the University of Cambridge.

When graphene is grown by CVD on a Cu catalyst, both sides are covered by graphene, however only one of the films can be transferred onto the target substrate. To prepare the graphene for the transfer process, one side of the graphene-covered Cu film is protected with PMMA and then an oxygen reactive ion etching (RIE) system is used to etch the graphene from the other side.

The transfer processed used in this work is a wet-transfer process similar to that described in Ref. [146]. The Cu is etched by floating the PMMA-graphene-Cu stack on the surface of a 1.2% solution of ammonium persulphate $(NH_4)_2S_2O_8$. The only check that Cu has been

fully etched is by eye. Once the Cu has been removed, the remaining PMMA-graphene stack is transferred to the surface of a bath of DI water for 1 minute and then transferred to a second bath of DI water for 1 hour in order to rinse away the etching solution. The PMMA-graphene can then be lifted out of the DI water, using the target substrate and is left to dry in air overnight. The sample is baked at 125 °C for 30 minutes to improve the adhesion between the graphene and the multiplexer surface [147] and then soaked in acetone over night to remove the PMMA support layer.

The photolithgraphy mask has a layer which can be used to pattern the graphene into 100 μm^2 channels, which was used for device CVD-MUX-A, however it is also possible to use electron beam lithography to create custom designs. Once the graphene etch pattern has been selected, the graphene is etched using an oxygen RIE process. An etch power of 30 W is applied for 30 s to etch monolayer graphene.

2.4.1 Surface pre-treatment

It is known that the wettability of the surface of the target substrate effects the quality of the transferred graphene film, which depends on the target substrate material and the surface pre-treatment performed prior to the graphene transfer [148–150]. In particular, cracks and wrinkles in the graphene film have been shown to occur when the contact angle of water on the target substrate surface is large which occurs when the surface is hydrophobic. Initially UV-ozone cleaning was used in an attempt to reduce the hydrophobicity of the multiplexer surface, treatments of 2, 3 and 5 minutes were tried however no device fabricated using this pre-treatment conducted. Upon SEM imaging, cracks with widths of the order of 10 nm were found to run across the width of all the channels, visible in the SEM image shown in Fig. 2.9a. The cracks in graphene may arise due to cracking of the PMMA layer during processing, however this was not confirmed experimentally. This method was abandoned and an RF ashing process was used instead. A power of 100 W was applied for 120 s. This method resulted with a different type of defect: as opposed to thin cracks across the width of the channel, bubbles formed under the PMMA-graphene stack, shown in Fig 2.9b. It is likely that the bubbles contain water, since the graphene-PMMA stack is removed from the surface of a water bath using the target substrate, however it is not possible to claim this with certainty. When the PMMA is removed, the graphene is absent in the regions where the bubbles were observed, since the graphene is unable to make contact with the substrate in these regions. An AFM scan of a section of a single bubble is shown in Fig. 2.9c. The scan covers a small region where the PMMA-graphene stack is flat on the substrate surface, labelled in Fig. 2.9c, and a black, dashed line has been drawn to highlight the boundary between the flat region and the surface of the bubble. The line traces marked in the AFM

images are plotted in Fig 2.9d. Trace 1 starts in the flat region, at $x = 0\,\mu$m in Fig. 2.9d, and moves across the boundary onto the bubble surface. From trace 1 the step at approximately $x = 0.5\,\mu$m is approximately 20 nm, which is the bubble thickness. Line trace 2 is entirely across the surface of the bubble, showing that the profile of the surface oscillates, with an amplitude of approximately 20 nm.

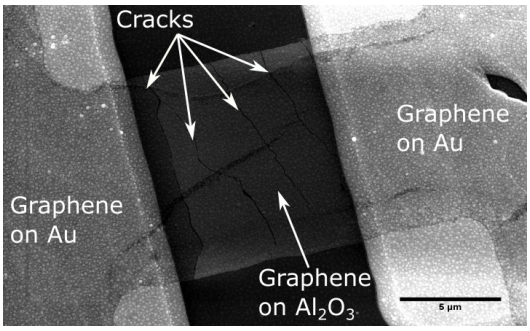

(a) Graphene channel with 2 minute UV-ozone pre-treatment.

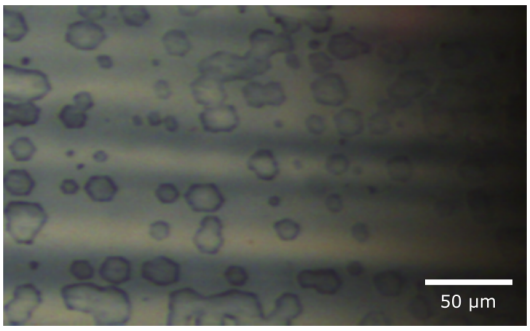

(b) Bubble formation under the PMMA-graphene stack.

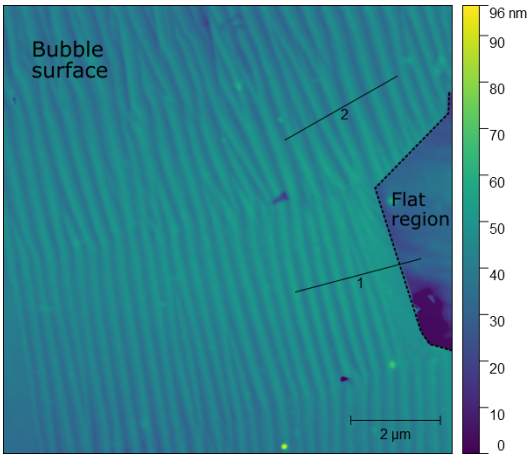

(c) AFM scan of part of the surface of bubble.

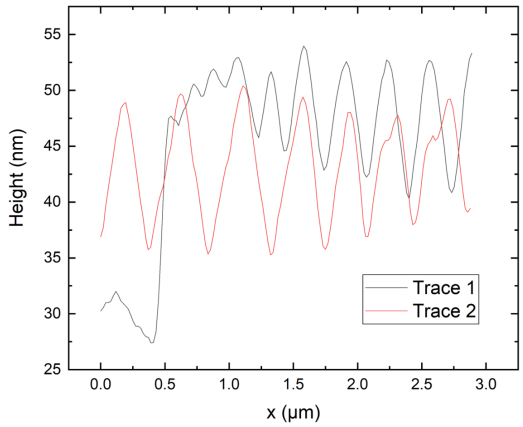

(d) Plots of the line profiles marked in (c)

Fig. 2.9 A bottom-contacted graphene channel is shown in (a). A 120 s UV-ozone clean was used before graphene transfer. Cracks can be seen running across the width of the channel. Figures (b), (c) and (d) are results of different pre-treatment, a 120 s RF ashing procedure which is more aggressive than a UV-ozone exposure, since the ions are accelerated towards the sample by a voltage between the RF source and the base of the reactor chamber. Bubbles appear under the PMMA-graphene stack as shown in the microscope image (b). The features in (b) were confirmed to be bubbles with AFM imaging; (c) shows an AFM scan of a section of a single bubble. The line traces marked 1 and 2 in the AFM image are plotted in (d), which shows the bubbles are approximately 20 nm thick.

Since device CVD-MUX-A, the primary device under study in this work was fabricated using a 120 s RF ashing pre-treatment, SEM images of all these channels will be shown in the

following section, where the aspect ratio of the channels will also be estimated. The channel shapes were defined using photolithography, and are intended to be $10\,\mu\text{m}\times 10\,\mu\text{m}$ squares. It will be seen in the following section that significant parts of these channels are missing, this is due to bubble formation under the PMMA-graphene stack in the regions where the channels are defined.

It was found later (after the magneto-transport experiments of CVD-MUX-A) that immersing the device in IPA solvent, directly after the PMMA-graphene stack has been transferred onto the multiplexer, for 5 s before drying in air reduced the occurrence of bubbles. This was done for a device measured at $T = 4.2\,\text{K}$ by Luke Smith of the Semiconductor Physics group at the University of Cambridge. SEM images showed that 75% of channels retained the intended square shape compared to 1 out of 12 channels taking the intended square shape on CVD-MUX-A.

2.5 Characterisation of device CVD-MUX-A

2.5.1 SEM imaging of channels

Figure 2.10 shows SEM images of all 16 channels of CVD-MUX-A. In all images, the source and drain contacts are seen in light grey at the top and bottom of each image, respectively. The graphene is the light region between the contacts. The shapes of the channels are have irregular shapes due to the formation of bubbles similar to those shown in Fig. 2.9b. Channel 6 is completely broken so that the source and drain are not connected. It will be shown in Chapter 3 that channels 8, 12, 13 and 15 also show zero conduction. The SEM images do not show any continuous breaks in the channel, as with channel 6 suggesting either that there are very narrow, continuous breaks which are unresolved by the SEM imaging, or that the ohmic contacts do not function in for those channels. Channel 2 tapers to a narrow region of width 440 nm at the contact yet still shows non zero-conduction. A magnification of the contact region of channel 2 is shown in Fig 2.11 where, the graphene is outlined by the dotted line.

2.5.2 Estimating the channel aspect ratio

The conductivity σ of a channel is calculated from the measured conductance G by multiplying by the aspect ratio of the device, sometimes called the number of squares. The aspect ratio is usually defined in terms of the resistance R and the sheet resistance R_s according to

$$R = R_s \frac{L}{W} = R_s N, \tag{2.1}$$

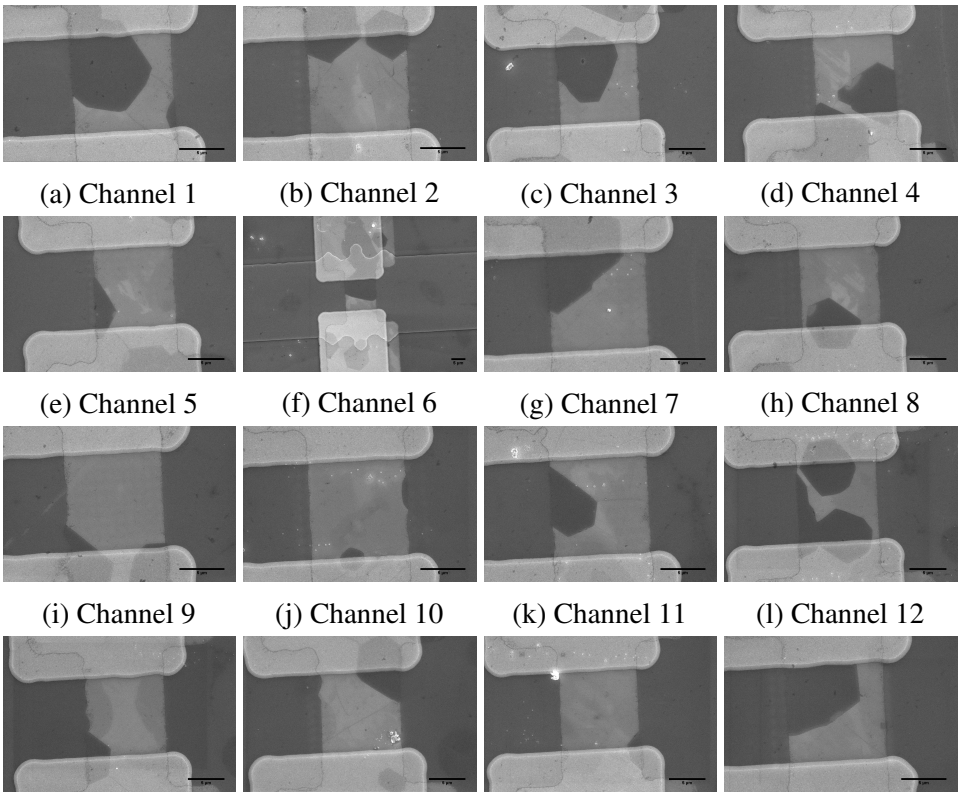

(a) Channel 1 (b) Channel 2 (c) Channel 3 (d) Channel 4

(e) Channel 5 (f) Channel 6 (g) Channel 7 (h) Channel 8

(i) Channel 9 (j) Channel 10 (k) Channel 11 (l) Channel 12

(m) Channel 13 (n) Channel 14 (o) Channel 15 (p) Channel 16

Fig. 2.10 SEM images of all of the channels of device CVD-MUX-A. The scale bar represents 5 μm in each image. All images were taken after electrical measurements were completed.

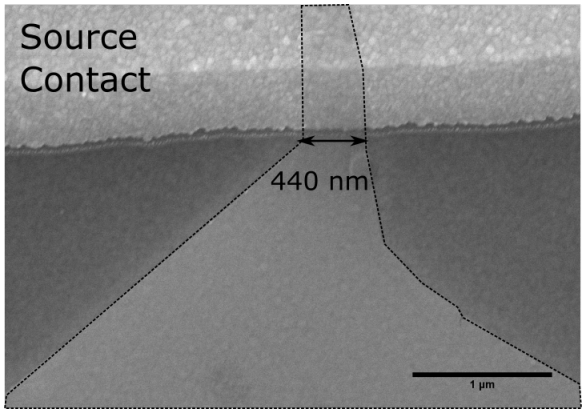

Fig. 2.11 Magnification of the source contact region of channel 2. The graphene is highlighted with a dashed black line. The width of the graphene channel is 440 nm at the source contact.

Channel	Aspect Ratio
1	2.75
2	2.45
3	2.75
4	2.83
5	1.07
7	1.50
9	0.97
10	1.00
11	1.47
14	0.83
16	2.70

Table 2.2 Estimated of the aspect ratio (L / W) of the irregular shape graphene channel shapes.

where $N \equiv L/W$ is defined to be the number of squares. The conductivity is the inverse of the sheet resistance and is given by:

$$\sigma = \frac{1}{R_s} = NG. \tag{2.2}$$

The sheet resistance/conductivity provides a geometry-independent measure of how resistive a sample is, since for any square, $R = 1 \cdot R_s$. This means that all squares regardless of their area have equal resistance. For rectangular samples it is simple to calculate the ratio L/W however for channels with irregular shape, as in the present device, it is less obvious. The method used here is to construct a resistor network by dividing the channel into squares which each have resistance R_s, and then solving to express the total resistance R in terms of R_s. An example for channel 1 is shown in Fig. 2.12. Each black square drawn in Fig. 2.12a has resistance R_s and the squares can be represented by the resistor network shown in Fig. 2.12b. Solving the resistor network in this case gives $R = 2.75R_s$ for channel 1, providing an estimate of L/W or the entire channel. The estimated values of the remaining channels are listed in Table 2.2.

2.5.3 Raman spectroscopy of graphene

Raman spectroscopy was used to confirm the presence of graphene after the transfer process and the graphene etching etching process. Specifically, graphene channels were mapped by acquiring 100 spectra in a $10\mu\text{m}\times10\mu\text{m}$ grid covering the channel area. Each spectrum is taken using a 514 nm laser and a 50x objective, with a power of approximately $50\,\mu$W. Two,

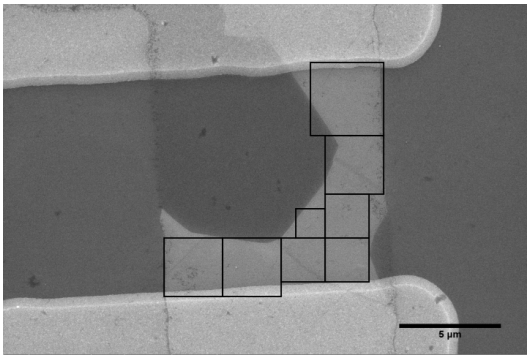

(a) Estimate of channel 1 geometry using squares.

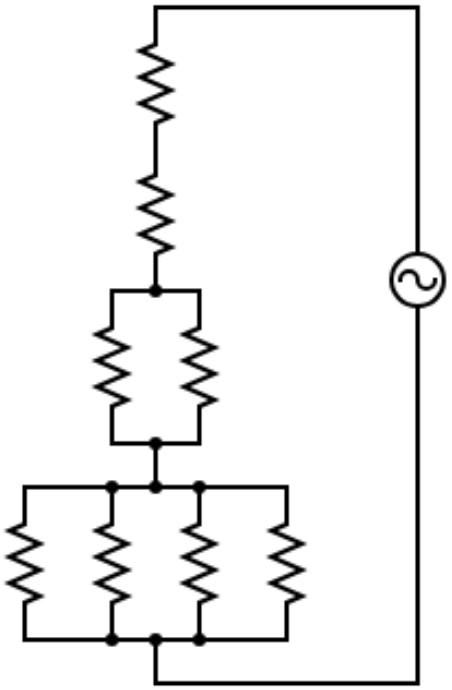

(b) A resistor network model of channel 1.

Fig. 2.12 The channel area is divided into squares which all have equal resistance R_s by definition. From these squares a resistor network model can be constructed and solved to estimate the aspect ratio of the channel.

separate acquisitions in identical positions are taken about the frequencies of the 2D peak and G peak to reduce the acquisition range, and hence the total time required to map the channel. For both the 2D and G peak the intensity I, peak position Pos (peak) and full-width at half-maximum Γ are extracted and analysed.

Intensity of the 2D and G peaks

The ratio of the intensity of the 2D peak to the intensity of the G peak is an indicator of the number of graphene layers, with $I_{2D}/I_G > 1$ indicating monolayer graphene. Figure 2.13 shows spatial maps of the ratio of the 2D peak to G peak intensities for each of the 11 conducting channels for device CVD-MUX-A. Grey regions in the heat maps indicate regions where no peak was detected. By comparing the grey regions in the Raman maps with the SEM images of each channel in Fig. 2.10 it can be seen that the grey regions correspond to regions where there is no graphene. In some cases small peak intensities are detected in the Raman signal noise which gives rise to some non-null values, that is non-grey pixels, in the regions where graphene is absent. This could be averted by smoothing or filtering the signal before detecting peaks, however filtering and smoothing operations can cause the centre of the peaks of interest to shift and the intensity to change. Since the 2D and G peak intensities and positions are of key interest, no filtering or smoothing operations were applied to the signal. Furthermore, in some of the heat maps there is a signal of low intensity in the top row, between y= 9μm and 10 μm. This is because the laser spot overlaps the gold contact metal which contributes to the signal. Since the primary quantity of interest is the ratio I_{2D}/I_G, only heat maps and histograms of I_{2D}/I_G will be included here. Heat maps and distributions of I_{2D} and I_G can be found in Appendix A.

From Fig. 2.13 it can be seen that $I_{2D}/I_G > 2$ across the entire area of every channel. An exception to this is channel 10, where the $I_G > I_{2D}$ in the region between $0 \leq x \leq 5$ and $0 \leq y \leq 4$, as can be seen in Fig. 2.13h. This indicates a patch of bi-layer graphene, which was indeed confirmed by taking a single Raman spectrum in the centre of the bilayer region. The mean value of $I_{2D}/I_G > 2$ for each channel was calculated and plotted as a histogram, shown in Fig. 2.14, which has a mean centred about 3.7, reflecting the fact that the channels are composed of monolayer graphene.

Linewidth of the 2D peak

It has been shown that while the width of the G peak in the graphene Raman spectrum is dependent upon electronic doping and inhomogenous charge distributions, the width of the 2D peak largely depends upon local strain variations [151, 152], and is only weakly

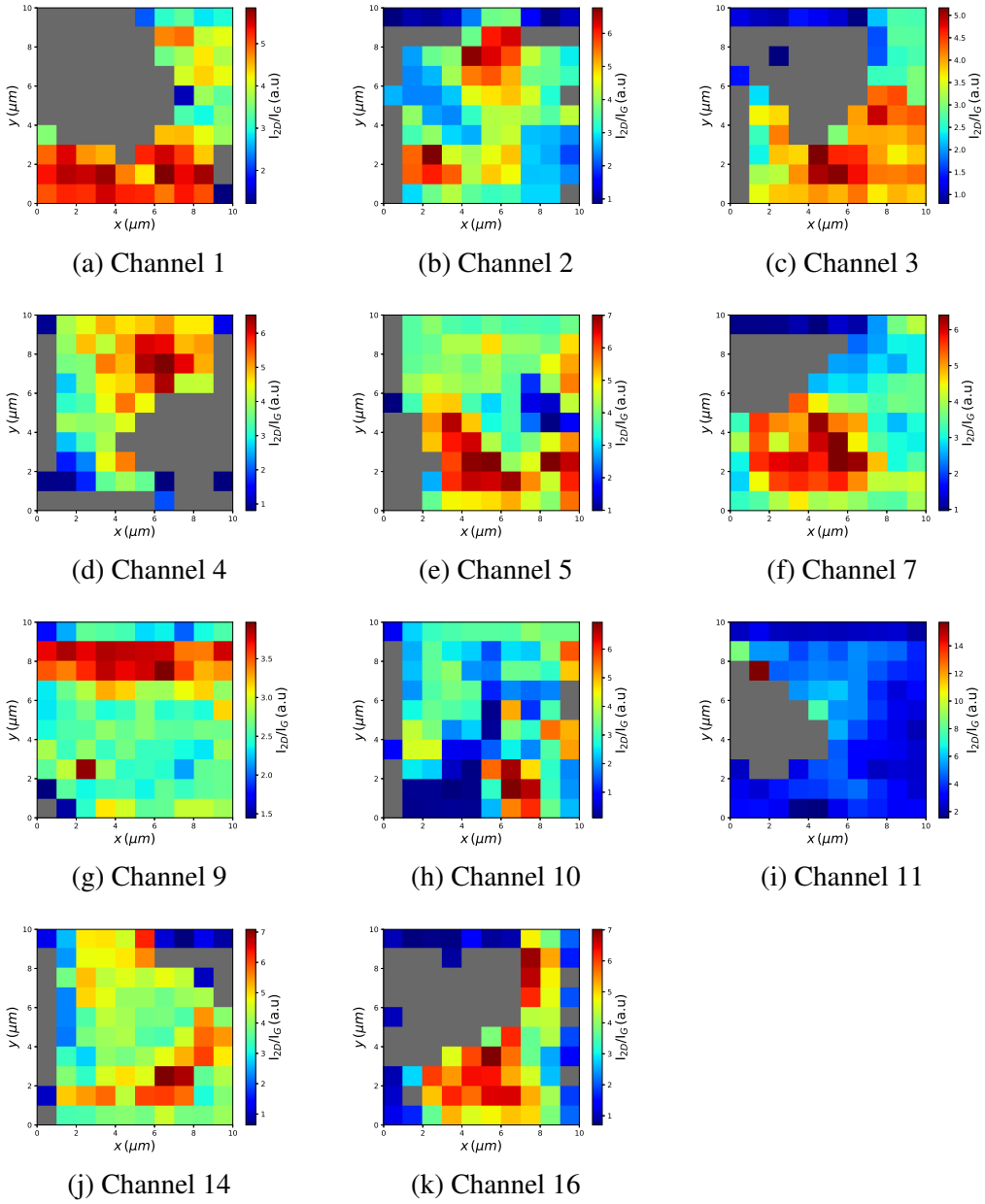

(a) Channel 1 (b) Channel 2 (c) Channel 3

(d) Channel 4 (e) Channel 5 (f) Channel 7

(g) Channel 9 (h) Channel 10 (i) Channel 11

(j) Channel 14 (k) Channel 16

Fig. 2.13 Heat maps representing the spatial distribution of I_{2D}/I_G for all channels.

Channel	$\overline{I_{2D}/I_G}$	σ_{I_{2D}/I_G}
1	4.4	1.1
2	3.7	1.4
3	3.3	1.2
4	4.0	1.5
5	4.4	1.3
7	3.8	1.4
9	2.8	0.5
10	2.7	1.6
11	4.0	1.9
14	4.1	1.3
16	3.8	2.0

Table 2.3 The mean, $\overline{I_{2D}/I_G}$ and standard deviation σ_{I_{2D}/I_G} of I_{2D}/I_G in each channel.

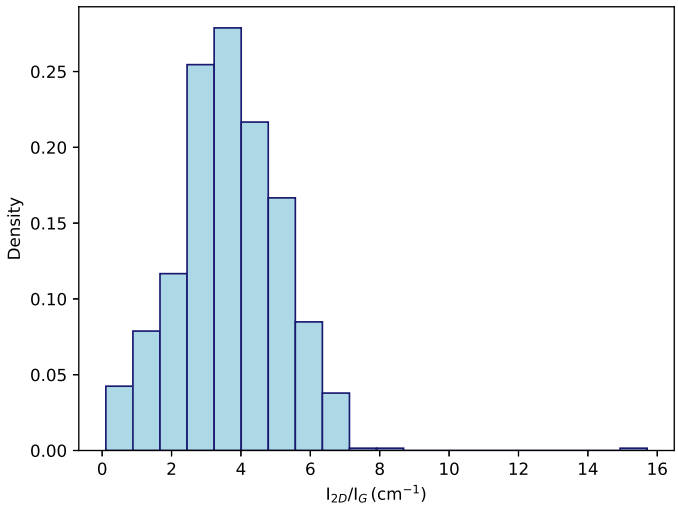

Fig. 2.14 Histogram of I_{2D}/I_G. The values from all channels are used.

Channel	$\overline{\Gamma}_{2D}\,(\mathrm{cm}^{-1})$	$\sigma_{\Gamma_{2D}}\,(\mathrm{cm}^{-1})$
1	28.8	3.3
2	31.0	5.3
3	33.1	10.0
4	30.8	10.5
5	31.2	9.0
7	31.7	9.1
9	32.4	2.8
10	32.7	7.3
11	31.4	5.1
14	33.2	9.0
16	34.0	9.8

Table 2.4 The mean, $\bar{\Gamma}_{2D}$ and standard deviation $\sigma_{\Gamma_{2D}}$ of Γ_{2D} in each channel.

affected by doping and global strain. This makes the linewidth Γ_{2D} a qualitative probe of the strain distribution in graphene, where a large value of Γ_{2D} relative to the zero strained value $\Gamma^0_{2D} \approx 17-20\,\mathrm{cm}^{-1}$ as measured in a hBN-graphene-hBN stack [152], indicates the presence of local strain. Figure 2.15 shows heat maps of values of Γ_{2D} in each channel, giving a qualitative image of the strain variation in each channel. In each channel, the variation of Γ_{2D} is quantified by the standard deviation. The mean $\overline{\Gamma}_{2D}$, and standard deviation $\sigma_{\Gamma_{2D}}$, are displayed in Table. 2.4. A histogram displaying the distribution of Γ_{2D} across all channels is shown in Fig. 2.16. Across all channels $\overline{\Gamma}_{2D} = 31.9$ and $\sigma_{\Gamma_{2D}} = 7.9$ which is similar to values of graphene on SiO_2 substrates [151–153], confirming substrate induced strain variations in all of the graphene channels.

Residual carrier density

The position of the G peak has been shown to be sensitive to the position of the Fermi level and can probe local density variations in graphene [154, 155]. The shift of Pos(G) away from its value at the Dirac point $\mathrm{Pos(G)}_0$, has been shown in Refs. [156, 157] to be linearly proportional to E_F according to $\Delta\mathrm{Pos(G)} = \lambda E_F$, where $\lambda \approx 42\,\mathrm{cm}^{-1}\mathrm{eV}^{-1}$ and $E_F = sgn(n)\hbar v_F\sqrt{\pi n}$.

There does not appear to be a large degree of correlation between the density maps shown in Fig. 2.17 and those of Γ_{2D} shown in Fig. 2.15 suggesting that strain is not the dominant cause of residual doping in these channels. From the histogram shown in Fig. 2.18 the modal density is $n \approx 1\times10^{12}\,\mathrm{cm}^{-2}$, however some localised regions have densities up to $n = 7\times10^{12}\,\mathrm{cm}^{-2}$ which causes the skew in the distribution shown in Fig. 2.18.

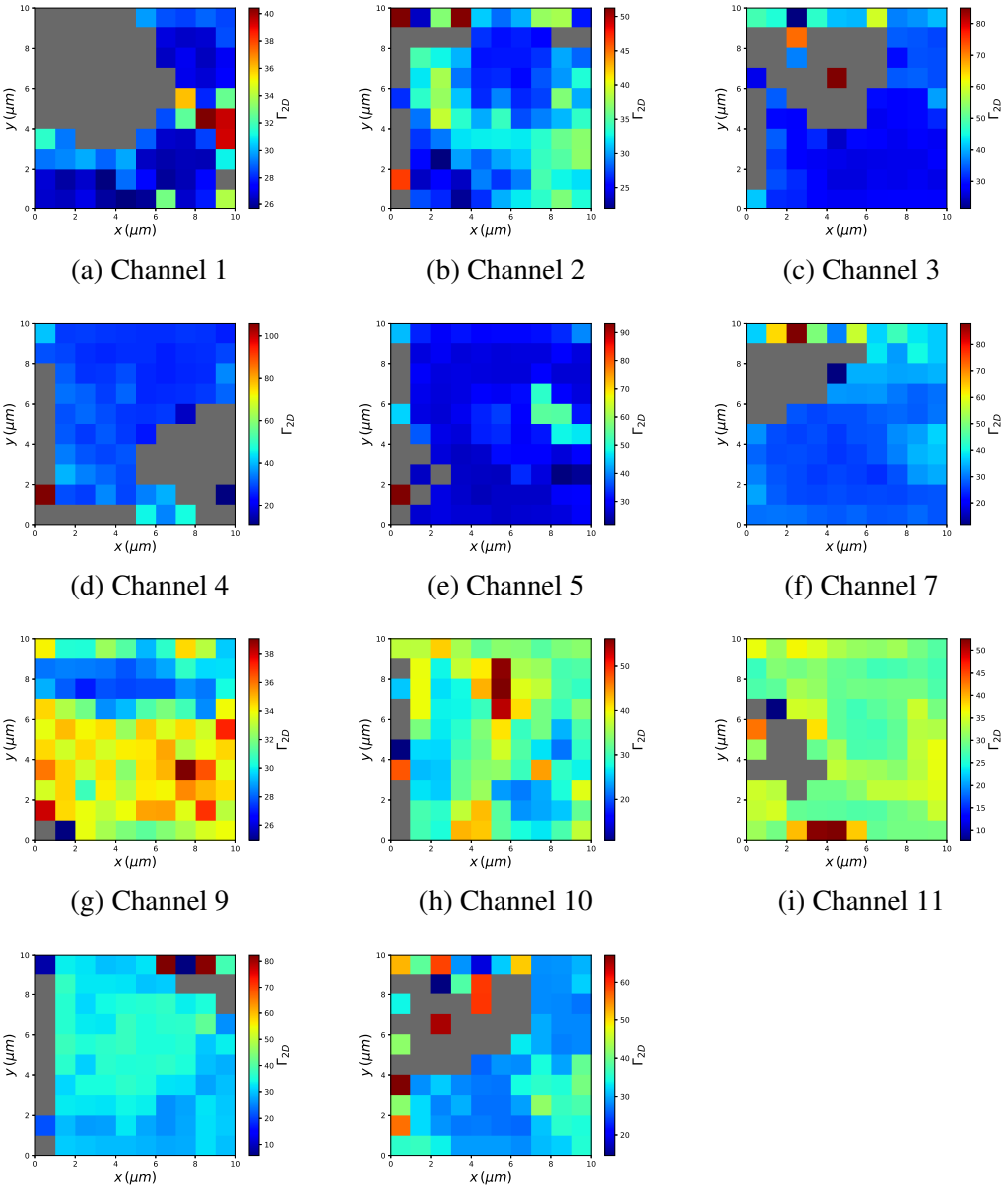

(a) Channel 1 (b) Channel 2 (c) Channel 3

(d) Channel 4 (e) Channel 5 (f) Channel 7

(g) Channel 9 (h) Channel 10 (i) Channel 11

(j) Channel 14 (k) Channel 16

Fig. 2.15 Heat maps representing the spatial distribution of Γ_{2D} for all channels.

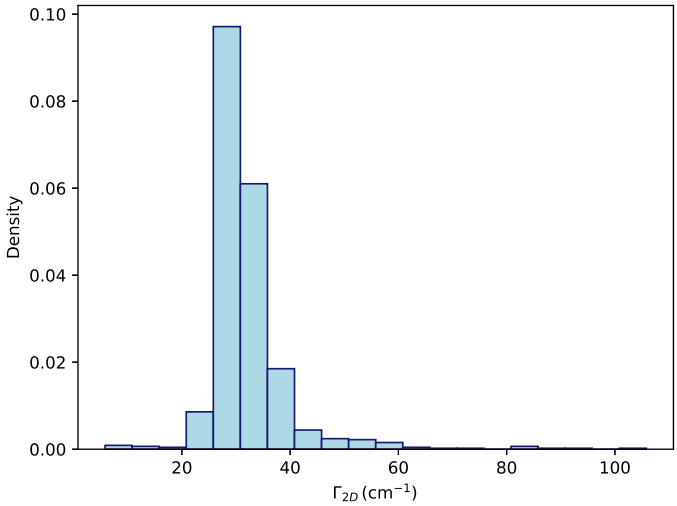

Fig. 2.16 Histogram of Γ_{2D}. The values from all channels are used.

Channel	$\bar{n}\,(10^{12}\mathrm{cm}^{-2})$	$\sigma_n\,(10^{12}\mathrm{cm}^{-2})$
1	1.2	0.8
2	1.9	1.4
3	2.0	1.1
4	1.1	0.9
5	1.1	0.7
7	2.0	1.7
9	2.4	0.9
10	1.0	0.6
11	1.8	1.5
14	0.7	0.8
16	1.0	0.9

Table 2.5 The mean carrier density, $\bar{n}$ and standard deviation $\sigma_{\bar{n}}$ in each channel.

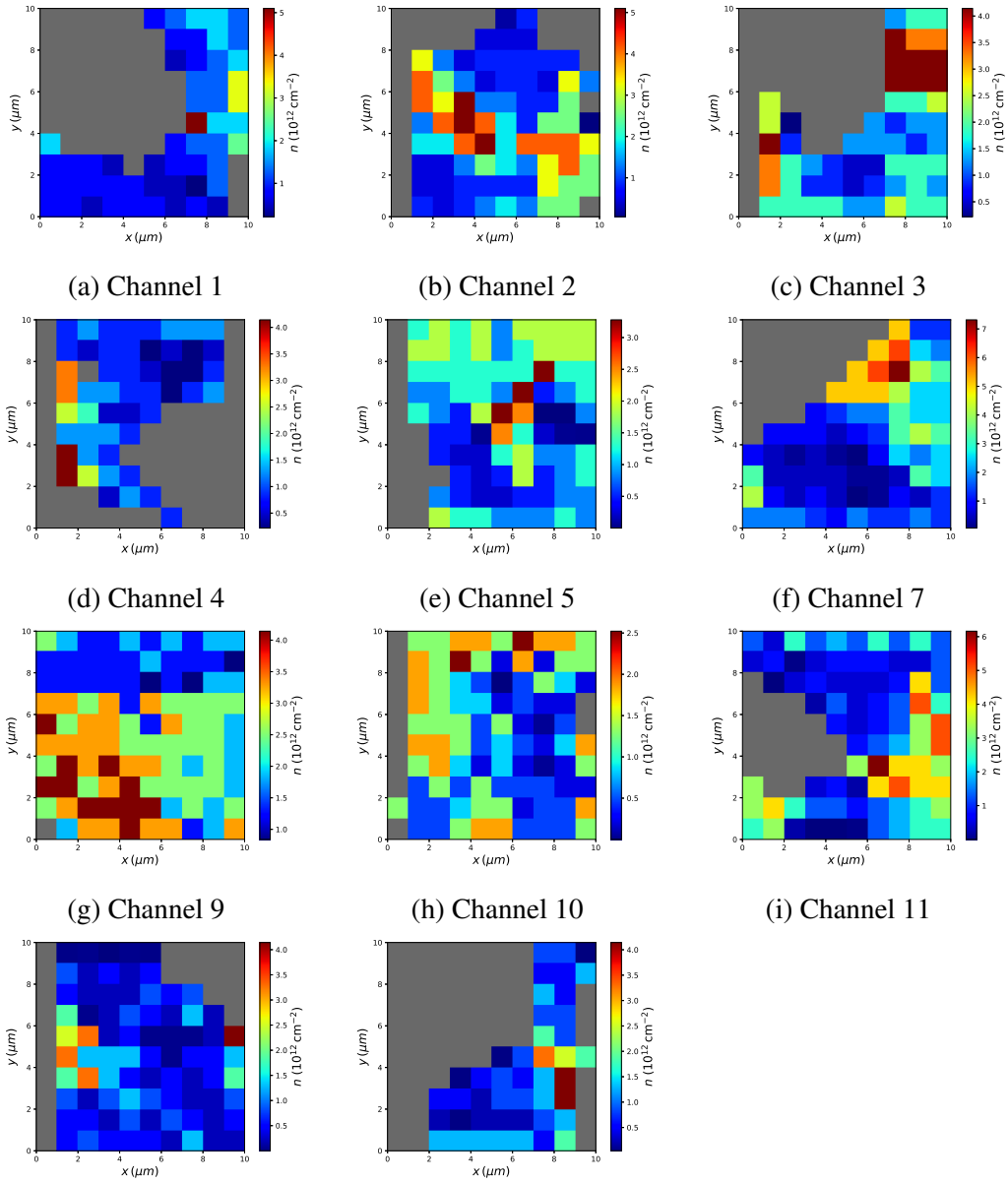

(a) Channel 1 (b) Channel 2 (c) Channel 3

(d) Channel 4 (e) Channel 5 (f) Channel 7

(g) Channel 9 (h) Channel 10 (i) Channel 11

(j) Channel 14 (k) Channel 16

Fig. 2.17 Heat maps representing the spatial distribution of the residual carrier density n for all channels in units of $10^{12}\,\mathrm{cm}^{-2}$.

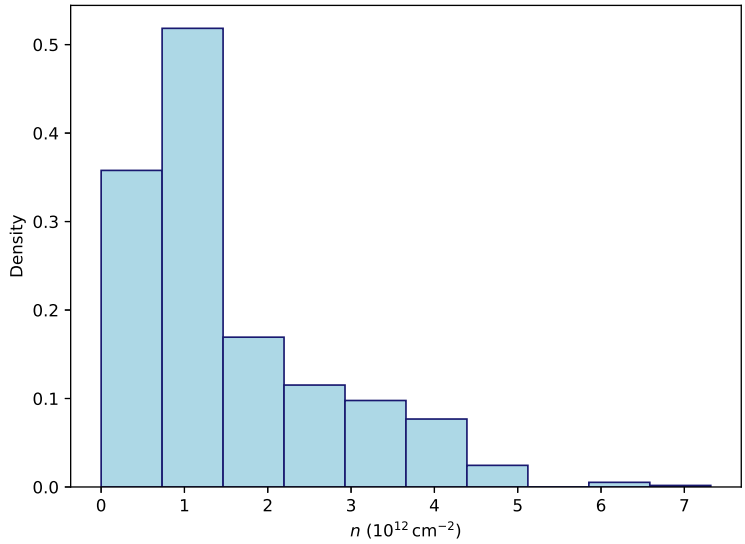

Fig. 2.18 Histogram of residual carrier density n as obtained from Raman spectroscopy. The values from all channels are used.

2.6 Conclusions

This chapter describes two on-chip multiplexing designs: one with 16 outputs and another with 128 outputs. The relevant dimensions of the device design are provided to give the reader an understanding of the size of each device. This is followed by a description of the fabrication methods, which should contain enough detail for the reader to reproduce these devices given the necessary materials and equipment.

Magneto-transport experiments on a short-circuited 16 output multiplexer device showed that at $B = 10\,\mathrm{T}$ the resistance of each channel is of the order of $200\,\mathrm{k\Omega}$, however it is possible for some channels to exceed this value, with channel 3 of the studied device reaching approximately $7\,\mathrm{M\Omega}$. The weak localisation effect was found to be small in most channels, with a mean magneto-resistance change of $110\,\Omega$, with standard deviation $240\,\Omega$.

An oxygen RF ashing process using 100 W for 120 s was found to give a higher yield of conducting graphene channels than a UV-ozone pre-treatment. The RF ashing did lead to the formation of bubbles under the transferred PMMA-graphene stack which caused irregular channel shapes in the resulting graphene film. This was the case for device CVD-MUX-A which is studied throughout the following three chapters. Before allowing the PMMA-graphene stack to dry over night on the surface of the multiplexer, immersing the sample in IPA was found to decrease the number of bubbles and increase the uniformity of the resultant graphene film. This may be because the IPA environment helps to draw-out water from under the PMMA-graphene stack.

The graphene channels in device CVD-MUX-A are characterised by SEM imaging and Raman spectroscopy. The SEM images reveal the unintentional, irregular shape of the graphene channels and Raman spectroscopy confirms that the channels observed in the SEM images are indeed monolayer graphene. Maps of the 2D peak linewidth are used to qualitatively examine local strain variations, and indicate substrate-induced strain variations similar to those observed in graphene on SiO_2/Si substrates, reported elsewhere. The position of the G peak is used to estimate the local doping variations in the channel. There is no evidence that carrier density variations are caused by the strain distribution in the channel, and the modal residual carrier density is $n \approx 1 \times 10^{12}\,\mathrm{cm}^{-2}$. The D peak, often used to quantify disorder in graphene, was not detectable in almost all spectra, indicating high crystalline quality of the graphene samples used in the present data.

This chapter is followed by the low temperature electrical characterisation of device CVD-MUX-A in the absence of an external applied magnetic field.

Chapter 3

Electrical Transport Measurements of Multiplexed Graphene Field-Effect Transistors at Zero Magnetic Field

3.1 Introduction

This chapter presents the results of electrical transport measurements of device CVD-MUX-A in the absence of a magnetic field. For each GFET, the common device parameters used to evaluate their performance are calculated by modelling the behaviour of $R(V_g)$. A general discussion of the results is given before being compared to non-multiplexed devices reported in the literature. It will be shown that multiplexed devices have similar parameter values to non-multiplexed devices, thereby showing the multiplexer can be used as a useful tool for gathering statistics on the performance of nanomaterial devices, which is the primary purpose of this chapter. Additionally, this chapter serves to illustrate the basic experiments that can be performed by using a multiplexer device with transferable nanomaterials and the analysis which can be done with the data that is obtained when using a multiplexing device. The device was measured during two separate cool-downs, the first in a a ^{4}He dewar with temperature $T = 4.2\,K$, and the second in a ^{3}He cryostat system at $T = 0.28\,\mathrm{K}$.

3.2 Results and Analysis

The device CVD-MUX-A was measured in two separate cool-downs, the first at $T = 4.2\,\mathrm{K}$ and the second at $T = 0.28\,\mathrm{K}$. Figure 3.1 shows the resistance R plotted as a function of back-gate voltage V_g for both cool-downs. In order to characterise these devices a model from

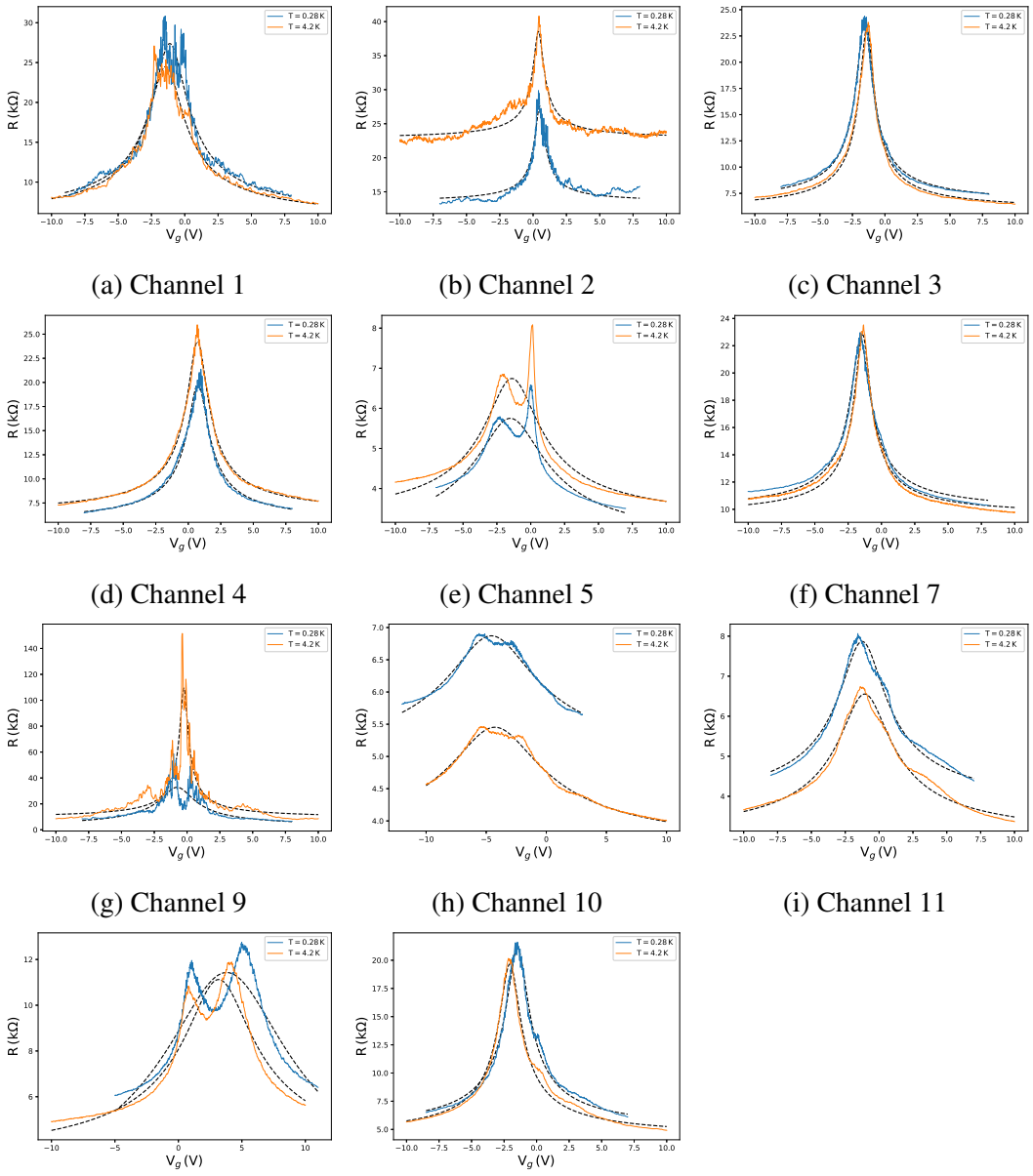

(a) Channel 1 (b) Channel 2 (c) Channel 3

(d) Channel 4 (e) Channel 5 (f) Channel 7

(g) Channel 9 (h) Channel 10 (i) Channel 11

(j) Channel 14 (k) Channel 16

Fig. 3.1 The resistance R plotted as a function of back gate voltage V_g for all conducting channels. Blue curves shows data taken at $T = 0.28\,\mathrm{K}$ and orange curves show data taken at $T = 4.2\,\mathrm{K}$ in a separate cool-down. Black dashed lines represent fits of Eqn. 3.1 to the data. Note that the y-axes use different scales in order to make the detail of the data clear in all channels.

Ref. [158] was fit to the resistance data, which uses the Dirac voltage V_d, contact resistance R_c, mobility μ and the carrier density in the region of minimum conductivity n_0 as fitting parameters. The equation used to model the resistance is given by:

$$R(V_g) = R_c + \frac{L/W}{e\mu\sqrt{(C_{ox}(V_g - V_d)/e)^2 + n_0^2}}. \tag{3.1}$$

Note that here the model is presented as $R(V_g)$ as opposed to $R(n_{ind})$ as in Ref. [158] by making the substitution $n_{ind} = C_{ox}(V_g - V_d)/e$. The gate capacitance is $C_{ox} = \varepsilon_r\varepsilon_0/t_{ox} \approx 87.1\,\mathrm{nFcm}^{-2}$ for a 95 nm-thick film of Al_2O_3. The value of $\varepsilon_r = 9$ for Al_2O_3 is taken from Ref. [159] and was not measured. The contact resistance R_c denotes the total resistance of the rest of the circuit, which has contributions from: the resistance of the ohmic contacts (AuGeNi), the resistance of the 2DEG, the resistance between the ohmic contacts and Au contacts, the resistance between Au contacts and graphene and the resistance of all of the off-chip wiring. Note that this fitting method assumes that both electrons and holes have equal, density-independent mobility, which is not always true in reality. Furthermore, uncertainties arise in the parameter estimates due to the estimate of L/W, however this was found to effect the estimate of μ only.

For most channels, a single peak is observed in $R(V_g)$. This peak occurs because the the density of states is proportional to the energy, $\rho(E) \propto |E|$ which is zero at the point where the the conductance and valance bands meet, called the Dirac point, as shown in Ref. [28]. For example, when V_g is negative and far from the Dirac point, that is $|V_g - V_d| \ll 0$, there are many free holes in the valence band available for transport and the main contribution to R is from the contacts. As E_F moves closer towards the Dirac point due the field-effect caused by V_g, the hole density approaches zero $n_h \to 0$, and R increases until it reaches a maximum at $|V_g - V_d| \approx 0$, where holes and electrons coexist due to disorder. Once E_F moves past the Dirac point, that is $|V_g - V_d| > 0$ the density of free electrons in the conduction band begins to increase and the R begins to decrease until it becoming constant again once $|V_g - V_d| \gg 0$ due the contacts.

For channels 5, 10 and 14, two resistance peaks are observed. In these cases further fitting was performed, using a the sum of two functions described in Eqn. 3.1:

$$R(V_g) = R_c + \frac{L/W}{e\mu\sqrt{(C_{ox}(V_g - V_d)/e)^2 + n_0^2}} + \frac{L/W}{e\tilde{\mu}\sqrt{(C_{ox}(V_g - \tilde{V}_d)/e)^2 + \tilde{n}_0^2}}. \tag{3.2}$$

These fits are displayed in Fig. 3.3 and the extracted parameter values at 4.2 K and 0.28 K are displayed in Tables 3.3 and 3.4, respectively. When using Eqn. 3.2, much higher values

of μ are obtained than when a single fit is performed to both peaks together, as in Figs. 3.1e, 3.1h and 3.1j. Assuming two distinct regions with different values of V_d, μ and n_0 the mobility values can be combined according to Matthiessen's rule $1/\mu = 1/\mu_1 + 1/\mu_2$, since μ is proportional to the scattering time τ. At $T = 4.2\,\mathrm{K}$ the total mobilities according to Matthiessen's rule are $\mu = 3100,\ 2500,\ 1100\,\mathrm{cm^2V^{-1}s^{-1}}$ for channels 5, 10 and 14, respectively; at $T = 0.28\,\mathrm{K}$ the total mobilities are $\mu = 3400,\ 1300,\ 3400\,\mathrm{cm^2V^{-1}s^{-1}}$ for channels 5, 10 and 14, respectively.

Note that Eqn. 3.2 assumes that R_c is equal for both electrons and holes. Furthermore, far from the Dirac point, when V_g approaches $\pm 10\,\mathrm{V}$ the fit to channel 5 deviates from the data. This could not be fixed by adjusting fitting weights or by adjusting the fitting range which suggests that Eqn. 3.2 does not properly describe the transport away from the charge neutrality region. This leads to a slight underestimate of R_c in channel 5. Nonetheless, the fits around the peaks are accurate which means the remaining parameter estimates are accurate.

This deviation highlights the fact that R_c is different depending on whether the channel is electron doped or hole doped, since the model is failing when trying to treat them as equal, and implies that there is an imbalance between the amount of electrons and holes injected into the channel from the contacts. This imbalance between electron and hole injection was studied in Refs. [160, 161] and the authors found experimentally and numerically that an imbalance between the injection of electrons and holes does lead to conductance asymmetry, as observed in the present data. This imbalance arises when the charge neutrality point (CNP) of the graphene in contact with the Au contact metal is at a different value to that of the CNP in the graphene in the channel, which can be caused by doping in the channel due adsorbants or by doping in the graphene touching with the metal contacts. This concept is illustrated by the diagram shown in Fig. 3.2 which is an adaptation of Fig. 4 from of Ref. [161]. Consider the middle diagram which shows the energy E of carriers plotted as a function of the density of states, denoted $D(E)$ on the x-axis. The channel has uniform doping and E_F is shifted relative to the position of E_F in the contacts (left and right diagrams). In graphene, the CNP (red square) is at the point where $D(E) = 0$ by definition, and the density of electron and hole states are symmetric about this point. Now consider the contacts. The energy of the CNP in the channel corresponds to an energy where $D(E) \neq 0$ in the contacts due to the offset between E_F in the contacts and in the channel, this is illustrated by the red dotted line labelled CNP. This in turn means that the density of electron states and hole states are no longer symmetric relative to the CNP of the channel. As a consequence, more electrons will be injected into the channel than holes and conductance of holes will be suppressed, causing an asymmetry in the measured $G(V_g)$. This argument also holds when the the channel is undoped but the graphene in the contact region is doped due to the metallic contacts.

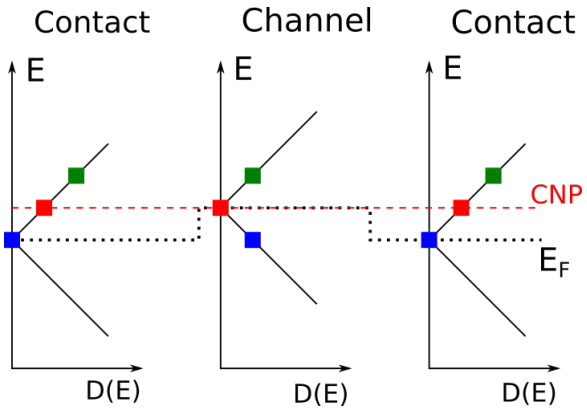

Fig. 3.2 Diagram showing how a change in E_F (black dotted line) leads to conductance asymmetry. In the channel, the density electron (green square) and hole (blue square) states are symmetric about the charge neutrality point (CNP) (red square), where $D(E) = 0$ by definition. The energy of the CNP in the channel corresponds to an energy with non-zero $D(E)$ in the contacts, which means that the density of hole and electron states are no longer symmetric about the CNP in the channel. This leads to an imbalance of charge injection and $G(V_g)$ asymmetry.

The reason why only channels 5, 10 and 14 show this behaviour may be because the channels have been unintentionally doped more than the other channels, however this is not obvious from SEM imaging. An alternative hypothesis is that the graphene above the contact metal may be doped in these channels more than the others. The authors of Ref. [162] show that graphene doping due to the contact metal depends strongly on the separation d between the graphene sheet and the metal, since this effects the overlap of the wavefunctions for electrons in the graphene and in the metal. For Au they calculate that the Fermi level in graphene is shifted from the CNP by $\Delta E_F(d) = 0.4\,\text{eV}$ when $d = 5\,\text{Å}$; this changes to $\Delta E_F(d) = 0.25\,\text{eV}$ at $d = 3\,\text{Å}$ separation. Therefore, large variations in the position of E_F may arise from small variations in the graphene-metal separation d, which could arise from atomic-scale ripples, strain or tears which may be present. Consequently, it is reasonable to postulate that the graphene is closer to the contact metal in channels 5, 10, and 14 than it is in the other channels, causing a large shift of E_F in the graphene at the electrode regions and resulting in the observation two $R(V_g)$ peaks. Reference [163] confirms experimentally that the Fermi level pinning causes a conductance asymmetry, but did not observe two local conductance minima, as is the case in the present work. Similar asymmetry has been found in other reports [164, 165] however none report two local minima in $G(V_g)$.

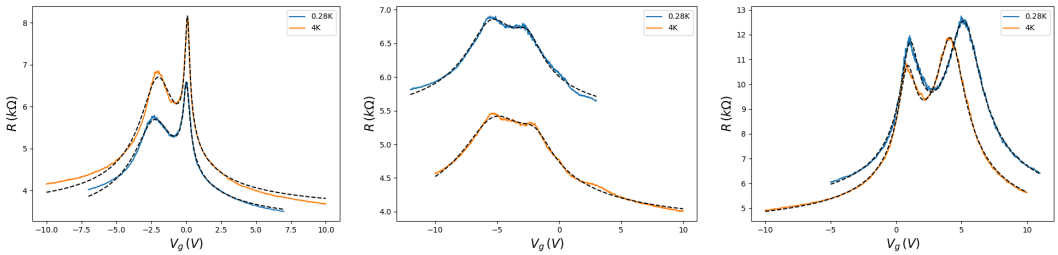

(a) Channel 5 (b) Channel 10 (c) Channel 14

Fig. 3.3 The resistance $R(V_g)$ for channels 5, 10 and 14 which show two prominent peaks. The two peaks have been fit simultaneously using Eqn. 3.2

Channel	$V_d\,(V)$	$\mu\,(cm^2V^{-1}s^{-1})$	$R_c\,(k\Omega)$	$n_0\,(10^{12}cm^{-2})$
1	-1.42	1800	5.16	0.67
2	0.40	4900	22.70	0.20
3	-1.39	3600	5.86	0.27
4	0.71	2500	6.25	0.40
5	-1.39	1800	3.08	1.02
7	-1.41	2300	9.49	0.30
9	-0.24	400	8.87	0.16
10	-4.28	1600	3.51	1.96
11	-1.06	2600	2.90	0.98
14	3.17	500	2.99	1.38
16	-2.05	2600	4.27	0.42
Mean	-0.81	2200	6.83	0.71
Std	1.80	1200	5.47	0.55

Table 3.1 The extracted fitting parameters for device CVD-MUX-A, to 3 significant figures. These results are at $T = 4.2\,\mathrm{K}$. The final two rows represent the mean and the standard deviation of each column, respectively.

Channel	$V_d\,(V)$	$\mu\,(cm^2V^{-1}s^{-1})$	$R_c\,(k\Omega)$	$n_0\,(10^{12}cm^{-2})$
1	-1.13	1600	5.36	0.65
2	0.50	5900	13.43	0.18
3	-1.58	3300	6.46	0.30
4	0.75	3100	5.39	0.40
5	-1.51	1600	2.53	1.29
7	-1.57	2000	9.77	0.37
9	-0.76	300	2.04	0.66
10	-4.57	1600	4.82	1.87
11	-1.25	2500	3.64	0.87
14	3.80	200	0.02	2.53
16	-1.47	2400	4.81	0.44
Mean	-0.80	2200	5.30	0.87
Std	2.00	1500	3.52	0.71

Table 3.2 The extracted fitting parameters for device CVD-MUX-A, to 3 significant figures. These results are at $T = 0.28\,\mathrm{K}$. The final two rows represent the mean and the standard deviation of each column, respectively.

Channel	$V_g\,(V)$		$\mu\,(cm^2V^{-1}s^{-1})$		$R_c\,(k\Omega)$		$n_0\,(10^{12}cm^{-2})$	
	Left	Right	Left	Right	Left	Right	Left	Right
5	-2.04	-0.01	3500	26000	3.47	3.47	0.64	0.08
10	-5.28	-1.93	3100	12000	3.72	3.72	1.39	0.78
14	0.85	4.15	3900	1500	4.08	4.08	0.35	0.58

Table 3.3 The extracted fitting parameters from using Eqn. 3.2 to model the left and right peak for channels 5, 10 and 14 at $T = 4.2\,\mathrm{K}$.

Channel	$V_g\,(V)$		$\mu\,(cm^2V^{-1}s^{-1})$		$R_c\,(k\Omega)$		$n_0\,(10^{12}cm^{-2})$	
	Left	Right	Left	Right	Left	Right	Left	Right
5	-2.28	-0.02	3900	26000	3.14	3.14	0.74	0.12
10	-5.51	-2.53	4000	1900	5.28	5.28	0.86	1.41
14	1.11	4.97	4500	14000	4.53	4.53	1.05	0.62

Table 3.4 The extracted fitting parameters from using Eqn. 3.2 to model the left and right peak for channels 5, 10 and 14 at $T = 0.28\,\mathrm{K}$.

3.2.1 Reproducibility of device parameters

The device parameters extracted from transport measurements during two, separate cool-downs are compared using box plots in Fig. 3.4 and are tabulated in Tables 3.1 and 3.2. Students t-tests were used to confirm there is no statistically significant difference between the parameter values between cool-downs. Explanations of Students t-test and other statistical tests are provided in Appendix B. In some channels, the curves take similar shapes between cool-downs, but have shifted vertically, in a inconsistent manner. It is possible that the contact resistance between the Au and graphene has changed over time between cool-downs, which were taken over a week apart. The main difference between two cool-downs is the behaviour of channel 9 which becomes much more resistive close to the charge neutrality point during the first cool-down compared to the second, as shown in Fig. 3.1g. During the first cool-down at $T = 4.2\,\mathrm{K}$ there appear to be two peaks in the resistance, whereas in the second cool-down the $R(V_g)$ curve appears to be better described by a single peak. The extracted values of R_c and n_0 are similar between both measurements, suggesting that the observed difference in resistance could be due to a conductance fluctuation pattern changing between cool-downs.

3.2.2 Comparison of extracted parameters to literature

Comparison of μ values

The mean value of the mobility found in the present data is approximately $\overline{\mu} = 2,000\,\mathrm{cm^2V^{-1}s^{-1}}$ during both cool-downs, consistent with values reported elsewhere, which are summarised in Table 3.5. It can be seen that the mobilities found here are comparable to both non-encapsulated devices and devices with an Al_2O_3 or HfO_2 encapsulation layer deposited on top of the graphene. References [166, 167] also measured the mobility at $T = 77\,\mathrm{K}$ and observed an approximate mobility increase of 20% and 10%, respectively, which is explained by a suppression of surface optical phonon modes, which lower mobility through electron-phonon scattering [168–170]. Note that Refs. [171, 172] used a Ni catalyst for graphene growth, while Refs. [146, 173] used a Cu catalyst and the mobility values are similar to each other and to what was found in the present work. The authors in Ref. [174] also used a Cu catalyst but compared different Cu etching methods; the value reported in Table 3.5 is for devices fabricated using an $(NH_4)_2S_2O_8$ solution, as used for the devices reported here in the present work. Again, there is consistency between the mobility value reported there and what is reported here in the present work. The mobility is far lower in the present devices than in those reported in Ref. [175] which uses a dry-transfer process

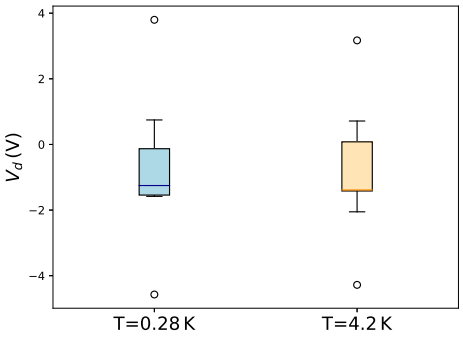

(a) Distribution of V_d values.

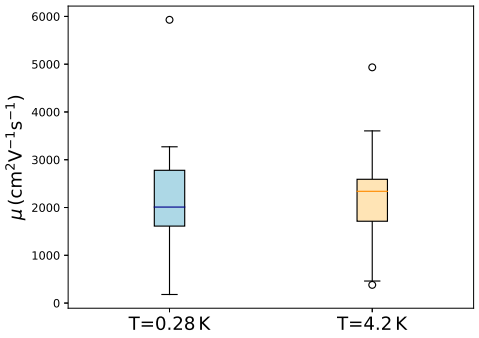

(b) Distribution of μ values.

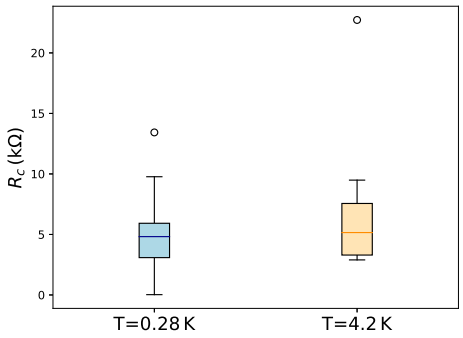

(c) Distribution of R_c values.

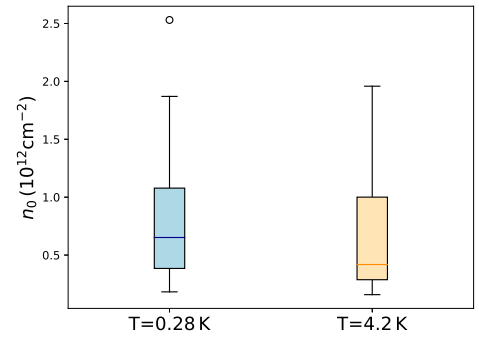

(d) Distribution of n_0 values.

Fig. 3.4 Box plots comparing the distribution of extracted device parameters V_d, μ, R_c and n_0 across two different cool-downs.

Reference	Dielectric	Encapsulation	T (K)	μ ($cm^2V^{-1}s^{-1}$)
[171]	SiO_2	No	4.2	1,000 - 4,000
[172]	SiO_2	No	RT	100 - 2,000
[146]	SiO_2	No	RT	4,300
[173]	SiO_2	No	RT	3,180
[174]	SiO_2	No	RT	3,046
[176]	SiO_2/HfO_2	Yes	RT	800 - 2,200
[166]	SiO_2/HfO_2	Yes	RT	2,000 - 6,000
[177]	SiO_2/Al_2O_3	Yes	RT	6,000
[167]	SiO_2/Al_2O_3	Yes	RT	8,600
[175]	hBN	Yes	RT	70,000
[175]	hBN	Yes	9.0	120,000

Table 3.5 Summary of mobility values of CVD-grown GFETs reported elsewhere. The dielectric material and whether or not the graphene is encapsulated are included for comparison. The temperature of the measurements are also included, where RT denotes room temperature.

to encapsulate CVD-grown graphene between mechanically exfoliated hBN flakes, which represents the current state-of-the-art in terms of mobility of CVD-grown graphene.

Comparison of V_d values

The measured shift of the V_d away from $V = 0\,\mathrm{V}$ depends upon amount of doping in the graphene induced by charged defects in the gate dielectric, chemical adsorbates on the graphene surface and cleaning procedures [178–184]. It has been shown that oxygen plasma cleaning of SiO_2 dielectrics prior to graphene transfer induces p-doping in graphene [148]. Furthermore, p-doping has been shown to occur due to adsorption of oxygen and water present in atmospheric conditions [179, 183], as well as PMMA and some types of photoresist which are present from the fabrication process [180–182, 184]. The oxygen plasma cleaning process reported in Ref. [148] caused the charge neutrality point to shift from $V_d = 15\,\mathrm{V}$ to beyond $V_d > 50\,\mathrm{V}$. The authors of Ref. [183] observed a shift in the measured value of V_d in the positive direction by up to 30 V after exposing a GFET device to atmosphere for 141 minutes, while the authors of Refs. [180, 184] saw V_d decrease from approximately $20V$ to values close to 0 V upon the removal of PMMA using high temperature annealing and an AFM tip, respectively. The fact that the mean measured value of V_d is negative and $|V_d| < 1\,\mathrm{V}$ suggests that both charged defects and chemical adsorbates cause only small amounts of doping compared to results reported elsewhere. However, to quantitatively compare the multiplexed devices reported here to those reported in the literature, the difference in the gate capacitance

must be accounted for. This can be achieved by calculating the ratio of the capacitance per unit area for the gate used on the multiplexed devices and those in the literature. Using $\varepsilon_r = 9$ for Al_2O_3 and $\varepsilon_r = 3.4$ for SiO_2, the ratio of the capacitance per unit area for Al_2O_3 and SiO_2 gate dielectrics with thickness 95 nm and 300 nm respectively is $C_{Al_2O_3}/C_{SiO_2} \approx 7.89$. Hence if the multiplexed GFETs used a 300 nm-thick SiO_2 gate dielectric the mean measured value of V_d would be expected to be (for cool-down 2), $V_d = -0.74\,\text{V} \times 7.9 = -5.84\,\text{V}$, which is still small compared to many devices reported in the literature, where the substrate has been cleaned by oxygen plasma and there has been no post-transfer cleaning process.

Comparison of n_0 values

In this section the extracted values of n_0 are compared to other publications which use Eqn. 3.1 to extract device parameters. The authors of Ref. [158] uses Eqn. 3.1 to fit $R(V_g)$ of a back gated GFET which uses mechanically exfoliated graphene, and extract a value of $n_0 = 0.46 \times 10^{12}\text{cm}^{-2}$, very close to the mean value of n_0 extracted during both cool-downs in the multiplexed devices. This also shows that the intrinsic doping in the CVD-grown graphene used in the multiplexed devices is similar to that of in mechanically exfoliated graphene, in this case. Reference [167] uses the same equation to fit to $R(V_g)$ curves obtained from dual-gated GFETs using CVD-grown graphene. In that work the authors sweep the top-gate voltage for a range of constant back-gate voltages between $V_{bg} = -40\,\text{V}$ and $V_{bg} = +10\,\text{V}$ and extract $n_0 = 0.23 \times 10^{12}\text{cm}^{-2}$ for all measurements, which is consistent with the values obtained for the multiplexed GFETs. These density values are consistently lower than the mean values of n_0 determined by Raman spectroscopy in chapter 2. The discrepancy is commented upon in Ref. [34] and is believed to be due to the fact that Raman scattering processes occur on different time scales to scattering processes measured in transport experiments, which influences the measured value of n_0.

Comparison of R_c values

The multiplexed GFETs reported here use a "metal-on-bottom-architecture" where the graphene is transferred onto pre-patterned Au contacts. Reference [185] transferred CVD-grown graphene onto gold contacts pattered in the transmission-line geometry, and measured values of R_c between 1200 and 2000 kΩ, approximately three to six times lower than the values reported here. The higher value of R_c in the multiplexed devices is due to the resistance of the multiplexer itself. The resistance of each channel of the multiplexer is variable, however the resistance is often in the range of 2-4 kΩ, which has been measured in a short-circuited multiplexer device, as stated Chapter 2. Channel 2 shows a resistance of 22.7 kΩ which is

likely due to the small contact area between the graphene and the drain contact, which has a width of approximately 440 nm, determined from SEM imaging.

3.2.3 Scattering time and the mean free path

Before moving on to look for correlations between the extracted device parameters, the minimum conductivity and the results from the Raman spectroscopy experiments, the carrier dependence of the scattering time τ and the mean free path l_{mfp} are provided, since these are commonly used as an indicator of material quality. The definition of l_{mfp} is taken from Ref [67]:

$$l_{mfp} = \frac{h}{2e^2 k_F \rho}, \tag{3.3}$$

where ρ is the resistivity and $v_F \approx 10^6 \mathrm{ms}^{-1}$ is the Fermi velocity. The scattering time is then obtained using $l_{mfp} = v_F \tau$. Figure 3.5 shows τ and l_{mfp} plotted as functions of n on logarithmic axes. By definition both τ and l_{mfp} begin to diverge as $n \to 0$ which causes the linear increase at low carrier densities, below approximately $n = 1 \times 10^{15}\,\mathrm{m}^{-2}$. When $n > 1 \times 10^{15}\,\mathrm{m}^{-2}$ the values of τ vary between 0.003 and 0.09 ps, while l_{mfp} varies between 3 and 100 nm across all channels.

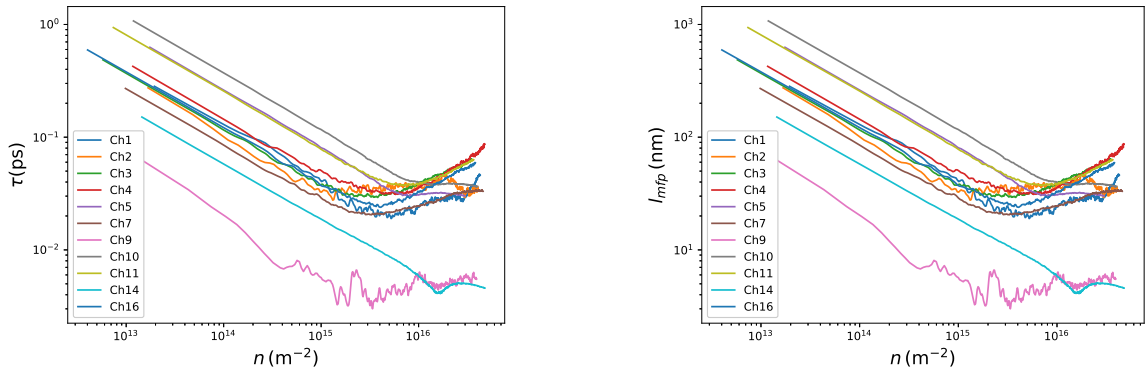

(a) $\tau(n)$ plotted as a function of n.

(b) $l_{mfp}(n)$ plotted as a function of n.

Fig. 3.5 The scattering rate $\tau(n)$ and the mean free path $l_{mfp}(n)$ plotted as a function of the induced carrier density n for each conducting channel of the device. Note density is plotted in units of m^2.

3.2.4 The minimum conductivity

The conductivity for each channel is obtained from the conductance by first subtracting the extracted value of R_c and then scaling by L/W, so the conductivity described here is intrinsic to the graphene. This histogram in Fig. 3.6 shows the distribution of the minimum conductivity σ_{min}, which has a mean value of $\overline{\sigma}_{min} = 3.8\,(e^2/h)$ and a standard deviation $\sigma_{\sigma_{min}} = 2.7\,(e^2/h)$. This is consistent with other studies of the minimum conductivity which report values of σ_{min} between 2 and $12\,(e^2/h)$, while outside of the charge neutrality region σ was found to have a linear dependence on V_g as opposed to sub-linear, which indicates that charged Coulomb scattering is the dominant scattering mechanism at low carrier density [33, 34, 36, 37].

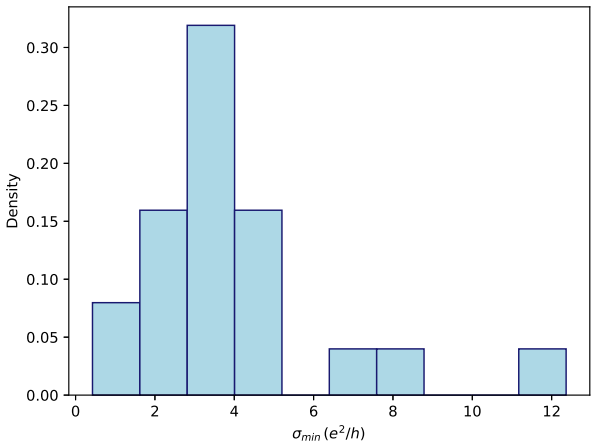

Fig. 3.6 Histogram of the minimum conductivity σ_{min}. Data from both cool-downs have been used, totalling 22 data points.

3.2.5 Correlations between device parameters

Figure 3.7 shows the extracted parameters from both cool-downs plotted against each other, with the purpose of visualising any correlations which may be present between the parameters. The values of μ for channels 5, 10 and 14 are those calculated using Matthiessen's rule in Section 3.2 whereas the values of V_d, R_c and n_0 are taken from Tables 3.1 and 3.2. From Fig. 3.7a it is clear that V_d is not correlated with any of the other parameters however from Figs. 3.7b, 3.7c and 3.7d, there does appear to be correlation between the other three parameters. In particular it seems that:

Parameters	R^2	F-statistic	p-value
(μ, R_c)	0.46	17.2	0.0005
(μ, n_0^{-1})	0.30	8.4	0.0088
(n_0, R_c^{-1})	0.34	9.6	0.0059

Table 3.6 Results from linear regression analysis of the relationship between μ, R_c and n_0.

$$\mu \propto R_c \tag{3.4}$$

$$\mu \propto n_0^{-1} \tag{3.5}$$

$$n_0 \propto R_c^{-1}. \tag{3.6}$$

Note that relations 3.4 and 3.5 imply relation 3.6, which shows self-consistency and indicates that the observed dependence is not observed by chance. Linear regression can be used to quantify the correlation between these variables.

Figures 3.8a, 3.8b and 3.8c show lines of best fit between (μ ,R_c), (μ ,1/n_0) and (n_0 ,1/R_c), respectively. The results of the regression analysis are tabulated in Table. 3.6, which gives the R^2 statistic, the F-statistic and the p-value. The R^2 statistic quantifies how much of the variance in the data is explained by a first-order polynomial fit, the F-statistic quantifies how much more of the variance is explained by a first-order polynomial model compared to a zero-order model, that is a horizontal line through the mean, and the p-value is a measure of statistical significance. A more complete explanation of these statistical quantities can be found in Appendix B. The p-values are all much below the chosen significance level of $\alpha = 0.05$ which indicates there is a very small probability of the observed trend occurring by chance and that the linear relationship is statistically significant. The R^2 values show that the first-order polynomial models explain between 30% and 46% of the observed variance observed between μ, R_c and n_0. The inverse relationship between μ and n_0 is expected and has been observed in transport experiments elsewhere [50, 153, 186]. On the other hand, the strong linear relationship between μ and R_c has not been reported elsewhere and is unexpected since the field-effect mobility is proportional to the transconductance $g_m = \partial I_{sd}/\partial V_g$, which in turn can be shown to be related to the contact resistance by $g_m \propto R_c^{-2}$ [187]. However, in this case the mobility μ is not calculated from g_m and is instead obtained as a fitting parameter in Eqn. 3.1. After subtracting R_c from both sides, Eqn. 3.1 becomes:

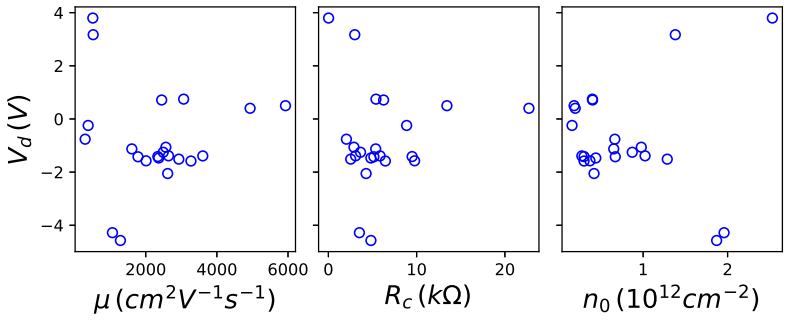

(a) V_d plotted as a function of μ, R_c and n_0.

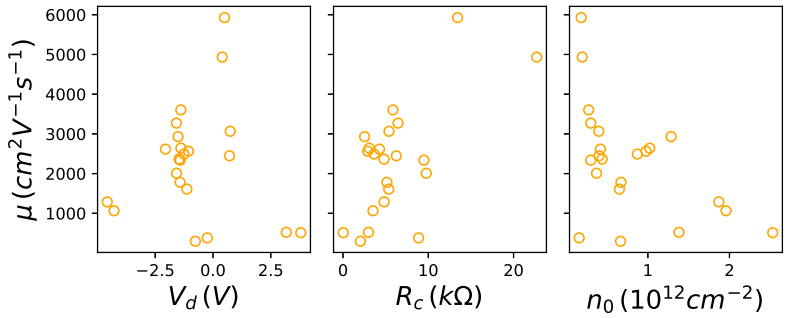

(b) μ plotted as a function of V_d, R_c and n_0.

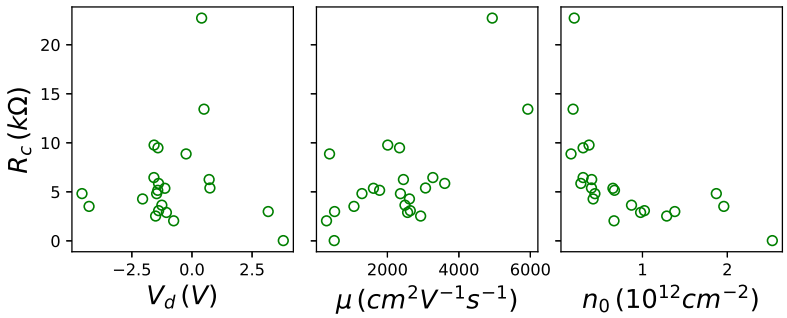

(c) R_c plotted as a function of V_d, μ and n_0.

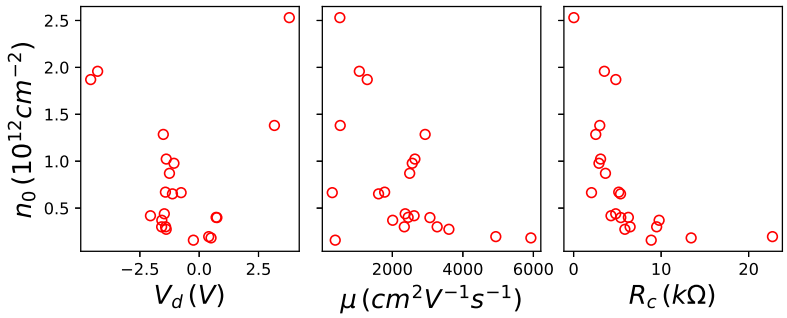

(d) n_0 plotted as a function of V_d, μ and R_c.

Fig. 3.7 The values of V_d, μ, R_c and n_0, taken from both cool-downs, plotted against each other for the purpose of highlighting any possible correlations between parameters.

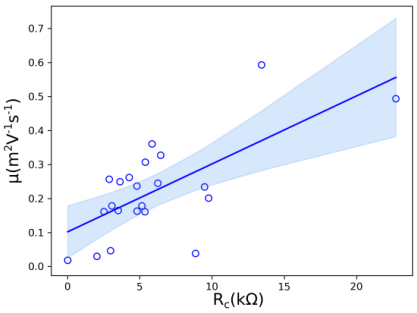

(a) μ plotted as a function of R_c.

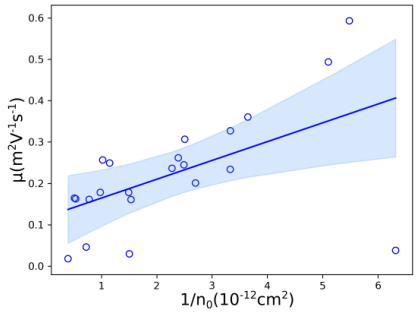

(b) μ plotted as a function of $1/n_0$.

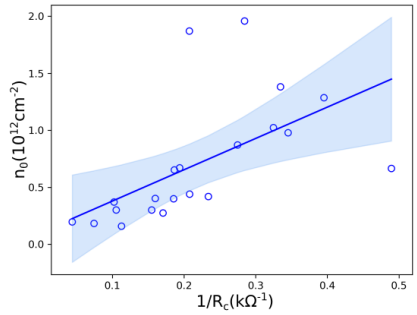

(c) n_0 plotted as a function of $1/R_c$.

Fig. 3.8 Linear regression plots showing the relationship between μ, R_c and n_0. Solid blue lines represent the line of best fit, and the blue shaded region is the 95% confidence interval.

$$R - R_c = \frac{L/W}{e\mu\sqrt{(C_{ox}(V_g - V_d)/e)^2 + n_0^2}}. \tag{3.7}$$

It is evident from Eqn. 3.7 that the left hand side $R - R_c$ becomes small as R_c increases, which can be compensated for on the right hand side by an increase in μ for given value of V_g, V_d and R. Therefore the observed linear relationship between μ and R_c can be explained as a consequence of the particular form of the model described by Eqn. 3.1.

3.2.6 Correlations between device parameters and Raman peak properties

The dependence of mean values and standard deviations of the Raman spectrum peak properties, $\mathrm{I}_{2D/G}$, $\mathrm{E}_{2D/G}$, $\Gamma_{2D/G}$ and the values of n_0 from E_G, on the device parameters V_d, μ, R_c and n_0 were studied in order to investigate possible correlations. None of the peak properties correlated with the parameters extracted from fitting $R(V_g)$ and in particular, no correlation was observed between n_0 obtained from Raman spectroscopy and n_0 obtained from the fitting procedure. This lack of consistency indicates that while the values of the peak parameters themselves agree with findings reported elsewhere, they should not be used to infer values of n_0 or μ in these experiments, and should only be used to confirm the presence of graphene and to probe the number of layers.

3.3 Conclusions

This chapter provides results from the first stage of the electrical characterisation of multiplexed GFETs. This began by fitting $R(V_g)$ with a model and showing that the extracted device parameters, V_d, μ, R_c and n_0, are consistent with each other between cool-downs, which can be seen from the box plots in Fig. 3.4. This was further confirmed by performing t-tests between pairs of data sets which showed there is no statistically significant difference between the mean value of each parameter. By comparing these values to those reported in the current literature it is confirmed that the multiplexed GFETs show performance metrics consistent with existing reports. This is an important step in verifying that the multiplexing technique does not significantly effect the measured properties of graphene and therefore can be used to make comparisons between GFETs, which is seen as a key application of the multiplexer device, especially when scaled-up to study large numbers of devices. The correlations between the device parameters were studied and explained in terms of the current literature and in the context of the model used to obtain them. No correlation was found

between the properties of the Raman spectra and the values of the parameters extracted from fitting $R(V_g)$ with a model function. Furthermore, the value of n_0 estimated from fitting $R(V_g)$ was found to be inconsistent with the values of n_0 obtained from Raman spectroscopy. As a result the Raman spectra are only used to confirm the presence of graphene and to measure the number of layers.

Chapter 4

Low-Field Magneto-Transport Measurements of Multiplexed Graphene Field-Effect Transistors

This chapter discusses the results of three magneto-transport experiments of CVD-MUX-A, where the magnetic field magnitude is restricted to $|B| \leq 0.2\,\mathrm{T}$, and is applied perpendicular to the graphene plane. In all graphene channels the weak localisation effect is observed as a positive change in magneto-conductance, $G(B)$ and the characteristic scattering rates are extracted by modelling the data using Eqn. 1.16. The weak localisation signal is then subtracted from the data and the variance of the conductance fluctuations are analysed and the resulting dephasing length L_ϕ is compared to the predictions obtained from Eqn. 1.16. Again, a constant voltage measurement circuit is used to measure the conductance of the device. A magnetic field dependent series resistance (explained in section 4.1.3) is estimated and subtracted from the raw conductance data before analysis. Before fitting the weak localisation signal with Eqn. 1.16, conductance G is converted to conductivity σ using the ratios of L/W listed in Table 2.2. Note that when Eqn. 1.16 is fit to the data, the estimated fitting parameter is the characteristic field B_θ ($\theta = \phi$, i, $*$), and is converted to a scattering length using $L_\theta = \sqrt{\hbar/4eB_\theta}$. When extracting the conductance fluctuations, the conversion to conductivity is not performed. This chapter makes use of statistical testing in order to quantify the relationship between the calculated scattering rates and experimental parameters, namely the gate voltage V_g and temperature T. Statistical significance is determined by calculating a p-value from an F-test, and finally the more familiar R^2 statistic is calculated to quantify the magnitude of the relationship. Furthermore, the means of different groups of measurements are compared using Students t-tests and ANOVA tests, to determine if the mean value of these groups are significantly different. For example, the mean value of L_ϕ

obtained from fitting the weak localisation signal in all channels will be compared the mean value of L_ϕ obtained from the autocorrelation function of the conductance fluctuations using statistical testing. An explanation of the relevant statistical hypothesis tests is provided in Appendix B, which is intended to be accessible to a reader with no background in hypothesis testing.

The first experiment investigates the gate voltage dependence of the scattering processes in channel 1 only, by calculating the scattering lengths at 50 different values of V_g between $\pm 10\,\mathrm{V}$, in steps of $\Delta V_g = 0.4\,\mathrm{V}$ at $T = 0.28\,\mathrm{K}$. This experiment was conducted as an initial exploration of the parameter space. Regression analysis showed a statistically significant, but small, linear dependence of L_ϕ and L_i on V_g and a non-linear dependence of L_* on V_g.

The second experiment measures $G(B)$ for all of the conducting channels of the device at $T = 0.28\,\mathrm{K}$. Measurements were taken at three values of V_g per channel, corresponding to hole transport, electron transport and the charge neutrality region. Additionally, the transport was measured using two separate methods, referred to as averaging and not-averaging. The averaging procedure is similar to the method used in Ref. [67], to remove the contribution of conductance fluctuations from the weak localisation signal. The not-averaging method is simply sweeping the magnetic field between $B = \pm 0.2\,\mathrm{T}$. An ANOVA test was used to quantify the effect of carrier type and measurement method on the mean value of L_ϕ. The statistics describing the distribution of values of L_ϕ and τ_ϕ^{-1} across the different channels are reported.

The third experiment measured $G(B)$ at different values of T for channels 1, 2 and 3. Again, measurements were three values of V_g per channel, corresponding to p-type, n-type and neutral transport regions. The temperatures considered were: 0.6 K, 1.0 K, 2.0 K, 5.0 K, 7.0 K, 9.0 K, 11.0 K, 13.0 K, 15.0 K, 18.0 K and 25.0 K. The dephasing rate τ_ϕ, was found to have a strong linear dependence on temperature indicating electron-electron scattering in the diffusive limit as the dominant dephasing mechanism.

4.1 Methods

4.1.1 Choosing experimental parameters

Before measuring all available channels it is important to look at how $G(B)$ changes when the magnitude of the excitation voltage, V_{ex}, and the sweep-rate of the magnetic field are changed. This step is important because it can distinguish reproducible features in $G(B)$ from noise. This calibration experiment was performed on channel 3 at the Dirac point, since

this channel showed no conductance fluctuations as a function of V_g, and also showed the largest change in G as a function of V_g, at zero magnetic field.

Changing the excitation voltage

Figure 4.1 shows four, repeat B sweeps for each selected value of V_{ex}. Every sweep is recorded in the positive direction, from B=- 0.2 T to B= 0.2 T at a rate of 5 T / hour and at $T = 0.28$ K.

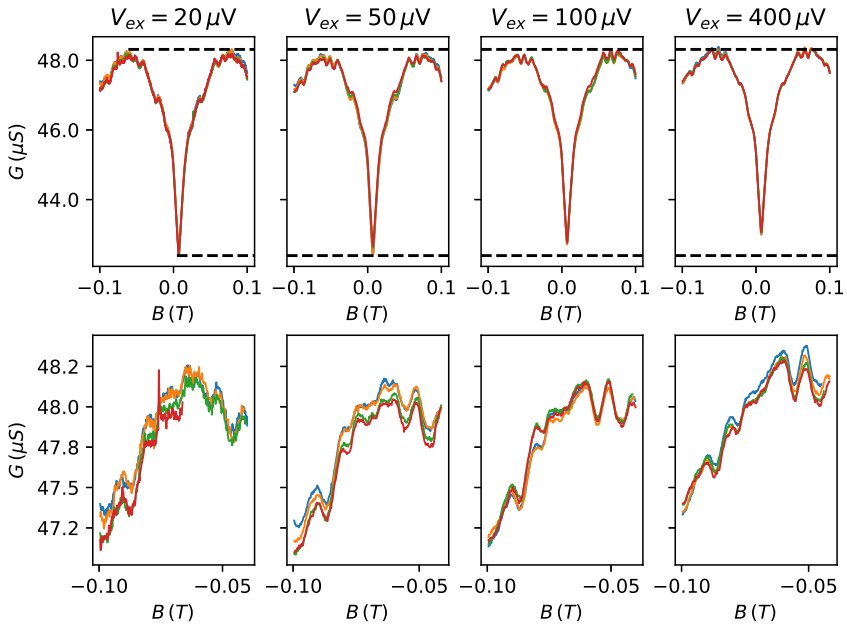

Fig. 4.1 Four, repeat $G(B)$ traces of channel 3 at each value of V_{ex} and $T = 0.28$ K. Each trace is collected in the positive direction at a rate of 5 T / hour. The top row shows the entire trace, while the bottom row shows only a subset to display the reproducibility of small features. Black, dashed lines serve as guides to the eye, highlighting how the weak localisation peak shrinks as V_{ex} is increased.

It is clear that increasing V_{ex} reduces the noise, which is expected since the current through the devices increases. However, increasing the V_{ex} also causes the magnitude of the weak localisation peak to decrease which indicates electron heating. The change in conductance between $V_{ex} = 20\,\mu$V and $V_{ex} = 50\,\mu$V is negligible; between $V_{ex} = 20\,\mu$V and $V_{ex} = 100\,\mu$V the height of the peak reduces by $\Delta G \approx 0.35\,\mu$S and between $V_{ex} = 20\,\mu$V and $V_{ex} = 400\,\mu$V the height of the peak reduces by $\Delta G \approx 0.60\,\mu$S.

The temperature increase associated with an increase of V_{ex} can be estimated by equating the thermal and electrical energy scales $k_B \Delta T = e\Delta V$, where e is the electron charge and

k_B is the Boltzmann constant. Increasing V_{ex} from $20\,\mu$V to $100\,\mu$V corresponds to a temperature increase of $\Delta T \approx 0.9$ K, whereas increasing from $20\,\mu$V to $400\,\mu$V corresponds to a temperature increase of $\Delta T \approx 4.4$ K.

Features of magnitude $\delta G \approx 0.2\,\mu$S are reproducible and are likely to be universal conductance fluctuations, although the magnitude of the fluctuations is much smaller then e^2/h. The reduced magnitude of the conductance fluctuations is because the sample dimensions are much larger than L_ϕ, determined in the following results.

An excitation voltage $V_{ex} = 100\,\mu$S was chosen for all experiments, since this value showed reproducibility, a reduced level of noise relative to $20\,\mu$S. It is estimated that the true electron temperature will be approximately 0.9 K higher than the lattice temperature (assuming the electron temperature is equal to the lattice temperature when $V_{ex} = 20\,\mu$V) set by the cryostat due to heating effects arising from the choice of V_{ex}.

Changing the sweep rate

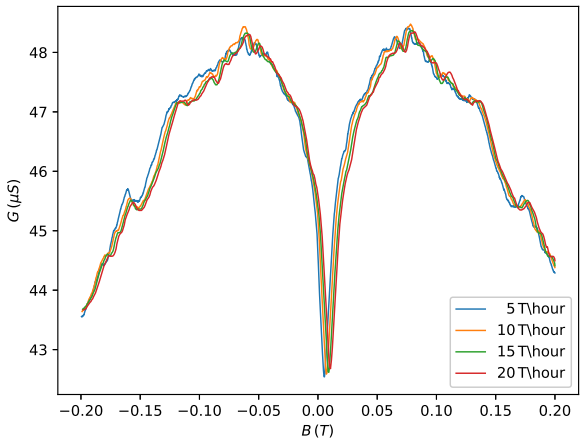

Fig. 4.2 Measurement of $G(B)$ for channel 3 ,using four, different B field sweep rates. Each trace is taken in the forward direction using an excitation voltage of $V_{ex} = 100\,\mu$V.

Figure 4.2 shows $G(B)$ for channel 3 when a perpendicular magnetic field was swept from $B = -0.2$ T to $B = +0.2$ T at rates 5 T / hour, 10 T / hour, 15 T / hour and 20 T / hour, using an excitation voltage of $V_{ex} = 100\,\mu$V. Qualitatively, the curves look very similar, however it is noticeable that increasing the rate shifts the weak localisation peak position further away from $B = 0$ T, this shift away from zero is commonly observed in weak localisation measurements which may be a consequence of flux trapping in the superconducting magnet. It is also noticeable that the peak height is slightly reduced when the sweep-rate is increased

which again indicates electron heating, so a rate of 5 T / hour was used for all small-field magneto-transport measurements in order to reduce both of these effects.

4.1.2 The averaging procedure

The averaging method is very similar to the method reported in Ref. [67]. First, B is stepped and held at a fixed value, then the back gate is swept across a 1 V range.

The mean value of the voltage sweep is taken to be the value of the $G(B)$ at the current value of B. Then, B is stepped to the next value and the process is repeated. In this way $G(B)$ can be constructed in discrete steps. In the experiments reported here, this is done for 24 magnetic field values between -0.01 T and 0.2 T.

4.1.3 Approximating the series resistance

With the current device designs, there is no way to directly measure the series resistance of each channel and model is created to estimate the resistance. The total series resistance to a single channel can be written:

$$R_{series}(B) = R_{2DEG}(B) + R_{Ohmic} + R_{Au/Gr} + R_{Wiring}. \tag{4.1}$$

When $B = 0$ T this resistance is equal to R_c obtained from fitting the $R(V_g)$ curves shown in Chapter 3. The resistance of the 2DEG alone was measured using separate Hall bar devices fabricated from the same wafer by Melanie Tribble of the Semiconductor Physics group at the University of Cambridge. The value of $R_{2DEG}(B = 0)$ was calculated for each channel according to $R = L\rho/W$, where $\rho = 1/ne\mu$ is the resistivity of the 2DEG and L/W is the number of squares N contributing to the mesa structure of a single channel. For the 16-output multiplexer presented in Chapter 2, $N = 10$ for channels 1, 2, 15 and 16, $N = 9$ for channels 3, 4, 7, 8, 9, 10, 13 and 14, and $N = 8$ for channels 5, 6, 11 and 12, corresponding to $R_{2DEG}(B = 0)$ = 500, 450 and 400 Ω, respectively. The resistance of the 2DEG alone changes by approximately $\Delta R_{2DEG}(B) \approx 1$ kΩ between $B = 0$ T and $B = 0.2$ T, also measured using Hall bar devices. All of the off-chip wiring is represented by $R_{Wiring} < 100\,\Omega$ and $R_{Au/Gr}$ represents the resistance between the Au contact and graphene, which is typically of the order of 1 kΩ. The total series resistance can then be re-written as:

$$R_{series}(B) = R_c + R_{2DEG}(B) - R_{2DEG}(B = 0). \tag{4.2}$$

Note that in Eqn. 4.2 the first two terms on the right hand side both contain $R_{2DEG}(B = 0)$, therefore the third term is included so that this resistance is not counted twice.

In summary, $R_{series}(B)$ is estimated by taking the data $R_{2DEG}(B)$ from the measurement of a Hall bar, adding the constant value of R_c determined from the model in Chapter 3, and finally subtracting $R_{2DEG}(B=0)$.

4.2 Gate-voltage dependence of quantum interference

4.2.1 Weak localisation

The first experiment examines the dependence of the scattering lengths on V_g. This experiment was performed first in order to decide how many V_g values were worth considering in future experiments. In this experiment the averaging method was not used, and data was collected for both up and down B sweep directions.

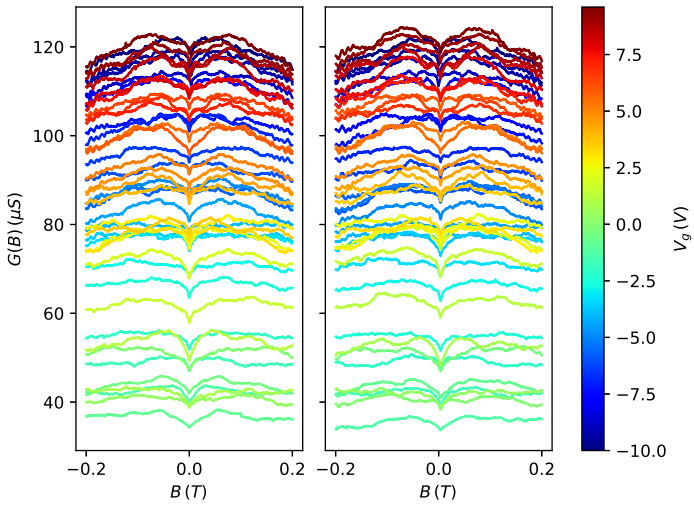

Fig. 4.3 Measurement of $G(B)$ in channel 1 at 50 different values of V_g between ± 10 V, with a step size of $\Delta V = 0.4$ V. The plot on the left is $G(B)$ measured when sweeping B from negative to positive, the plot on the right is data taken in the opposite direction.

Figure 4.3 shows the raw $G(B)$ data in channel 1 of the multiplexer at 50 different back gate voltages for both sweep directions of the magnetic field. The conductance increases as $|V_g - V_d|$ increases, as expected and traces near $G(B) = 40\,\mu$S correspond to values of V_g close to V_d and those near $G(B) = 120\,\mu$S represent gate voltages furthest from V_d. Shubnikov-de-Haas oscillations appear at $|B| > 0.15$ T, which arise from the 2DEG in the GaAs/Al_xGa_{1-x}As heterostructure. They are known to arise from the 2DEG because they also appear in shorted-circuited multiplexer devices at similar values of B and have been

observed to occur at $B \approx 10\,\mathrm{T}$ in graphene [188, 189]. There are aperiodic fluctuations in the $G(B)$ traces since the averaging procedure was not used, however the detail is difficult to see at the given scale of Fig. 4.3. Before fitting the weak localisation signal, the series resistance is subtracted using the model described in Sec. 4.1.3 and then converted into a conductivity $\sigma(B)$ using $L/W = 2.75$.

The extracted values of L_i and L_* at gate voltage values 2.4 V, 4.0 V, 5.2 V, 8.0 V, 8.8 V and 9.6 V are unreliable, since the uncertainty of the fitting parameters is between $10^5\,\mathrm{nm} - 10^6\,\mathrm{nm}$, consequently these data points have been removed from the following analysis. The unreliability of estimates of L_i and L_* have been remarked upon elsewhere [68, 73] and is often explained by the fact that these two parameters are estimated from the last two terms of Eqn. 1.16 which describe anti-localisation, and are therefore small when conventional weak localisation is observed. The values of L_ϕ remain reliable and are included in the following analysis.

A further consideration is the presence of outliers, which were observed for L_ϕ, L_i and L_* and are identified by the circles on the box plot shown in Fig. 4.5 and are indicated by arrows in Figs. 4.4b, 4.4c and 4.4d. These values defined to be greater than $1.5\times\mathrm{IQR}+\mathrm{Q}_3$, where IQR and Q_3 denote the interquartile range and the third quartile of the data set, respectively. Note that the outlier boundaries have been calculated separately for up and down sweep direction data sets. Outliers either indicate skewed distributions, that is, the distributions of L_ϕ, L_i and L_* are skewed, or they indicate an error in the measurement/estimation process. The outliers have been retained in the data set since there were no large fitting uncertainties (as returned by the Levenberg-Marquardt curve fitting algorithm) associated with these values and it is not possible to definitely say they are erroneous estimates. Their presence in the data set effect values of R^2 associated with the lines of best fit shown in Figs. 4.4b, 4.4c and 4.4d as will be discussed in the following sections.

		R^2		F-statistic		p-value	
Length	Outliers	Up	Down	Up	Down	Up	Down
L_ϕ	Yes	0.23	0.24	14.0	15.0	4.8 e-04	3.2 e-04
L_ϕ	No	0.36	0.36	25.7	25.1	7.1 e-06	9.2 e-06
L_i	Yes	0.13	0.16	6.3	8.2	1.6 e-02	6.7 e-03
L_i	No	0.24	0. 30	12.5	16.6	1.1 e-03	2.3 e-04

Table 4.1 The statistics describing the fits to the scattering lengths shown in Fig. 4.4 for data taken both the up and down directions. The outliers columns indicated if the outliers are included in the data set; Yes indicates they have been included, No indicates they have been discarded.

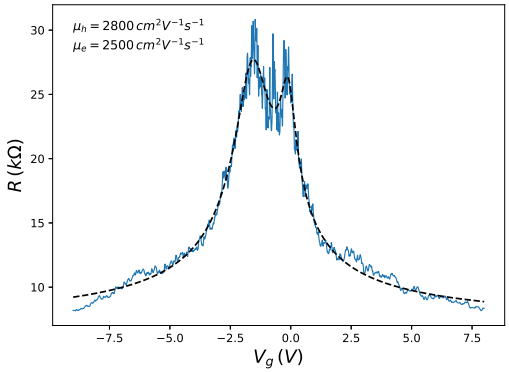

(a) Fit of Eqn. 3.2 to $R(V_g)$, to estimate electron and hole mobility.

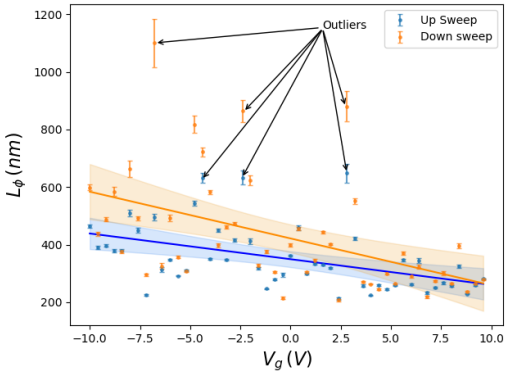

(b) First-order polynomial fits to L_ϕ for both sweep directions.

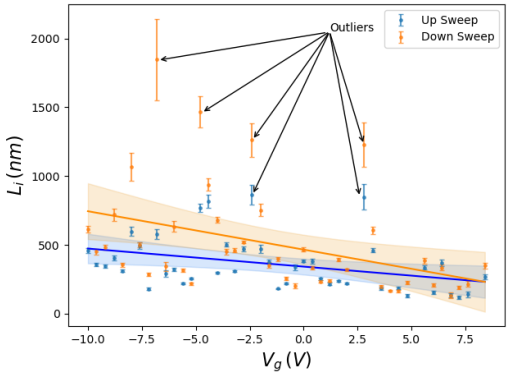

(c) First-order polynomial fits to L_i for both sweep directions.

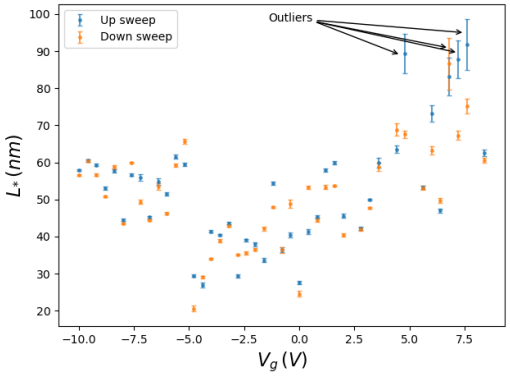

(d) Plots of $L_*(V_G)$ for both sweep directions. No fit has been performed on this data set.

Fig. 4.4 A fits of Eqn. 3.2 to the hole and electron sides of $R(V_g)$ are shown in (a) and used to determine the values of the electron and hole mobilities independently. Plots of $L_\phi(V_g)$, $L_i(V_g)$ and $L_*(V_g)$ in both the up and down sweep directions are shown in (b), (c), (d), respectively, along with lines of best fit and annotations of outliers identified from the box plot shown in Fig. 4.5. The shaded area around each fit line represents the 95% confidence interval about the fit. Linear fits are performed for $L_\phi(V_g)$ and $L_i(V_g)$ and no fit is performed for $L_*(V_g)$. Note that the y-axes for each sub-figure have different scales for clarity.

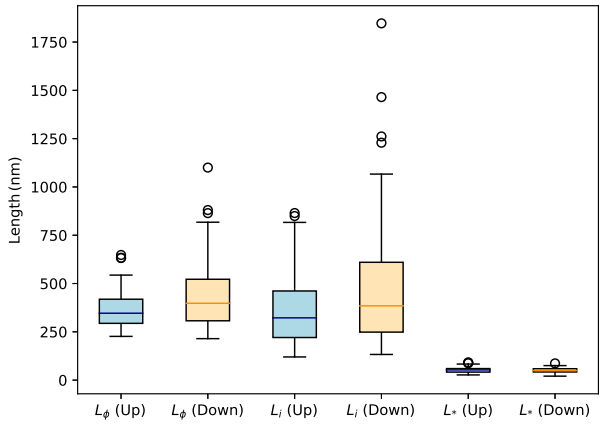

Fig. 4.5 Box plot of all of the scattering lengths in both the up and down direction, showing the distribution of the scattering length values, which can be used to visualise the distribution of values and identify outliers.

Discussion of L_ϕ and L_i

Since $\mu = q\tau/m^*$, (q is carrier charge, τ is average scattering time and m^* is effective mass), high carrier mobility implies a long average scattering time τ and therefore long scattering lengths, compared to low carrier mobility. As a consequence it may be expected that the scattering lengths are different for electrons and holes if they have different mobilities. In Chapter 3, $R(V_g, B = 0)$ was modelled using Eqn. 3.1, which assumes the mobility of electrons and holes are equal, here denoted as μ_e and μ_h, respectively. In order to investigate the difference between μ_e and μ_h in channel 1, two separate fits to the electrons and hole side of $R(V_g)$ were performed by splitting the data about the Dirac point $V_d = -1.42\,\mathrm{V}$ as determined by the fitting procedure for channel 1 performed in Chapter 3. From the two separate fits, shown in Fig 4.4a, it was found that $\mu_e = 2500\,\mathrm{cm^2V^{-1}s^{-1}}$ and $\mu_h = 2800\,\mathrm{cm^2V^{-1}s^{-1}}$. Consequently, it may be expected that the scattering lengths will be larger for holes than electrons and a negative trend will observed in a plot of the scattering lengths as a function of V_g. This is indeed the case for $L_\phi(V_g)$ and $L_i(V_G)$, shown by the lines of best fit in Figs. 4.4b and 4.4c (not observed for $L_*(V_g)$ which will be discussed separately in the following section). The results of the fitting procedures are given in Table. 4.1 which indicate that the linear trend accounts for approximately 25% of the variance of L_ϕ values and 15% of the variance of L_i. When the outliers shown in Figs. 4.4b, 4.4c and 4.4d were removed from the data set and the fitting procedure was repeated, the R^2 values increased to $R^2 = 0.36$ for L_ϕ in both sweep directions, and $R^2 = 0.3$ for L_i in both sweep directions. The low values of R^2 reflect the fact that the mobility difference between electrons and holes

is small, $300\,\mathrm{cm^2V^{-1}s^{-2}}$ (to 2 s.f), but are found to be statistically significant by the high values of the F-statistic and low p-values (see Appendix B for explanations of statistical significance and hypothesis testing). Note that the calculated values of $L_\phi(V_g)$, $L_i(V_g)$ and $L_*(V_g)$ also depend upon the diffusion constant $D(V_g)$, however this is approximately equal for electrons and holes and constant at values of V_g away from $V_d = -1.42\,\mathrm{V}$ (see Fig. 4.7a), so should not cause the observed linear trend of the scattering lengths. It is possible that the variance unaccounted for by the linear models arises from the presence of conductance fluctuations. The conductance fluctuations pattern in $G(B)$ should change if V_g is changed by a value greater than the correlation energy $E_c = \hbar\pi^2 D/L^2$ as shown in Ref. [93]. In this case $e\Delta V_g = 0.4\,\mathrm{eV}$ and $E_c \approx 0.13\mu eV$, so $\Delta V_g \gg E_V$ and each $G(B)$ measurement will exhibit a different fluctuation pattern, which in turn may cause some of the unexplained variance of the scattering lengths.

Next, the mean value of L_ϕ and L_i were compared using a t-test: no statistically significant difference between the mean value of L_ϕ and the mean value of L_i was observed as expected, since L_i must be similar to, or less than L_ϕ in order for conventional weak localisation to be observed in graphene, as discussed in Section 1.2.2.

Intervalley scattering is associated with defects which are 'sharp' on the atomic scale, such as point defects and edges. The most narrow regions of the graphene channel, determined from SEM imaging, are approximately $2.1\,\mu m$ wide, much longer than the mean value of L_i, so it is expected that edges have negligible contribution to the total intervalley scattering. Therefore, most of the intervalley scattering must occur in the bulk of the channel from sources such the Al_2O_3 substrate, atomic vacancies and dislocation centres.

Discussion of L_*

Examining the elastic scattering lengths, $L_*(V_g)$ does not behave as $L_i(V_g)$ and appears to show non-linear behaviour, taking a minimum about the $V_g \approx V_d$ and increases as $|V_g - V_d|$ increases. The only scattering mechanism reported in the literature which could qualitatively explain this behaviour, theoretically, is intravalley scattering of carriers due to the strain field resulting from a random distribution of dislocations in the graphene, as derived by Morpurgo and Guinea in Ref. [65]. All other reported scattering mechanisms: scattering due to to electrostatic potential gradients between the sublattices (Ref. [65]) and scattering due due to Fermi surface anisotropy (Ref. [64]) would theoretically cause $L_*(V_g)$ to decrease with increasing $|V_g - V_d|$.

By considering a finite distribution of dislocations with their own respective random Burgers vector, the authors of Ref. [65] showed that the scattering rate due to this dislocation induced gauge field is approximately equal to:

$$\tau_{gauge}^{-1} \approx \frac{v_F}{k_F d^2}, \tag{4.3}$$

where d is the average distance between dislocations in the graphene and $k_F = \sqrt{\pi n}$ is the Fermi wavenumber. Substituting Eqn. 4.3 into the relation $L = \sqrt{D\tau}$ it can be shown that:

$$L_{gauge} = \left(\sqrt{\frac{k_F D}{v_F}} \right) d. \tag{4.4}$$

Equation. 4.4 could qualitatively explain the observed behaviour of $L_*(V_g)$ if it is the dominant, elastic intravalley scattering mechanism: that $L_*(V_g)$ takes a minimum near the charge neutrality region and increases as $|V_g - V_D|$ increases. It is stated in Ref. [65] that dislocation centres contribute to intervalley scattering. Therefore, by assuming that dislocations centres are the main cause of intervalley scattering and the resulting strain in the lattice is responsible for the majority of elastic intravalley scattering, the value of d in equation 4.4 should be of similar length to L_i. It is possible to estimate the value d corresponding to each data point L_* by equating $L_{gauge} = L_*$ and solving for d. By this method the mean value of d was calculated to be approximately 50 nm, much smaller than the mean value L_i. This is similar to the values of d calculated in Ref. [67]. This result does not discount strain in the lattice being the principle cause of time-reversal symmetry breaking, it only discounts that the strain is caused by dislocations in the crystal. It may be possible that other factors which are not atomically sharp, such as tension from the wet transfer process or local folds in the graphene can induce strain in the graphene channel and cause the observed behaviour of L_*. However, it is possible that there is a different scattering mechanism responsible for this behaviour. Note that between $V_g = -4.8$ V and $V_g = -5.2$ V, $L_*(V_g)$ shows a discontinuity: it is possible that this is due to a parameter estimation error from the curve fitting process, however the returned parameter uncertainties are small, as shown by the error bars. An alternative possibility is that this sudden change is related to the fluctuations of $G_(V_G)$ surrounding the charge neutrality region of channel 1. It is this jump which gives rise to the apparent non-linearity; since it is not possible to explain this feature with confidence, no line of best fit has been made to this data set.

Scattering Rates

Using $D = v_F l_{mfp}/2$ and $v_F = 10^6\,\mathrm{ms}^{-1}$, the scattering lengths are converted into scattering rates. The mean dephasing rate τ_ϕ^{-1} is $0.14\,\mathrm{ps}^{-1}$ and $0.17\,\mathrm{ps}^{-1}$, in the up and down sweep directions, respectively. This is consistent with values reported elsewhere [67, 86]. The mean value of τ_i^{-1} is $0.15\,\mathrm{ps}^{-1}$ and $0.21\,\mathrm{ps}^{-1}$ in the up and down sweep directions, respectively,

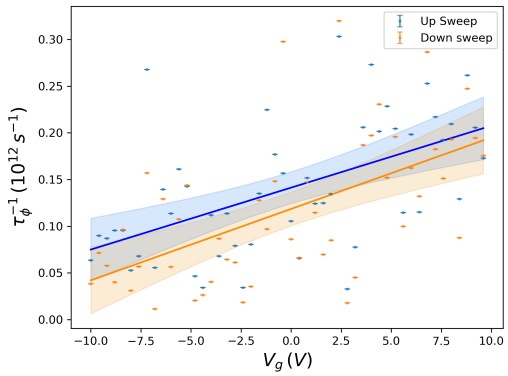

(a) First-order polynomial fits to τ_ϕ^{-1} for both sweep directions.

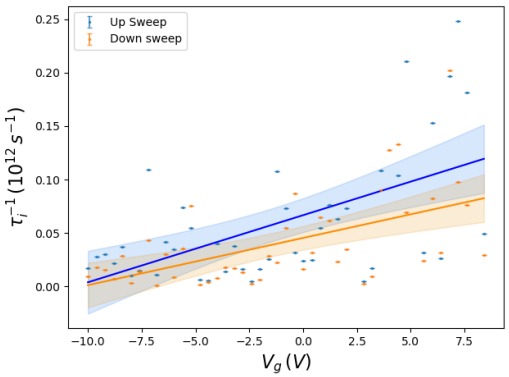

(b) First-order polynomial fits to τ_i^{-1} for both sweep directions.

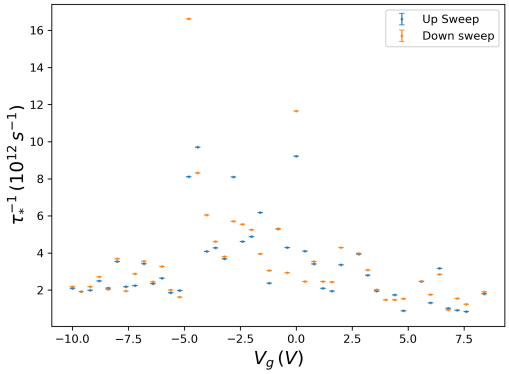

(c) Plot of $\tau_*^{-1}(V_g)$ for both sweep directions.
No fit has been performed on this data set.

Fig. 4.6 Plots of $\tau_\phi^{-1}(V_g)$, $\tau_i^{-1}(V_g)$ and $\tau_*^{-1}(V_g)$ in both the up and down sweep directions, with linear fits and 95% confidence intervals shown in (a) and (b). Note that the y-axes for each sub-figure have different scales for clarity.

	R^2		F-statistic		p-value	
Rate	Up	Down	Up	Down	Up	Down
τ_ϕ^{-1}	0.30	0.30	20.0	23.9	4.0 e-05	1.4 e-05
τ_i^{-1}	0.32	0.32	19.3	19.3	7.7 e-05	7.3 e-05

Table 4.2 The statistics describing the fits to the scattering rates shown in Fig. 4.6 for data taken in both the up and down sweep directions.

similar to τ_ϕ^{-1}, since the corresponding lengths are also similar. The intravalley scattering rate τ_*^{-1} is approximately two orders of magnitude larger than τ_ϕ^{-1} and τ_i^{-1}, as expected since L_* was the shortest length scale in the system. First-order polynomial fits to τ_ϕ^{-1} and τ_i^{-1} (no fit to τ_*^{-1} performed) are shown in Fig 4.6, with the fitting results shown in Table 4.2. The values of R^2 are similar to those obtained from the linear fits of $L_\phi(V_g)$ and $L_i(V_g)$ and reflect the higher scattering rate experienced by electrons compared to holes in this sample. The statistical significance of these linear fits are again confirmed by a high value of the F-statistic and the low p-value. The behaviour of τ_*^{-1} again shows non-linear behaviour and takes a maximum around the charge neutrality region.

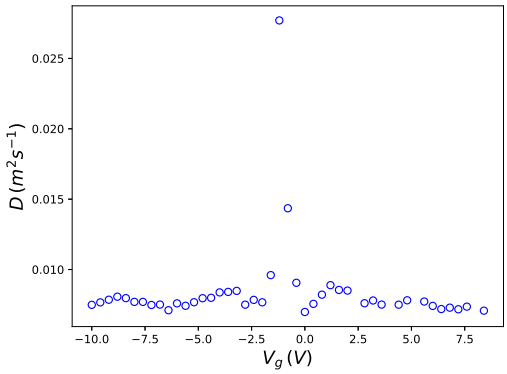

(a) The diffusion constant D plotted as a function of back gate voltage V_g.

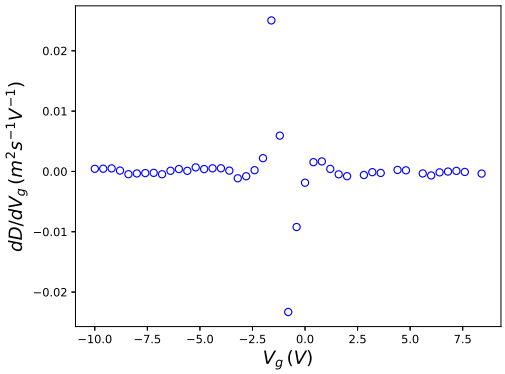

(b) The derivative dD/dV_g plotted as a function of V_g.

Fig. 4.7 The variation of the diffusion constant D and it's derivative with respect to the back gate voltage V_g, plotted as a function of V_g. Away from the charge neutrality region, D is approximately constant.

4.2.2 Conductance fluctuations

The fluctuating part of $G(B)$, is obtained by subtracting the weak localisation contribution from the signal, and the dephasing length L_ϕ is calculated from the autocorrelation function of the resultant signal. The calculation of the autocorrelation function is performed using the Statsmodels package in Python, see Ref. [190] for details. The conductance fluctuations $\delta G(B)$ are shown in Fig. 4.8a. As explained in Section. 1.2.3, the correlation field B_c is defined as the amount by which B must change from zero in order to induce a phase-shift of the electron wavefunction, such that pairs of propagating states lose coherence. The value of B_c can be calculated from the autocorrelation function through the following relation:

$$ACF(\delta G)(B_c) = \frac{1}{2}, \tag{4.5}$$

which in turn, is related to L_ϕ according to:

$$L_\phi = \sqrt{\frac{h}{eB_c}}. \tag{4.6}$$

Figure 4.8c shows a plot of the autocorrelation function $ACF(\delta G)(B)$ as a function of the number of lags, which is the relative shift in position between the two arrays containing the values of $\delta G(B)$. The autocorrelation between a vector y and itself at a given lag ℓ is given by $ACF_{yy}(\ell) = \sum_{n \in Z} y(n)\overline{y(n-\ell)}$, where the overline denotes the complex conjugate of y and n is the number of elements in y. The value of $ACF_{yy}(\ell)$ is calculated at 50 values of ℓ, ranging from 0 to 49 in steps of 1. The number of values of ℓ used can be chosen and in this case 50 values were used in all cases. The plot shown in Fig. 4.8c is a plot of $ACF_{yy}(\ell)$, normalised by dividing by $ACF_{yy}(\ell = 0)$, where in this case $y = \delta G(B)$. The shaded blue region in Fig. 4.8c represents the 95% confidence interval, a value of ACF_{yy} outside of the 95% confidence interval means there is a only a 5% chance that the calculated value of ACF_{yy} is a false-positive result, that is that a non-zero autocorrelation is measured when in fact there is no correlation. The ℓ'th lag can be converted into a change in magnetic field ΔB by calculating the difference between the 0'th value of the array containing B and the ℓ'th value. The correlation field B_c is found by finding the value of ℓ for which $ACF(\delta G) = 0.5$ and then finding the corresponding value of ΔB; in the case of the plot shown in Fig. 4.8c, $\ell = 26$ and $B_c = 5.9\,\text{mT}$.

Figure 4.8d shows that Eqn. 4.6 predicts similar values of L_ϕ as predicted by fitting the weak localisation signal. Using the autocorrelation function, the mean predicted value of the phase-coherence length is $L_\phi \approx 414\,\text{nm}$ with a standard deviation of 108 nm. This is similar to the mean value of $L_\phi \approx 350\,\text{nm}$ with standard deviation 85 nm obtained from fitting the weak localisation signal. To test if the mean values of L_ϕ are significantly different from each other, a two-valued t-test can be performed. The null hypothesis is that the mean value of L_ϕ predicted by the autocorrelation function is equal to the mean value predicted by fitting the weak localisation signal; the alternative hypothesis is that they are not equal.

- H_0: $\mu_{ACF} = \mu_{WL}$
- H_1: $\mu_{ACF} \neq \mu_{WL}$

The two-sample t-test returns a t-statistic of $t = -3.29$ and a p-value of 0.0014 which shows that the mean value of L_ϕ predicted by the two methods is significantly different. The difference between the mean values of the two groups is $\Delta\mu = 64\,\text{nm}$. The number of data points in each group is $n_1 = n_2 = 50$ and the pooled standard deviation is $s_p = 98\,\text{nm}$, which

gives a Cohen's d value $d = 0.65$, interpreted to mean that the mean values of the two groups differ by 0.65 standard deviations and is considered to be a moderate difference.

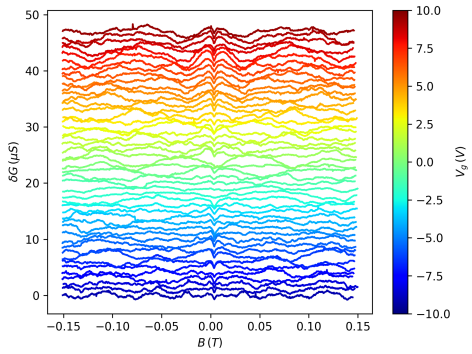

(a) The fluctuations $\delta G(B)$ as a function of V_g.

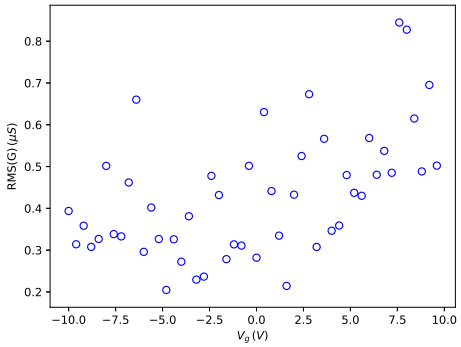

(b) The root-mean-square amplitude of $\delta G(B)$ as a function of V_g.

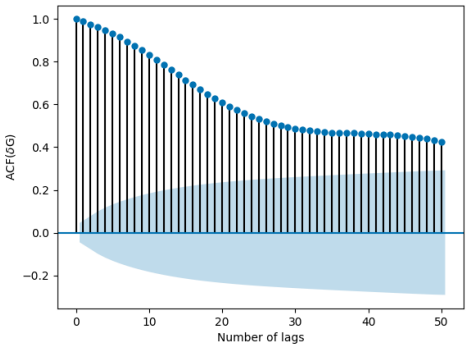

(c) The autocorrelation function of $\delta G(B)$ at $V_g = 10V$. The shaded blue region represents the 95% confidence interval.

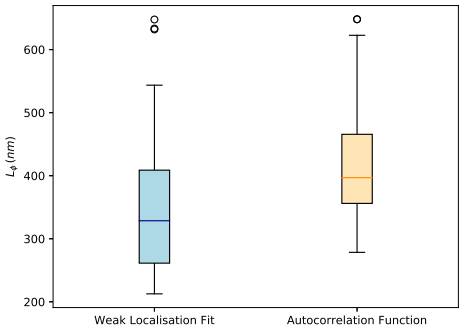

(d) Box plots of L_* extracted from Eqn. 1.16 and from the autocorrelation function of the conductance fluctuations.

Fig. 4.8 The results from processing $\delta G(B)$ as a function of V_g. In (a), the traces of $\delta G(B)$ are truncated to the range $|B| < 0.15\,\mathrm{T}$ in order to remove the Shubnikov-de-Haas oscillations from the signals. Traces are vertically offset by $1.0\mu\mathrm{S}$ for clarity. The RMS amplitudes of $\delta G(B)$ are plotted as a function of V_g in (b), showing that they decrease as V_g approaches the charge neutrality region. An example of the autocorrelation function is shown in (c) and a box plot in (d) compares the distribution of L_ϕ values obtained from fitting the weak localisation signal and from the autocorrelation of $\delta G(B)$.

4.3 Magneto-transport in all channels

4.3.1 Weak localisation

In this section the results of magneto-transport experiments of all channels are presented. From the first experiment described previously, the change in V_g accounted for approximately $15\% - 35\%$ of the variance of L_ϕ and L_i. Since the effect of V_g on L_ϕ is small, this experiment measured the $G(B)$, at only three values of V_g, per channel, corresponding to three transport regimes: electrons transport, hole transport and the charge neutrality region, which contains both electrons and holes. Additionally, the signals were measured using two different techniques: by averaging and by not-averaging, as explained in the introduction.

The experiment investigates whether or not the carrier type and the measurement method have a significant impact on the measured phase-coherence length L_ϕ, and investigates the variation of the measured values of L_ϕ across the conducting channels. The fitting procedure yielded unreliable results for L_i and L_* for all of the channels, in a manner similar to some of the results in the previous experiment. The uncertainty of the fitting parameters were of the order of 10^5 nm-10^6 nm, despite the curve fitting the data well. In an attempt to achieve accurate values of L_i and L_* the fitting range was reduced and a quadratic approximation of Eqn. 1.16 as described in Ref. [86] was used, however the fitting uncertainties were of a similar magnitude using this method.

The dependence of L_ϕ on carrier type and measurement method can be quantified by a two-way ANOVA test. The carrier type and measurement method constitute two categorical variables, denoted Type and Method, respectively: Type takes three values, electrons, holes and neutral; Method takes two values, averaged and not-averaged. In total there are six groups of measurements. The two-way ANOVA tests three null hypotheses, which are:

1. The carrier type has no effect on the mean value of L_ϕ.
2. The measurement method has no effect on the mean value of L_ϕ.
3. There is no interaction between the carrier type and the measurement method that effects the mean value of L_ϕ.

An interaction effect means that the continuous variable L_ϕ is changed by specific combinations of the independent variables Type and Method. The significance level is chosen to be $\alpha = 0.05$.

Table 4.4 shows the results of the ANOVA test. The Sum of Squares column is describes the variance in the data set unaccounted for by each categorical variable. The column DoF records the number of statistical degrees of freedom associated with each variable and the

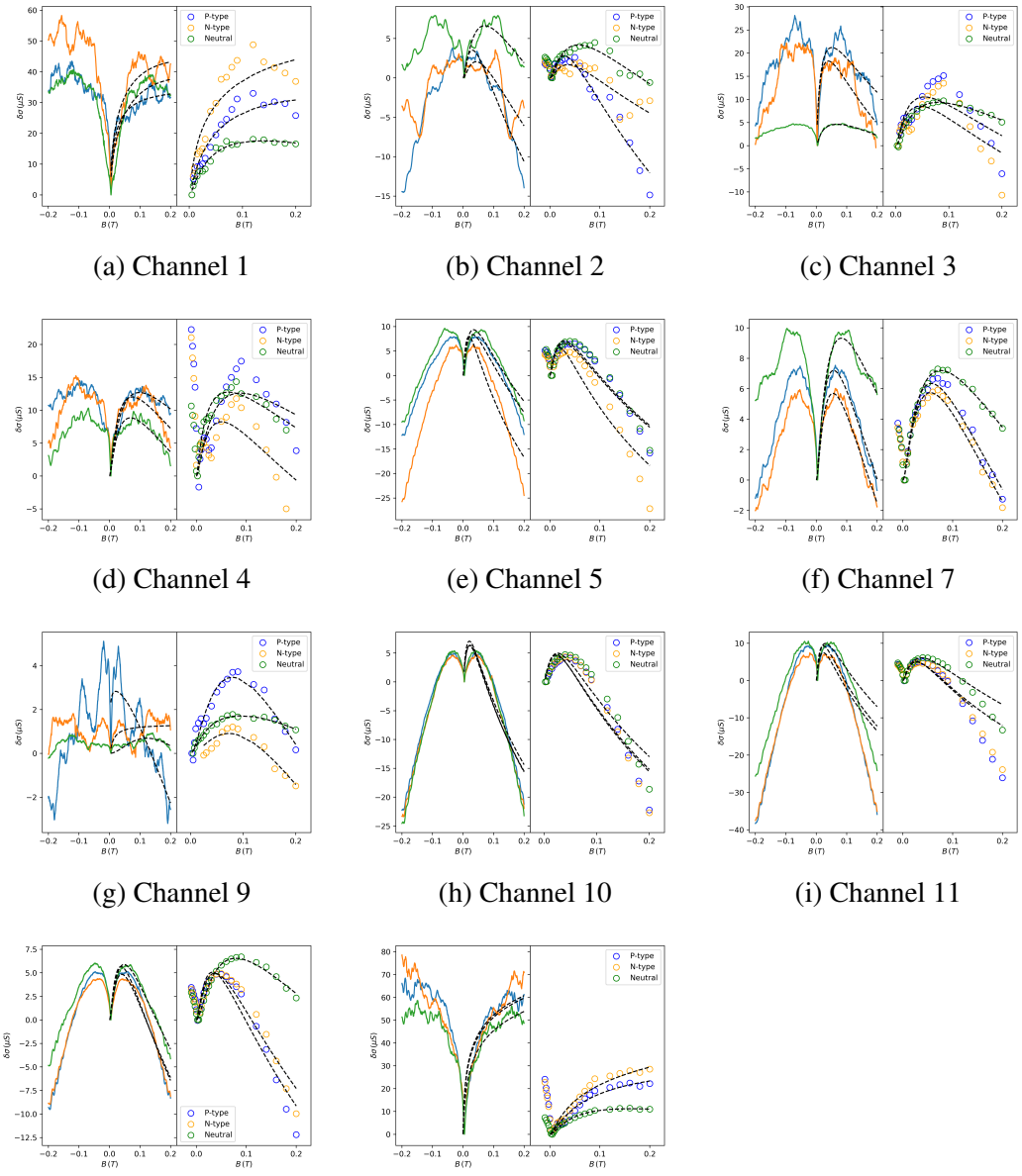

(a) Channel 1 (b) Channel 2 (c) Channel 3

(d) Channel 4 (e) Channel 5 (f) Channel 7

(g) Channel 9 (h) Channel 10 (i) Channel 11

(j) Channel 14 (k) Channel 16

Fig. 4.9 Weak localisation data for every conducting channel of multiplexer CVD-MUX-A. In each sub-figure the plot on the left is of non-averaged data and the plot on the right is of averaged data. Black dashed lines are fits of Eqn. 1.16 to the data.

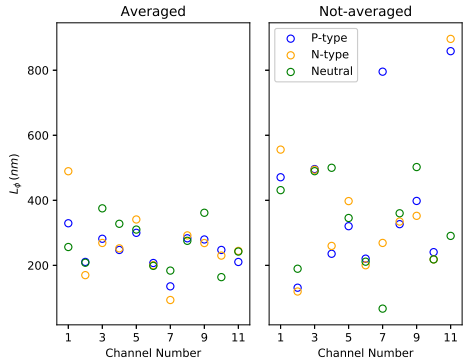

(a) L_ϕ extracted from both averaged and not-averaged weak localisation data, plotted as a function of channel number.

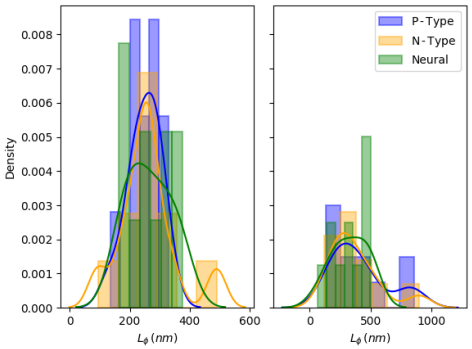

(b) Histograms and approximated probability density functions of the values of L_ϕ obtained from fitting the averaged and not-averaged weak localisation signals.

Fig. 4.10 The variation of the obtained values of L_ϕ across the difference conducting channels.

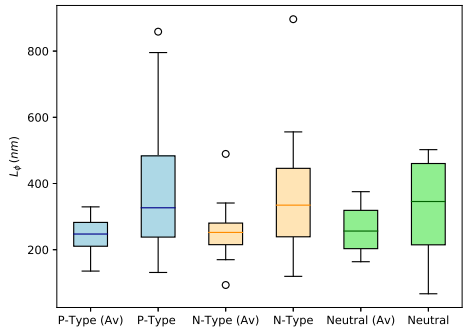

(a) Box plots of L_ϕ, grouped by carrier type and measurement method; (AV) denotes data sets that were obtained using the averaging method.

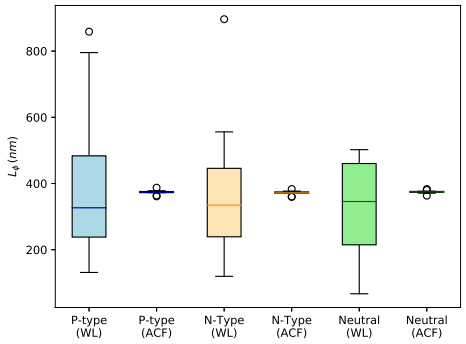

(b) Box plots of showing the distribution of L_ϕ values obtained from fitting the weak localisation signal and from the autocorrelation function of $\delta G(B)$.

Fig. 4.11 Box plots comparing the distribution of L_ϕ values: (a) compares the variation between different carrier types and between data obtained through averaging and not-averaging; (b) compares the variation of values obtained from fitting the weak localisation signal to those obtained from the autocorrelation of $\delta G(B)$.

	P-type (Av)	N-type (Av)	Neutral (Av)	P-type	N-type	Neutral
Mean	248	259	263	408	372	327
Std	54	100	72	234	215	145
Min	135	93	163	131	119	66
Q1	210	215	203	238	239	214
Q2	247	252	256	326	334	345
Q3	282	280	318	483	445	460
Max	329	489	375	858	896	502

Table 4.3 The numerical statistics, to the closest integer, describing the distribution of L_ϕ for each group shown in Fig. 4.11a. Mean, Std, Min, Q1, Q2, Q3 and Max denote the mean, standard deviation, minimum, first quartile, second quartile (median), third quartile, and maximum values in each group of measurements, respectively.

	Sum of Squares	DoF	F-statistic	p-value
Type	1.2 e+04	2	0.3	0.8
Method	2.1 e+05	1	8.9	4 e-03
Type:Method	2.6 e+04	2	0.5	0.6
Residual	1.4 e+06	60	NA	NA

Table 4.4 Results of the ANOVA test. The table shows the sum of squares, the number of degrees of freedom (DoF), the F-statistic and the associated p-value for each independent variable, Type and Method and their interaction, denoted Type:Method.

Carrier type	$\Delta\mu$ (nm)	s_p (nm)	Cohen's d
Electron	160.2	170.1	0.9
Hole	113.4	168.4	0.7
Neutral	63.9	115.1	0.6

Table 4.5 The difference between the mean value of L_ϕ when the averaging method is used and when it is not used, for each carrier type.

Residuals row shows the sum of squares not explained by the model and the number of degrees of freedom, which is given by the number of categories (6 in this case) multiplied by $n-1$, where $n=11$ is the number of data points in each group. The p-values show that null hypothesis 1 and null hypothesis 3 must be accepted: Type has no effect on the mean value of L_ϕ and there is no interaction effect between Type and Method that affects the mean value of L_ϕ. Since the p-value for Method is smaller than the chosen significance level, null hypothesis 2 is rejected and it can be said that the measurement method, averaging or not averaging, has a significant effect on the mean value of L_ϕ. This is reflected in the box plot, Fig. 4.11a: the median (and mean) value of the data sets collected using the averaging method are all lower than those which have not used the averaging method, yet for both averaged and non-averaged data, the median values are similar across the different carrier types. The results in Table 4.5 quantify how much using the averaging method affects the calculated mean value of L_ϕ. The observed difference between the means is smaller in the charge neutrality region than in the electron and hole regions; in the charge neutrality region they differ by approximately half of the pooled standard deviation, compared to 0.94 and 0.67 standard deviations for the electron and hole regions respectively.

From Fig. 4.11a and Table 4.3 it can be seen that the interquartile range of the data collected using the averaging method is consistently smaller than the interquartile range of the data collected, not using the averaging method. Furthermore, the standard deviation of the data collected using averaging is roughly half that of the data collected not using averaging. The most obvious reason for this is that the data collected without averaging contains conductance fluctuations, which adds variation to the signal.

However it can be seen in Fig. 4.9 that some of the weak localisation curves constructed by averaging show deviations from the ideal shape described by Eqn. 1.16. This means that the averaging procedure has either not fully removed the conductance fluctuation effect, or that the deviation from the ideal weak localisation signal is caused by some other effect. A change of $\Delta V_g = 1\,V$ corresponds to an approximate change in the Fermi energy of $\Delta E_F \approx 84\,\text{meV}$. As stated earlier, the disorder configuration of a metal can be considered to change when the

Fermi energy is changed by an amount greater than $E_c = \hbar\pi^2 D/L^2$ [93], which in the case of the devices measured in this work is approximately $E_c \approx 0.13\mu eV$. A voltage range of $\Delta V_g = 1V$ should be averaging over a large number of disorder configurations and therefore should be sufficient to eliminate conductance fluctuations from the weak localisation signal. It is unclear which other factors could cause these features to be present in the averaged data.

Figure 4.10b shows density histograms of the L_ϕ values along with probability density functions estimated from those histograms, using a kernel density estimation. The histograms and the estimated probability density functions are approximately normal distributions about 260 nm for the averaged measurements and about 350 nm for the not-averaged measurements. There are some smaller peaks at values greater than the mean and the estimates of the probability density functions gives non-zero probabilities of obtaining negative values of L_ϕ: this is because only 11 data points are used to estimate each probability density function. Since the distributions already appear to be normal, it is expected that with more measurements, the histograms and the estimated probability density functions would converge towards a normal distribution, about the true mean value of L_ϕ for these samples.

4.3.2 Conductance fluctuations

Figure 4.12 shows the extracted $\delta G(B)$ signals and Fig. 4.11b shows the distribution of L_ϕ values obtained by fitting the weak localisation signal and from the autocorrelation function of the conductance fluctuations. The results of t-tests for each carrier type comparing the means value of L_ϕ obtained from fitting to weak localisation and from the autocorrelation of $\delta G(B)$ are shown in Table 4.6, and show there is no statistically significant different between the two. This is in contrast to the results found in the previous experiment ($G(B)$ measured at 50 values of V_g), where the mean values of L_ϕ from fitting to weak localisation and from the autocorrelation of $\delta G(B)$ did have a statistically significant difference. This is because the difference of mean values of L_ϕ obtained using the autocorrelation function predicts considerably smaller values of L_ϕ than weak localisation analysis in this experiment. It is clear from these results that both methods of determining L_ϕ are consistent with each other and predict similar mean values. The main difference is that the variance of the data obtained from the weak localisation fitting is approximately 100 times larger than the variance of the data obtained from the autocorrelation function, as seen in Fig 4.11b. This result suggests that when $Var(\delta G(B)) \ll e^2/h$, as is the case for large samples, the method of determining L_ϕ from the autocorrelation function of $\delta G(B)$ has statistical bias. This means that this method frequently predicts the same value of L_ϕ regardless of the details of the fluctuations, which may occur when the fluctuation amplitude is small.

(a) Channel 1 (b) Channel 2 (c) Channel 3

(d) Channel 4 (e) Channel 5 (f) Channel 7

(g) Channel 9 (h) Channel 10 (i) Channel 11

(j) Channel 14 (k) Channel 16

Fig. 4.12 The fluctuations $\delta G(B)$ are shown in Fig. 4.9. Blue, orange and green represent electron, hole and neutral transport regions, respectively. Traces have been vertically offset by 2.5 μS for clarity. The data for channels 5, 10, 11 and 14 have been truncated to the region $|B| < 0.15$ T to remove Shubnikov-de-Haas oscillations.

Carrier type	t-statistic	p-value	$\Delta\mu$ (nm)	s_p (nm)	Cohen's d
Electron	-0.5	0.6	-35.3	165.7	-0.2
Hole	-0.0	1.0	-1.1	152.7	-0.0
Neutral	1.1	0.3	46.9	103.1	0.5

Table 4.6 The results of t-tests to 1 d.p. comparing the mean value of L_ϕ obtained from fitting to the weak localisation signal and from the autocorrelation of the conductance fluctuations for each carrier type.

4.4 Temperature dependence of magneto-transport

4.4.1 Weak localisation

Scattering lengths

Figure. 4.13 shows the scattering lengths plotted as a function of T on a semi-logarithmic axis. The dephasing length L_ϕ across $T = 0.6\,\mathrm{K}$, $1.0\,\mathrm{K}$ and $2.0\,\mathrm{K}$ is approximately constant, showing that L_ϕ has saturated for temperatures $T < 2.0\,\mathrm{K}$ similar to the result found in [67]. For most data sets, L_* appears to slightly increase as a function of temperature, although other weak localisation studies of graphene state that L_* is independent of temperature. It is difficult to interpret the behaviour of L_i because the uncertainty of the estimate is so large.

The dephasing rate

The temperature dependence of the weak localisation signal was measured for channels 1, 2 and 3. As discussed in Section 1.2.2 the behaviour of $\tau_\phi^{-1}(T)$ is used to determine the dephasing mechanism. Here, the data is modelled considering only high-frequency, quasi-elastic electron-electron interactions, and statistical analysis is employed to quantify the goodness-of-fit. The model is taken from Ref. [67]:

$$\tau_\phi^{-1} = \gamma \frac{k_B T}{2 E_F \tau_p} \ln\left(\frac{E_F \tau_p}{\hbar}\right), \tag{4.7}$$

where γ is a constant of order unity [86, 83] (denoted by α elsewhere: γ is used here to avoid confusion with the significance level of statistical tests, also denoted by α) and $\tau_p = l_{mfp}/v_F$ is the momentum relaxation time. The authors of Ref. [67] found γ to fall between 1 and 2 for all samples, which is similar to the results found here, although γ at the Dirac point is considerably smaller.

	Channel 1			Channel 2			Channel 3		
	γ	R^2	p-value	γ	R^2	p-value	γ	R^2	p-value
P-type	1.3	1.0	4.3 e-07	0.8	0.0	0.7	1.9	0.9	5.0 e-05
N-type	1.2	1.0	3.0 e-08	1.1	0.8	2.8 e-05	1.6	0.9	7.6 e-06
Neutral	4.6 e-04	0.9	1.5 e-05	6.2 e-04	0.8	7.0 e-05	2.0 e-04	1.0	3.0 e-10

Table 4.7 The results of fitting the data in Fig. 4.14 to Eqn. 4.7 given to 1 d.p. The value γ is the fitting parameter and R^2 and the p-values are stated to evaluate the goodness-of-fit, as explained in the main text.

The values of τ_ϕ^{-1} and the corresponding linear fits are displayed in Fig. 4.14, and the fitting results displayed in Table 4.7. It can be seen in Fig. 4.14 that there is a strong linear relationship between τ_ϕ^{-1} and T for all but channel 2 in the hole regime. The R^2 value ranges from 0.79 to 0.99 for all but one data set, with p-values many orders of magnitude below 0.05, so it can be claimed with confidence that Eqn. 4.7 that the data does not display linear behaviour by chance and that high-frequency, quasi-elastic electron-electron interactions are responsible for dephasing. In the hole regime of channel 2, there is no statistically significant linear relationship between τ_ϕ^{-1} and T. This is illustrated by the fact that a horizontal line could be drawn within the 95% confidence level, and is reflected by the low value of R^2 and high p-value. As a result, it cannot be claimed that high-frequency, quasi-elastic electron-electron interactions are the primary dephasing mechanism of holes in channel 2.

4.4.2 Conductance fluctuations

The traces of $\delta G(B)$ at each value of T are shown in Fig. 4.15. It is obvious that the amplitude of the fluctuations decrease as the temperature is raised to $T = 25.0\,\mathrm{K}$, where they have almost completely vanished. The value of $RMS(\delta G(B))$ falls by an approximate factor of 10 between $T = 0.6\,\mathrm{K}$ and $T = 25.0\,\mathrm{K}$, from approximately $0.5\,\mu\mathrm{S}$ to $0.05\,\mu\mathrm{S}$ for all channels and carrier types. The predicted values of B_c, L_ϕ and τ_ϕ^{-1} appear approximately constant for temperatures above $T = 1\,\mathrm{K}$ as shown in Fig 4.16. In particular, τ_ϕ^{-1} does not show the linear T dependence as observed in Fig. 4.14. It is possible that this occurs because $Var(\delta G(B)) \ll e^2/h$ at $T = 0.6\,\mathrm{K}$ and almost vanishes at 25 K, so the autocorrelation function considers the signals approximately the same, as discussed earlier.

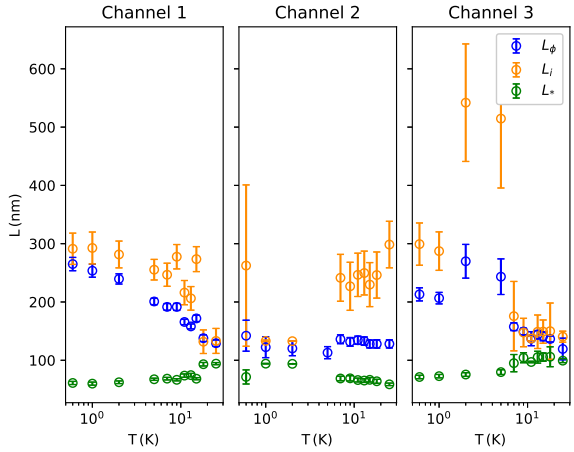

(a) Hole region.

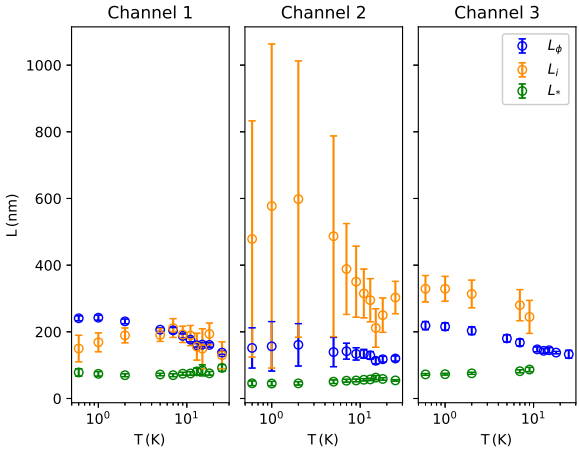

(b) Electron region.

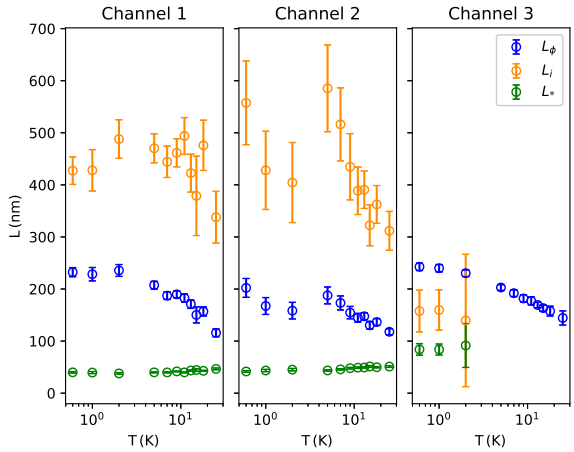

(c) Charge neutrality region.

Fig. 4.13 The scattering lengths extracted from fitting weak localisation signal, as a function of temperature. Temperature is plotted on a logarithmic axis. Some values of L_i and L_* have been discarded due to very large uncertainty in their estimates.

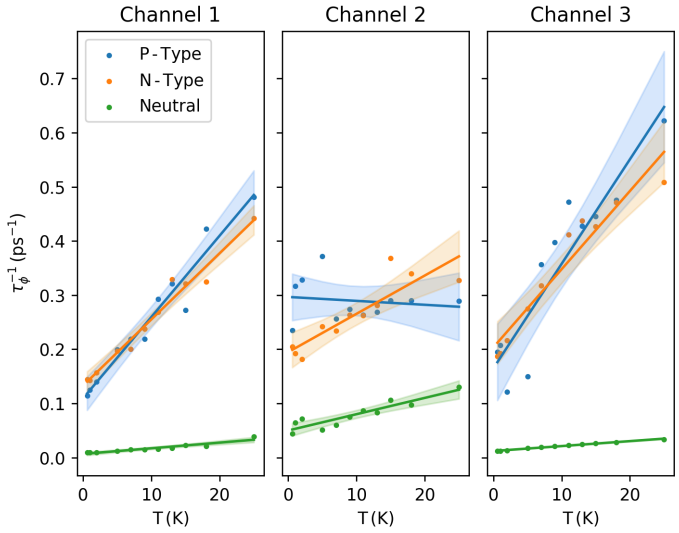

Fig. 4.14 The change in dephasing rate τ_ϕ^{-1} as a function of temperature T, plotted for channel 1, 2 and 3 for device CVD-MUX-A. The blue, orange and green points represent data taken in the p-type, n-type and neutral transport regimes, respectively. The solid lines are linear fits to the data and the shaded regions are the corresponding 95 % confidence intervals.

4.5 Conclusions

The results from three magneto-transport experiments, analysing the behaviour of weak localisation signals and conductance fluctuations have been presented. An explanation of the chosen experimental parameters is provided and a model of the B dependent series resistance is explained before discussion of the results.

It was found from the first experiment that there is a weak but statistically significant dependence of L_ϕ and L_i on V_g, which may be a manifestation of the difference between electron and hole mobility values. Furthermore, there is evidence of a non-linear dependence of L_* on V_g, however no consensus on the mechanism behind this behaviour is made. These dependencies were reflected in the corresponding scattering rates, which have values in agreement with those reported elsewhere.

In all channels, L_ϕ was calculated from analysis of weak localisation signals and from the autocorrelation function of the conductance fluctuations. Furthermore, two data collection methods were also compared, one where $G(B)$ is averaged over a 1 V voltage window, and one where it is not. It was found that the data collection method caused a statistically significant difference between the predicted mean value of L_ϕ, an effect which has not been commented upon elsewhere. Furthermore, it was found that using the autocorrelation function to predict L_ϕ may show statistical bias when the amplitude of $\delta G(B)$ is small.

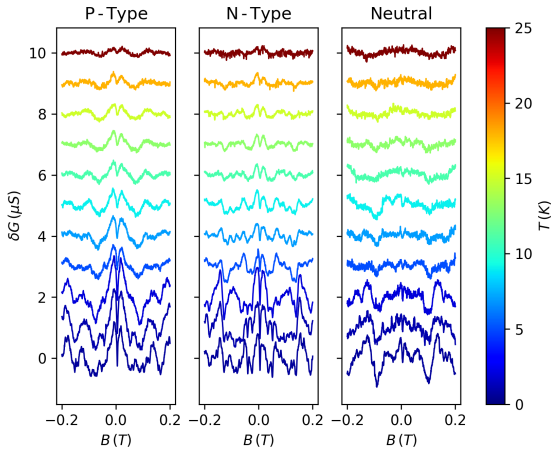

(a) Channel 1

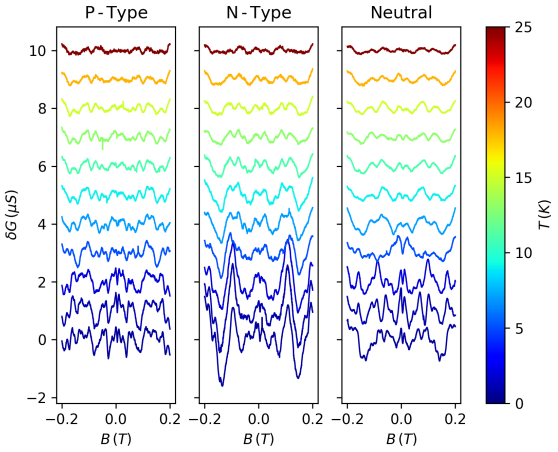

(b) Channel 2

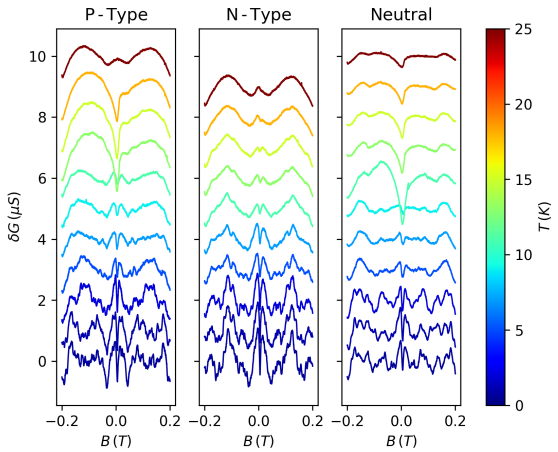

(c) Channel 3

Fig. 4.15 Measurements of $\delta G(B)$ as a function of T for p-type, n-type and neutral regions in channels 1, 2, 3. The data at $T = 9\,\mathrm{K}$ for channel 3 in the n-type region was not taken. Traces vertically offset by $1.0\,\mu\mathrm{S}$ for clarity.

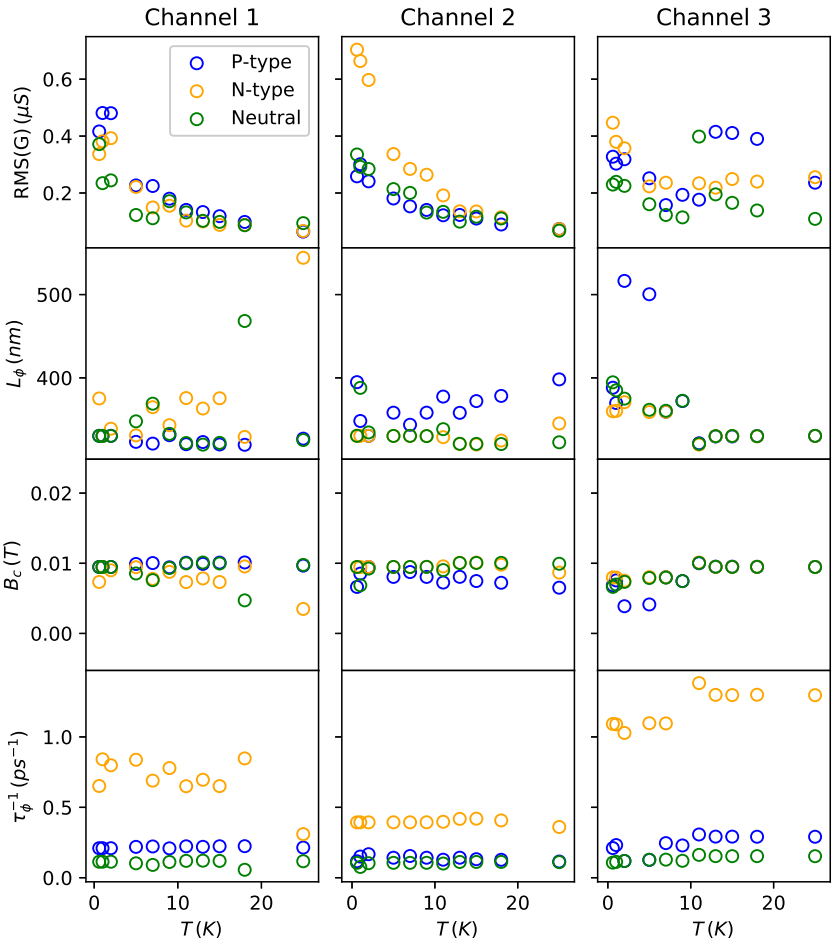

Fig. 4.16 The results of the analysis of $\delta G(B)$ as a function of T for channels 1, 2 and 3. The figure shows the $RMS(G)$, the phase-coherence length L_ϕ, the critical field B_c and the decoherence rate τ_ϕ^{-1} as a function of temperature for each carrier type.

Finally, the behaviour $\tau_\phi^{-1}(T)$ was analysed using regression analysis, where very strong evidence of dephasing due to high-frequency, quasi-elastic electron-electron interactions was found. This behaviour was not reproduced by analysing the T dependence of $\delta G(B)$, again suggesting statistical bias in this method.

Chapter 5

High-Field Magneto-Transport Measurements of Multiplexed Graphene Field-Effect Transistors

5.1 Introduction

This chapter presents the results and analysis of magneto-transport experiments of device CVD-MUX-A in magnetic fields up to $B = 10\,\mathrm{T}$ and completes the characterisation of multiplexed CVD-grown graphene. For all conducting channels, V_g was swept across the charge neutrality region at 50 different values of the magnetic field, ranging between 0 and 10 T, incremented in steps of $\Delta B = 0.2\,\mathrm{T}$. Quantisation of energy is observed in channels 2, 3, 4 and 7, and the Landau levels have a separation proportional to $\sqrt{B}$, as expected from graphene. From the Landau level spacing, the Fermi velocity v_F and the cyclotron mass m^* of charge carriers are calculated and agree well with values reported in existing literature, which provides evidence that these channels are in the quantum Hall regime. A further interesting observation is an insulating transition of the $N = 0$ Landau level in channel 2, and Section 5.2.2 is dedicated to further exploration of this insulating state. The remaining channels show fan-like features, however, these are distorted and are not analysed, for reasons discussed briefly in the conclusion.

As shown in Chapter 2, the 2DEG in the multiplexer attains a resistance of the order of $200\,\mathrm{k}\Omega$ at $B = 10\,\mathrm{T}$ which can make the Landau levels difficult to observe in these two-terminal graphene devices. The highest Landau levels observed are the $N = \pm 2$ levels and are identified as peaks in the $R(V_g)$ curve, since some states are localised in the quantum Hall regime of disordered conductors and thus R will increase as the Fermi level moves through

a Landau level. Nonetheless, it is still possible to estimate values of v_F and m^* since these quantities do not depend on R and therefore are independent of the series resistance. Since these quantities are independent of R, no attempt is made here to subtract a series resistance in this section. In Section 5.2.2 the resistance does become relevant to the analysis, and so the series resistance is estimated and subtracted from the data. The method for estimating the series resistance is explained in 5.2.2.

5.2 Results and analysis of high-field magneto-transport measurements

5.2.1 The quantum Hall effect in channels 2, 3, 4 and 7

As mentioned in the introduction, it was possible to identify clear Landau quantisation in channels 2, 3, 4, and 7. Figures 5.1, 5.2, 5.3 and 5.4 show the results of the magneto-transport experiments for these channels. For channels 2 and 3 it was possible to identify the 0, ± 1 and ± 2 Landau levels from Figs. 5.1a and 5.2a, respectively, which show the emergence of the resistance peaks as B increases from 0 to 10 T. In Figs 5.1a and 5.2a the bottom trace corresponds to $B = 0$ T and the top trace corresponds to $B = 10$ T. The $N = 0$ Landau level is robust and its energy stays constant with increasing magnetic field, while the other Landau levels separate with a gap proportional to $\sqrt{B}$. The black crosses mark the position of the peaks for each Landau level at 4, 5, 6, 7, 8, 9 and 10 T and the black dashed lines are quadratic fits to the peak positions. For channel 4, the $N = -2$ Landau level was not observable in Fig. 5.3a and for channel 7, both the $N = \pm 2$ levels are not observable in 5.4a. In order for the Landau levels to be observable, the level broadening must be less than the separation, $\Gamma < \hbar\omega_c$, where Γ is the broadening and ω_c is the cyclotron frequency. The exact form of the level broadening in graphene is debated and is believed to depend on B, the index N and the specific types of disorder present in the system [191–194]. Since the scattering rates for electron and holes can be different to each other in a given disorder potential, electrons and holes can have different mobility values. It is possible then, that the broadening for hole-populated Landau levels with carrier density $n < 0$ is different to the broadening of electron-populated Landau levels with $n > 0$, and could explain why the $N = -2$ level is not observable in channel 4, while the $N = 2$ level is observable. A strong disorder potential corresponds to low mobility and also broad Landau levels, therefore Landau level broadening may explain why only the $N = 0, \pm 1$ levels are observable in channel 7, since this had the lowest mobility value ($\mu = 2010\,\mathrm{cm^2 V^{-1} s^{-1}}$) of the four channels considered here.

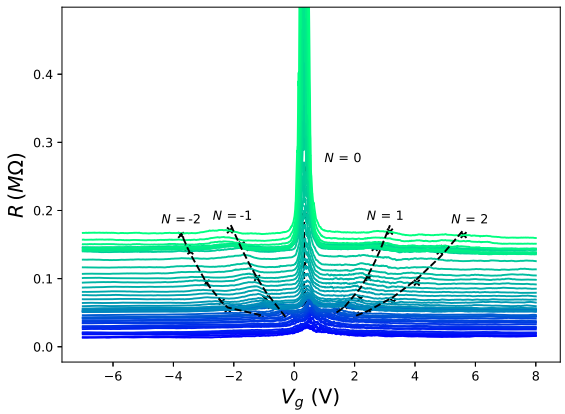

(a) R plotted a function V_g for different values of B.

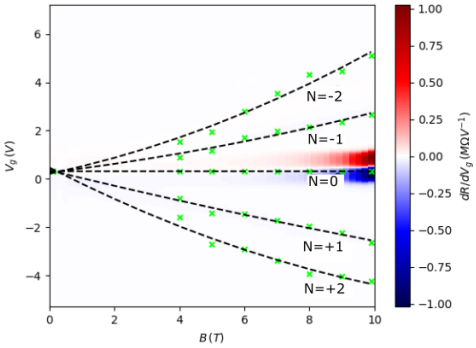

(b) The derivative dR/dVg plotted on a heat map as a function of V_g and B.

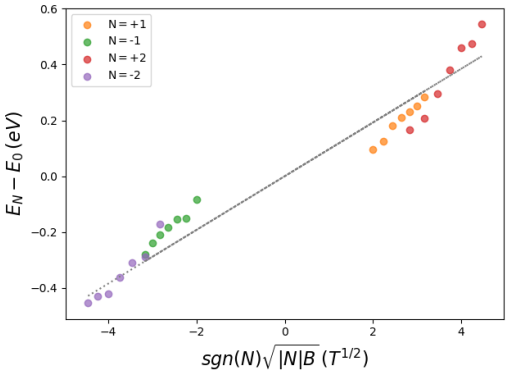

(c) Landau level energies plotted against $sgn(N)\sqrt{|N|B}$.

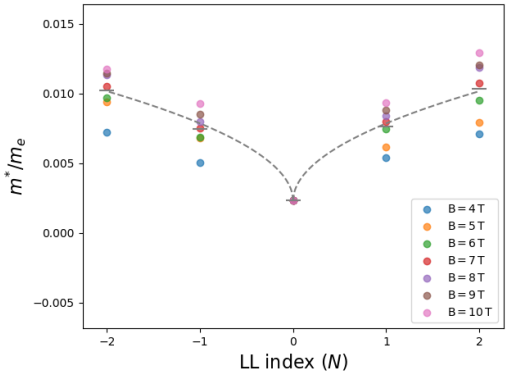

(d) The cyclotron mass of carriers in each Landau level.

Fig. 5.1 The data and analysis of channel 2. The resistance R as a function of V_g is plotted for 50 values of B between 0 and 10 T and the black, dotted lines are quadratic fits to the Landau level peak positions; (b) shows dR/dV_g plotted as a function of B and V_g with black dotted lines showing the position of the Landau levels. The plot in (c) shows the distance in energy of each Landau level from the Dirac energy plotted against $sgn(N)\sqrt{|N|B}$ and the grey dotted line is a linear fit, to the data; (d) shows the cyclotron mass m^* in units of the electron rest mass m_e, as a function of the Landau level index N, for different B values. The horizontal lines drawn through each group of points are the mean value of the m^* in each Landau level, and the grey dotted lines are fits showing the square root dependence of m^* on N.

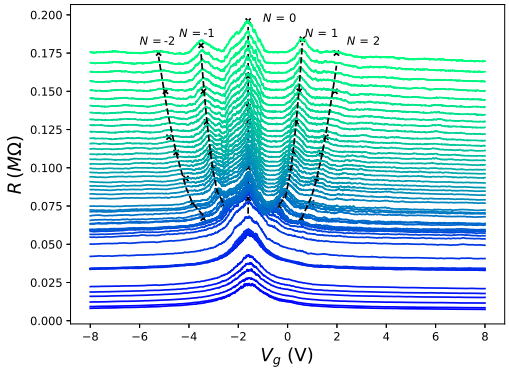

(a) R plotted a function V_g for different values of B.

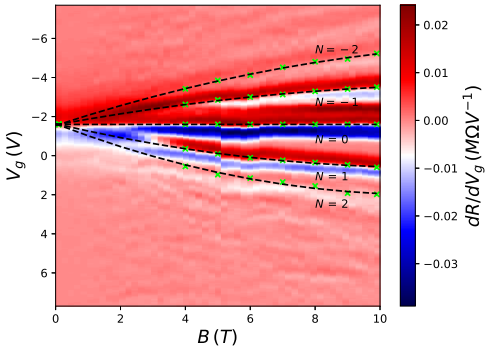

(b) The derivative dR/dVg plotted on a heat map as a function of V_g and B.

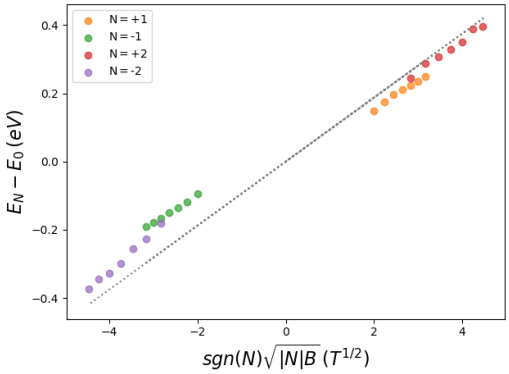

(c) Landau level energies plotted against $sgn(N)\sqrt{|N|B}$.

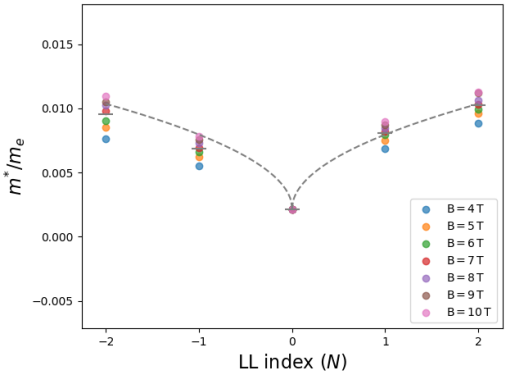

(d) The cyclotron mass of carriers in each Landau level.

Fig. 5.2 The data and analysis of channel 3. The resistance R as a function of V_g is plotted for 50 values of B between 0 and 10 T and the black, dotted lines are quadratic fits to the Landau level peak positions; (b) shows dR/dV_g plotted as a function of B and V_g with black dotted lines showing the position of the Landau levels. The plot in (c) shows the distance in energy of each Landau level from the Dirac energy plotted against $sgn(N)\sqrt{|N|B}$ and the grey dotted line is a linear fit, to the data; (d) shows the cyclotron mass m^* in units of the electron rest mass m_e, as a function of the Landau level index N, for different B values. The horizontal lines drawn through each group of points are the mean value of the m^* in each Landau level, and the grey dotted lines are fits showing the square root dependence of m^* on N.

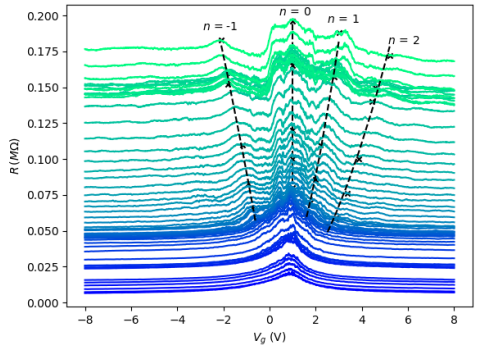

(a) R plotted a function V_g for different values of B.

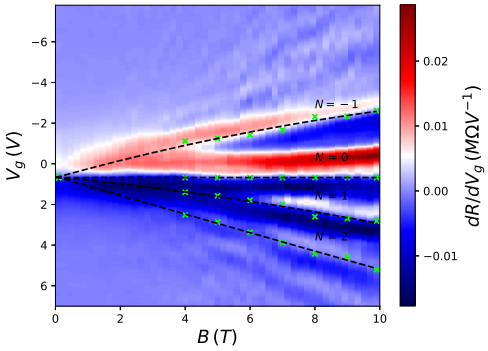

(b) The derivative dR/dVg plotted on a heat map as a function of V_g and B.

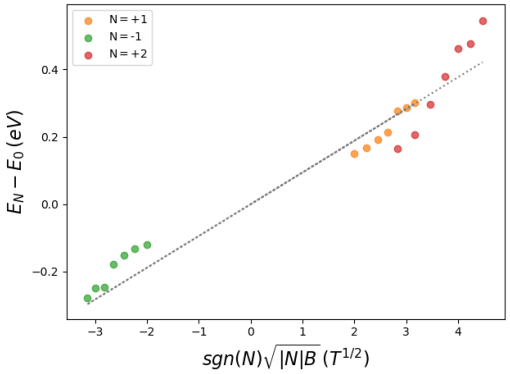

(c) Landau level energies plotted against $sgn(N)\sqrt{|N|B}$.

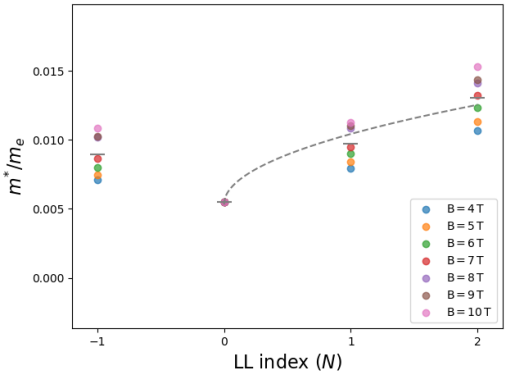

(d) The cyclotron mass of carriers in each Landau level.

Fig. 5.3 The data and analysis of channel 4. The resistance R as a function of V_g is plotted for 50 values of B between 0 and 10T and the black, dotted lines are quadratic fits to the Landau level peak positions; (b) shows dR/dV_g plotted as a function of B and V_g with black dotted lines showing the position of the Landau levels. The plot in (c) shows the distance in energy of each Landau level from the Dirac energy plotted against $sgn(N)\sqrt{|N|B}$ and the grey dotted line is a linear fit, to the data; (d) shows the cyclotron mass m^* in units of the electron rest mass m_e, as a function of the Landau level index N, for different B values. The horizontal lines drawn through each group of points are the mean value of the m^* in each Landau level, and the grey dotted lines are fits showing the square root dependence of m^* on N

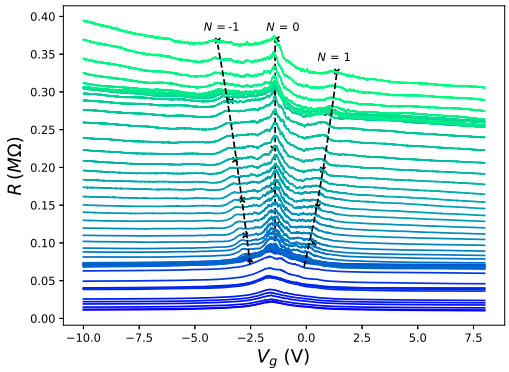

(a) R plotted a function V_g for different values of B.

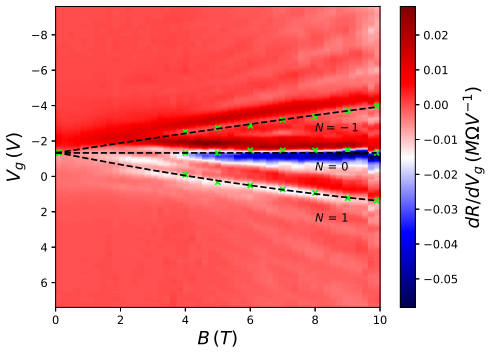

(b) The derivative dR/dVg plotted on a heat map as a function of V_g and B.

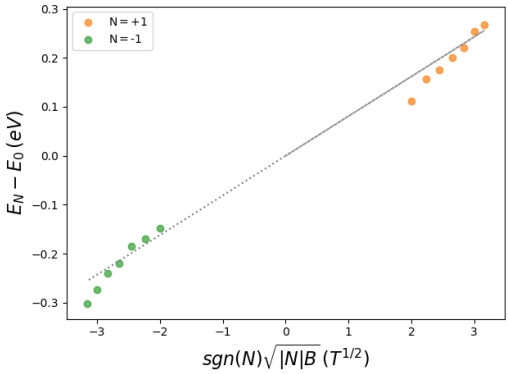

(c) Landau level energies plotted against $sgn(N)\sqrt{|N|B}$.

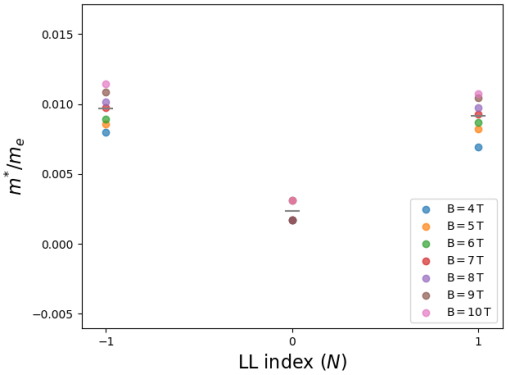

(d) The cyclotron mass of carriers in each Landau level.

Fig. 5.4 The data and analysis of channel 7. The resistance R as a function of V_g is plotted for 50 values of B between 0 and 10 T and the black, dotted lines are quadratic fits to the Landau level peak positions; (b) shows dR/dV_g plotted as a function of B and V_g with black dotted lines showing the position of the Landau levels. The plot in (c) shows the distance in energy of each Landau level from the Dirac energy plotted against $sgn(N)\sqrt{|N|B}$ and the grey dotted line is a linear fit, to the data; (d) shows the cyclotron mass m^* in units of the electron rest mass m_e, as a function of the Landau level index N, for different B values. No fits are shown for the dependence of m^* on N since there there are only the $N = 0$ and $N = 1/-1$ Landau levels to fit too.

The heat maps shown in Figs. 5.1b, 5.2b, 5.3b and 5.4b show dR/dV_g plotted as a function of B and V_g for channels 2, 3, 4 and 7. The crosses that denote the Landau level peak positions in the $R(V_g)$ plots are mapped onto the heat map image and are shown by green crosses. The black dotted lines show the quadratic fits to the peak positions. The fits are extrapolated back to $B = 0$ and follow curves which correspond to $dR/dV_g = 0$. The Landau levels appear as fans spreading out from $|V_g - V_d| = 0$ and some finite value of B where the Landau levels begin to separate. In Fig. 5.1b it is difficult to observe the fans corresponding to the non-zero Landau levels since the gradient is much larger about the $N = 0$ level than any other, since the resistance of this level extends to approximately $2.6\,\mathrm{M\Omega}$, approximately 14 times more resistive than the other Landau levels, which have a resistance of approximately $0.175\,\mathrm{k\Omega}$ at $B = 10\,\mathrm{T}$ (including series resistance). For channels 3, 4 and 7, other fan features are visible which are not observable in the $R(V_g)$ curves, which suggests higher Landau levels have become separated but are difficult to observe because the change in R is small as the Fermi energy moves through them. These Landau levels have not been included in the subsequent calculation of v_F and m^* since it is difficult to determine exactly where the derivative is equal to zero from the heat map alone.

Discussion of the Fermi velocity

By plotting the difference between the energy of each Landau level and the energy of the Dirac voltage $E_n - E_0$ against $sgn(N)\sqrt{|N|B}$ it is clear from Eqn. 1.27 that the points will, ideally, collapse onto a straight line with a gradient equal to $v_F\sqrt{2e\hbar}$. This technique is used in scanning probe experiments described in Refs. [195–199] to extract Fermi velocities of the order of $v_F \approx 1 \times 10^6\,\mathrm{ms}^{-1}$. In these experiments the energy of each Landau level is measured by sweeping a bias voltage applied V to the probe tip, and measuring the tunnelling current I between the tip and the surface; peaks in the graph of $I(V)$ are centred at values of V for which electrons can tunnel from the tip into an Landau level. The bias voltage is converted into a potential energy using $E_p = eV/\varepsilon_r$. This methodology is applied to the present experiments, where peaks in the graph of $R(V_g)$ are used to identify Landau level positions and the gate voltage V_g is converted into an energy by the same method as is in the scanning probe experiments. In the present experiment, the gate electrode plays the role of the scanning probe tip, the Al_2O_3 gate dielectric plays the role of the vacuum between the probe tip and the sample surface, and the graphene channel is analogous to the sample surface. The presence of a magnetic field does not influence the potential difference between the scanning probe tip and the sample surface, or in this case the gate electrode and the channel. This is because the magnetic field B can only influence the electrical potential of carriers in the channel if it time-dependent during the measurement due to Faraday's law,

$\mathscr{E} = d/dt(\iint_\Sigma \mathbf{B}(t) \cdot d\mathbf{A})$, where $\mathscr{E}$ is the electromotive force (EMF) induced by $\mathbf{B}(t)$ and Σ is the surface area of the channel. Since the data displayed in Figs. 5a,b,c,d, is taken with a time-independent magnetic field applied in the direction perpendicular to the graphene channel, $\mathbf{B}(t) = B$ (V_g is swept at constant values of B), the EMF induced in the channel by B is exactly zero and the relationship $E_p = eV/\varepsilon_r$ holds true. The factor of $1/\varepsilon$ in the expression for E_p arises because the electric field will polarise the material between the gate electrode and the channel. The scanning probe experiments cited above are performed in vacuum so $\varepsilon = 1$, however in the present experiment the dielectric constant of Al_2O_3 is taken to be $\varepsilon_r = 9$ taken from [159].

Since only a maximum of two electron populated and two hole populated Landau levels were measured in the present experiments, a single linear fit was made too all of the data, implying that the Fermi velocity of electrons and holes are equal. This assumption is not strictly true, Ref. [197] showed that charged impurities and ripples in the graphene can cause an asymmetry between the Fermi velocity of electrons and holes with a magnitude of up to $0.3 \times 10^6\,\mathrm{ms}^{-1}$. The Fermi velocity for channels 2, 3, 4, and 7 are $v_F = 1.5 \times 10^6$, 1.3×10^6, 1.7×10^6, and $1.6 \times 10^6\,\mathrm{ms}^{-1}$, respectively. The uncertainties from the linear fits are of the order of $10^1\,\mathrm{ms}^{-1}$. These values are slightly higher than the values reported in the scanning probe experiments, however it is known from theory and angle resolved photoemission spectroscopy (ARPES) experiments that many-body interactions renormalise and increase the value of v_F [200–203].

The authors of Ref. [203] control the electron-electron interaction strength by controlling the dielectric environment (substrate material) of their graphene samples, thereby changing the degree of screening between carriers. They define the dielectric constant to be $\varepsilon = (\varepsilon_{vacuum} + \varepsilon_r)/2$ and find that for graphene on metallic substrates (where $\varepsilon = \infty$) $v_F \approx 0.85 \times 10^6\,\mathrm{ms}^{-1}$, consistent with scanning probe measurements of v_F of graphene on metallic foils. For graphene on quartz, where $\varepsilon = 1.8$, $v_F \approx 2.8 \times 10^6\,\mathrm{ms}^{-1}$ similar to the value of $v_F \approx 3 \times 10^6\,\mathrm{ms}^{-1}$ measured in suspended graphene samples in magneto-transport experiments in Ref. [204]. For a hBN substrate with $\varepsilon = 4.7$, which is comparable to the effective dielectric constant for Al_2O_3 using the above formula, ($\varepsilon = (1+9)/2 = 5$) they measure $v_F \approx 1.5 \times 10^6\,\mathrm{ms}^{-1}$. This is very similar to the values of v_F measured here in the multiplexed graphene channels which suggests that the values of v_F observed here are explained by a renormalisation of the Fermi velocity due to many-body electron interactions. This is consistent with with the result of the temperature-dependent weak localisation measurements of channels 1, 2 and 3 from Chapter 4, which showed that the dominant dephasing mechanism was due to electron-electron interactions for all three channels. The observed variation in v_F values the multiplexed devices may be due to variations in charged impurity densities

Channel	$\bar{m}_0^*$	$\bar{m}_1^*$	$\bar{m}_{-1}^*$	$\bar{m}_2^*$	$\bar{m}_{-2}^*$
2	0.004	0.013	0.012	0.017	0.017
3	0.004	0.016	0.013	0.020	0.19
4	0.008	0.013	0.012	0.014	-
7	0.011	0.013	0.014	-	-

Table 5.1 The mean value of m^* in each observable Landau level, denoted $\bar{m}_N^*$, for channels 2, 3, 4 and 7. Subscripts denote the Landau level index and values are given in units of m_e.

between channels or slightly different effective gate dielectrics between channels, which may arise if the ALD process of the Al_2O_3 dielectric across the multiplexer device was not perfectly uniform. In SI units, the interaction parameter is given by $\alpha = e^2/4\pi\hbar\varepsilon v_0$, where v_0 is the bare Fermi velocity, that is, the Fermi velocity with no many-body effects. Using $v_0 = 0.85 \times 10^6\,\mathrm{ms}^{-1}$ as in Ref. [203], the interaction parameter for the multiplexed graphene devices is $\alpha \approx 0.51$. It is worth noting that other sources take different values of v_0, such as in Ref. [205] which will lead to slightly different values of α.

Discussion of the cyclotron mass

The cyclotron mass m^* is obtained from the Fermi velocity through the relation $E_F = m^* v_F^2$ shown in Ref. [28]. By equating $E_F = E_N$ the equation for the cyclotron mass in the N'th Landau level is $m_N^* = sgn(N)\sqrt{2e\hbar|N|B}/v_F + E_0/v_F^2$ and it can be seen that m^* scales as the square root of the Landau level index N and B. Note that this equation is not stating that mass is quantised, since m^* depends continuously on B. Figures 5.1d, 5.2d, 5.3d and 5.4d show m^* as a function of B in each observable Landau level for channels 2, 3, 4 and 7, respectively. For channels 2 and 3, where four non-zero Landau levels were observable, it can be seen that m^* is indeed increasing as $\sqrt{|N|}$ and is highlighted by the grey dashed curves, which are obtained by taking the mean value of m^* in the $N = 0, 1, 2$ Landau levels and fitting the function $m^* = A\sqrt{N}$ where A is an arbitrary fitting parameter. The same procedure can be performed to obtain a fit to the $N = 0, -1, -2$ Landau levels. The fitting procedure has not been done for channel 7, since only two data points are available for fitting, $N = 0$ and $N = \pm 1$, which could each be fit with straight lines. These figures show that in all cases m^* is lowest in the $N = 0$ Landau level and in each Landau level, m^* increases with B as expected.

Table 5.1 shows the mean value of $\bar{m}_N^*$ in each Landau level N, in channels 2, 3, 4, 7. In the $N = 0$ Landau level, $\bar{m}_0^* = 0.004\,m_e$ in channels 2 and 3, and this increases to $0.008\,m_e$ in channel 4 and $0.010\,m_e$ in channel 7 indicating that m^* increases when mobility decreases. This makes intuitive sense, since in pristine graphene, where $E_F = 0$, $\bar{m}_0^* = 0$; as more

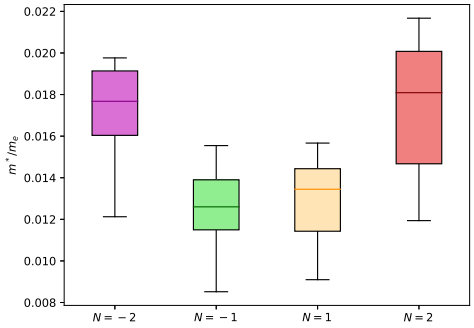

(a) Channel 2.

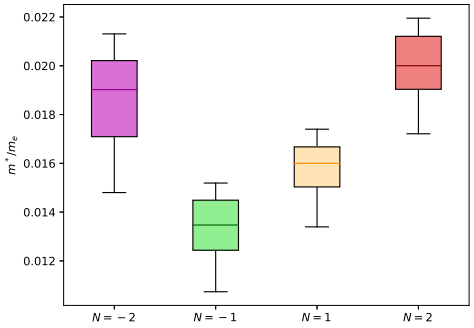

(b) Channel 3.

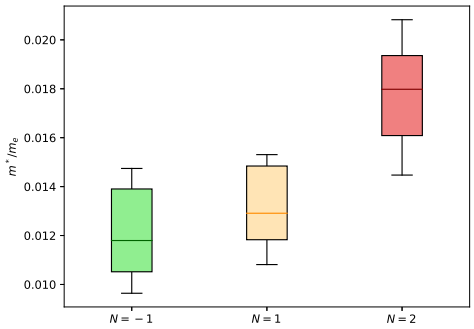

(c) Channel 4.

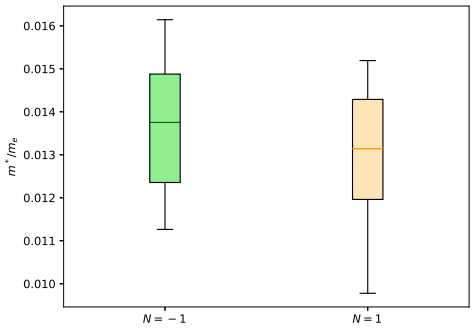

(d) Channel 7.

Fig. 5.5 Box plots representing the distribution of m^* as a function of B in each observable, non-zero Landau level.

impurities / disorder is introduced into the system, the mobility in general decreases and E_F becomes non-zero due to doping, leading to non-zero values of m_0^*. The box plots in Figs. 5.1d, 5.2d, 5.5c and 5.5d show the distribution of m^* for different B in each non-zero Landau level. It is clear that the distributions are not exactly equal for hole populated and electron populated landau levels with equal values of $|N|$. This is because the Landau level peak positions are located at slightly asymmetric distances from the energy of the Dirac point E_0, for hole and electron populated energy levels.

Early cyclotron resonance studies performed by Deacon *et al.* [206] observed an asymmetry between effective mass of electrons and holes in graphene, similar to what has been found here. Taking the average value of the effective mass, they report $m^* = 0.009\,m_e$, which is comparable to the values found here for the $N = \pm 1$ for channels 2 and 3, and comparable to m^* in all observed Landau levels for channels 4 and 7. Another common technique for extracting m^* is by studying the temperature dependence of the frequency of Shubnikov de-Haas oscillations in $1/B$ [33, 123, 207, 189, 74]. One benefit of this technique is that it is easy to measure m^* as a function of carrier density. Close the Dirac voltage, in the $N = 0$ Landau level, Ref. [123] reports $m^* = 0.005\,m_e$, while Fig. 5 of Ref. [207] indicates a similar value of m^* near the charge neutrality point. These values are in close agreement with the values of m^* in the zero Landau level reported here, confirming that the present results are consistent with what has been reported elsewhere. Away from the Dirac point, Ref. [207] reported values of m^* vary from between approximately 0.02 to $0.07\,m_e$ depending on the carrier density used. The values of m^* reported here in the non-zero Landau levels are at the low-end of what has been found elsewhere.

Properties of the cyclotron orbits

Unlike conventional, non-relativistic 2D systems, the cyclotron frequency ω_c in graphene is dependent only on v_F but not m^*, given by:

$$\omega_c = \frac{\sqrt{2}v_F}{l_B} = v_F\sqrt{\frac{2eB}{\hbar}}, \tag{5.1}$$

where $l_B = \sqrt{\hbar/eB}$ in SI units is the magnetic length. This implies the cyclotron radius $r_c = v/\omega_c$ is simply $r_c = l_B/\sqrt{2}$ which is independent of the carrier density. The quantity $l_B^2/2$ is the minimum area that a cyclotron orbit can occupy, limited by the uncertainty principle. This statement can be demonstrated by calculating the commutator $[\hat{x},\hat{y}] = il_B^2$ of the position operators $\hat{x}$, $\hat{y}$ representing the centre of a cyclotron orbit. This implies that in graphene, r_c always takes the smallest value possible, which is a result of the relativistic spectrum and the vanishing mass of charge carriers.

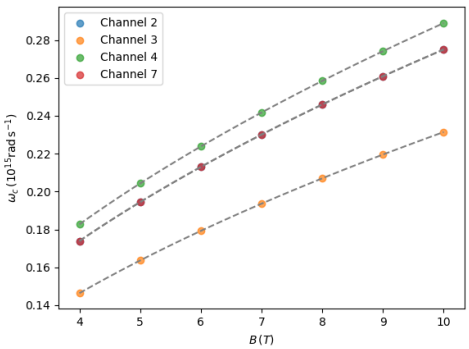

(a) The cyclotron frequency ω_c plotted as a function of B for channels 2, 3, 4 and 7.

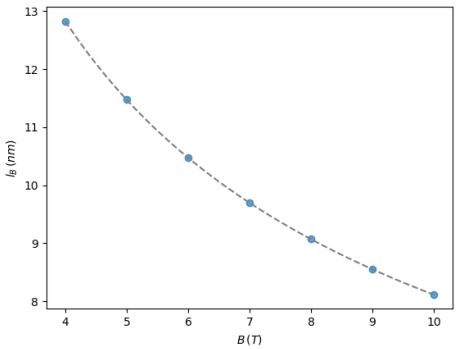

(b) The magnetic length l_B plotted as a function of B.

Fig. 5.6 The values of ω_c according to Eqn. 5.1 and l_B which describe the cyclotron motion of charge carriers in graphene.

Figure 5.6 shows ω_c scaling as $\sqrt{B}$ for all channels and l_B scaling as $1/\sqrt{B}$ as defined. The values of ω_c in Fig. 5.6a are of the order of $0.1 \times 10^{15}\,\mathrm{rad\,s^{-1}}$: using $f = \omega/2\pi$ charge carriers complete approximately 10^{13} orbits per second, corresponding to a period of $T \approx 0.1$ ps. For all channels ω_c approximately doubles between 4 and 10 T.

The magnetic length l_B is by definition independent of the system and reduces from $l_B \approx 13$ nm at B=4 T to $l_B \approx 8$ nm at B=10 T. Assuming circular orbits with area $A = \pi l_B^2/2$ the density of non-overlapping cyclotron orbits is approximately $3.9 \times 10^3\,\mu\mathrm{m}^{-2}$ at 4 T, increasing to $9.8 \times 10^3\,\mu\mathrm{m}^{-2}$ at 10 T.

5.2.2 Insulating transition of channel 2

Channel 2 is interesting because the $N = 0$ Landau level appears to be approaching an insulating state at low temperature and at high magnetic fields, as shown in Figs 5.7a and 5.7b. As discussed in the introduction, in large magnetic fields the low-energy states of graphene can be in one of a variety of phases characterised by the filling factor ν. Here arguments are made that the insulating behaviour is a result of a phase transition from a metallic quantum Hall phase into a quantum Hall insulator phase. As the system transitions between the metallic and insulating phases, reproducible features emerge at $|\nu| < 1$ and the origin of these features are discussed.

Estimating the contact resistance

Since the insulating regime is identified by a diverging value of R, a contact resistance R_c is estimated and subtracted from the data. Equation 3.1 failed to fit the data at high B so the contact resistance is estimated by noting that Eqn. 3.1 predicts a mean value of R_c that is 0.9 times the observed minimum resistance of a device.

To elaborate, when $V_g \to \infty$ the resistance saturates at some value due to the contact resistance, (as opposed to tending to zero) denoted R_{min}. The model described by Eqn. 3.1 predicts a value of the contact resistance R_c^{model}, which is always less than the experimental R_{min}. For each of the 11 conducting channels, at $B = 0\,\mathrm{T}$, a factor $F = R_c^{model}/R_{min}$ is calculated. This factor has a mean value of 0.9 with a standard deviation of 0.0098. This factor 0.9 can be used to estimate a contact resistance from the $R(V_g)$ curve when V_g is far from the charge neutrality region. Since the factor 0.9 is a mean value, its error is given by the standard deviation over the square root of the number of measurements, that is $\sigma/\sqrt{n}$. In this case the error in the factor $F = 0.9$ is approximately 2.8%. In the following the contact resistance is estimated to be $R_c = 0.9R_{min}$ and the error is 2.8% of the obtained value.

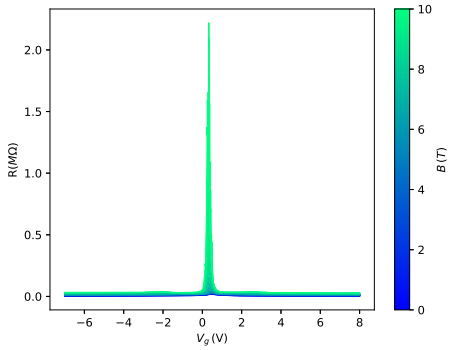

(a) $R(Vg, B)$ as plotted as a function of V_g for different values of B at $T = 0.28\,\mathrm{K}$.

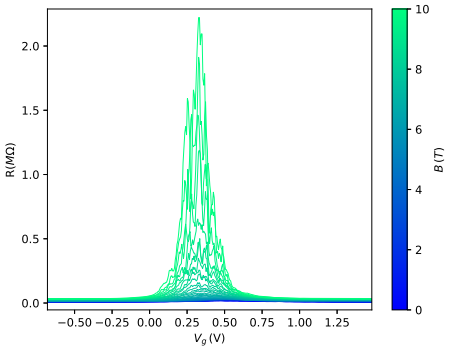

(b) A zoomed image of (a) showing detail of the high resistance region.

Fig. 5.7 Plots of $R(V_g, B)$ plotted as a function of V_g at 50 values of B between 0 and 10 T at $T = 0.28\,\mathrm{K}$.

Testing for Coulomb blockade

Since the graphene in channel 2 forms a constriction of width $W \approx 440\,\mathrm{nm}$, see Fig. 5.8, it is possible that the insulating behaviour could be due to the Coulomb blockade or a 1-dimensional quantisation effect.

At $B = 10\,\mathrm{T}$, $l_B \approx 8\,\mathrm{nm} < W$, so it would not be expected that transverse confinement would cause an energy gap to appear, however SEM imaging alone is not sufficient to

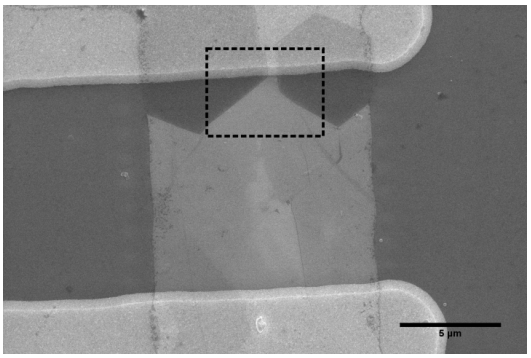

(a) An SEM image of channel 2 with the most narrow region highlighted.

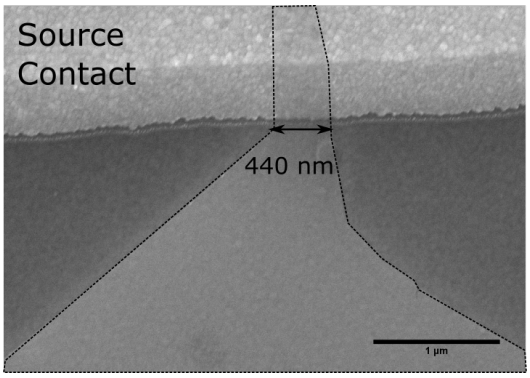

(b) A magnification of the region inside the box drawn in (a).

Fig. 5.8 An SEM image of channel 2. The region inside the box indicated by the black, dashed line is magnified in (b), showing the that the width of the graphene channel at the source contact is 440 nm.

definitively disprove size effects causing an insulating state. To investigate possible Coulomb blockade behaviour a direct-current bias voltage source V_{DC} is added into the measurement circuit and the conductance G is measured as a function of V_g and V_{DC} at varying temperatures between 0.28 K and 25 K. Figure 5.9 displays 3D visualisations of $R = 1/G$ as a function of V_g and V_{DC} after the subtraction of R_c estimated using the method described above. There is a clear resistance peak centred about $V_g = V_d$ and $V_{DC} = 0$ with a magnitude of approximately $R = 2.1\,\mathrm{M\Omega}$ at $T = 0.28\,\mathrm{K}$. As the temperature increases the peak begins to reduce in magnitude and by $T = 8\,\mathrm{K}$ the peak has almost vanished, and the maximum resistance is approximately $30\,\mathrm{k\Omega}$. As the temperature increases beyond 8 K the region of maximum resistance becomes less localised in $V_g - V_{DC}$ space, illustrated by the yellow region which indicates high resistance expanding with increasing temperature. There is no indication of diamond-shaped structures characteristic of the Coulomb blockade, which eliminates the Coulomb blockade as possible cause of the observed insulating behaviour.

Testing for a gapless excitations

Reference [126] reported an insulating transition which was different to the results of groups reporting a diverging ρ_{xx}. Above a certain critical magnetic field B_c, the resistance begins to diverge as a function of B, however when $B < B_c$ the longitudinal conductivity saturates for a given value of B as T drops below $2\,K$. This behaviour is explained in Refs. [126, 141] as a type of Kosterlitz-Thouless transition, where the resistance plays the role of a correlation length, related to B via:

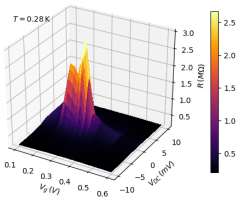

(a) $T = 0.28\,\mathrm{K}$.

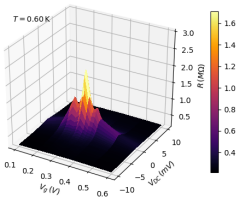

(b) $T = 0.60\,\mathrm{K}$.

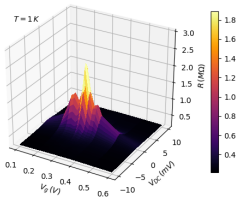

(c) $T = 1\,\mathrm{K}$.

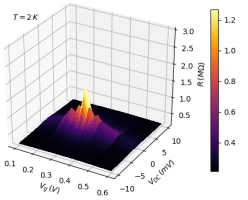

(d) $T = 2\,\mathrm{K}$.

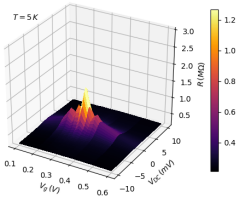

(e) $T = 5\,\mathrm{K}$.

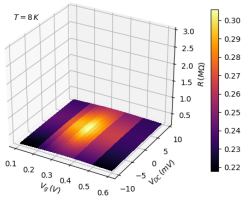

(f) $T = 8\,\mathrm{K}$.

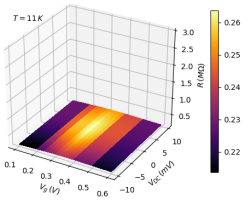

(g) $T = 11\,\mathrm{K}$.

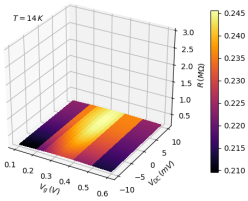

(h) $T = 14\,\mathrm{K}$.

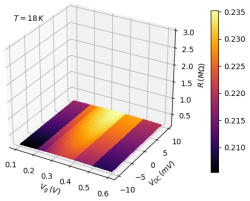

(i) $T = 18\,\mathrm{K}$.

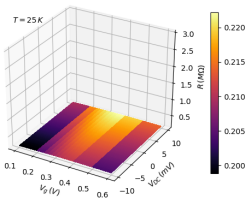

(j) $T = 25\,\mathrm{K}$.

Fig. 5.9 Surface plots of R as a function of V_g and V_{DC} for 10 temperatures between 0.28 K and 25 K. The DC bias V_{DC} is swept continuously between $\pm 10\,\mathrm{mV}$ while V_g is stepped across the insulating region, as explained in the main text.

$$R_{xx} \sim e^{2a/\sqrt{B_c - B}}, \tag{5.2}$$

for a critical magnetic field B_c and constant a, determined from experiment. Notice that Eqn. 5.2 diverges at $B = B_c$ indicating a phase transition, and is undefined for $B > B_c$. It will be shown that the present results do not match those of Ref. [126] despite the divergent nature of R. Figures 5.10a and 5.10b show R plotted as a function of B for different values of T. A T- and B-dependent contact resistance is estimated by measuring $R(T,B)$, the same as in Figs. 5.10a and 5.10b but at $V_g = -6\,\mathrm{V}$, so that the graphene is metallic. This data is then scaled and subtracted in a manner similar to that described in the introduction to this section.

Although the curves in Figs. 5.10a and 5.10b look similar to the results displayed in Ref. [126] (see Figs. 3b and 3c), they does not obey Eqn. 5.2. In earlier experiments with GaAs/Al_xGa_{1-x}As systems, the phase boundary between metallic and insulating regimes is marked by a critical magnetic field B_c where $R(B;T)$ isotherms cross, that is where the resistance is T-independent [208, 136, 137]. These features can clearly be seen in the present data, which is most clear in the $G(B)$ curve Fig. 5.10b but is also present in the $R(B)$ curves. The crossing point is at $B = 6.4\,\mathrm{T}$. Immediately it is clear that Eqn. 5.2 becomes undefined at $B \geq 6.4\,\mathrm{T}$. Suppose then that the critical magnetic field is $B = 10.1\,\mathrm{T}$, just so that Eqn. 5.2 remains well-defined for all values of B used in the present experiment. A plot of $\ln(R)$ against $(B_c - B)^{-1/2}$ should be a straight line with gradient $2a$ as seen in Fig. 4b of Ref. [126]. This is not the case here as shown in Fig .5.10c which is a plot of $\ln(R)$ against $(B_c - B)^{-1/2}$. Choosing larger values of B_c does eventually lead to the linear relationship observed in [126], however a value of $B_c > 10\,\mathrm{T}$ is paradoxical in this case, since the magnetic field used in the experiment never exceeds 10 T, yet R is already observed to be diverging. This could be interpreted to mean that the true point of divergence has not been reached in the present experiment, and that B_c is beyond 10 T, but this interpretation contradicts the traditional method of determining B_c as in the earlier experiments of Refs. [208, 136, 137].

Figure 5.10d shows the resistance $R(B;T)$ and displayed as a contour plot $B-T$ plane, where B ranges from 0 to 6 T, that is below the critical field. It can be seen that there is no temperature below which R saturates to a T-independent value, in contrast to Fig. 4a of Ref. [126].

In summary, the present results could only be explained by Eqn. 5.2 as in Refs. [126] if the critical magnetic field B_c was larger than those used in the experiment, leading to a contradiction. Note that in Ref. [126] the critical field is obtained by plotting $(\mathrm{d}\ln R/dH)^{-2/3}$ against H (auxiliary magnetic field) and extracting H_c by extrapolating to $(\mathrm{d}\ln R/dH)^{-2/3} = 0$ (see Fig 4c of the reference), however a similar plot could not be reproduced here. For magnetic fields $B < B_c$ the present data is also different to what is observed in Ref. [126],

in that the resistance is seen to be T dependent for $T < 2\,\mathrm{K}$. This is then evidence that the observed behaviour is different to that observed in Ref. [126] and is not explained by the corresponding theory of Ref. [141].

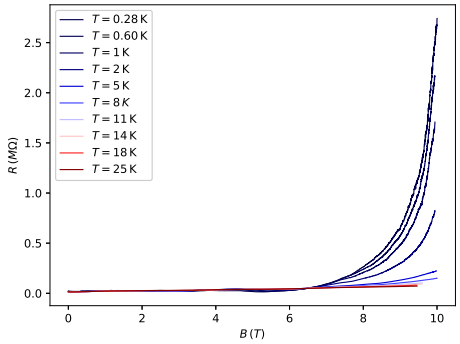

(a) R plotted a function B for different values of T.

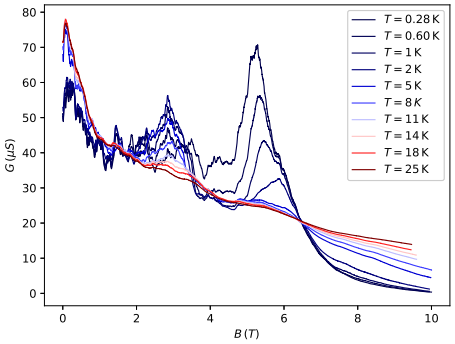

(b) Plots of $R(B)$ for different values of T.

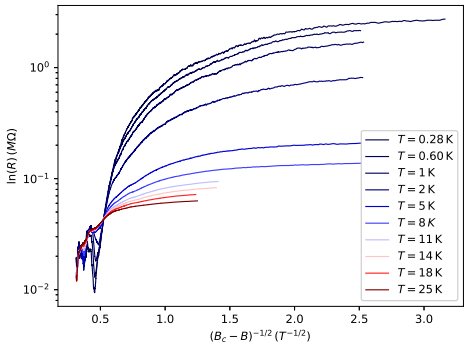

(c) $\log(R)$ plotted against $(B_c - B)^{-1/2}$, where B_c is artificially chosen to be 10.1 T.

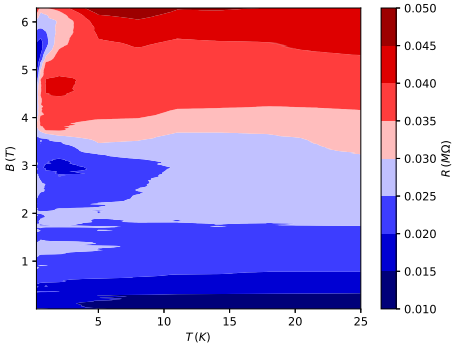

(d) A contour plot of $R(T,B)$. Colour scale increment is 5.0 kΩ.

Fig. 5.10 Line traces of R and G as a function of B at different values of T are shown in (a) and (b), respectively; (c) is a plot of $\log(R)$ against $(B_c - B)^{-1/2}$ and (d) shows a contour plot of $R(T,B)$. Only B values up to 6.3 T are shown so that the variation in R is visible, and not washed-out by the diverging resistance at $B = 10\,\mathrm{T}$. The gate voltage is held at $V_g = 0.3\,\mathrm{V}$ for all measurements.

Resistance plateaux at $|\nu| < 1$

A series of reproducible resistance plateaux become visible in the trace of $R(V_g)$ at $B = 10\,\mathrm{T}$ and $T = 0.28\,\mathrm{K}$ as the carrier density approaches its minimum. Figure 5.11 shows R plotted as a function of filling factor $\nu = nh/Be$. These plateaux are not visible for $T > 0.28\,\mathrm{K}$ suggesting that they only arise when the system transitions into an insulating state. Plotted as a func-

tion of ν, plateaux are seen at negative filling factors $\nu = -0.2, -0.27, -0.38, -0.43, -0.50$, and positive filling factors $\nu = 0.30, 0.38, 0.45, 0.5, 0.58$. The features at positive ν appear more like peaks than plateaux which is a known consequence of two-terminal measurement of the quantum Hall effect in graphene: the conductance overshoots it's expected quantised value and before dropping back towards that quantised value [209]. Some of these correspond to known fractional filling factors however the corresponding values of R are not equal to $R = h/(e^2\nu)$, which may be due to mixing of longitudinal and transverse components of the resistance [210, 209]. The corresponding values of R and G are stated in Table 5.2. The difference between fractional filling factors arising from composite fermions becomes smaller as the factor increases, which can be seen by considering the sequence $\nu = 1/3$, $2/5$, $3/7$.... The difference between $\nu = 1/3$ and $\nu = 2/5$ is approximately 0.1 however the difference between $\nu = 2/5$ and $\nu = 3/7$ is approximately 0.03. This makes verifying that the features are genuine Hall plateaux difficult in two-terminal devices, since higher fractional filling factors require greater measurement accuracy of $R = h/(e^2\nu)$ compared to low fractional filling factors and integer filling factors. Since the resistance values of the plateaux are not equal to $R = h/(e^2\nu)$ it is not possible to claim that they are definitely due to the fractional quantum Hall effect, despite their reproducibility. This issue was encountered in Ref. [211] who observed the fractional quantum Hall effect in two-terminal, suspended GFET samples. In that report, reproducible plateaux are observed in the conductance at $\nu = 0.48$ and $\nu = 0.68$, but the corresponding values of G do not take their expected, quantised values, making it difficult to understand their origin. Despite the lack of conclusive evidence pertaining to the origin of these features in the present work, it could be speculated that $\nu = -0.27/0.3$, ± 0.38, $-0.43/0.45$ could correspond to the well known fractional sequence $\nu = \pm 1/3$, $\pm 2/5$, $\pm 3/7$ indicating the presence of composite fermions with filling factor $\nu = n/(2n+1)$, since they occur at both positive and negative filling factors. Interestingly, the plateau $\nu = -0.5$ has a resistance of $2h/e^2$ and so does take its quantised value. The Hall plateau at $\nu = 1/2$ has been recently observed in monolayer graphene, along with another at $\nu = 1/4$ [212], where it is argued that the emergence of the even-denominator fractional quantum Hall plateaux are evidence of a transition between different ground states described in Refs. [141, 213]. Alternatively, these plateaux have been observed in GaAs/AlGaAs systems [214] and have been shown to be of different origin to fractional quantum Hall states, since there is no corresponding plateau of ρ_{xy} and the feature persisted up to $T = 10\,\mathrm{K}$, however they are believed to be many-body electron states. With the data available from two terminal measurements it is not possible to distinguish between the two mechanisms since it is not possible to check for a plateau at $\rho_{xy} = 2h/e^2$.

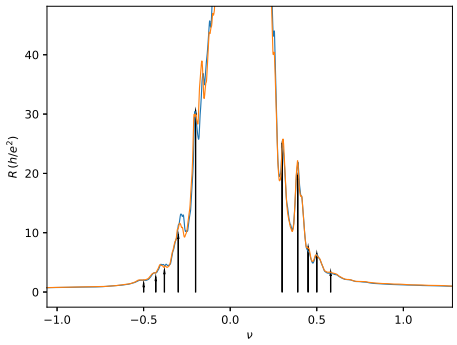

(a) R plotted as a function of ν in units of h/e^2.

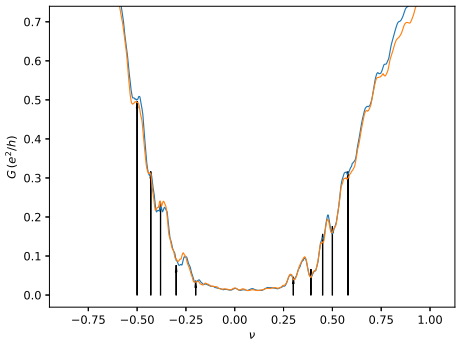

(b) G plotted as a function of ν in units of e^2/h.

Fig. 5.11 Two repeat traces of R and G plotted as a function of ν showing reproducible plateaux features which are indicated by black arrows.

ν	$R\,(h/e^2)$	$G\,(e^2/h)$
-0.50	2.0(9)	0.50(9)
-0.43	3.2(9)	0.31(9)
-0.38	4.4(9)	0.23(9)
-0.27	11.0(9)	0.09(9)
-0.20	29.5(9)	0.03(9)
0.58	3.2(9)	0.31(9)
0.50	5.0(9)	0.16(9)
0.45	7.4(9)	0.14(9)
0.38	21.6(9)	0.05(9)
0.30	25.3(9)	0.04(9)

Table 5.2 The values of R and G of the reproducible features occurring at the given values of $\nu < 1$. The uncertainty is determined from the uncertainty of the subtracted series resistance, which for R is $0.09\,h/e^e$ and for G is $0.009\,e^2/h$.

Metal-insulator transition boundary

Regardless of the nature of the emergent plateaux at $\nu < 1$, the system becomes insulating in the charge neutrality region, and appears metallic as the ν moves away from the charge neutrality region. This can also be seen in Fig. 5.12b which shows $R(V_g)$ for different values of T and at $B = 10\,\mathrm{T}$. As discussed in the introduction, a plateau at $\sigma_{xy} = 0$ indicates that a gap has opened in the zero-energy Landau level and at low filling factors the system undergoes a a phase transition into a quantum Hall insulator state. Since the multiplexed devices have only two terminals, it is impossible to measure σ_{xy}, however T-independent crossing points of R plotted as V_g have been shown to correspond to the boundary of a quantum Hall phase transition in Ref. [129]. Similar features can be seen in Refs. [126] although they are are not commented upon. This is a similar technique to the one mentioned earlier, used to identify the boundary between insulating and metallic quantum Hall phases in GaAs/$Al_xGa_{1-x}As$ systems [208, 136, 137].

The data of $R(V;T)$ are shown in Fig. 5.12b. Only one crossing point is observed in this plot however, occurring at $V_1 = 0.14\,\mathrm{V}$ which corresponds to filling factors $\nu_1 = -0.33$. The corresponding resistance value are $R_1 = 26.3 \pm 4.8\,\mathrm{k\Omega}$. It is not clear why only one crossing point occurs, however this value is similar to those reported in Ref. [129] who measure the crossing points at $R_{xx} \approx 32\,\mathrm{k\Omega}$ and $38\,\mathrm{k\Omega}$, respectively in graphene. Since $R \neq h/(e^2\nu)$ at these filling factors, the resistance is not quantised at the phase transition points. Figures 5.10a and 5.10b show a T-independent crossing of the $R(B;T)$ curves indicating a critical magnetic field $B_c = 6.4\,\mathrm{T}$, beyond which the resistance begins to diverge at low temperature. This is reflected in Fig. 5.7b which shows large resistances for values magnetic values below $10\,T$.

Estimating the size of the transport gap

It is common to determine the size of the transport gap by modelling $G(T)$ using the Arrhenius equation, which takes the form:

$$G = A \cdot \exp(-E_A/k_B T), \tag{5.3}$$

where A is a constant and E_A is the activation energy of the process. Figure 5.12a shows $\ln(G)$ plotted against $1/T$: when $1/T < 0.5\,\mathrm{K}^{-1}$ ($T > 2\,\mathrm{K}$), $G(T)$ obeys Eqn. 5.3 well, as shown by the linear fit represented as a grey, dashed line; when $1/T > 0.5\,\mathrm{K}^{-1}$ ($T < 2\,\mathrm{K}$) however, $G(T)$ deviates from the behaviour predicted by Eqn. 5.3 significantly. There are more than one possible interpretations of this result. The authors of Ref. [127] claim that deviation from Eqn. 5.3 is due to variable range hopping, as measured in GaAs / $Al_xGa_{1-x}As$ devices

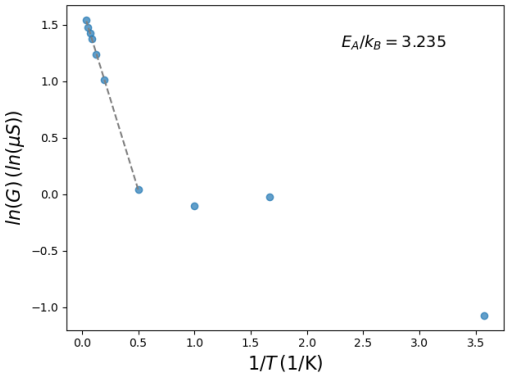

(a) Arrhenius plot ($\ln(G)$ against $1/T$) used to determine if the temperature dependence of G obeys Eqn 5.3.

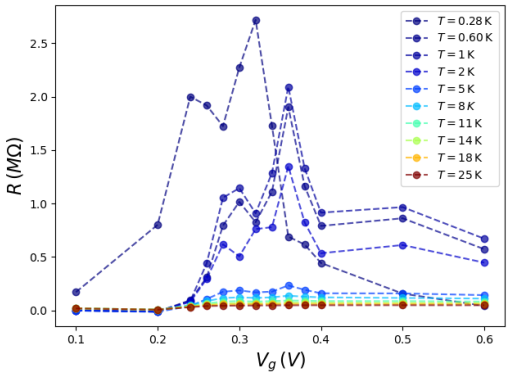

(b) Plots of $R(V_g;T)$ at $V_{DC} = 0\,\mathrm{V}$ and $B = 10\,\mathrm{T}$.

Fig. 5.12 Arrhenius plot at $V_{DC} = 0\,\mathrm{V}$ and $B = 10\,\mathrm{T}$ is shown in (a), which can be used to estimate E_A under certain assumptions discussed in the text. Shown in (b) is $R(V_g;T)$ for many values of T, $V_{DC} = 0\,\mathrm{V}$ and $B = 10\,\mathrm{T}$. The plots are constructed by taking cuts through the surface plots displayed in Fig. 5.9 at $V_{DC} = 0\,\mathrm{V}$.

in Ref [215], becoming the main transport mechanism once $T < 1\,\mathrm{K}$. Following the work of Ref. [127], the gradient of the linear fit is used to extract the value of E_A and the energy gap is defined as $\Delta E = 2E_A$, which for the present result is $\Delta E \approx 2 \times 3.2\,k_B \approx 0.5\,\mathrm{meV}$, where the temperature 3.2 K is obtained from the linear fit shown in Fig. 5.12a. The deviation from activated behaviour is much stronger in the present work than in Ref. [127], and non-monotonic behaviour is observed. This is non-monotonic behaviour was not observed in the experiments described in Ref. [215] in GaAs / $Al_xGa_{1-x}As$, which measured variable range hopping down to $T = 10\,\mathrm{mK}$, which suggests that the behaviour in the present work is not due to variable range hopping.

A second explanation is that there are two thermally activated processes, where the system transitions from a quantum hall state into some intermediate state which has activation energy E_A and then undergoes a second transition into the final, insulating state, which requires a further energy of $E_A^{'} < E_A$. In this case a second linear fit should be drawn on Fig. 5.12a between $1/T = 0.5\,\mathrm{K}^{-1}$ and $1/T = 3.6\,\mathrm{K}^{-1}$ but this would assume that the point at $1/T \approx 1.7\,\mathrm{K}^{-1}$ is a random deviation from linear behaviour and is not genuine, non-monotonic behaviour of $\ln(G)$. There is no reason to assume that this data point is a random variation, especially since the data points for $1/T < 0.5\,\mathrm{K}^{-1}$ all show no deviation from linear behaviour. Furthermore, it is unclear what the intermediate state would be; the authors of Ref. [124] show that the spin degeneracy of the $N = 0$ Landau Level lifts at approximately 11 T, before the sublattice symmetry lifts at 17 T, which could be considered two separate

ground states. However, this transition is driven by increasing the magnetic field, not by decreasing temperature therefore there is not obvious that this type of transition is occurring in the present system.

The third interpretation of the data displayed in Fig. 5.12a is that G does not display thermally activated behaviour as reported elsewhere and does not obey Eqn. 5.3. The non-monotonic T-dependence of G suggests that there are competing processes occurring at low ν and $B = 10\,\mathrm{T}$, since for a gapped system $dG/dT > 0$, so G decreases as T decreases, whereas in a metallic system $dG/dT < 0$ and G increases as T decreases. Non-monotonic relationship between resisitivity ρ and T has been reported in CVD-grown graphene in Ref [216] and considered theoretically in Ref. [217]. The competing processes are electron-phonon scattering, temperature dependent electron screening, Fermi surface smearing and activated transport across potential barriers produced by electron-hole puddles; it is shown that the interaction of these effects indeed causes a non-monotonic relationship between ρ and T. However, the experiment in Ref. [216] is not directly comparable to the data shown here, since the experiment is at $B = 0\,\mathrm{T}$ and does not show diverging R as is found here. Furthermore, the theory of Ref. [217] and the interpretation of the results in Ref. [216] is semi-classical, neglecting electron-electron interactions, Klein tunnelling and strong magnetic fields. These explanations therefore, cannot sufficiently describe the results obtained here, where the spectrum is quantised due to strong magnetic fields and electron-electron scattering has been shown to occur. Possible mechanisms which could cause the observed insulating behaviour are discussed in the following section.

Since it is unclear from the T dependence of G if the transport is thermally activated, it may be more useful to fit a peak-shaped function to R and use the width of the peak, extracted as a fitting parameter, to determine the size of the energy gap. Figure 5.13 shows R about the Dirac point at $T = 0.28\,\mathrm{K}$ and $B = 10\,\mathrm{T}$ along with a Lorenztian curve fit and a Gaussian curve fit.

From the Lorentzian fit the *half*-width at half-maximum is extracted as HWHM$= 0.076\,\mathrm{V}$. To estimate the energy gap, the change in V_g is first converted into a change in carrier density using using $\Delta n = C_{ox}\Delta V_g/e$ which is then substituted into $\Delta E_F = \hbar v_F\sqrt{\pi\Delta n}$. This procedure yields an energy gap $\Delta E \approx 37\,\mathrm{meV}$. From the Gaussian fit, the *full*-width at half-maximum is FWHM$= 0.084\,\mathrm{V}$, corresponding to an energy gap of $\Delta E \approx 27\,\mathrm{meV}$, slightly smaller than that predicted by the Lorentzian fit. Values $C_{ox} = 87.1\,\mathrm{nFcm^{-2}}$ and $v_f = 1.1\times10^6\,\mathrm{ms^{-1}}$ are used in the conversion.

Since the Lorentzian fit is closer to the true peak height than the Gaussian fit, it is likely that the Lorentzian is a better estimate of the FWHM of the data and gives a more accurate

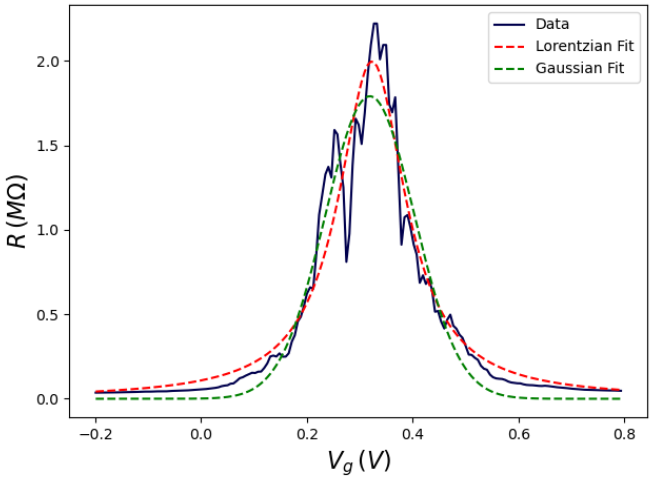

Fig. 5.13 A Lorentzian fit and a Gaussian fit to the $R(V_g)$ curve of channel 2 at $T = 0.28\,\mathrm{K}$ and $B = 10\,\mathrm{T}$.

estimate of the energy gap than the Gaussian. Nonetheless, the Lorentzian fit is not perfect and it is likely that the true energy gap falls somewhere in between these values.

Candidate mechanisms causing an insulating transition

The most simple effect which could cause a transport gap is the Zeeman effect, which lifts the real spin degeneracy in an external magnetic field. The Zeeman energy is given by:

$$\Delta E = g\mu_B B, \tag{5.4}$$

which is approximately 1.2 meV at $B = 10\,\mathrm{T}$ and taking $g = 2$. Therefore the Zeeman effect alone is unlikely to cause the observed behaviour.

It is possible that spontaneous symmetry breaking of the ground state, driven by electron-electron interactions, could lift the ground state degeneracy and open a gap. Reference [218] provides a review of spontaneous symmetry breaking mechanisms in graphene. The first proposal is a transition into a quantum Hall ferromagnetic state which is characterised by Hall plateaux arising at all integer ν, including odd integers such as $\nu \pm 3$ as discussed in Refs [39, 139]. This is in contrast to the usual sequence $\nu = \pm 2, \pm 6 \pm 10...$ consisting of even integers. Reference [139] showed that a paramagnetic state can show Hall plateaux at $\nu = 0, \pm 1, \pm 4$ when the Zeeman interaction is accounted for, but cannot show plateaux at $\nu = \pm 3, \pm 5$. This means that the appearance of plateaux at ± 3 and ± 5 filling factors are true indicators of the quantum Hall ferromagnetic phase. These features are not observed in the so there is no evidence that the quantum Hall ferromagnetic phase occurs in this

experiment. As discussed in the introduction, other microscopic configurations which lift the 4-fold degeneracy of the zero Landau level have been predicted to occur, but the specific phase that the system takes depends upon the energy anisotropy in sub-lattice-valley space, which is not probed in the present experiments. Therefore it is not possible to determine microscopic description of the insulating phase.

Elsewhere, it has been proposed that in the zero-energy Landau level in graphene, a magnetic field could cause pairs of electrons and holes to form bound states, which subsequently form an excitonic condensate, producing a gap in the single-particle spectrum [219, 220]. This process is known as magnetic catalysis and has been used to explain metal insulator transitions in bulk graphite [221–225] and has been theoretically predicted to occur in monolayer graphene [226–228, 144]. Note that in Refs. [223–225] the metal-insulator transition means that dR/dT changes sign, not that there is a divergent resistance. Nonetheless, the theory presented in Ref. [222] does show that the resistance can diverge due to this phase transition. The temperature at which this transition occurs is dependent upon B, which is given in Ref. [221] by (see Eqn. 13):

$$T_c = \left(\frac{\sqrt{B}\ln(N)}{16\pi N} \right), \tag{5.5}$$

where $N = 2$ is the number of (real) spin states in graphene. According to Eqn. 5.5, at B=10 T, a temperature below $T \approx 20$ mK would be required to observe this transition, more than a factor of 10 smaller than the temperature used, 280 mK. As a result it is not possible to say that this mechanism is responsible for the generation of an energy gap in the lowest Landau level either.

5.3 Conclusions

In conclusion to this chapter, section 5.2.1 showed that the quantum Hall effect was observable in channels 2, 3, 4 and 7. The main evidence of this is the emergence of peaks in the $R(V,B)$ curves as the strength of the external magnetic field is increased. Tracking the position of these peaks as B is increased showed that the separation between them scales as $\sqrt{B}$ which is characteristic of the relativistic fermions. The remaining 7 conducting channels did not show this behaviour which is most likely because the disorder was too high. A large amount of disorder may cause Landau levels to broaden so much that their separation is no longer detectable, in a sense destroying the quantised behaviour. It was argued in Chapter 3 that the Fermi level of carriers in graphene directly above the contact metal could become pinned at a value different to that in the channel, with a difference large enough that two peaks appear

in the $R(V_g)$ curve. If this is the case, then it follows that carriers above the metallic contacts occupy different filling factors to carriers in the graphene channel, in turn occupying different Landau levels. This would also obscure the $\sqrt{B}$ separation of Landau levels in graphene. Consequently, these channels were not analysed in this chapter.

From the Landau level separation the Fermi velocity was estimated and found to be in good agreement with previous experiments and indicate that electron-electron interactions play a role in transport, since the values of v_F for all channels are larger than the expected bare value, $v_F \approx 0.85 \times 10^6\,\mathrm{ms}^{-1}$.

From the Fermi velocity the cyclotron mass was calculated according to $E = m^* v_F^2$ and plotted as a function of Landau level index. This illustrates that the cyclotron mass varied as both the square root of B and N as expected for graphene. Again, the values of m^* were in good agreement with previous experiments showing that the multiplexing technique can be used to measure intrinsic material properties of graphene in strong magnetic fields, yielding results in agreement with existing work.

Unexpected behaviour was observed in channel 2 which highlights another benefit of the multiplexing approach, that by measuring many samples, 'rare' physics may be observed. It would be expected that by using multiplexing architectures with more than 16 channels, more such unexpected and interesting results would be observed.

The insulating behaviour of channel 2 was investigated by temperature dependent magneto-transport measurements, and by including a DC, source-drain bias into the measurement circuit. Measurements of $R(V_{DC}; V_g, T)$ showed no evidence of Coulomb blockade and the results that prove a Kosterlitz-Thouless transition as presented in Ref. [126] were not reproducible with the present data. As the filling factor approached zero, small reproducible plateaux were observed when $T = 0.28\,\mathrm{K}$ and $B = 10\,\mathrm{T}$. Their possible origin is discussed but no firm evidence proves that they are fractional quantum Hall states, since these states require accurate resistance measurements which is difficult to achieve in two-terminal devices because the series resistance cannot be measured directly. A critical magnetic field of $B_c = 6.4\,\mathrm{T}$ was identified by finding the crossing point of $R(B;T)$ isotherms at the charge neutrality point. Theoretical arguments in Ref. [134] showed that the a gap implies the emergence of a plateau at $\sigma_{xy} = 0$ and a transition into a quantum Hall insulator state, which is the current hypothesis to explain this result. The temperature dependence of the maximum resistivity at $B = 10\,\mathrm{T}$ showed non-monotonic behaviour which is not characteristic of activated behaviour observed elsewhere. As an alternative method, the magnitude of the gap was estimated by fitting a Lorentzian function and a Gaussian function to the $R(V_g)$ curve at $T = 0.28\,\mathrm{K}$ and $B = 10\,\mathrm{T}$. Using this method the magnitude of the gap is estimated to be in the range $18\,\mathrm{meV} < \Delta E < 54\,\mathrm{meV}$. Possible microscopic mechanisms are discussed which

could be responsible for opening a band gap, however this remains unclear since none of the proposed theories matched experimental observations.

Chapter 6

Ongoing Work and Conclusions

6.1 Introduction

This chapter includes results from ongoing multiplexing work, for devices which have not been fully characterised with magneto-transport experiments as device CVD-MUX-A. There are currently three ongoing directions of research: multiplexing mechanically exfoliated 2D materials, multiplexing at room temperature and multiplexing of InAs nanowires. These topics are discussed in the following sections.

6.2 Mechanically exfoliated graphene

Mechanically exfoliated graphene flakes were transferred onto a multiplexer substrate by Shin-Jr Fung of National Cheng Kung University, Taiwan and Luke Smith of the Semiconductor Physics group at the University of Cambridge. Contacts were fabricated using electron beam lithography followed by electron beam evaporation of a 100 nm-thick Cr/Au layer. The contacts were fabricated by Yu-Chiang Hsieh of National Cheng Kung University. Images of the exfoliated flakes placed on the multiplexer are shown in Fig. 6.1.

Eight graphene flakes were transferred onto the multiplexer and six of those channels showed conduction. Measurements were performed by Luke Smith of the Semiconductor Physics Group at the University of Cambridge. A Keithley 2400 source meter was used to apply a DC bias of $-500\,\mathrm{mV}$ which was required to observe the change in R as a function of V_g. The measurements were performed in a ^{4}He dewar at $T = 4.2\,\mathrm{K}$. The channels are all very resistive between $V_g = \pm 20\,\mathrm{V}$, with the maximum resistance ranging between approximately $1.3\,\mathrm{M\Omega}$ in channel 7 and $22.5\,\mathrm{M\Omega}$ in channel 11. Most of this resistance is expected to occur between the graphene flakes and the Cr/Au contacts, although it cannot be ruled out that the

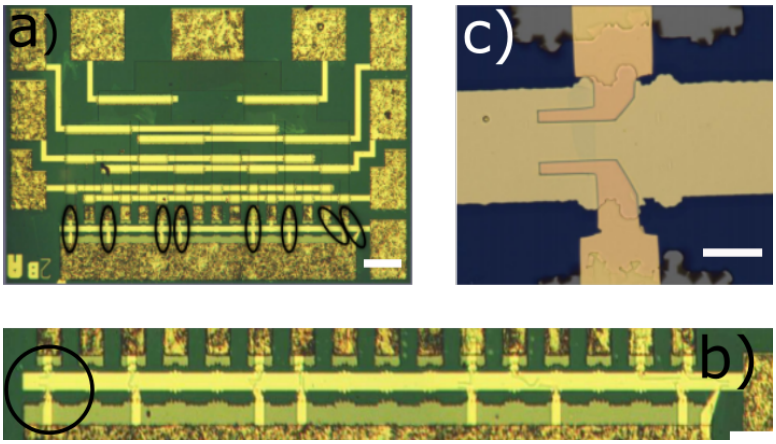

Fig. 6.1 Images of the mechanically exfoliated graphene flakes on a multiplexer device. The entire device is shown in (a), where the black rings indicate where the graphene flakes are placed; scale 250 μm A magnification of the back-gate region is shown in (b) where the e-beam defined contacts can be seen; 100 μm. The region inside the black circle in (b) is shown in (c) where single contacted graphene flake can be seen; scale 15 μm.

multiplexer itself was not the primary source of the observed resistance. Despite the fact that optimisation of the fabrication process is required to reduce the resistance of these devices, these results show that in principle, mechanically exfoliated materials can be transferred onto a multiplexer and electrically characterised. This opens the possibility of studying materials which cannot currently be grown as large-area crystals and transferred through a process similar to CVD-grown graphene.

6.3 Multiplexing at room temperature

Work has been done towards the fabrication of multiplexing devices which are capable of operating at both room temperature and cryogenic temperature. By modifying the fabrication process of the multiplexer it has been shown that it is possible to pinch-off the 2DEG at room temperature. Traditionally, GaAs / $Al_xGa_{1-x}As$ high electron mobility transistors (HEMTs) do not operate at room temperature, because charge carriers are not confined to the quantum well at the GaAs / $Al_xGa_{1-x}As$ interface due to thermal excitation. This allows charge to leak from the heterostructure to surface gates and so the device does not pinch-off when a negative voltage is applied to the gate, and it does not behave as a transistor. This problem was overcome by depositing a 15 nm film of Al_2O_3 over the regions where originally Au addressing gates would make contact with the GaAs surface. Figure 6.3 shows diagrams of the cross section taken perpendicular to two adjacent channels. For example, they represent the cross section taken through the red, dashed line labelled ‘CS’ in Fig. 6.3c. In the diagrams,

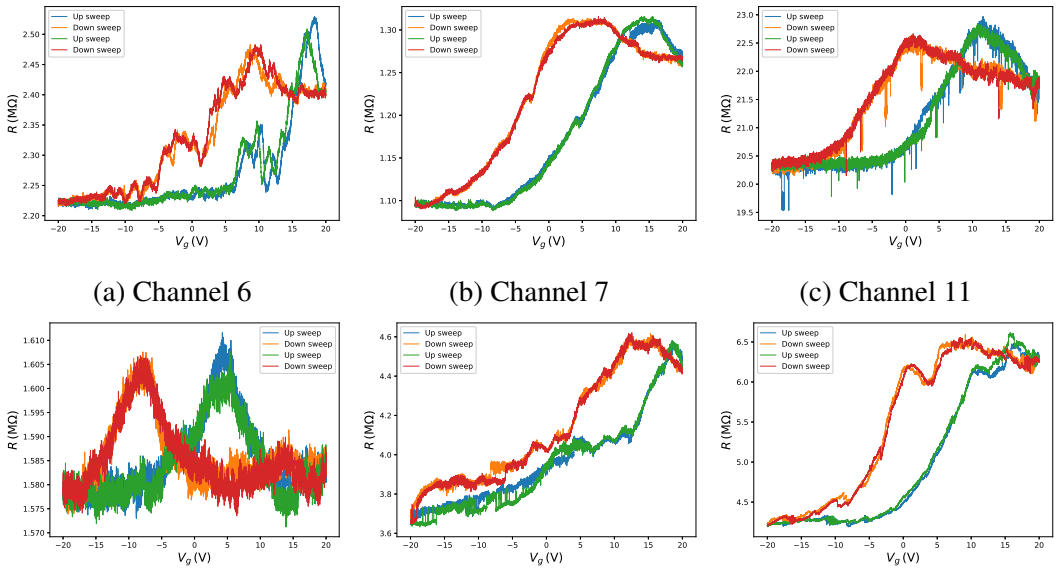

(a) Channel 6 (b) Channel 7 (c) Channel 11

(d) Channel 12 (e) Channel 15 (f) Channel 16

Fig. 6.2 *R-V* characteristics of mechanically exfoliated graphene flakes transferred onto a multiplexer device. Four traces are shown for each channel: two up sweeps and two down sweeps. Data taken at $T = 4.2\,\mathrm{K}$.

the conducting 2DEG is represented by the red horizontal line at the doped AlGaAs / GaAs interface. In reality, there is also a 40 nm spacer layer of undoped AlGaAs below the doped-AlGaAs layer, and there is a 10 nm-thick capping layer of GaAs on top of the doped-AlGaAs layer, which is also 40 nm thick. The undoped AlGaAs layer and GaAs capping layer have been omitted from the diagram for simplicity. Channel A is covered by 15 nm of Al_2O_3 which stops charge leaking from the 2DEG to the Ti/Au gate on the surface at room temperature. At approximately $V = -1.5\,\mathrm{V}$ and at room temperature, the 2DEG in A is depleted and stops conducting but B remains conducting, since this is covered by a total of 110 nm of Al_2O_3. A 10 nm-thick layer was also tested instead of 15 nm, however the channel did not pinch-off at room temperature for these devices and 10 nm was deemed to be too thin to prevent the leakage of charge from the 2DEG to the surface gate.

Figure 6.4 shows the pinch-off and addressing curves for a multiplexer device designed to operate at room temperature. These measurements were performed by Luke Smith of the Semiconductor Physics Group at the University of Cambridge. Figures 6.4a and 6.4b show the multiplexer pinch-off at room temperature and 4.2 K, respectively, as negative voltages are applied to gates B1 and D1. At room temperature the pinch-off voltage is shifted to approximately $V = -1.5\,\mathrm{V}$, from $-0.3\,\mathrm{V}$ at 4.2 K. Changing V_g at room temperature did not result in a change of G, however it did modulate G as normal at 4.2 K. This may be

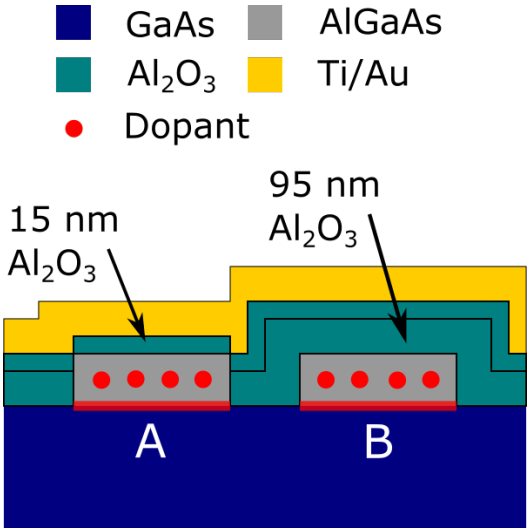

(a) Cross sectional view of two conducting mesa channels, labelled A and B. When the voltage on the surface gate is set to $V = 0\,\mathrm{V}$ both channels conduct.

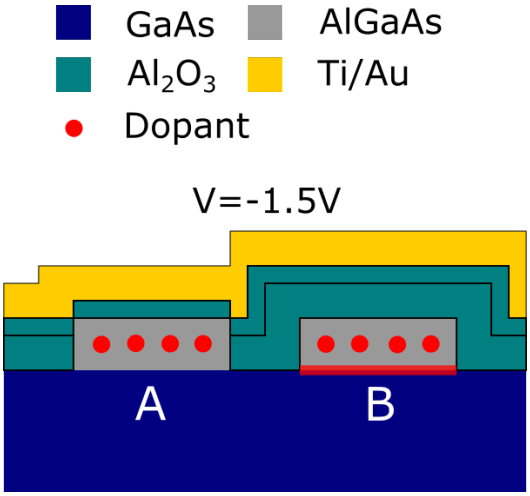

(b) When $V = -1.5\,\mathrm{V}$ on the surface gate at room temperature, charge carriers are depleted from the quantum well A, while B remains conducting

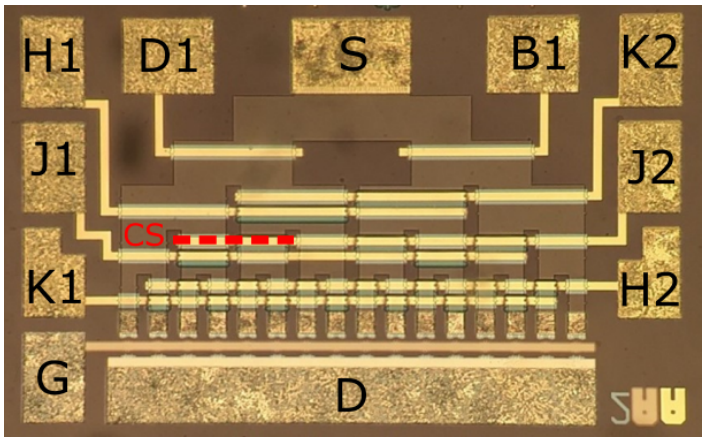

(c) Microscope image of a multiplexer device with a red, dashed line labelled CS to indicate the position of the cross sections illustrated in (a) and (b).

Fig. 6.3 Front, cross-sectional diagrams of the room temperature multiplexer, showing two conducting channels labelled A and B. In this design, two, separate Al_2O_3 layers are deposited, the first 95 nm, the second 15 nm. (a) shows both channels conducting, illustrated by the red horizontal lines at the interface of the doped AlGaAs/GaAs interface; (b) shows a negative voltage applied to the Ti/Au surface gate, which stops A conducting, while B remains conducting.

because the back gate is in contact with the GaAs substrate and charge is able to leak from the substrate to the back gate, thereby removing the potential difference between the back gate and graphene channel. Work is ongoing to modify the design so that the back gate is fully encapsulated in Al_2O_3 and electrically isolated from the substrate. By multiplexing at room temperature it is possible the check if gates are functioning as expected before cooling the device to cryogenic temperature, as well as enabling the investigation of temperature dependent phenomena between room temperature and cryogenic temperature.

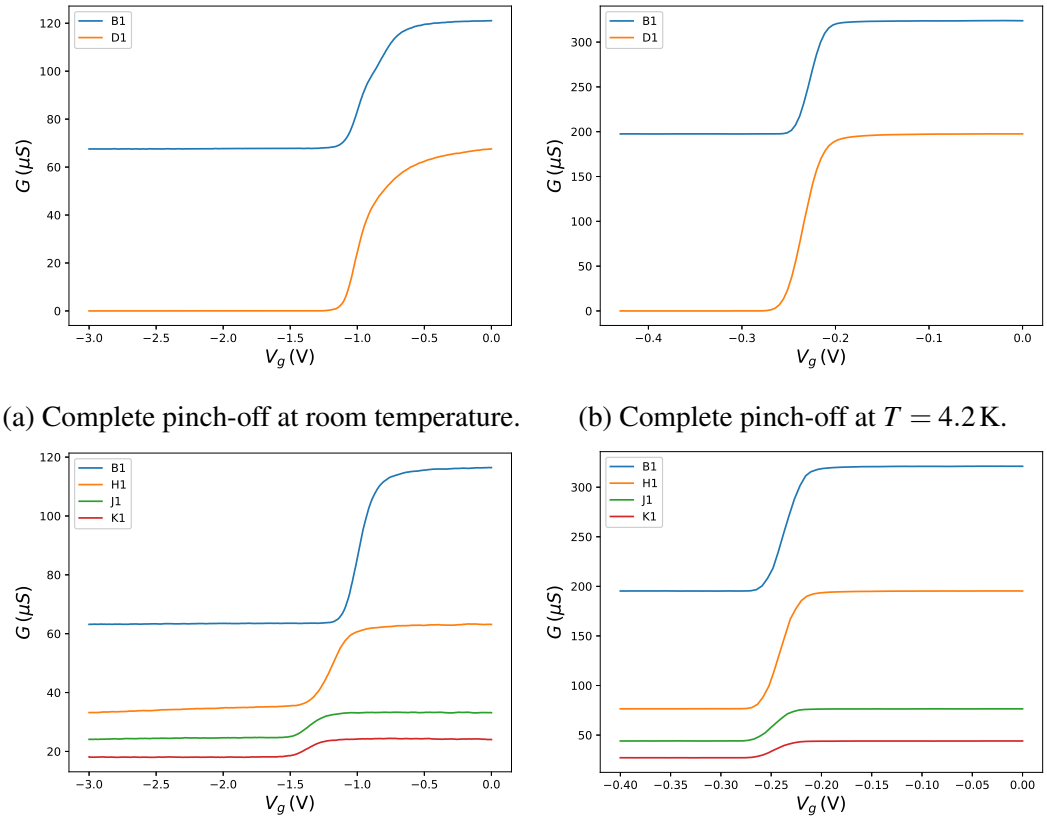

(a) Complete pinch-off at room temperature.

(b) Complete pinch-off at $T = 4.2\,\mathrm{K}$.

(c) Addressing channel 9 at room temperature.

(d) Addressing channel 9 at $T = 4.2\,\mathrm{K}$.

Fig. 6.4 Comparison of a multiplexer device operating at room temperature and 4.2 K. Subfigures (a) and (b) show negative voltages applied to gates B1 and D1 at room temperature and 4.2 K, respectively and the conductance drops to zero in both cases; (c) and (d) show channel 9 being addressed at room temperature and 4.2 K, respectively.

6.4 Indium arsenide nanowires

InAs nanowires grown by Hannah Joyce of the Department of Engineering at the University of Cambridge were transferred onto a multiplexer device by Dimitars Jevtics and Joshua

Robertson of Dr. Antonio Hurtado's research group at the University of Strathclyde. A transfer printing technique was used to position nanowires onto the multiplexer, the details of which can be found in Refs. [229, 230]. Figure 6.5 shows the stages of transferring and contacting InAs nanowires onto the multiplexer device. Electrical contact is made to the InAs nanowires by first etching the native oxide from the nanowire surface with an $(NH_4)_2S$ solution for 10 minutes at 40 °C, followed by sputter deposition of Ni metal. The native oxide etch and Ni deposition was done by Jack Alexander-Webber of the Department of Engineering at the University of Cambridge. Nanowires were originally transferred onto two, different multiplexer devices, one with 16 nanowires with zinc-blende crystal structure, the other with 16 nanowires with wurtzite crystal structure. The multiplexer device containing zinc-blende type nanowires had malfunctioning addressing gates and the electrical characterisation data is not shown here. SEM images were taken of this device and it was found that channels 1-8 were short-circuited due to an unsuccessful lift-off process, while channels 9-16 showed successful lift-off. There was no indication from the SEM images of why the addressing gates did not function as expected. The SEM image in Fig. 6.5 shows a contacted nanowire with zinc-blende crystal structure. The multiplexer containing wurtzite nanowires did function as expected, however channels 1-8 were also short-circuited. Figure 6.6 shows the transfer characteristics of Channels 9, 10, 11, 12, 13, 14 and 16. During the second cool-down, the nanowires became detached from the multiplexer before magneto-transport measurements could be performed, which was confirmed by SEM imaging. From the SEM images, the mean length of channels 9-12 is measured to be 606 nm with a standard deviation of 17 nm; the mean length of channels 13-16 is 401 nm with a standard deviation of 9 nm. The radius of the wurtzite nanowires could not be measured from the SEM images since they had detached from the substrate, however they are known to have a mean diameter of 65 nm from previous size measurements performed by Hannah Joyce.

Channels 9-16 (excluding channel 15) display n-type field-effect transistor behaviour, where the current increases with increasing positive back-gate voltage. Nanowire field-effect transistors are commonly characterised by their mobility μ, the carrier concentration in the saturation region n, the subthreshold swing (SS), the on/off ratio, the contact resistance R_c and the value of the threshold voltage V_t, which can all be calculated from the transfer characteristics in Fig. 6.6. The field-effect mobility of a nanowire on a planar substrate is defined as:

$$\mu_{FE} = \frac{L^2}{C_{ox}} \frac{g_m}{V_{sd}}, \tag{6.1}$$

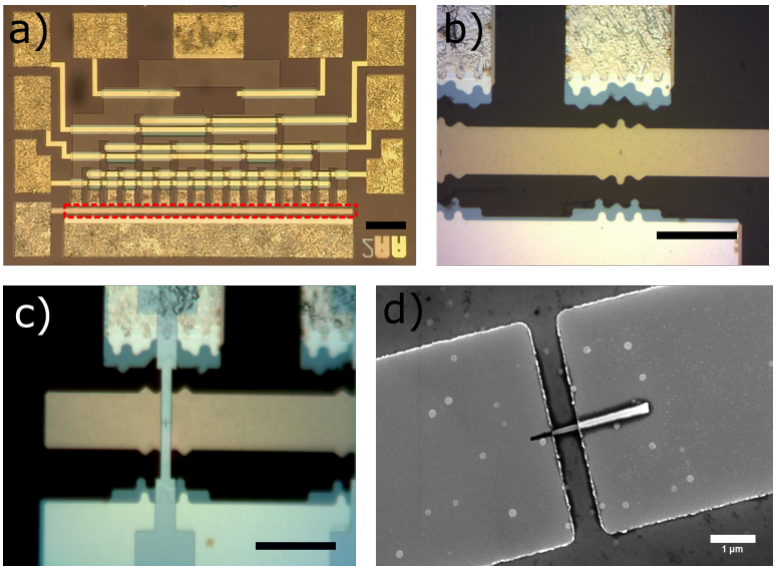

Fig. 6.5 Images of the nanowire transfer and contacting process. Nanowires are transfer printed onto the back-gate, which is the region inside the red box shown in (a). A magnified image of a single nanowire placed on the back gate is shown in (b). Ni contacts are then sputtered onto the nanowire, as shown in (c). An SEM image of a contacted InAs nanowire on the multiplexer is shown in (d). Scale bar represents 250 μm, 50 μm, 50 μm and 1 μm in (a), (b), (c) and (d), respectively.

where $g_m = \partial I_{sd}/\partial V_g$ is the transconductance of the device, $I_{sd} = GV_{sd}$ is the source-drain current, $V_{sd} = 10\,\mu V$ is the rms source-drain voltage, L is the channel length and the gate capacitance C_{ox} is given by a cylinder-on-plane model [231]:

$$C_{ox} = \frac{2\pi\varepsilon_0\varepsilon_r L}{\ln\left(\frac{t_{ox}+r+\sqrt{(t_{ox}+r)^2-r^2}}{r}\right)}. \tag{6.2}$$

In equation 6.2, ε is the dielectric constant, $t_{ox} = 50\,\text{nm}$ is the oxide thickness (not 95 nm as for graphene devices) and r is the radius of the nanowire. The capacitance of channels 9-12, using the channel dimensions stated above is 0.19 fF, and for channels 13-16 the capacitance is 0.13 fF.

The carrier concentration in the saturation region is defined as:

$$n = \frac{C_{ox}}{e\pi r^2 L}\frac{I_{sd}}{g_m}, \tag{6.3}$$

where the value of I_{sd} is taken to be a constant in the saturation region. The subthreshold swing is defined as $SS = (\partial(\log_{10} I_{sd})/\partial V_g)^{-1}$ measured in units of mV/decade and evaluates the gate voltage change required to change the source-drain current by a factor of 10. Similarly,

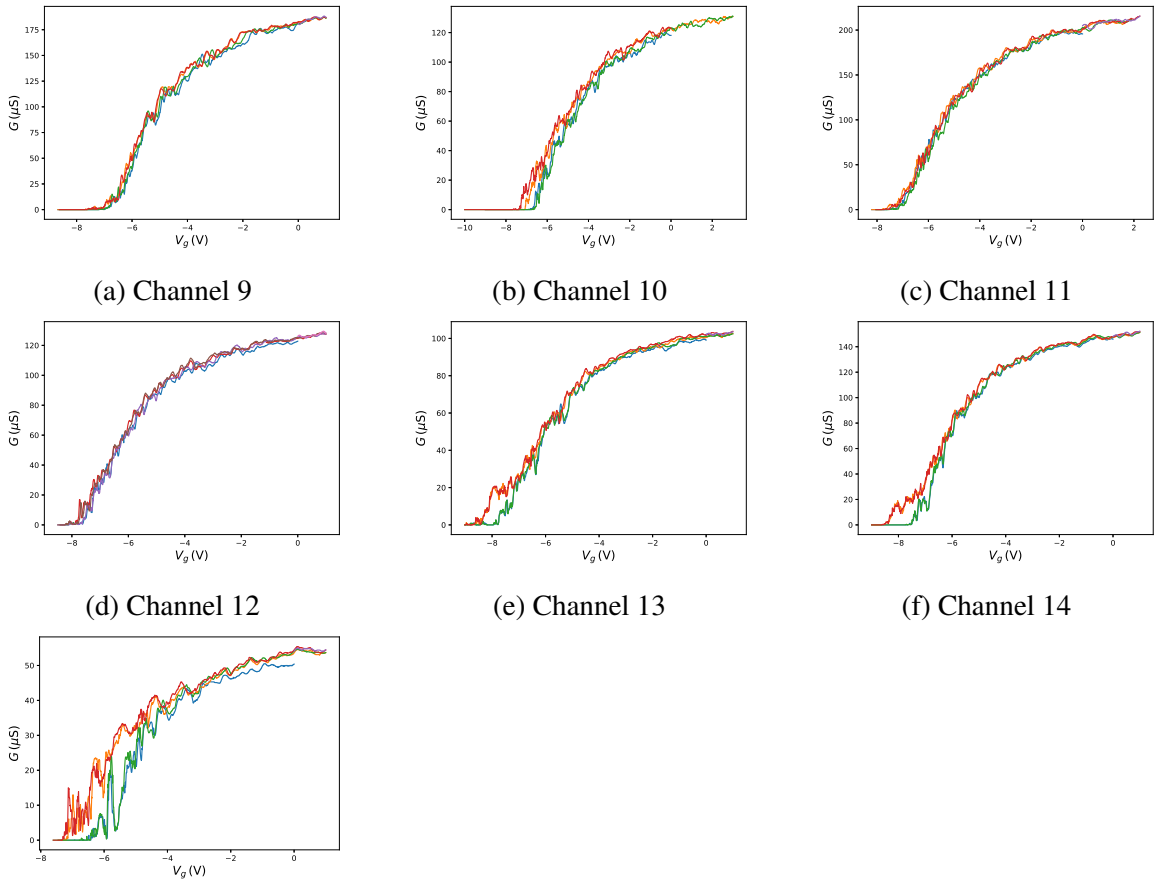

(a) Channel 9

(b) Channel 10

(c) Channel 11

(d) Channel 12

(e) Channel 13

(f) Channel 14

(g) Channel 16

Fig. 6.6 Transfer characteristics of multiplexed InAs nanowires. Repeat traces are shown for all channels. Measurements performed at $T = 4.2\,\mathrm{K}$.

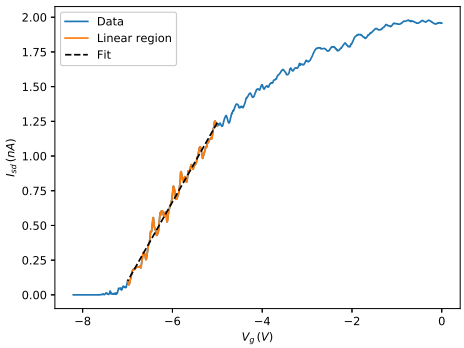

(a) Plot of $I_{sd} - V_g$, the blue curve represents the data and the orange section highlights the linear operating region of the device. The black dashed line is a linear fit used to calculate g_m.

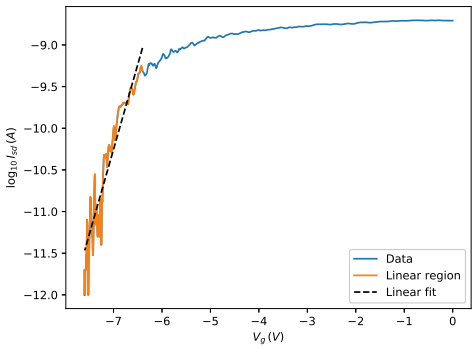

(b) Plot of $\log_{10} I_{sd} - V_g$, the blue curve represents the data and the orange section highlights the linear operating region of the device. The black dashed line is a linear fit used to calculate SS.

Fig. 6.7 Plots of $I_{sd} - V_g$ and $\log_{10} I_{sd} - V_g$ showing the linear regions of the device and the linear fits used to calculate the g_m in the case of sub-figure (a) and SS in sub-figure (b).

the on/off ratio is measured in decades and describes how many orders of magnitude the source-drain current changes by. When the current is zero the logarithm of the current diverges and so the value of $\log_{10} I_{sd}(V = V_t)$ is read off from the plot of $\log_{10} I_{sd}$-V. Figure 6.7 shows an example of fitting to the linear region of the I_{sd}-V curve and $\log_{10} I_{sd}$-V curve.

The values in Table 6.1 are in good agreement with different studies which use similar nanowires [231, 232]. These results show that the multiplexer is not limited to 2D materials but also quasi-1D materials. Currently, the nanowire transfer is a manual process meaning that placing large numbers of nanowires onto a large multiplexer array would be time consuming and would somewhat undermine the reduction in measurement time gained from using a multiplexing approach. However, advances in automated transfer systems, similar to those developed for 2D crystals [233] would solve this drawback.

Currently, 16 new nanowires have been transferred onto another multiplexer device, and the contacts on all 16 channels appear to have successfully lifted-off. A second Al_2O_3 layer has been deposited on top of the nanowires in order to encapsulate them, with the intention of preventing the nanowires from detaching from the surface as a result of thermal cycling.

Channel	μ ($cm^2V^{-1}s^{-1}$)	n ($10^{17}cm^{-3}$)	SS (mV/dec)	on/off (dec)	R_c (kΩ)	$V_{t,up}$ (V)	$V_{t,down}$ (V)	ΔV (V)
9	930	13.1	231.04	3.26	5.77	-7.01	-7.24	0.23
10	709	11.2	119.00	3.07	8.49	-6.71	-7.10	0.39
11	1,085	12.1	386.58	3.29	5.62	-7.61	-7.82	0.21
12	672	12.2	330.42	3.09	8.18	-6.71	-7.78	1.07
13	350	8.3	34.96	3.00	10.17	-7.78	-8.48	0.70
14	663	6.46	114.61	3.16	6.97	-7.50	-8.63	1.13
16	223	6.52	1,444.06	2.70	20.12	-6.42	-7.16	0.74
Mean	662	10.0	380.1	3.08	9.33	-7.11	-7.74	0.64
Std	228	2.8	485.54	0.20	5.02	0.53	0.62	0.38

Table 6.1 The calculated values of mobility, carrier density, subthreshold swing, on/off ratio, contact resistance and threshold voltage in the up/down sweep directions and the hysteresis.

6.5 Thesis conclusions

An end-to-end account of the development and assessment of multiplexing technology, capable of electrically characterising nanomaterials at cryogenic temperature has been presented. The primary result is that CVD-grown graphene, mechanically exfoliated graphene and InAs nanowires can be incorporated as field effect transistors into an GaAs / $Al_xGa_{1-x}As$ on-chip multiplexing circuit. Specifically, CVD-grown graphene has been incorporated into an on-chip multiplexing device and has been characterised in cryogenic transport experiments, in magnetic fields up to 10 T, as well as by SEM imaging and Raman spectroscopy. In the absence of a magnetic field, the Dirac voltage, V_d, mobility μ, contact resistance R_c and intrinsic carrier density n_0 were estimated using established models of $R(V_g)$. These values were similar over two separate cool-downs, demonstrating that the results obtained from multiplexed GFETs are reproducible. The values of V_d, μ and n_0 obtained from modelling were contestant with the values reported elsewhere in the literature, which demonstrates that the data obtained from using the multiplexing technique can be interpreted in terms of existing results. This is an important proof-of-principle and one of the primary objectives of this work. Care must be taken when accounting for the series resistance however, since the 2DEG in the multiplexer makes the series resistance dependent upon B. So far this has been accounted for by modelling the contact resistance, since there is no way to directly measure the contact resistance in this design. The inability to directly measure the contact resistance is inherent to two-terminal transistors, therefore it is difficult to use this multiplexer design to

probe phenomena which require an estimation of the contact resistance to a high degree of accuracy, for example measuring fractional quantum Hall states, as discussed in Chapter 5.

In Chapter 4 the scattering processes were investigated by analysing the weak localisation signal and the conductance fluctuations in all conducting channels. The value of the L_ϕ and τ_ϕ^{-1} were in agreement with values reported in other experiments which implies that the multiplexing technique does not cause the intrinsic properties of the CVD-graphene to change by a significant amount. Since the mobility of the multiplexer 2DEG is approximately $8 \times 10^5\,\mathrm{cm^2V^{-1}s^{-1}}$ (determined from separate Hall bar measurements, not reported here), the dephasing length in the 2DEG is expected to far exceed the dephasing length in graphene, that is $L_{\phi,2DEG} \gg L_{\phi,Gr}$. This makes $L_{\phi,Gr}$ the dominant length scale over which dephasing occurs, so dephasing of carriers in the 2DEG is not expected to affect the measured values of L_ϕ.

The measured value of L_ϕ was found to be significantly affected by the method employed to measure the weak localisation signal. When an averaging procedure is used, the mean value of L_ϕ was approximately 260 nm, when an averaging procedure was not used the mean value of L_ϕ was approximately 350 nm. Using a multiplexing approach to collect data from multiple devices made it possible to compare the two methods using statistical tests, where the difference between methods was confirmed. This result highlights a benefit of the multiplexing approach, and similar statistical tests are expected to become more beneficial when using larger multiplexer arrays.

The amplitude of the conductance fluctuations in all experiments were small, of the order of 0.01 μS, much less than the universal value of e^2/h, although universality is debated in graphene. It was found that using the autocorrelation of the fluctuations to calculate L_ϕ predicted very similar values for all conducting channels which may be an indication of statistical bias. It is speculated that this occurs because the amplitude of the fluctuations are too weak. The primary reason for such small fluctuations are that the device dimensions are much larger than L_ϕ; stronger fluctuations signals would could be observed by reducing the dimensions of the graphene channel, which would be achieved using electron beam lithography.

In the final section of Chapter 4 it was shown that the primary dephasing mechanism in channels 1, 2, and 3 was high-frequency, quasi-elastic electron-electron interactions.

In strong magnetic fields, the quantum Hall effect was observed in 4 of the 11 conducting channels, that is 36%. From the Landau level spacing, the Fermi velocity of carriers was calculated, with values larger than the bare value in the absence of electron-electron interactions. This was evidence of Fermi velocity renormalisation due to many-body interactions which was consistent with the finding in Chapter 4, that electron-electron interactions were

the primary cause of phase decoherence. From the Fermi velocities, the cyclotron mass was calculated and shown to scale as the square root of the Landau level index. This is conclusive proof of the relativistic properties of the graphene channels and demonstrates that fundamental material properties can be measured within the multiplexing circuit.

Channel 2 showed a transition into an insulating state in strong magnetic fields and low temperature. Temperature independent crossing points of $R(V_G)$ curves are indirect evidence of a plateau forming at $\nu = 0$ which subsequently implies a transition into a quantum Hall insulator state. The microscopic mechanism behind this transition could not be determined, however it could be expected that a many-body interaction is responsible for lifting the 4-fold degeneracy of the zero Landau level and opening an energy gap. It is reasonable to expect many-body effects are relevant because they have been shown to cause particle dephasing and Fermi velocity renormalisation. This unexpected observation highlights the benefit of the multiplexing approach, that unexpected physics may be observed; with larger multiplexing arrays it is expected that more such observations would be made.

Together, these experiments demonstrate that on-chip multiplexing can be used as a useful tool for increasing the throughput of magneto-transport experiments of CVD-grown graphene. One of the largest challenges to multiplexing CVD-graphene was optimising the transfer process. Many devices did not conduct due to cracking and breakage of the graphene channels. As mentioned in Chapter 2, briefly immersing the device in IPA solvent after transferring the PMMA-graphene film onto multiplexer helped reduce the formation of bubbles and reduce breakage in the channels. Further investigation into the transfer process is required so that this process can be optimised, then the process can be up-scaled onto a 128-output multiplexer device. A systematic investigation into the wetting properties of the back gate may help to optimise the wet transfer process.

As discussed earlier in this chapter, work is ongoing to extend the capabilities of this multiplexing technology. Perhaps most the most promising direction is the incorporation of InAs nanowires into the on-chip multiplexing circuit, since 9 nanowires were successfully characterised upon the first attempt, and shown to have properties comparable to those reported elsewhere. A new device has been shown to have no short-circuited channels and it is believed that encapsulation will prevent the nanowires detaching from the substrate between cool-downs. Once this has achieved the process will be reliable and the device can be up-scaled. Additionally, the device fabrication process can easily be changed so that the back gate is electrically isolated from the substrate, which is believed will permit room temperature device operation.

In all, substantial progress towards achieving scalable, on-chip multiplexing technology, capable of electrically characterising nanomaterials at cryogenic temperature and in strong

magnetic fields has been made. The experiments contained in this thesis demonstrate the reproducibility of data obtained by this method, by repeat experiments and through comparison to existing literature. Furthermore, it has been shown that statistical tests can be used in conjunction with the data gathered using a multiplexing technique to gain a deeper insight into experimental results. For these reasons, on-chip multiplexing presents itself as a valuable technique which can be used to accelerate the development of emerging nanomaterial, quantum electronic devices.

References

[1] S.B. Weinstein and P.M. Ebert. Data Transmission by Frequency-Division Multiplexing Using the Discrete Fourier Transform. *IEEE Transactions on Communications Technology*, 19(5):628–634, 1971.

[2] Amitabha Banerjee, Youngil Park, Frederick Clarke, Huan Song, Glen Kramer, and Kwangjoon Kim. Wavelength-division-multiplexed passive optical network (WDM-PON) technologies for broadband access : a review [Invited]. *Journal of Optical Networking*, 4(11):737–758, 2005.

[3] Yurii Vlasov, William M J Green, and Fengnian Xia. High-throughput silicon nanophotonic wavelength-insensitive switch for on-chip optical networks. *Nature Photonics*, 2:242–246, 2008.

[4] Yunhong Ding, Jing Xu, Francesco Da Ros, Bo Huang, Haiyan Ou, and Christophe Peucheret. On-chip two-mode division multiplexing using tapered directional coupler-based mode multiplexer and demultiplexer. *Optics Express*, 21(8):10376–10382, 2013.

[5] M J Collins, C Xiong, I H Rey, T D Vo, J He, S Shahnia, C Reardon, T F Krauss, M J Steel, A S Clark, and B J Eggleton. Integrated spatial multiplexing of heralded single-photon sources. *Nature Communications*, 4(2582):1–7, 2013.

[6] Nicholas C Harris, Davide Grassani, Angelica Simbula, Mihir Pant, Matteo Galli, Tom Baehr-jones, Michael Hochberg, Dirk Englund, Daniele Bajoni, and Christophe Galland. Integrated Source of Spectrally Filtered Correlated Photons for Large-Scale Quantum Photonic Systems. *Physical Review X*, 4(4):1–10, 2014.

[7] D. Grassani, S. Azzini, M. Liscdini, M.Galli, M.J. Strain, M.Sorel, J.E. Sipe, and D. Bajoni. Micrometer-scale integrated silicon source of time-energy entangled photons. *Optica*, 2(2):88–94, 2015.

[8] Philip J Poole, Iman Esmaeil Zadeh, Andreas Fognini, Michael E Reimer, Dan Dalacu, Val Zwiller, and Klaus D Jöns. On-chip single photon filtering and multiplexing in hybrid quantum photonic circuits. *Nature Communications*, 8(379):1–8, 2017.

[9] T.-M Chen, A C Graham, M Pepper, I Farrer, and D A Ritchie. Bias-controlled spin polarization in quantum wires Spin current source based on a quantum point contact with local spin-orbit interaction Bias-controlled spin polarization in quantum wires. *Citation: Appl. Phys. Lett. Applied Physics Letters Applied Physics Letters*, 931(10), 2008.

[10] T Ã Chen, A C Graham, M Pepper, I Farrer, and D A Ritchie. Spontaneous spin polarisation in one dimension under finite DC-bias. *Physica E*, 40(5):1295–1297, 2008.

[11] T. M. Chen, M. Pepper, I. Farrer, G. A C Jones, and D. A. Ritchie. All-electrical injection and detection of a spin-polarized current using 1D conductors. *Physical Review Letters*, 109(17), 2012.

[12] Pojen Chuang, Sheng-chin Ho, L W Smith, F S, M Pepper, Chin-hung Chen, Ju-chun Fan, J P Grif, I Farrer, H E Beere, G A C Jones, D A Ritchie, and Tse-ming Chen. All-electric all-semiconductor spin field-effect transistors. *Nature Nanotechnology*, 10(January):35–39, 2015.

[13] Daniel Loss and David P. DiVincenzo. Quantum computation with quantum dots. *Physical Review A - Atomic, Molecular, and Optical Physics*, 57(1):120–126, 1998.

[14] T Hayashi, T Fujisawa, H D Cheong, Y H Jeong, and Y Hirayama. Coherent Manipulation of Electronic States in a Double Quantum Dot. *Physical Review Letters*, 91(22):1–4, 2003.

[15] R Hanson. Spins in few-electron quantum dots. *Reviews of Modern Physics*, 79:1217–1265, 2007.

[16] M J Kelly. Intrinsic top-down unmanufacturability. *Nanotechnology*, 24:1–2, 2011.

[17] M J Kelly and M C Dean. A specific nanomanufacturing challenge. *Nanotechnology*, 27(11), 2016.

[18] H. Al-Taie, L. W. Smith, B. Xu, P. See, J. P. Griffiths, H. E. Beere, G. A.C. C Jones, D. A. Ritchie, M. J. Kelly, and C. G. Smith. Cryogenic on-chip multiplexer for the study of quantum transport in 256 split-gate devices. *Applied Physics Letters*, 102(24), 2013.

[19] Q.Z. Yang, M.J. Kelly, I. Farrer, and G.A.C. Jones. The potential of split-gate transistors as one-dimensional electron waveguides revealed through the testing and analysis of yield and reproducibility. *Applied Physics Letters*, 95(3):10–13, 2009.

[20] L. W. Smith, H. Al-Taie, F. Sfigakis, P. See, A. A.J. Lesage, B. Xu, J. P. Griffiths, H. E. Beere, G. A.C. Jones, D. A. Ritchie, M. J. Kelly, and C. G. Smith. Statistical study of conductance properties in one-dimensional quantum wires focusing on the 0.7 anomaly. *Physical Review B - Condensed Matter and Materials Physics*, 90(4), 2014.

[21] L. W. Smith, H. Al-Taie, A. A J Lesage, F. Sfigakis, P. See, J. P. Griffiths, H. E. Beere, G. A C Jones, D. A. Ritchie, A. R. Hamilton, M. J. Kelly, and C. G. Smith. Dependence of the 0.7 anomaly on the curvature of the potential barrier in quantum wires. *Physical Review B - Condensed Matter and Materials Physics*, 2015.

[22] L. W. Smith, H. Al-Taie, A. A.J. Lesage, K. J. Thomas, F. Sfigakis, P. See, J. P. Griffiths, I. Farrer, G. A.C. Jones, D. A. Ritchie, M. J. Kelly, and C. G. Smith. Effect of Split Gate Size on the Electrostatic Potential and 0.7 Anomaly within Quantum Wires on a

Modulation-Doped GaAs/AlGaAs Heterostructure. *Physical Review Applied*, 5(4), 2016.

[23] K J Thomas, J T Nicholls, M Y Simmons, M Pepper, D R Mace, and D A Ritchie. Possible Spin Polarization in a One-Dimensional Electron Gas. *Physical Review Letters*, 77(1):135–138, 1996.

[24] A.P. Micholich. What lurks below the last plateau : experimental studies of the 0 . 7 × 2 e 2 / h conductance anomaly in one-dimensional systems. *Journal of Physics Condensed Matter*, 23(44), 2011.

[25] C Scho, L Hofstetter, S Csonka, and J Nyga. Cooper pair splitter realized in a two-quantum-dot Y-junction. *Nature*, 461:960–963, 2009.

[26] T W Larsen, K D Petersson, F Kuemmeth, T S Jespersen, P Krogstrup, J Nygård, and C M Marcus. Semiconductor-Nanowire-Based Superconducting Qubit. *Physical Review Letters*, 115(12):1–5, 2015.

[27] Giuseppe Iannaccone, Francesco Bonaccorso, Luigi Colombo, and Gianluca Fiori. Quantum engineering of transistors based on 2D materials heterostructures. *Nature Nanotechnology*, 13(March):183–191, 2018.

[28] A. H. Castro Neto, F. Guinea, N. M.R. Peres, K. S. Novoselov, and A. K. Geim. The electronic properties of graphene. *Reviews of Modern Physics*, 81(1):109–162, 2009.

[29] P.R. Wallace. The Band Theory of Graphite. *Physical Review*, 71(9):622 – 634, 1946.

[30] Gordon W. Semenoff. Condensed-Matter simulation of a three-Dimensional anomaly. *Physical Review Letters*, 53(26):2449–2452, 1984.

[31] M. I. Katsnelson. Zitterbewegung, chirality, and minimal conductivity in graphene. *European Physical Journal B*, 51(2):157–160, 2006.

[32] J. Tworzydło, B. Trauzettel, M. Titov, A. Rycerz, and C. W.J. Beenakker. Sub-poissonian shot noise in graphene. *Physical Review Letters*, 96(24):1–4, 2006.

[33] K. S. Novoselov, A. K. Geim, S. V. Morozov, D. Jiang, M. I. Katsnelson, I. V. Grigorieva, S. V. Dubonos, and A. A. Firsov. Two-dimensional gas of massless Dirac fermions in graphene. *Nature*, 438(7065):197–200, 2005.

[34] Y. W. Tan, Y. Zhang, K. Bolotin, Y. Zhao, S. Adam, E. H. Hwang, S. Das Sarma, H. L. Stormer, and P. Kim. Measurement of scattering rate and minimum conductivity in graphene. *Physical Review Letters*, 99(24):10–13, 2007.

[35] Vadim V. Cheianov and Vladimir I. Fal'ko. Friedel oscillations, impurity scattering, and temperature dependence of resistivity in graphene. *Physical Review Letters*, 97(22):1–4, 2006.

[36] Shaffique Adam, E. H. Hwang, V. M. Galitski, and S. Das Sarma. A self-consistent theory for graphene transport. *Proceedings of the National Academy of Sciences of the United States of America*, 104(47):18392–18397, 2007.

[37] E. H. Hwang, S. Adam, and S. Das Sarma. Carrier transport in two-dimensional graphene layers. *Physical Review Letters*, 98(18):2–5, 2007.

[38] Kentaro Nomura and A. H. MacDonald. Quantum transport of massless dirac fermions. *Physical Review Letters*, 98(7):1–4, 2007.

[39] Kentaro Nomura and Allan H. MacDonald. Quantum hall ferromagnetism in graphene. *Physical Review Letters*, 96(25):1–5, 2006.

[40] Tsuneya Ando. Screening effect and impurity scattering in monolayer graphene. *Journal of the Physical Society of Japan*, 75(7):1–7, 2006.

[41] Eduardo Fradkin. Critical behavior of disordered degenerate semiconductors. II. Spectrum and transport properties in mean-field theory. *Physical Review B*, 33(5):3263–3268, 1986.

[42] Patrick A Lee. Localized States in a d-Wave Superconductor. *Physical Review Letters*, 71(12):1887–1890, 1993.

[43] Andreas W.W. Ludwig, Matthew P.A. Fisher, R. Shankar, and G. Grinstein. Integer quantum Hall transition: An alternative approach and exact results. *Physical Review B*, 50(11):7526–7552, 1994.

[44] Nguyen Hong Shon and Tsuneya Ando. Quantum Transport in Two-Dimensional Graphite System. *Journal of the Physical Society of Japan*, 67(7):2421–2429, 1998.

[45] N. M.R. Peres, F. Guinea, and A. H. Castro Neto. Electronic properties of disordered two-dimensional carbon. *Physical Review B - Condensed Matter and Materials Physics*, 73(12):1–23, 2006.

[46] J. Martin, N. Akerman, G. Ulbricht, T. Lohmann, J. H. Smet, K. Von Klitzing, and A. Yacoby. Observation of electron-hole puddles in graphene using a scanning single-electron transistor. *Nature Physics*, 4(2):144–148, 2008.

[47] Victor M. Galitski, Shaffique Adam, and S. Das Sarma. Statistics of random voltage fluctuations and the low-density residual conductivity of graphene. *Physical Review B - Condensed Matter and Materials Physics*, 76(24):1–7, 2007.

[48] Vadim V. Cheianov, Vladimir I. Fal'ko, Boris L. Altshuler, and Igor L. Aleiner. Random resistor network model of minimal conductivity in graphene. *Physical Review Letters*, 99(17):1–4, 2007.

[49] Maxim Trushin and John Schliemann. Minimum electrical and thermal conductivity of graphene: A quasiclassical approach. *Physical Review Letters*, 99(21):5–8, 2007.

[50] J Chen, C Jang, S Adam, M S Fuhrer, E D Williams, and M Ishigami. Charged-impurity scattering in graphene. *Nature Physics*, 4:377–381, 2008.

[51] D. S. Novikov. Numbers of donors and acceptors from transport measurements in graphene. *Applied Physics Letters*, 91(10), 2007.

[52] Gerd Bergmann. Physical interpretation of weak localization: A time-of-flight experiment with conduction electrons. *Physical Review B*, 28(6):2914–2920, 1983.

[53] E. Abrahams, P. W. Anderson, D. C. Licciardello, and T. V. Ramakrishnan. Scaling theory of localization: Absence of quantum diffusion in two dimensions. *Physical Review Letters*, 42(10):673–676, 1979.

[54] P. W. Anderson, E. Abrahams, and T. V. Ramakrishnan. Possible explanation of nonlinear conductivity in thin-film metal wires. *Physical Review Letters*, 43(10):718–720, 1979.

[55] L.P. Gorkov, A.I. Larkin, and D.E. Khmelnitskii. Particle conductivity in a two-dimensional random potential. *JEPT Letters*, 30(4):248–252, 1979.

[56] G. J. Dolan and D. D. Osheroff. Nonmetallic conduction in thin metal films at low temperatures. *Physical Review Letters*, 43(10):721–724, 1979.

[57] B.L. Altshuler, D.E. Khmelnitskii, A.I. Larkin, and P.A. Lee. Magnetoresistance and Hall effect in a disordered two-dimensional electron gas. *Physical Review B*, 22(11):5412–5153, 1980.

[58] S. Hikami, A. I. Larkin, and Y. Nagaoka. Spin-Orbit Interaction and Magnetoresistance in the Two Dimensional Random System. *Progress of Theoretical Physics*, 63(2):707–710, 1980.

[59] G. Bergmann. Weak localization in thin films: a time-of-flight experiment with conduction electrons. *Physica Scripta*, 1986(T14):99, 1986.

[60] Tsuneya Ando and Takeshi Nakanishi. Impurity Scattering in Carbon Nanotubes - Absence of Back Scattering, 1998.

[61] T. Ando, T. Nakanishi, and R. Saito. Berry's Phase and Absence of Back Scattering in Carbon Nanotubes. *Journal of the Physical Society of Japan*, 67(8):2857–2862, 1998.

[62] Hidekatsu Suzuura and Tsuneya Ando. Crossover from Symplectic to Orthogonal Class in a Two-Dimensional Honeycomb Lattice. *Physical Review Letters*, 89(26):1–4, 2002.

[63] M Berry. Quantal phase factors accompanying adiabatic changes. *Proceedings of the Royal Society*, 392:45–57, 1983.

[64] E. Mccann, K. Kechedzhi, Vladimir I. Fala'Ko, H. Suzuura, T. Ando, and B. L. Altshuler. Weak-localization magnetoresistance and valley symmetry in graphene. *Physical Review Letters*, 2006.

[65] A. F. Morpurgo and F. Guinea. Intervalley scattering, long-range disorder, and effective time-reversal symmetry breaking in graphene. *Physical Review Letters*, 97(19):1–4, 2006.

[66] S. V. Morozov, K. S. Novoselov, M. I. Katsnelson, F. Schedin, L. A. Ponomarenko, D. Jiang, and A. K. Geim. Strong suppression of weak localization in graphene. *Physical Review Letters*, 2006.

[67] F. V. Tikhonenko, D. W. Horsell, R. V. Gorbachev, and A. K. Savchenko. Weak localization in graphene flakes. *Physical Review Letters*, 2008.

[68] Dong Keun Ki, Dongchan Jeong, Jae Hyun Choi, Hu Jong Lee, and Kee Su Park. Inelastic scattering in a monolayer graphene sheet: A weak-localization study. *Physical Review B - Condensed Matter and Materials Physics*, 78(12):1–5, 2008.

[69] Yung Fu Chen, Myung Ho Bae, Cesar Chialvo, Travis Dirks, Alexey Bezryadin, and Nadya Mason. Magnetoresistance in single-layer graphene: Weak localization and universal conductance fluctuation studies. *Journal of Physics Condensed Matter*, 22(20), 2010.

[70] Helin Cao, Qingkai Yu, L. A. Jauregui, J. Tian, W. Wu, Z. Liu, R. Jalilian, D. K. Benjamin, Z. Jiang, J. Bao, S. S. Pei, and Yong P. Chen. Electronic transport in chemical vapor deposited graphene synthesized on Cu: Quantum Hall effect and weak localization. *Applied Physics Letters*, 96(12):28–31, 2010.

[71] Luis A Jauregui, Helin Cao, Wei Wu, Qingkai Yu, and Yong P Chen. Electronic properties of grains and grain boundaries in graphene grown by chemical vapor deposition. *Solid State Communications*, 151(16):1100–1104, 2011.

[72] Qingkai Yu, Luis A. Jauregui, Wei Wu, Robert Colby, Jifa Tian, Zhihua Su, Helin Cao, Zhihong Liu, Deepak Pandey, Dongguang Wei, Ting Fung Chung, Peng Peng, Nathan P. Guisinger, Eric A. Stach, Jiming Bao, Shin Shem Pei, and Yong P. Chen. Control and characterization of individual grains and grain boundaries in graphene grown by chemical vapour deposition. *Nature Materials*, 10(6):443–449, 2011.

[73] Xiaochang Miao, Sefaattin Tongay, and Arthur F. Hebard. Strain-induced suppression of weak localization in CVD-grown graphene. *Journal of Physics Condensed Matter*, 24(47):0–6, 2012.

[74] X. C. Yang, H. M. Wang, T. R. Wu, F. Q. Huang, J. Chen, X. X. Kang, Z. Jin, X. M. Xie, and M. H. Jiang. Magnetotransport of polycrystalline graphene: Shubnikov-de Haas oscillation and weak localization study. *Applied Physics Letters*, 102(23), 2013.

[75] C. Berger, X. Wu, N. Brown, C. Naud, X. Li, Z. Song, D. Mayou, T. Li, J. Hass, A. Marchenkov, E. H. Conrad, P. N. First, and W. a. De Heer. Electronic Confinement and Coherence in Patterned Epitaxial Graphene. *Science*, 312(May):1191–1196, 2006.

[76] Xiaosong Wu, Xuebin Li, Zhimin Song, Claire Berger, and Walt A. De Heer. Weak antilocalization in epitaxial graphene: Evidence for chiral electrons. *Physical Review Letters*, 98(13):2–5, 2007.

[77] Samuel Lara-Avila, Alexander Tzalenchuk, Sergey Kubatkin, Rositza Yakimova, T. J.B.M. Janssen, Karin Cedergren, Tobias Bergsten, and Vladimir Fal'Ko. Disordered Fermi liquid in epitaxial graphene from quantum transport measurements. *Physical Review Letters*, 107(16):1–5, 2011.

[78] A. M.R. Baker, J. A. Alexander-Webber, T. Altebaeumer, T. J.B.M. Janssen, A. Tzalenchuk, S. Lara-Avila, S. Kubatkin, R. Yakimova, C. T. Lin, L. J. Li, and R. J. Nicholas. Weak localization scattering lengths in epitaxial, and CVD graphene. *Physical Review B - Condensed Matter and Materials Physics*, 86(23):5–9, 2012.

[79] A. M.R. Baker, J. A. Alexander-Webber, T. Altebaeumer, S. D. McMullan, T. J.B.M. Janssen, A. Tzalenchuk, S. Lara-Avila, S. Kubatkin, R. Yakimova, C. T. Lin, L. J. Li, and R. J. Nicholas. Energy loss rates of hot Dirac fermions in epitaxial, exfoliated, and CVD graphene. *Physical Review B - Condensed Matter and Materials Physics*, 87(4):3–8, 2013.

[80] Gabriele F Giuliani and John J Quinn. Lifetime of a quasiparticle in a two-dimensional electron gas. *Phys. Rev. B*, 26(8):4421–4428, 10 1982.

[81] E. Abrahams, P.W. Anderson, P.A. Lee, and T. V. Ramakrishnan. Quasiparticle lifetime in disordered two-dimensional metals. *Physical Review B*, 24(12), 1981.

[82] H. Fukuyama and E. Abrahams. Inelastic Scattering Time in Disordered Metals. *Physical Review Applied*, 27(10):2865–2867, 1983.

[83] B. L. Altshuler, A. G. Aronov, and D. E. Khmelnitsky. Effects of electron-electron collisions with small energy transfers on quantum localisation. *Journal of Physics C: Solid State Physics*, 15(36):7367–7386, 1982.

[84] R. Taboryski and P. E. Lindelof. Weak localisation and electron-electron interactions in modulation-doped GaAs/AlGaAs heterostructures. *Semiconductor Science and Technology*, 5(9):933–946, 1990.

[85] J. E. Hansen, R. Taboryski, and P. E. Lindelof. Weak localization in a GaAs heterostructure close to population of the second subband. *Physical Review B*, 47(23):16040–16043, 1993.

[86] F. V. Tikhonenko, A. A. Kozikov, A. K. Savchenko, and R. V. Gorbachev. Transition between electron localization and antilocalization in graphene. *Physical Review Letters*, 103(22):1–4, 2009.

[87] C. P. Umbach, S. Washburn, R. B. Laibowitz, and R. A. Webb. Magnetoresistance of small, quasi-one-dimensional, normal-metal rings and lines. *Physical Review B*, 30(7):4048–4051, 1984.

[88] R. A. Webb, S. Washburn, C. P. Umbach, and R. B. Laibowitz. Observation of h/e Aharonov-Bohm oscillations in normal-metal rings. *Physical Review Letters*, 54(25):2696–2699, 1985.

[89] A. D. Benoit, S. Washburn, C. P. Umbach, R. B. Laibowitz, and R. A. Webb. Asymmetry in the Magnetoconductance of Metal Wires and Loops. *Physical Review Letters*, 57(14):1765–1768, 1986.

[90] A. Douglas Stone. Magnetoresistance fluctuations in mesoscopic wires and rings. *Physical Review Letters*, 54(25):2692–2695, 1985.

[91] M. Ya Azbel. Quantum delta -dimensional Landauer formula. *Journal of Physics C: Solid State Physics*, 14(9), 1981.

[92] M. Buttiker, Y. Imry, R. Landauer, and S. Pinhas. Generalized many-channel conductance formula with application to small rings. *Physical Review B*, 31(10):6207–6215, 1985.

[93] P. A. Lee and A. Douglas Stone. Universal conductance fluctuations in metals. *Physical Review Letters*, 55(15):1622–1625, 1985.

[94] B L Altshuler and D E Khmel'nitskii. Fluctuation properties of small conductors, 1985.

[95] P. A. Lee, A. Douglas Stone, and H. Fukuyama. Universal conductance fluctuations in metals: Effects of finite temperature, interactions, and magnetic field. *Physical Review B*, 35(3):1039–1070, 1987.

[96] C W J Beenakker and H Van Houten. Quantum Transport in Semiconductor Nanostructures. 228:1–111, 1991.

[97] M Titov, Wei Ren, Fuming Xu, and Jian Wang. Anomalously large conductance fluctuations in weakly disordered graphene Anomalously large conductance fluctuations in weakly disordered graphene. 2007.

[98] Maxim Yu Kharitonov and Konstantin B Efetov. Universal conductance fluctuations in graphene. *Physical Review B*, 78:2–5, 2008.

[99] D W Horsell, A K Savchenko, F V Tikhonenko, K Kechedzhi, I V Lerner, and V I Fal. Mesoscopic conductance fluctuations in graphene. *Solid State Communications*, 149(27-28):1041–1045, 2009.

[100] D Graf, F Molitor, T Ihn, and K Ensslin. Phase-coherent transport measured in a side-gated mesoscopic graphite wire. *Physical Review B*, 75, 2007.

[101] Hubert B Heersche, Pablo Jarillo-herrero, Jeroen B Oostinga, Lieven M K Vandersypen, and Alberto F Morpurgo. Bipolar supercurrent in graphene. *Nature*, 446:56–59, 2007.

[102] Neal E Staley, Conor P Puls, and Ying Liu. Suppression of conductance fluctuation in weakly disordered mesoscopic graphene samples near the charge neutral point. *Physical Review B*, 77:1–5, 2008.

[103] Saverio Russo, Jeroen B Oostinga, Dominique Wehenkel, Hubert B Heersche, Samira Shams Sobhani, Lieven M K Vandersypen, and Alberto F Morpurgo. Observation of Aharonov-Bohm conductance oscillations in a graphene ring. *Physical Review B*, 77(8):1–5, 2008.

[104] Viera Skákalová, Alan B Kaiser, Jai Seung Yoo, Dirk Obergfell, and Siegmar Roth. Correlation between resistance fluctuations and temperature dependence of conductivity in graphene. *Physical Review B*, 80(15), 2009.

[105] Mark B Lundeberg and Joshua A Folk. Spin-resolved quantum interference in graphene. *Nature Physics*, 5(December):894–897, 2009.

[106] Simon Branchaud, Alicia Kam, Piotr Zawadzki, and Andrew S Sachrajda. Transport detection of quantum Hall fluctuations in graphene. *Physical Review B*, 81(12), 2010.

[107] Yung Fu Chen, Myung Ho Bae, Cesar Chialvo, Travis Dirks, Alexey Bezryadin, and Nadya Mason. Magnetoresistance in single-layer graphene: Weak localization and universal conductance fluctuation studies. *Journal of Physics Condensed Matter*, 22(20), 2010.

[108] Keoni K Mahelona, Alan B Kaiser, and Viera Ska. Resistance and mesoscopic fluctuationsin graphene. *Physica Status Solidi B*, 247:2983–2987, 2010.

[109] C. Ojeda-Aristizabal, M Monteverde, R Weil, M Ferrier, S Gueron, and H Bouchiat. Conductance Fluctuations and Field Asymmetry of Rectification in Graphene. *Physical Review Letters*, 104(18):1–4, 2010.

[110] G. Bohra, R. Somphonsane, N. Aoki, Y. Ochiai, D. K. Ferry, and J.P. Bird. Robust mesoscopic fluctuations in disordered graphene. *Applied Physics Letters*, 101, 2012.

[111] G Bohra, R Somphonsane, N Aoki, Y Ochiai, R Akis, D K Ferry, and J P Bird. Nonergodicity and microscopic symmetry breaking of the conductance fluctuations in disordered mesoscopic graphene. *Physical Review B*, 86(16):1–5, 2012.

[112] C Chuang, M Matsunaga, F-h Liu, T-p Woo, N Aoki, L-h Lin, and B-y Wu. Probing weak localization in chemical vapor deposition graphene wide constriction using scanning gate microscopy. *Nanotechnology*, 27, 2016.

[113] Nam-hee Kim, Yun-sok Shin, Serin Park, Hong-seok Kim, Jun Sung, Chi Won, Jeong-o Lee, and Yong-joo Doh. Quantum interference effects in chemical vapor deposited graphene. *Current Applied Physics*, 16(1):31–36, 2016.

[114] Bobo Liu, Richard Akis, David K Ferry, and Girish Bohra. Conductance fluctuations in graphene in the presence of long-range disorder. *Journal of Physics Condensed Matter*, 28, 2016.

[115] Kazi Rafsanjani Amin, Samriddhi Sankar Ray, Nairita Pal, Rahul Pandit, and Aveek Bid. Exotic multifractal conductance fluctuations in graphene. *Communications Physics*, 1(1):1–7, 2018.

[116] E Rossi, J H Bardarson, M S Fuhrer, and S Das Sarma. Universal Conductance Fluctuations in Dirac Materials in the Presence of Long-range Disorder. *Physical Review Letters*, 109(09):1–5, 2012.

[117] K. Von Klitzing, G. Dorda, and M. Pepper. New Method for High-Accuracy Determination of the Fine-Structure Constant Based on Quantized Hall Resistance. *Physical Review Letters*, 45(6):494–497, 1980.

[118] Tsuneya Ando, B Fowler, Frank Stern, I B M Thomas J, and B Devices. Electronic properties of two-dimensional systems. *Reviews of Modern Physicsv*, 54(2):437–672, 1982.

[119] R.B. Laughlin. Quantized Hall conductivity in two dimenstions. *Physical Review B*, 23(10):5632–5634, 1981.

[120] B.I. Halperin. Quantized Hall conductance, current-carrying edge states, and the existance of extended states in a two-dimensional disordered potential. *Physical Review B*, 25(4):2185–2190, 1982.

[121] Yisong Zheng and Tsuneya Ando. Hall conductivity of a two-dimensional graphite system. *Physical Review B - Condensed Matter and Materials Physics*, 65(24):2454201–24542011, 2002.

[122] V. P. Gusynin and S. G. Sharapov. Unconventional integer quantum hall effect in graphene. *Physical Review Letters*, 95(14):2–5, 2005.

[123] Yuanbo Zhang, Yan Wen Tan, Horst L. Stormer, and Philip Kim. Experimental observation of the quantum Hall effect and Berry's phase in graphene. *Nature*, 438(7065):201–204, 2005.

[124] Y. Zhang, Z. Jiang, J. P. Small, M. S. Purewal, Y. W. Tan, M. Fazlollahi, J. D. Chudow, J. A. Jaszczak, H. L. Stormer, and P. Kim. Landau-level splitting in graphene in high magnetic fields. *Physical Review Letters*, 96(13):1–4, 2006.

[125] Mikhail I Katsnelson. *Graphene: Carbon in Two Dimensions*. Cambridge University Press,, 2012.

[126] Joseph G. Checkelsky, Lu Li, and N. P. Ong. Zero-energy state in graphene in a high magnetic field. *Physical Review Letters*, 100(20):2–5, 2008.

[127] A. J.M. Giesbers, L. A. Ponomarenko, K. S. Novoselov, A. K. Geim, M. I. Katsnelson, J. C. Maan, and U. Zeitler. Gap opening in the zeroth Landau level of graphene. *Physical Review B - Condensed Matter and Materials Physics*, 80(20):1–4, 2009.

[128] L. Zhang, J. Camacho, H. Cao, Y. P. Chen, M. Khodas, D. E. Kharzeev, A. M. Tsvelik, T. Valla, and I. A. Zaliznyak. Breakdown of the N=0 quantum Hall state in graphene: Two insulating regimes. *Physical Review B - Condensed Matter and Materials Physics*, 80(24):2–5, 2009.

[129] Liyuan Zhang, Yan Zhang, M. Khodas, T. Valla, and I. A. Zaliznyak. Metal to insulator transition on the N=0 landau level in graphene. *Physical Review Letters*, 105(4):1–4, 2010.

[130] F Amet, J R Williams, K Watanabe, and T Taniguchi. Insulating Behavior at the Neutrality Point in Single-Layer Graphene. *Physical Review Letters*, 110(21), 2013.

[131] Dmitry A. Abanin, Kostya S. Novoselov, Uli Zeitler, Patrick A. Lee, A. K. Geim, and L. S. Levitov. Dissipative quantum hall effect in graphene near the dirac point. *Physical Review Letters*, 98(19):1–4, 2007.

[132] Z. Jiang, Y. Zhang, H. L. Stormer, and P. Kim. Quantum hall states near the charge-neutral dirac point in graphene. *Physical Review Letters*, 99(10):1–4, 2007.

[133] A. J.M. Giesbers, U. Zeitler, M. I. Katsnelson, L. A. Ponomarenko, T. M. Mohiuddin, and J. C. Maan. Quantum-hall activation gaps in graphene. *Physical Review Letters*, 99(20):1–4, 2007.

[134] S. Das Sarma and Kun Yang. The enigma of the $\nu = 0$ quantum Hall effect in graphene. *Solid State Communications*, 149(37-38):1502–1506, 2009.

[135] Steven Kivelson and J Watson. Global phase diagram in the quantum Hall effect. *Physical Review B*, 46(4), 1992.

[136] R. J.F. Hughes, J. T. Nicholls, J. E.F. Frost, E. H. Linfield, M. Pepper, C. J.B. Ford, D. A. Ritchie, G. A.C. Jones, E. Kogan, and M. Kaveh. Magnetic-field-induced insulator-quantum Hall-insulator transition in a disordered two-dimensional electron gas. *Journal of Physics: Condensed Matter*, 6(25):4763–4770, 1994.

[137] M. Hilke, D. Shahar, S. H. Song, D. C. Tsui, Y. H. Xie, and Don Monroe. Experimental evidence for a two-dimensional quantized Hall insulator. *Nature*, 395(6703):675–677, 1998.

[138] Maxim Kharitonov. Phase diagram for the $\nu = 0$ quantum Hall state in monolayer graphene. *Physical Review B*, 85(15), 2012.

[139] Jason Alicea and Matthew P.A. Fisher. Graphene integer quantum Hall effect in the ferromagnetic and paramagnetic regimes. *Physical Review B - Condensed Matter and Materials Physics*, 74(7):1–13, 2006.

[140] Igor F Herbut. Theory of integer quantum Hall effect in graphene. *Physical Review B*, 75(16):1–5, 2007.

[141] Kentaro Nomura, Shinsei Ryu, and Dung-hai Lee. Field-Induced Kosterlitz-Thouless Transition in the N = 0 Landau Level of Graphene. 216801(November):1–4, 2009.

[142] J Jung and A H Macdonald. Theory of the magnetic-field-induced insulator in neutral graphene sheets. *Physical Review B*, 80(23), 2009.

[143] V. P. Gusynin, V. A. Miransky, S. G. Sharapov, and I. A. Shovkovy. Excitonic gap, phase transition, and quantum Hall effect in graphene. *Physical Review B - Condensed Matter and Materials Physics*, 74(19):1–10, 2006.

[144] Gordon W. Semenoff and Fei Zhou. Magnetic catalysis and quantum Hall ferromagnetism in weakly coupled graphene. *Journal of High Energy Physics*, 2011(7), 2011.

[145] M.J. Kelly. *Low-dimensional Semiconductors: Materials, Physics, Technology, Devices*. 1995.

[146] Xuesong Li, Weiwei Cai, Jinho An, Seyoung Kim, Junghyo Nah, Dongxing Yang, Richard Piner, Aruna Velamakanni, Inhwa Jung, Emanuel Tutuc, Sanjay K. Banerjee, Luigi Colombo, and Rodney S. Ruoff. Large-area synthesis of high-quality and uniform graphene films on copper foils. *Science*, 324(5932):1312–1314, 2009.

[147] Ji Won Suk, Alexander Kitt, Carl W. Magnuson, Yufeng Hao, Samir Ahmed, Jinho An, Anna K. Swan, Bennett B. Goldberg, and Rodney S. Ruoff. Transfer of CVD-grown monolayer graphene onto arbitrary substrates. *ACS Nano*, 5(9):6916–6924, 2011.

[148] S. Goniszewski, M. Adabi, O. Shaforost, S. M. Hanham, L. Hao, and N. Klein. Correlation of p-doping in CVD Graphene with Substrate Surface Charges. *Scientific Reports*, 6(March):1–9, 2016.

[149] Hyun Ho Kim, Seong Kyu Lee, Seung Goo Lee, Eunho Lee, and Kilwon Cho. Wetting-Assisted Crack- and Wrinkle-Free Transfer of Wafer-Scale Graphene onto Arbitrary Substrates over a Wide Range of Surface Energies. *Advanced Functional Materials*, 26(13):2070–2077, 2016.

[150] Marius Knapp, René Hoffmann, Volker Cimalla, and Oliver Ambacher. Wettability investigations and wet transfer enhancement of large-area CVD-graphene on aluminum nitride. *Nanomaterials*, 7(8), 2017.

[151] C. Stampfer, F. Molitor, D. Graf, K. Ensslin, A. Jungen, C. Hierold, and L. Wirtz. Raman imaging of doping domains in graphene on SiO$_2$. *Applied Physics Letters*, 91(241907), 2007.

[152] C Neumann, S. Reichardt, P. Venezuela, M. Drogeler, L. Banszerus, M. Schmitz, K. Watanabe, T. Taniguchi, F. Mauri, B. Beschoten, S.V. Rotkin, and C. Stampfer. Raman spectroscopy as probe of nanometre-scale strain variations in graphene. *Nature Communications*, (May):1–7, 2015.

[153] Nuno J G Couto, Davide Costanzo, Stephan Engels, Dong-keun Ki, Kenji Watanabe, Takashi Taniguchi, Christoph Stampfer, and Alberto F Morpurgo. Random Strain Fluctuations as Dominant Disorder Source for High-Quality On-Substrate Graphene Devices. *Physical Review X*, 041019:1–13, 2014.

[154] Simone Pisana, Michele Lazzeri, Cinzia Casiraghi, Kostya S Novoselov, A K Geim, Andrea C Ferrari, and Francesco Mauri. Breakdown of the adiabatic Born – Oppenheimer approximation in graphene. *Nature materials*, 6(March):3–6, 2007.

[155] A Das, S Pisana, B Chakraborty, S Piscanec, S K Saha, U V Waghmare, K S Novoselov, H R Krishnamurthy, A K Geim, A C Ferrari, and A K Sood. Monitoring dopants by Raman scattering in an electrochemically top-gated graphene transistor. *Nature Nanotechnology*, 3(April):1–6, 2008.

[156] Jun Yan, Yuanbo Zhang, Philip Kim, and Aron Pinczuk. Electric field effect tuning of electron-phonon coupling in graphene. *Physical Review Letters*, 98(16):1–4, 2007.

[157] Ryan Beams, Luiz Gustavo Cançado, and Lukas Novotny. Raman characterization of defects and dopants in graphene. *Journal of Physics Condensed Matter*, 27(8), 2015.

[158] Archana Venugopal, Luigi Colombo, and Eric M. Vogel. Issues with characterizing transport properties of graphene field effect transistors. *Solid State Communications*, 152(15):1311–1316, 2012.

[159] J. Robertson. High dielectric constant oxides. *European Physical Journal Applied Physics*, 28:265–291, 2004.

[160] John P. Robinson, Henning Schomerus, László Oroszlány, and Vladimir I. Fal'Ko. Adsorbate-limited conductivity of graphene. *Physical Review Letters*, 101(19):7–10, 2008.

[161] Damon B. Farmer, Golizadeh Mojarad Roksana, Vasili Perebeinos, Yu Ming Lin, George S. Tuievski, James C. Tsang, and Phaedon Avouris. Chemical doping and electron-hole conduction asymmetry in graphene devices. *Nano Letters*, 9(1):388–392, 2009.

[162] G. Giovannetti, P. A. Khomyakov, G. Brocks, V. M. Karpan, J. Van Den Brink, and P. J. Kelly. Doping graphene with metal contacts. *Physical Review Letters*, 101(2):4–7, 2008.

[163] B. Huard, N. Stander, J. A. Sulpizio, and D. Goldhaber-Gordon. Evidence of the role of contacts on the observed electron-hole asymmetry in graphene. *Physical Review B - Condensed Matter and Materials Physics*, 78(12), 2008.

[164] Wenjun Liu, Jun Wei, Xiaowei Sun, and Hongyu Yu. A study on graphene-metal contact. *Crystals*, 3(1):257–274, 2013.

[165] Akira Satou, Gen Tamamushi, Kenta Sugawara, Junki Mitsushio, Victor Ryzhii, and Taiichi Otsuji. A Fitting Model for Asymmetric I-V Characteristics of Graphene FETs for Extraction of Intrinsic Mobilities. *IEEE Transactions on Electron Devices*, 63(8):3300–3306, 2016.

[166] Babak Fallahazad, Seyoung Kim, Luigi Colombo, and Emanuel Tutuc. Dielectric thickness dependence of carrier mobility in graphene with HfO2 top dielectric. *Applied Physics Letters*, 97(12):2–5, 2010.

[167] Seyoung Kim, Junghyo Nah, Insun Jo, Davood Shahrjerdi, Luigi Colombo, Zhen Yao, Emanuel Tutuc, and Sanjay K. Banerjee. Realization of a high mobility dual-gated graphene field-effect transistor with Al2O3 dielectric. *Applied Physics Letters*, 94(6):2007–2010, 2009.

[168] S. Q. Wang and G. D. Mahan. Electron scattering from surface excitations. *Physical Review B*, 6(12):4517–4524, 1972.

[169] Aniruddha Konar, Tian Fang, and Debdeep Jena. Effect of high-κ gate dielectrics on charge transport in graphene-based field effect transistors. *Physical Review B - Condensed Matter and Materials Physics*, 82(11):1–7, 2010.

[170] K. Zou, X. Hong, D. Keefer, and J. Zhu. Deposition of high-quality HfO2 on graphene and the effect of remote oxide phonon scattering. *Physical Review Letters*, 105(12):1–4, 2010.

[171] Keun Soo Kim, Yue Zhao, Houk Jang, Sang Yoon Lee, Jong Min Kim, Kwang S. Kim, Jong Hyun Ahn, Philip Kim, Jae Young Choi, and Byung Hee Hong. Large-scale pattern growth of graphene films for stretchable transparent electrodes. *Nature*, 457(7230):706–710, 2009.

[172] Alfonso Reina, Xiaoting Jia, John Ho, Daniel Nezich, Hyungbin Son, Vladimir Bulovic, Mildred S. Dresselhaus, and Kong Jing. Large area, few-layer graphene films on arbitrary substrates by chemical vapor deposition. *Nano Letters*, 9(1):30–35, 2009.

[173] W. Wei, G. Deokar, M. Belhaj, D. Mele, E. Pallecchi, E. Pichonat, D. Vignaud, and H. Happy. Fabrication and characterization of CVD-grown graphene based Field-Effect Transistor. *European Microwave Week 2014: Connecting the Future, EuMW 2014 - Conference Proceedings; EuMC 2014: 44th European Microwave Conference*, pages 367–370, 2014.

[174] Ruizhi Wang, Patrick R. Whelan, Philipp Braeuninger-Weimer, Stefan Tappertzhofen, Jack A. Alexander-Webber, Zenas A. Van Veldhoven, Piran R. Kidambi, Bjarke S. Jessen, Timothy Booth, Peter Bøggild, and Stephan Hofmann. Catalyst Interface Engineering for Improved 2D Film Lift-Off and Transfer. *ACS Applied Materials and Interfaces*, 8(48):33072–33082, 2016.

[175] Domenico De Fazio, David G. Purdie, Anna K. Ott, Philipp Braeuninger-Weimer, Timofiy Khodkov, Stijn Goossens, Takashi Taniguchi, Kenji Watanabe, Patrizia Livreri, Frank H. L. Koppens, Stephan Hofmann, Ilya Goykhman, Andrea C. Ferrari, and Antonio Lombardo. High-Mobility, Wet-Transferred Graphene Grown by Chemical Vapor Deposition. *ACS Nano*, 13(8):8926–8935, 2019.

[176] Jakub Kedzierski, Pei Lan Hsu, Alfonso Reina, Jing Kong, Paul Healey, Peter Wyatt, and Craig Keast. Graphene-on-insulator transistors made using C on Ni chemical-vapor deposition. *IEEE Electron Device Letters*, 30(7):745–747, 2009.

[177] G. Lian S. Kim C. M. Corbet D. A. Ferrer L. Colombo B. Fallahazad, K. Lee and E Tutuc. Scaling of Al2O3 dielectric for graphene field- effect transistors. *Applied Physics Letters*, 093112(October 2011):10–14, 2012.

[178] Zhen Hua Ni, Ting Yu, Zhi Qiang Luo, Ying Ying Wang, Lei Liu, Choun Pei Wong, Jianmin Miao, Wei Huang, and Ze Xiang Shen. Probing charged impurities in suspended graphene using raman spectroscopy. *ACS Nano*, 3(3):569–574, 2009.

[179] Sunmin Ryu, Li Liu, Stephane Berciaud, Young Jun Yu, Haitao Liu, Philip Kim, George W. Flynn, and Louis E. Brus. Atmospheric oxygen binding and hole doping in deformed graphene on a SiO2 substrate. *Nano Letters*, 10(12):4944–4951, 2010.

[180] A. Pirkle, J. Chan, A. Venugopal, D. Hinojos, C. W. Magnuson, S. McDonnell, L. Colombo, E. M. Vogel, R. S. Ruoff, and R. M. Wallace. The effect of chemical residues on the physical and electrical properties of chemical vapor deposited graphene transferred to SiO2. *Applied Physics Letters*, 99(12):2009–2012, 2011.

[181] Ji Won Suk, Wi Hyoung Lee, Jongho Lee, Harry Chou, Richard D. Piner, Yufeng Hao, Deji Akinwande, and Rodney S. Ruoff. Enhancement of the electrical properties of graphene grown by chemical vapor deposition via controlling the effects of polymer residue. *Nano Letters*, 13(4):1462–1467, 2013.

[182] Zengguang Cheng, Qiaoyu Zhou, Chenxuan Wang, Qiang Li, Chen Wang, and Ying Fang. Toward intrinsic graphene surfaces: A systematic study on thermal annealing and wet-chemical treatment of SiO2-supported graphene devices. *Nano Letters*, 11(2):767–771, 2011.

[183] Yinxiao Yang, Kevin Brenner, and Raghu Murali. The influence of atmosphere on electrical transport in graphene. *Carbon*, 50(5):1727–1733, 2012.

[184] Woosuk Choi, Muhammad Arslan Shehzad, Sanghoon Park, and Yongho Seo. Influence of removing PMMA residues on surface of CVD graphene using a contact-mode atomic force microscope. *RSC Advances*, 7(12):6943–6949, 2017.

[185] B. Krishna Bharadwaj, Digbijoy Nath, Rudra Pratap, and Srinivasan Raghavan. Making consistent contacts to graphene: Effect of architecture and growth induced defects. *Nanotechnology*, 27(20), 2016.

[186] Suman Sarkar, Kazi Rafsanjani Amin, Ranjan Modak, Amandeep Singh, Subroto Mukerjee, and Aveek Bid. Role of different scattering mechanisms on the temperature dependence of transport in graphene. *Scientific Reports*, 5, 2015.

[187] U. Francesca, G. Lupina, A. Grillo, N. Martucciello, and A. Bartolomeo. Contact resistance and mobility in back-gate graphene transistors. *Nano Express*, 1, 2020.

[188] Jai Seung Yoo, Yung Woo Park, Viera Skákalová, and Siegmar Roth. Shubnikov-de Haas and Aharonov Bohm effects in a graphene nanoring structure. *Applied Physics Letters*, 96(14):1–4, 2010.

[189] Zhenbing Tan, Changling Tan, Li Ma, G. T. Liu, L. Lu, and C. L. Yang. Shubnikov-de Haas oscillations of a single layer graphene under dc current bias. *Physical Review B - Condensed Matter and Materials Physics*, 84(11):2–5, 2011.

[190] J.S. Seabold and J. Perktold. statsmodels: Econometric and statistical modeling with python. In *Proceedings of the 9th Python in Science Conference*, 2010.

[191] Risto M Nieminen. Electronic Properties of Two-Dimensional Systems. *Physica Scripta*, T23:54–58, 1988.

[192] C. H. Yang, F. M. Peeters, and W. Xu. Landau-level broadening due to electron-impurity interaction in graphene in strong magnetic fields. *Physical Review B - Condensed Matter and Materials Physics*, 82(7):1–6, 2010.

[193] M. Orlita, C. Faugeras, R. Grill, A. Wysmolek, W. Strupinski, C. Berger, W. A. De Heer, G. Martinez, and M. Potemski. Carrier scattering from dynamical magnetoconductivity in quasineutral epitaxial graphene. *Physical Review Letters*, 107(21):1–5, 2011.

[194] Hannah Funk, Andreas Knorr, Florian Wendler, and Ermin Malic. Microscopic view on Landau level broadening mechanisms in graphene. *Physical Review B - Condensed Matter and Materials Physics*, 92(20):1–11, 2015.

[195] David L. Miller, Kevin D. Kubista, Gregory M. Rutter, Ming Ruan, Walt A. De Heer, Phillip N. First, and Joseph A. Stroscio. Observing the quantization of zero mass carriers in graphene. *Science*, 324(5929):924–927, 2009.

[196] Young Jae Song, Alexander F. Otte, Young Kuk, Yike Hu, David B. Torrance, Phillip N. First, Walt A. De Heer, Hongki Min, Shaffique Adam, Mark D. Stiles, Allan H. MacDonald, and Joseph A. Stroscio. High-resolution tunnelling spectroscopy of a graphene quartet. *Nature*, 467(7312):185–189, 2010.

[197] Ke Ke Bai, Yi Cong Wei, Jia Bin Qiao, Si Yu Li, Long Jing Yin, Wei Yan, Jia Cai Nie, and Lin He. Detecting giant electron-hole asymmetry in a graphene monolayer generated by strain and charged-defect scattering via Landau level spectroscopy. *Physical Review B - Condensed Matter and Materials Physics*, 92(12):1–5, 2015.

[198] Long Jing Yin, Si Yu Li, Jia Bin Qiao, Jia Cai Nie, and Lin He. Landau quantization in graphene monolayer, Bernal bilayer, and Bernal trilayer on graphite surface. *Physical Review B - Condensed Matter and Materials Physics*, 91(11):6–11, 2015.

[199] Wei Yan, Si Yu Li, Long Jing Yin, Jia Bin Qiao, Jia Cai Nie, and Lin He. Spatially resolving unconventional interface Landau quantization in a graphene monolayer-bilayer planar junction. *Physical Review B*, 93(19):1–6, 2016.

[200] J. González, F. Guinea, and M. A.H. Vozmediano. Non-Fermi liquid behavior of electrons in the half-filled honeycomb lattice (A renormalization group approach). *Nuclear Physics, Section B*, 424(3):595–618, 1994.

[201] S. Das Sarma, E. H. Hwang, and Wang Kong Tse. Many-body interaction effects in doped and undoped graphene: Fermi liquid versus non-Fermi liquid. *Physical Review B - Condensed Matter and Materials Physics*, 75(12):1–4, 2007.

[202] Cheol Hwan Park, Feliciano Giustino, Catalin D. Spataru, Marvin L. Cohen, and Steven G. Louie. Angle-resolved photoemission spectra of graphene from first-principles calculations. *Nano Letters*, 9(12):4234–4239, 2009.

[203] Choongyu Hwang, David A. Siegel, Sung Kwan Mo, William Regan, Ariel Ismach, Yuegang Zhang, Alex Zettl, and Alessandra Lanzara. Fermi velocity engineering in graphene by substrate modification. *Scientific Reports*, 2:2–5, 2012.

[204] D. C. Elias, R. V. Gorbachev, A. S. Mayorov, S. V. Morozov, A. A. Zhukov, P. Blake, L. A. Ponomarenko, I. V. Grigorieva, K. S. Novoselov, F. Guinea, and A. K. Geim. Dirac cones reshaped by interaction effects in suspended graphene. *Nature Physics*, 7(9):701–704, 2011.

[205] C. Jang, S. Adam, J. H. Chen, E. D. Williams, S. Das Sarma, and M. S. Fuhrer. Tuning the effective fine structure constant in graphene: Opposing effects of dielectric screening on short- and long-range potential scattering. *Physical Review Letters*, 101(14):1–4, 2008.

[206] R. S. Deacon, K. C. Chuang, R. J. Nicholas, K. S. Novoselov, and A. K. Geim. Cyclotron resonance study of the electron and hole velocity in graphene monolayers. *Physical Review B - Condensed Matter and Materials Physics*, 76(8):2–5, 2007.

[207] H. Schmidt, T. Lüdtke, P. Barthold, and R. J. Haug. Temperature dependent measurements on two decoupled graphene monolayers. *Physica E: Low-Dimensional Systems and Nanostructures*, 42(4):699–702, 2010.

[208] H. W. Jiang, C. E. Johnson, K .L. Wang, and S. T. Hannahs. Observation of Magnetic-Field-Induced Delocalization: Transition from Anderson Insulator to Quantum Hall Conductor. *Physical Review Letters*, 71(9):1439–1442, 1993.

[209] R James, Dmitry A Abanin, Leonardo Dicarlo, S Leonid, Charles M Marcus, and Quantum Hall. Quantum Hall Conductance of Two-Terminal Graphene Devices. 2009.

[210] Dmitry A. Abanin and Leonid S. Levitov. Conformal invariance and shape-dependent conductance of graphene samples. *Physical Review B - Condensed Matter and Materials Physics*, 78(3):1–8, 2008.

[211] Kirill I Bolotin, Fereshte Ghahari, Michael D Shulman, Horst L Stormer, and Philip Kim. Observation of the fractional quantum Hall effect in graphene. *Nature*, 462(November):196–200, 2009.

[212] A A Zibrov, E M Spanton, H Zhou, C Kometter, T Taniguchi, K Watanabe, and A F Young. Even denominator fractional quantum Hall states at an isospin transition in monolayer graphene. *Nature Physics*, 14:930–935, 2018.

[213] E. V. Gorbar, V. P. Gusynin, and V. A. Miransky. Toward theory of quantum Hall effect in graphene. *Fizika Nizkikh Temperatur (Kharkov)*, 34(10):1007–1011, 2008.

[214] H.W. Jiang, H.L. Stormer, D.C. Tsui, L.N. Pfeiffer, and K.W. West. Transport anomalies in the lowest Landau level of two-dimensional electrons at half-filling. *Physical review B*, 40(17):0–3, 1989.

[215] G. Ebert, K. von Klitzing, C. Probst, E. Schuberth, K. Ploog, and G. Weimann. Hopping conduction in the Landau level tails in GaAs-AlxGa1-xAs heterostructures at low temperatures. *Solid State Communications*, 45(7):625–628, 1983.

[216] J. Heo, H. J. Chung, Sung Hoon Lee, H. Yang, D. H. Seo, J. K. Shin, U. In Chung, S. Seo, E. H. Hwang, and S. Das Sarma. Nonmonotonic temperature dependent transport in graphene grown by chemical vapor deposition. *Physical Review B - Condensed Matter and Materials Physics*, 84(3):1–7, 2011.

[217] Qiuzi Li, E H Hwang, and S Das Sarma. Disorder-induced temperature-dependent transport in graphene : Puddles , impurities , activation , and diffusion. 115442, 2011.

[218] Kun Yang. Spontaneous symmetry breaking and quantum Hall effect in graphene. *Solid State Communications*, 143(1-2):27–32, 2007.

[219] V. P. Gusynin, V. A. Miransky, and I. A. Shovkovy. Catalysis of dynamical flavor symmetry breaking by a magnetic field in 2 + 1 dimensions. *Physical Review Letters*, 73(26):3499–3502, 1994.

[220] Igor A. Shovkovy. Magnetic Catalysis: A Review. pages 13–49, 2013.

[221] D. V. Khveshchenko. Magnetic-field-induced insulating behavior in highly oriented pyrolitic graphite. *Physical Review Letters*, 87(20):206401–1, 2001.

[222] E. V. Gorbar, V. P. Gusynin, V. A. Miransky, and I. A. Shovkovy. Magnetic field driven metal-insulator phase transition in planar systems. *Physical Review B - Condensed Matter and Materials Physics*, 66(4):451081–4510822, 2002.

[223] Y. Kopelevich, V. V. Lemanov, S. Moehlecke, and J. H.S. Torres. Landau level quantization and possible superconducting instabilities in highly oriented pyrolitic graphite. *Physics of the Solid State*, 41(12):1959–1962, 1999.

[224] H. Kempa, Y. Kopelevich, F. Mrowka, A. Setzer, J. H.S. Torres, R. Höhne, and P. Esquinazi. Magnetic-field-driven superconductor-insulator-type transition in graphite. *Solid State Communications*, 115(10):539–542, 2000.

[225] M. S. Sercheli, Y. Kopelevich, R. Ricardo da Silva, J. H.S. Torres, and C. Rettori. Evidence for internal field in graphite: A conduction electron spin-resonance study. *Solid State Communications*, 121(9-10):579–583, 2002.

[226] Motohiko Ezawa. Intrinsic zeeman effect in graphene. *Journal of the Physical Society of Japan*, 76(9):1–12, 2007.

[227] E. V. Gorbar, V. P. Gusynin, V. A. Miransky, and I. A. Shovkovy. Dynamics in the quantum Hall effect and the phase diagram of graphene. *Physical Review B - Condensed Matter and Materials Physics*, 78(8):30–33, 2008.

[228] Igor F. Herbut. Pseudomagnetic catalysis of the time-reversal symmetry breaking in graphene. *Physical Review B - Condensed Matter and Materials Physics*, 78(20):6–9, 2008.

[229] D Jevtics, B Guilhabert, A Hurtado, Q Gao, H H Tan, C Jagadish, and M D Dawson. Transfer Printing of Semiconductor Nanowires. *2016 IEEE Photonics Conference (IPC)*, 2(c):712–713, 2016.

[230] Antonio Hurtado, Dimitars Jevtics, Benoit Guilhabert, Qian Gao, Hark Hoe Tan, and Martin D Dawson. Transfer printing of semiconductor nanowire lasers. *IET Optoelectronics*, 12(1):30–35, 2017.

[231] A. R. Ullah, H. J. Joyce, H. H. Tan, C. Jagadish, and A. P. Micolich. The influence of atmosphere on the performance of pure-phase WZ and ZB InAs nanowire transistors. *Nanotechnology*, 28(45), 2017.

[232] Jack A Alexander-webber, Catherine K Groschner, Abhay A Sagade, Gregory Tainter, M Fernando Gonzalez-zalba, Riccardo Di Pietro, Jennifer Wong-leung, H Hoe Tan, Chennupati Jagadish, Stephan Hofmann, and Hannah J Joyce. Engineering the Photoresponse of InAs Nanowires. *ACS Applied Materials and Interfaces*, 9, 2017.

[233] Satoru Masubuchi, Masataka Morimoto, Sei Morikawa, Momoko Onodera, Yuta Asakawa, Kenji Watanabe, Takashi Taniguchi, and Tomoki Machida. Autonomous robotic searching and assembly of two-dimensional crystals to build van der Waals superlattices. *Nature Communications*, 9(1413):4–6, 2018.

Appendix A

Spatial heat maps and histograms of Raman spectroscopy peak properties

This appendix shows the intensities I_{2D}, I_G and I_{2D}/I_G plotted as heat maps for all conducting channels of device CVD-MUX-A. The distribution of the intensities for each channel are also displayed as histograms.

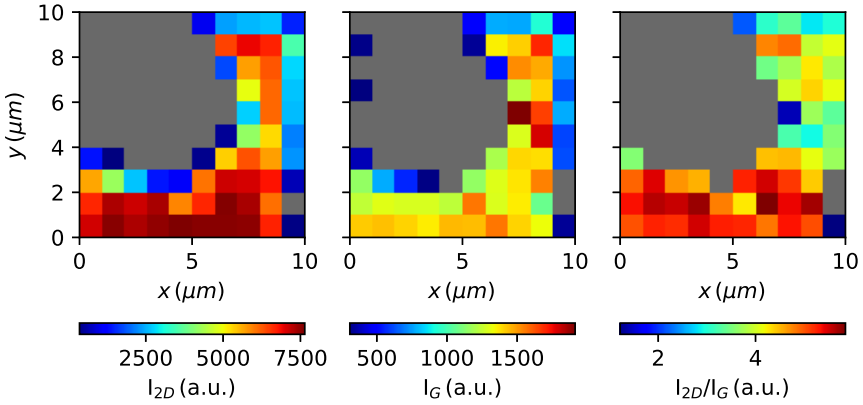

(a) Heat maps showing the spatial variation of I_{2D}, I_G and I_{2D}/I_G.

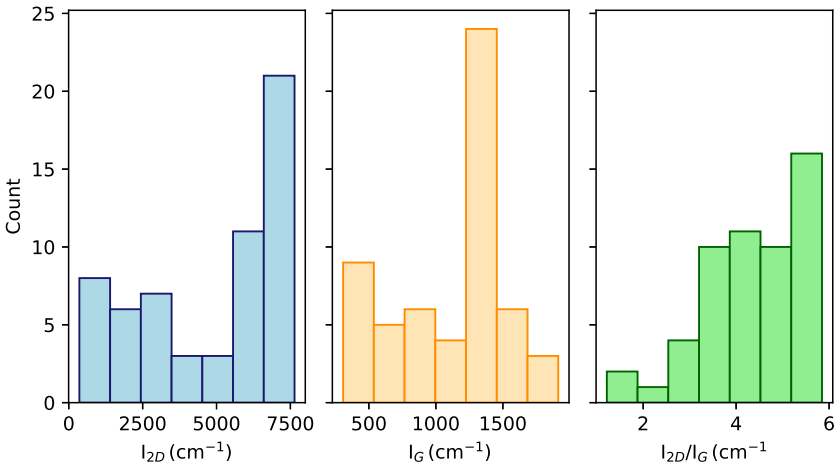

(b) Histograms of I_{2D}, I_G and I_{2D}/I_G.

Fig. A.1 Channel 1: Raman spectroscopy peak intensity data.

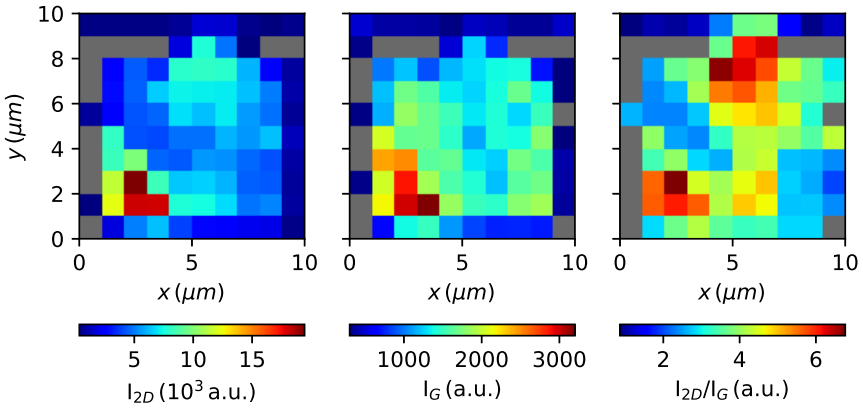

(a) Heat maps showing the spatial variation of I_{2D}, I_G and I_{2D}/I_G.

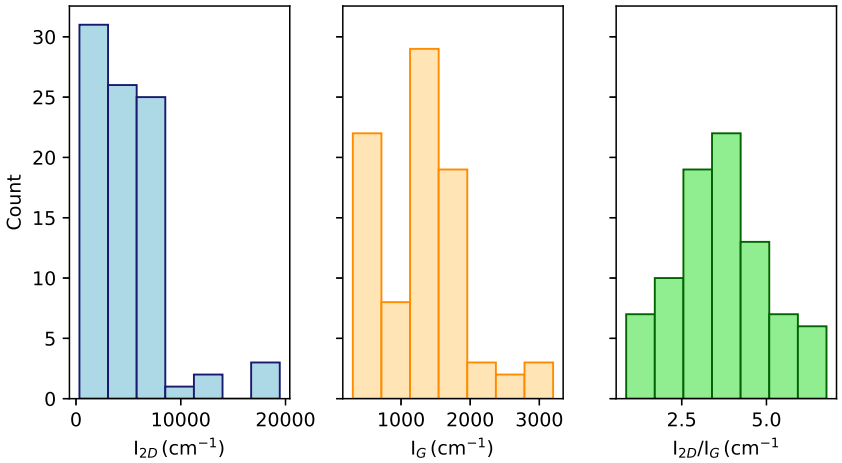

(b) Histograms of I_{2D}, I_G and I_{2D}/I_G.

Fig. A.2 Channel 2: Raman spectroscopy peak intensity data.

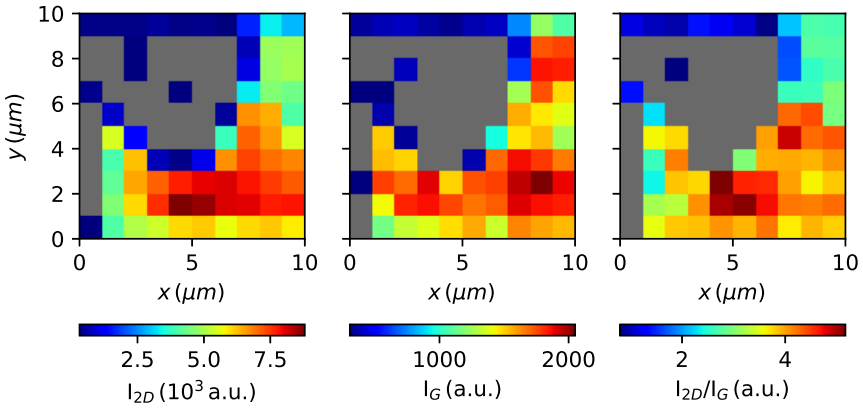

(a) Heat maps showing the spatial variation of I_{2D}, I_G and I_{2D}/I_G.

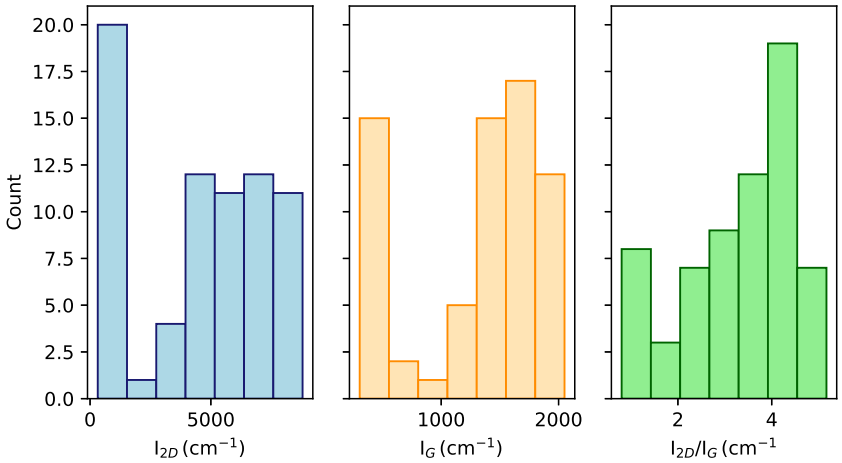

(b) Histograms of I_{2D}, I_G and I_{2D}/I_G.

Fig. A.3 Channel 3: Raman spectroscopy peak intensity data.

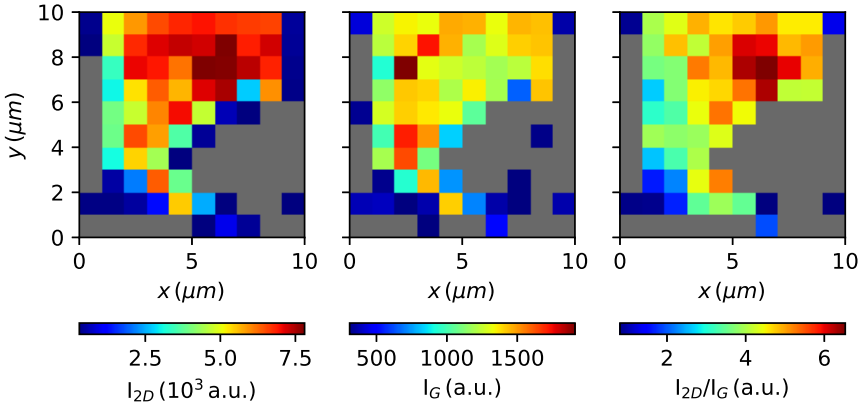

(a) Heat maps showing the spatial variation of I_{2D}, I_G and I_{2D}/I_G.

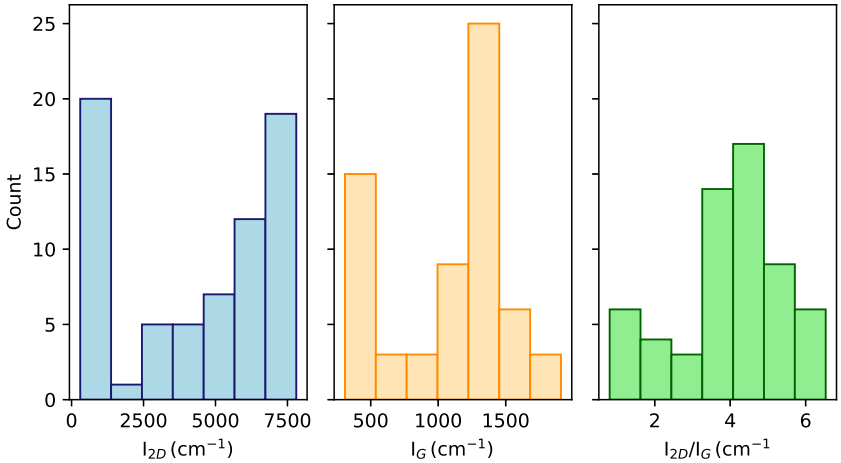

(b) Histograms of I_{2D}, I_G and I_{2D}/I_G.

Fig. A.4 Channel 4: Raman spectroscopy peak intensity data.

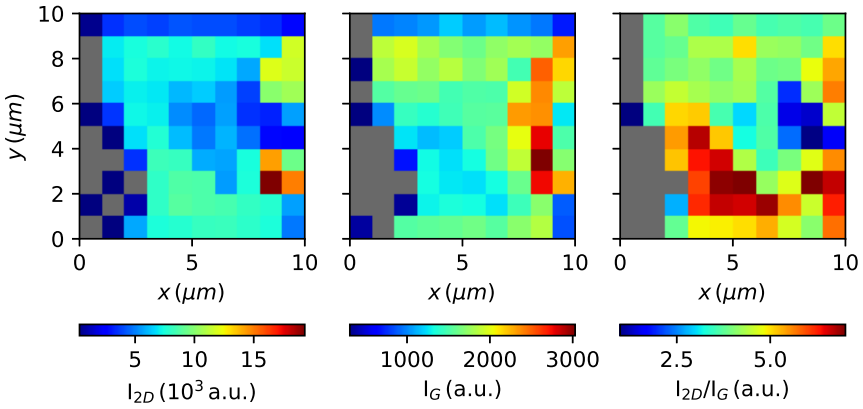

(a) Heat maps showing the spatial variation of I_{2D}, I_G and I_{2D}/I_G.

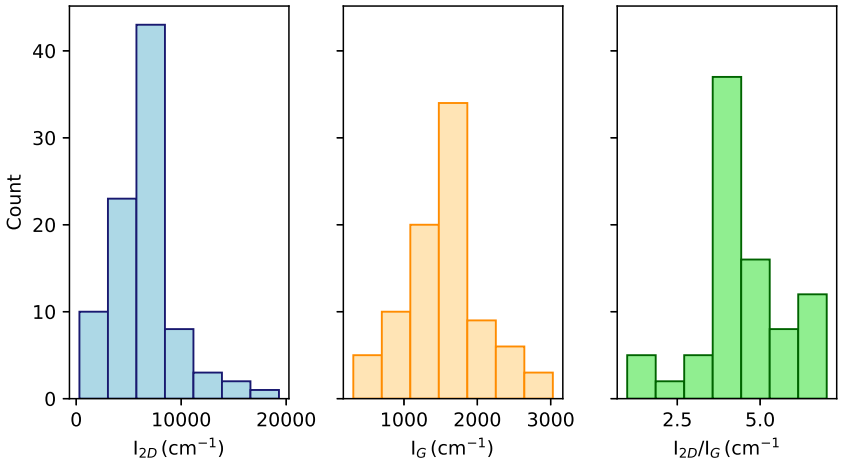

(b) Histograms of I_{2D}, I_G and I_{2D}/I_G.

Fig. A.5 Channel 5: Raman spectroscopy peak intensity data.

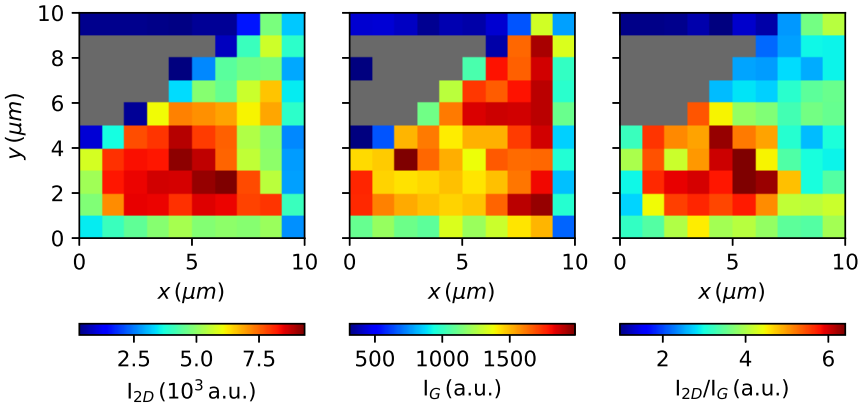

(a) Heat maps showing the spatial variation of I_{2D}, I_G and I_{2D}/I_G.

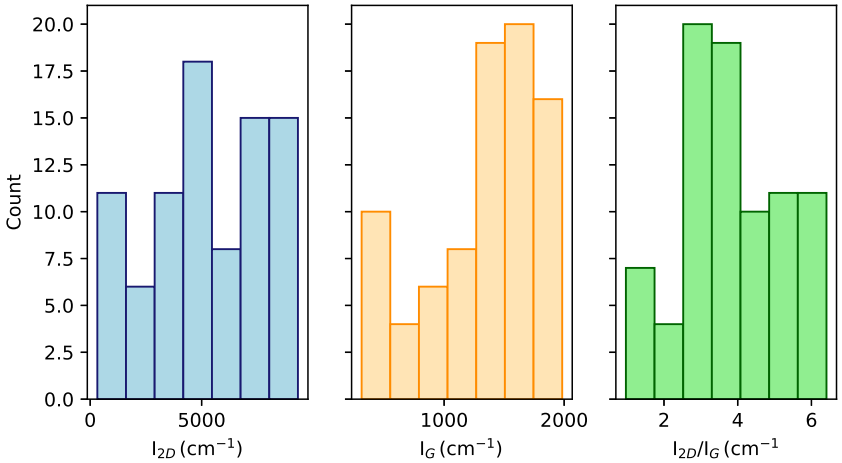

(b) Histograms of I_{2D}, I_G and I_{2D}/I_G.

Fig. A.6 Channel 7: Raman spectroscopy peak intensity data.

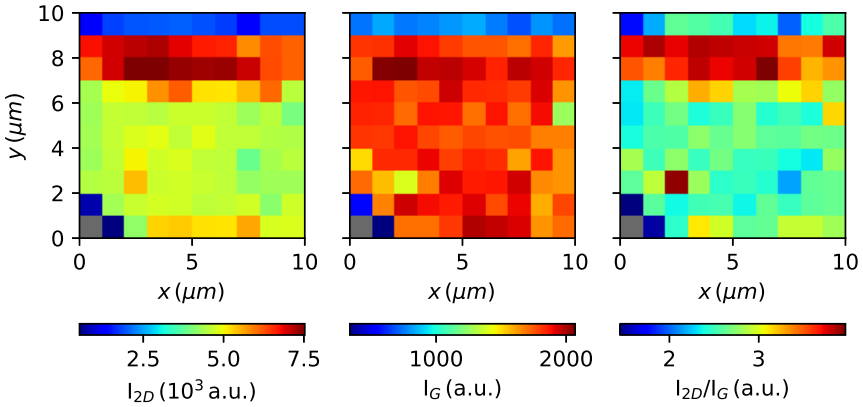

(a) Heat maps showing the spatial variation of I_{2D}, I_G and I_{2D}/I_G.

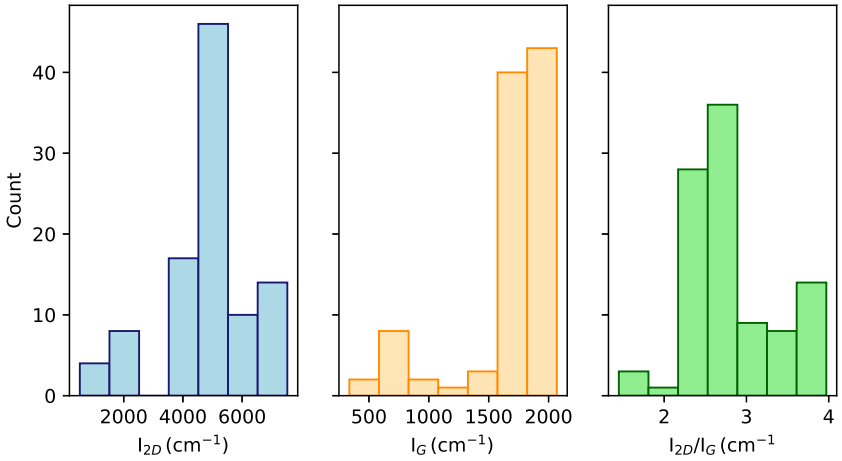

(b) Histograms of I_{2D}, I_G and I_{2D}/I_G.

Fig. A.7 Channel 9: Raman spectroscopy peak intensity data.

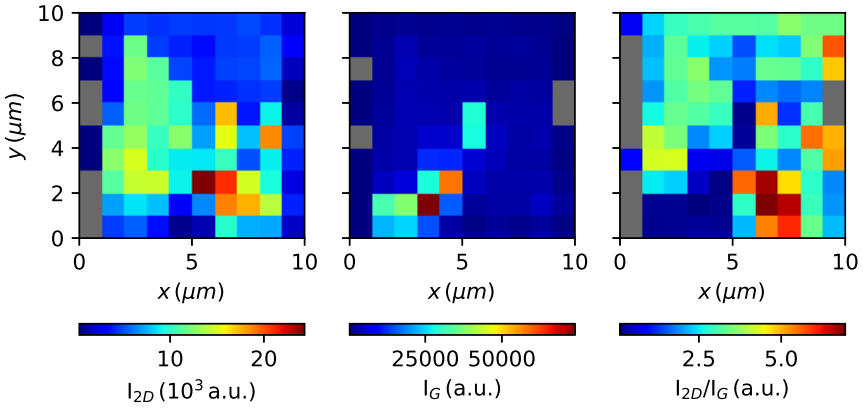

(a) Heat maps showing the spatial variation of I_{2D}, I_G and I_{2D}/I_G.

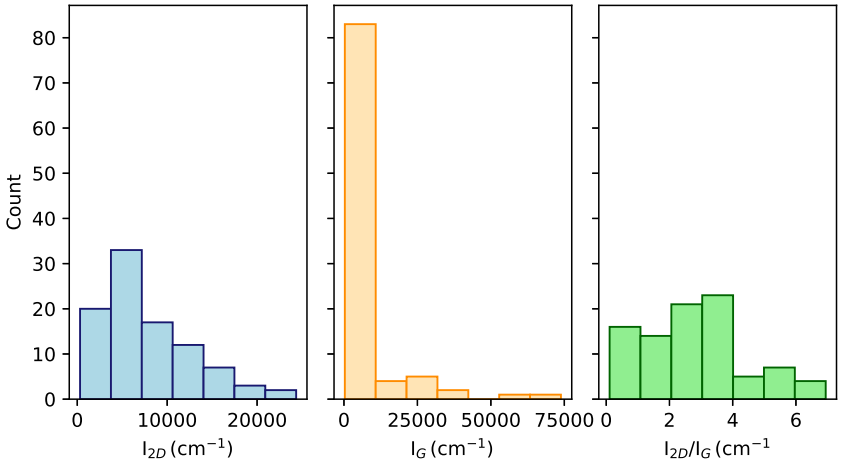

(b) Histograms of I_{2D}, I_G and I_{2D}/I_G.

Fig. A.8 Channel 10: Raman spectroscopy peak intensity data.

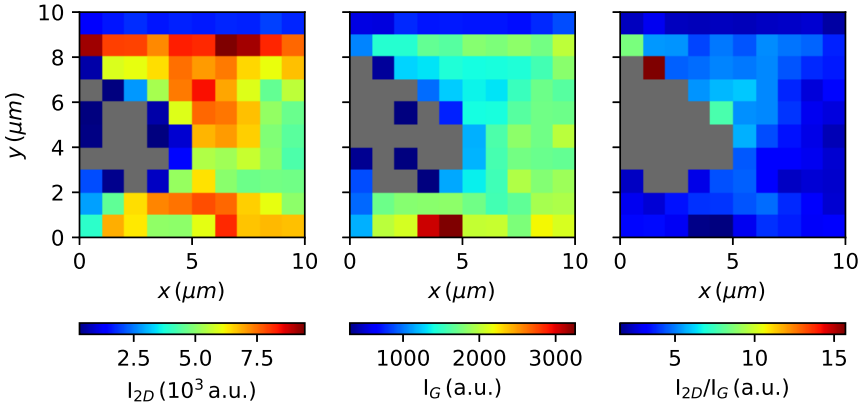

(a) Heat maps showing the spatial variation of I_{2D}, I_G and I_{2D}/I_G.

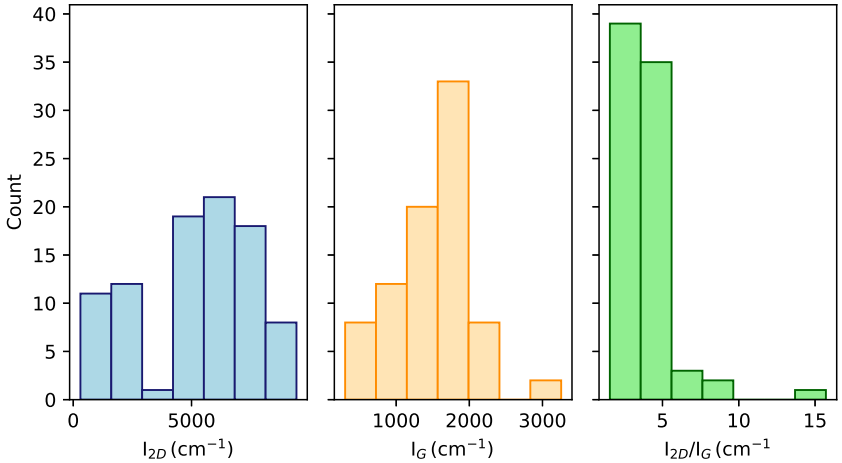

(b) Histograms of I_{2D}, I_G and I_{2D}/I_G.

Fig. A.9 Channel 11: Raman spectroscopy peak intensity data.

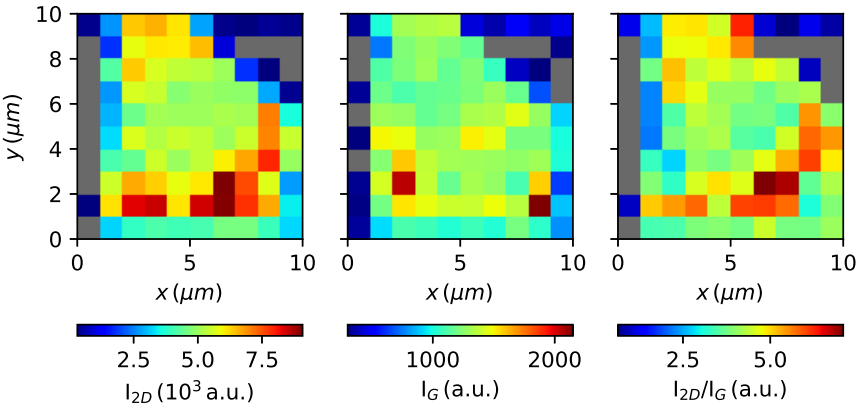

(a) Heat maps showing the spatial variation of I_{2D}, I_G and I_{2D}/I_G.

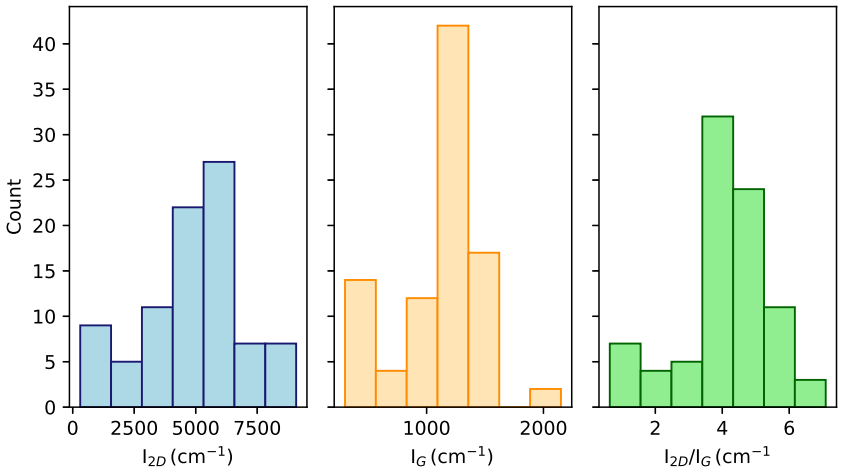

(b) Histograms of I_{2D}, I_G and I_{2D}/I_G.

Fig. A.10 Channel 14: Raman spectroscopy peak intensity data.

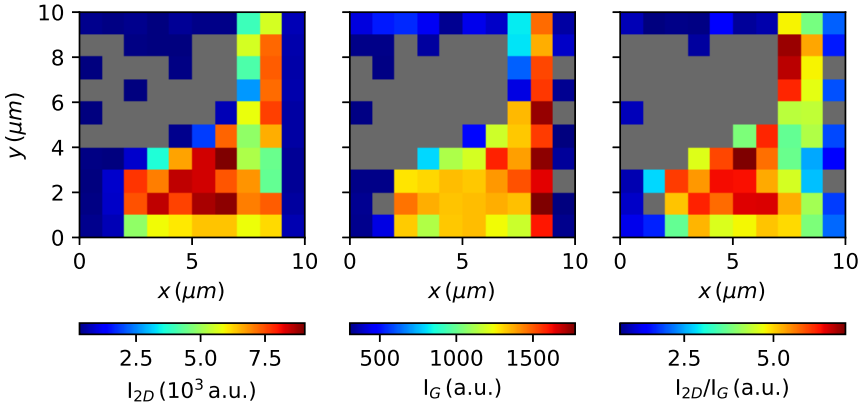

(a) Heat maps showing the spatial variation of I_{2D}, I_G and I_{2D}/I_G.

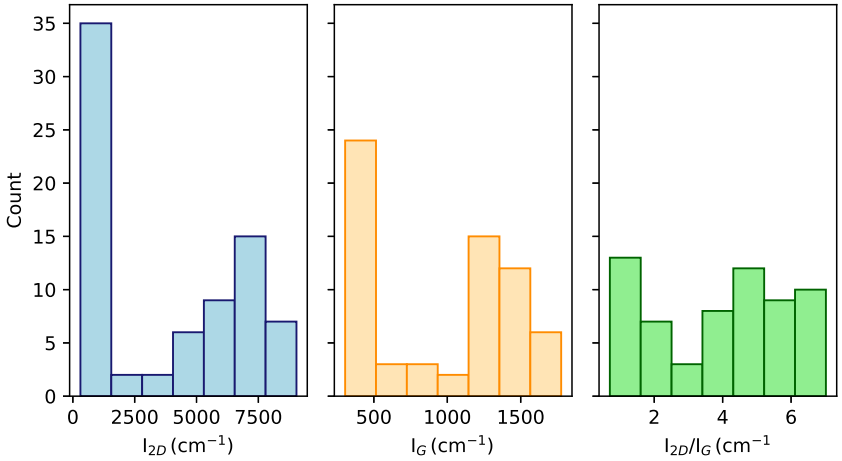

(b) Histograms of I_{2D}, I_G and I_{2D}/I_G.

Fig. A.11 Channel 16: Raman spectroscopy peak intensity data.

Appendix B

Statistical tests, explained

This appendix provides a brief explanation of the statistical tests used to analyse the significance of the experimental results presented later in this chapter. Linear regression is used to describe the relationship between a numerical, measured (response) variable and a numerical independent variable; analysis of variance (ANOVA) tests are used to describe the relationship between a numerical response variable and independent, categorical variables.

Linear regression and testing significance

Univariate linear regression attempts to fit the function

$$Y = \beta_0 + \beta_1 x + \varepsilon, \tag{B.1}$$

to the observed data, where (β_0, β_1) are the model parameters, x is the independent variable/ regressor, Y is the predicted value of the model and ε is the error in the model. The fit can be described by the statistic R^2, which quantifies how much of the total variation in the data is accounted for by Eqn. B.1. Given a set of n data points $\{y_i\}$, with mean value $\bar{y}$ and a function f which makes a set of predictions for each data point, $\{f_i\}$, R^2 is defined as:

$$R^2 = 1 - \frac{SS_{model}}{SS_{total}} = 1 - \frac{\sum_{i=0}^{n}(y_i - f_i)^2}{\sum_{i=0}^{n}(y_i - \bar{y})^2} \tag{B.2}$$

The term SS_{total} is the sum of squares about the mean value of the data $\bar{y}$ and is proportional to the total variance of the data. SS_{model} is the the sum of squared errors between the data predictions of the model, thus it is the unexplained variance. The ratio SS_{model}/SS_{total} is then the fraction of the total variance that is not explained by the model, so $1 - SS_{model}/SS_{total}$ is the fraction of variance that is explained by the model. A high value of R^2 then implies that the model accounts for a large amount of the variability in the data.

Hypothesis testing is required to determine if the observed trend in data is significant, that is that a non-zero value of R^2 is not observed by chance. For linear models, the appropriate test is an F-test.

The F-test compares the sum of squared errors between nested models. A nested model is a special case of a more general model; in the case of of univariate linear regression, the models which the F-test considers are:

$$Y = \beta_0 + \beta_1 x + \varepsilon \tag{B.3}$$

$$Y = \beta_0 + \varepsilon. \tag{B.4}$$

Equation B.4, called the restricted model, it is said to be nested within the full model, Eqn. B.3 since it is a special case when $\beta_1 = 0$. The F-test will determine if adding the extra variable x and parameter β_1 helps to predict the value of y, and so it can be used to decide if the relationship between x and y is significant. The F-test statistic is given by:

$$F = \frac{(SS_{restricted} - SS_{full})/(d_2 - d_1)}{SS_{full}/(n - d_2)}. \tag{B.5}$$

The term $SS_{restricted} - SS_{full}$ is proportional to the variance that is explained by including the extra variable x in the model, and SS_{full} is proportional to the variance not explained by including x, that is the variance not explained by the full model. Therefore the F-statistic is the ratio of variance explained by x to the variance not explained by x. Note that this is slightly different to the interpretation of R^2, which is the ratio of the variance explained by a model to the total variance of the data. The parameters d_1, d_2 are the number of degrees of freedom of the restricted and full models, respectively; in the case of the models described by Eqns. B.3 and B.4, $d_1 = 1$ and $d_2 = 2$. They are included to convert the sums of squares into variances. The null hypothesis, H_0 and the alternative hypothesis, H_1 of the F-test are:

- H_0: $\beta_1 = 0$
- H_1: $\beta_1 \neq 0$

If the variance explained by x is large, and the variance not explained by x is small, then the F-statistic will be large. Observing a large F-statistic is evidence that the null hypothesis is false, since if it was true, $SS_{restricted}$ and SS_{full} would be approximately equal.

The F-statistic is itself a random variable and follows a distribution, called the F-distribution, denoted F_{ν_1,ν_2}, who's shape depends on two parameters, $\nu_1 = d_2 - d_1$ and $\nu_2 = n - d_2$. The p-value is the probability of obtaining the observed value of the F-statistic,

denoted F_c, or a value equally or less probable, given that the null hypothesis is in fact true. Mathematically, this is expressed as:

$$p = \mathbb{P}(F_{\nu_1,\nu_2} \geq F_c) = \int_{F_c}^{\infty} F_{\nu_1,\nu_2} dx, \tag{B.6}$$

Large values of F have a small probability of occurring given that the null hypothesis is true; if this probability is less than the significance level of the experiment (the probability the null hypothesis is rejected given that it is in fact true) then the null hypothesis is rejected and the relationship between x and y is said to be significant. The p-value will be used in order to determine if there is a statistically significant trend between measured quantities and experimental parameters.

Linear regression can also be extended to fit models which are non-linear in the independent variable x but linear in the model parameters $\{\beta_i\}$ and the same analysis applies: linear regression can be used to fit a quadratic model to data, for example.

ANOVA tests

The ANOVA test determines if the mean values of three of more groups of measurements, defined by one or more categorical, independent variables, are significantly different from each other. For the case when there are two categorical variables, the appropriate test is called a 2-way ANOVA. Given a numerical, response variable y and two categorical variables x and z, which can take n and m values, respectively, the total number of groups will be $n \times m$. The 2-way ANOVA will test if there is a significant difference between mean values of the n groups corresponding to x; if there is a significant difference between mean values of the m groups corresponding to z; and if there is a significant difference between mean values of the $n \times m$ groups corresponding to both x and z. The 2-way ANOVA tests 3 null hypotheses:

- H_0: x has no effect on the mean value of y.
- H_0: z has no effect on the mean value of y.
- H_0: There is no interaction between x and z that has an effect on the mean value of y.

Significance is tested in a similar way to regression, in that for each null hypothesis, a p-value is calculated from the F-distribution and the F-statistic. In the case of ANOVA, the F-statistic is the ratio of variance between groups of measurements to the variance within each group of measurements. The variance between groups is sometimes referred to as the explained variance, and the the variance within groups is refereed to as unexplained variance. This can be written as:

$$F = \frac{\sum_{i=1}^{k}(\bar{y}_i - \bar{y})^2/(k-1)}{\sum_{i=1}^{k}\sum_{j=1}^{n_i}(y_{ij} - \bar{y}_i)^2/(n-k)}, \tag{B.7}$$

where k is the number of groups, n_i is the number of data points in group i, $\bar{y}_i$ is the mean of the ith group, $\bar{y}$ is the overall mean of the data, y_{ij} is the jth element of group i, and n is the total number of data points. Again the F-statistic follows the F-distribution under the null hypothesis, with degrees of freedom, $\nu_1 = k-1$, $\nu_2 = n-k$. F will be large when the variance between groups is large relative to the variance within each group, which is unlikely to occur if the null hypothesis is true. The p-value is then calculated from Eqn. B.6. The ANOVA test is useful because it tests multiple hypothesis at the same time however it does not say which mean values are significantly different, and further tests must be performed. The only further tests which is used in this work will be t-tests (sometimes called Student's t-test), which compare the mean value of only two groups of measurements, that is a single, binary categorical variable.

Student's t-test

The idea behind a t-test is similar to an F-test, however the t-statistic has a slightly different definition to the the F-statistic and it follows the t-distribution as opposed to the F-distribution, however the t-test still computes a p-value and compares it to a chosen significance level. The definition of the t-statistic is:

$$t = \frac{\bar{y}_1 - \bar{y}_2}{s_p\sqrt{2/n}}, \tag{B.8}$$

where $\bar{y}_1$ and $\bar{y}_2$ are the mean values of groups 1 and 2, and s_p is the pooled standard deviation of the two groups and the factor $\sqrt{2/n}$ converts the standard deviation into the standard error of the difference between the two group means. The t-distribution has only one parameter, $\nu_1 = n-1$. The exact form of s_p changes depending on if the group sizes are equal and if they have equal variance; in the data analysed here, groups have the same size and approximately equal variance, and the pooled standard deviation is given by:

$$s_p = \sqrt{\frac{s_1^2}{n_1} + \frac{s_2^2}{n_2}}, \tag{B.9}$$

where s_1^2 and s_2^2 are the variances of groups 1 and 2, respectively.

ANOVA and t-tests do not provide the actual magnitude of the difference between means, they only say if the difference is statistically significant. The absolute difference between the means is one metric which can be used to evaluate the difference. Another is a quantity

called Cohen's d, which expresses the difference between the means as a proportion of the pooled standard deviation of two groups:

$$d = \frac{\bar{y}_1 - \bar{y}_2}{s_p} = t\sqrt{2/n} \tag{B.10}$$